

DOE-ER-0313/49
Distribution
Categories
UC-423, -424

**FUSION MATERIALS
SEMIANNUAL PROGRESS REPORT
FOR THE PERIOD ENDING**

December 31, 2010

**Prepared for
DOE Office of Fusion Energy Sciences
(AT 60 20 10 0)**

DATE PUBLISHED: March 2011

**Prepared by
OAK RIDGE NATIONAL LABORATORY
Oak Ridge, Tennessee 37831
Managed by
UT-Battelle, LLC
For the
U.S. DEPARTMENT OF ENERGY**

FOREWORD

This is the forty-ninth in a series of semiannual technical progress reports on fusion materials science activity supported by the Fusion Energy Sciences Program of the U.S. Department of Energy. It covers the period ending December 31, 2010. This report focuses on research addressing the effects on materials properties and performance of exposure to the neutronic, thermal and chemical environments anticipated in the chambers of fusion experiments and energy systems. This research is a major element of the national effort to establish the materials knowledge base for an economically and environmentally attractive fusion energy source. Research activities on issues related to the interaction of materials with plasmas are reported separately.

The results reported are the product of a national effort involving a number of national laboratories and universities. A large fraction of this work, particularly in relation to fission reactor irradiations, is carried out collaboratively with partners in Japan, Russia, and the European Union. The purpose of this series of reports is to provide a working technical record for the use of program participants, and to provide a means of communicating the efforts of fusion materials scientists to the broader fusion community, both nationally and worldwide.

This report has been compiled under the guidance of F. W. (Bill) Wiffen, Renetta Godfrey, and Betty Waddell, Oak Ridge National Laboratory. Their efforts, and the efforts of the many persons who made technical contributions, are gratefully acknowledged.

G. R. Nardella
Research Division
Office of Fusion Energy Sciences

TABLE OF CONTENTS

1. FERRITIC/MARTENSITIC STEELS

See also items 6.1, 6.2, and 6.3.

1.1 TEM OBSERVATION OF DUAL ION BEAM IRRADIATED F82H MOD.3 AND MA957 – 1 T. Yamamoto, Y. Wu, G. R. Odette (University of California Santa Barbara), K. Yabuuchi, A. Kimura (Kyoto University)

Microstructures of tempered martensitic steel F82H mod.3 and NFA MA957 have been characterized after dual ion beam (Fe^{3+} and He^+) irradiation to a nominal condition of 10 dpa and 400 appm He at $\approx 480^\circ\text{C}$. The irradiations were performed at dual beam facility, DuET, located at Kyoto University in Japan. Helium bubbles were found at depths greater than 300 nm in F82H mod.3. The average bubble diameter was larger and the number density comparable to or lower than for those observed following in situ He implanter (ISHI) irradiations in the HFIR JP26 experiment at 500°C at similar dpa and He levels (9 dpa and 380 appm He), but at much lower dpa rates. A few larger cavities, that are likely voids, were observed following the DuET irradiation. However, a bimodal bubble and void size distribution was less apparent in the DuET case, compared to the ISHI results. No He bubbles were observed in MA957 following DuET irradiation to a condition similar to that for the JP26 ISHI experiment where bubbles were observed. Bubbles were only visible at DuET conditions of > 15 dpa and He > 550 appm, and they were less numerous than found in the ISHI irradiation at lower damage and He levels.

1.2 FURTHER ATOM PROBE TOMOGRAPHY STUDIES OF NANOSTRUCTURED 11 FERRITIC ALLOY MA957 IN THREE CONDITIONS – Nicholas J. Cunningham, G. Robert Odette and Erich Stergar, University of California – Santa Barbara

We report on atom probe tomography (APT) studies on nano-structured ferritic alloys (NFAs) that contain an ultrahigh density of nm-scale Y-Ti-O nanofeatures (NFs). A local electrode atom probe (LEAP) was used to characterize the NFs in both as-extruded bar (US) and thick walled tube (French) heats of MA957. APT was also carried out on the US MA957 following long-term thermal aging (LTTA) at 1000°C for 19 kh. The as-extruded US MA957 was found to contain $\approx 3.2 \times 10^{23}$ NFs/ m^3 with an average diameter of ≈ 2.4 nm. The French MA957 tubing contained an average of 6.1×10^{23} NFs/ m^3 with an average diameter of ≈ 2.8 nm. The average Y/Ti/O ratio of $\approx 13/47/40$ was similar in both heats. The NFs coarsen under 1000°C LTTA, with average number densities and diameters decreasing to 7×10^{22} NFs/ m^3 and increasing to ≈ 2.8 nm, respectively. The NF composition in the aged condition is relatively unchanged with only a slight increase in the Y/Ti ratio.

2. CERAMIC COMPOSITE STRUCTURAL MATERIALS

2.1 TITAN TASK 2-3 SILICON CARBIDE BEND STRESS RELAXATION CREEP STUDY: 17 PHASE-II EXPERIMENT – Y. Katoh, K. Ozawa (Oak Ridge National Laboratory), and T. Hinoki (Kyoto University)

A study of irradiation creep behavior of silicon carbide ceramics and composites is part of Task 2-3 of the US/Japan TITAN collaboration on fusion materials and blanket technology. In the Phase-I experiment, low fluence irradiation creep behavior of monolithic silicon carbide ceramics was

TABLE OF CONTENTS

studied using the bend stress relaxation (BSR) technique. The objective of the Phase-II experiment is to gain understanding of the stress relaxation and creep behavior of silicon carbide ceramics, fibers, and composites under neutron irradiation to higher fluences at elevated temperatures. The neutron irradiation will be performed using the fixed rabbit facilities of the High Flux Isotope Reactor. The Phase-II program will irradiate 13 rabbit capsules; 8 for monolithic and composite samples and 5 for fiber samples. Target irradiation temperatures are 300, 500, 800, and 1200°C. The present schedule assumes the initiation of irradiation in early 2011.

2.2 LOW ACTIVATION JOINING OF SiC/SiC COMPOSITES FOR FUSION APPLICATIONS – 25

C. H. Henager, Jr., R. J. Kurtz (Pacific Northwest National Laboratory, Richland, WA 99336, USA), and M. Ferraris, (Politecnico di Torino, Torino, Italy)

The use of SiC composites in fusion environments may require joining of plates using reactive joining or brazing. One promising reactive joining method is the use of solid-state displacement reactions between Si and TiC to produce $Ti_3SiC_2 + SiC$. We continue to explore the processing envelope for this type of joint for the TITAN collaboration to produce the best possible joints to undergo irradiation studies in HFIR. The TITAN collaboration has designed miniature torsion joints for preparation, testing, and irradiation in HFIR. As part of that project PNNL synthesized 40 miniature torsion joints and several were tested for shear strength prior to irradiation testing in HFIR. The resulting tests indicated that joint fixture alignment problems cause joint strengths to be lower than optimal but that several joints that were well aligned had high shear strengths and promising mechanical properties. High joint strengths cause non-planar shear fracture and complicate strength analysis for these miniature torsion joints.

2.3 CHARACTERIZATION BY SEM OF THE PYROCARBON FIBER COATING IN 2D-SiC/CVI-SiC – 31

G. E. Youngblood (Pacific Northwest National Laboratory)

The previous report examined electrical conductivity (EC) data from RT to 800°C for several forms of two-dimensional silicon carbide composite made with a chemical vapor infiltration (CVI) matrix (2D-SiC/CVSiC), an important quantity needed for the design of an FCI. We found that both in-plane and transverse EC-values for 2D-SiC/CVI-SiC strongly depended on the total thickness of the highly conductive pyrocarbon (PyC) fiber coating and the alignment of the carbon coating network. Furthermore, the transverse EC depended on the degree of interconnectivity of this network. For our EC-modeling efforts we used either “nominal” coating thickness values provided by the composite fabricator or we made thickness estimates based on a limited number of fiber cross-section examinations using SEM. Because of the importance of using a truly representative coating thickness value in our analysis, we examined numerous new SEM cross-sectional views to reassess the reliability of our limited number of original coating thickness measurements as well as to obtain an estimate of the variation in thickness values for different composite configurations.

TABLE OF CONTENTS

- 2.4 EVALUATION OF DAMAGE TOLERANCE OF ADVANCED SiC/SiC COMPOSITES AFTER NEUTRON IRRADIATION – 38**
 K. Ozawa, Y. Katoh, L.L. Snead (Oak Ridge National Laboratory), T. Nozawa (Japan Atomic Energy Agency), T. Hinoki (Kyoto University)
- The effect of neutron irradiation on damage tolerance of two nuclear grade SiC/SiC composites (plain-woven Hi-Nicalon™ Type-S fiber-reinforced, CVI SiC matrix composites with a multilayer interphase and unidirectional Tyranno™-SA3 fiber-reinforced, NITE matrix with a carbon monolayer interphase) was evaluated by means of miniaturized single-edged notched-beam test. No significant changes in crack extension behavior and in the load-loadpoint displacement characteristics such as the peak load and hysteresis loop width were observed after irradiation to 5.9×10^{25} n/m² ($E > 0.1$ MeV) at 800°C and to 5.8×10^{25} n/m² at 1300°C. The global energy balance analysis based on non-linear fracture mechanics estimated the energy release rate contributed by macro-crack initiation to be 3 ± 2 kJ/m² for both the unirradiated and irradiated composites. The effects of neutron irradiation on fracture resistance of these composites appeared insignificant for the conditions examined.
- 3.0 REFRACTORY METALS AND ALLOYS**
- See also item 6.4.*
- 3.1 THERMO-MECHANICAL DAMAGE OF TUNGSTEN SURFACES EXPOSED TO RAPID TRANSIENT PLASMA HEAT LOADS – 44**
 T. Crosby and N.M. Ghoniem (University of California, Los Angeles)
- Tungsten has one of the highest melting points of any metallic material, and for this reason, it is used in applications where extreme heat fluxes and thermo-mechanical conditions are expected. Recently, international efforts have focused on the development of tungsten surfaces that can intercept energetic ionized and neutral atom and heat fluxes in the divertor region of magnetic fusion confinement devices, and as armor in chamber wall applications in inertial confinement fusion energy systems. The combination of transient heating and local swelling due to implanted helium and hydrogen atoms has been experimentally shown to lead to severe surface and sub-surface damage. The thermo-mechanical model is based on elasticity, coupled with a reaction-diffusion model of material swelling and grain boundary degradation due to helium and deuterium bubbles resulting from the plasma flux. This material state is also coupled with a transient heat conduction model for temperature distributions following rapid thermal pulses. The multi-physics model includes contact cohesive elements for grain boundary sliding and fracture. Results of the computational model are compared to experiments on tungsten bombarded with energetic helium and deuterium particle fluxes.
- 3.2 MECHANICAL PROPERTIES OF W-1.1%TiC ALLOY – 52**
 M. A. Sokolov (Oak Ridge National Laboratory)
- A small disk of W-1.1%TiC alloy produced by Japanese researchers led by Hiroaki Kurishita was sent to ORNL for mechanical testing and characterization. The purpose of the study is to evaluate the effect of small additions of TiC in improving the performance of W-based materials designed for operation in the divertor environment. This is part of on-going efforts of the international fusion community to understand and improve the ductility and toughness of W-based materials using nano-scale microstructural modification. A test plan was developed to perform limited

TABLE OF CONTENTS

fracture toughness and tensile evaluation of this alloy. The results of this evaluation will be presented in the next semi-annual report.

4.0 OTHER STRUCTURAL AND SPECIAL PURPOSE MATERIALS

No contributions this period.

5. CORROSION AND COMPATIBILITY

5.1 COMPATIBILITY OF MATERIALS EXPOSED TO ISOTHERMAL Pb-Li – 54 B. A. Pint and K. A. Unocic (Oak Ridge National Laboratory, USA)

Initial isothermal capsule experiments were conducted to compare the behavior of oxide dispersion strengthened (ODS) Fe-Cr alloys to prior results on wrought ferritic-martensitic (FM) alloys. Also, the performance of corrosion resistant, Al-rich diffusion coatings on these alloys was investigated. To further understand the performance of these coatings in Pb-Li, several experiments are in progress including a time series of experiments and a more detailed study of the unexpectedly high Al loss observed in prior experiments. New Pb-Li was cast to eliminate the prior issue of Li composition variability. Finally, to investigate any potential dissimilar material interaction between Fe and SiC, a set of capsules with SiC inner capsules is being assembled for exposures at 500, 600 and 700°C.

6.0 THEORY AND MODELING

6.1 DIFFUSION OF He INTERSTITIALS AND He CLUSTERS IN α -Fe – 58 H. Deng (Hunan University), F. Gao, H. L. Heinisch and R. J. Kurtz (Pacific Northwest National Laboratory)

The accumulation of He atoms in materials will significantly degrade the mechanical properties of materials; therefore, understanding the properties of He interstitials and their clusters in materials is of fundamental importance within a fusion reactor environment. The diffusion properties of single He interstitials and He clusters in the bulk and grain boundaries of α -Fe are being studied using molecular dynamics with a new Fe-He potential. It is found that the migration barrier for a single He interstitial in the bulk is very low, which is consistent with the result obtained using *ab initio* methods. Large He clusters can cause Fe self-interstitial atoms (SIA) to be formed, which can be trapped by the resulting vacancy, forming a He-vacancy complex. It is found that for He interstitials in grain boundaries (GBs), the He migration is one-dimensional in a $\Sigma 11$ GB, while it is two-dimensional in a $\Sigma 3$ GB at 600 K and three-dimensional at higher temperatures.

6.2 ATOMISTIC STUDIES OF PROPERTIES OF HELIUM IN BCC IRON USING THE 66 NEW He-Fe POTENTIAL –

David M. Stewart, Stanislav Golubov (Oak Ridge National Laboratory and the University of Tennessee), Yuri Ostesky, Roger E. Stoller, Tatiana Seletskaya, and Paul Kamenski (Oak Ridge National Laboratory)

We have performed atomistic simulations of helium bubble nucleation and behavior in iron using a new 3-body Fe-He inter-atomic potential combined with the Ackland iron potential. Updated results from ongoing large simulations examining the nucleation of helium defects are presented. MS simulations of the change in pressure when a void is added to a perfect crystal are used to

TABLE OF CONTENTS

estimate the pressure of an equilibrium helium bubble of the same size. This method is independent of the choice of helium potential. When an Fe interstitial encounters a helium bubble, it can recombine with one of the vacancies in the bubble, leading to a bubble with a higher He/V ratio and hence pressure. We investigate how far this process can go before the bubble will not accept any more SIAs.

6.3 **A MULTI-SCALE MODEL OF HELIUM TRANSPORT AND FATE IN IRRADIATED TEMPERED MARTENSITIC STEELS AND NANOSTRUCTURED FERRITIC ALLOYS –** 73

T. Yamamoto, G.R. Odette (Department of Mechanical Engineering, University of California Santa Barbara), R.J. Kurtz (Materials Science Division, Pacific Northwest National Laboratory) and B.D. Wirth (University of Tennessee, Knoxville)

Development and application of a multiscale model of the transport and fate of He in irradiated nanostructured ferritic alloys and tempered martensitic steels are described. Model predictions for He bubble average size, size distribution and number density are in reasonably good agreement with recent observations in in situ helium implanter experiments on F82H mod.3, 12YWT and MA957.

6.4 **FIRST-PRINCIPLES INVESTIGATION OF THE INFLUENCE OF ALLOYING ELEMENTS ON THE ELASTIC AND MECHANICAL PROPERTIES OF TUNGSTEN –** 90

G. D. Samolyuk, Y. N. Osetskiy, and R. E. Stoller (Oak Ridge National Laboratory)

The equilibrium lattice parameter, elastic constants and phonon dispersions were calculated for a set of binary $W_{1-x}Tm_x$ alloys with different transition metal, Tm, concentrations within the local density approximation of density functional theory. Reasonable agreement between results obtained using conventional super-cell and virtual crystal approximation approaches has been demonstrated. Alloying W with transition metals with larger number of d-electrons changes the symmetry of the core of a dislocation from symmetric to asymmetric and reduces the value of the Peierls barrier.

7. **IRRADIATION AND EXPERIMENTAL METHODS AND ANALYSIS**

7.1 **IRRADIATION TEMPERATURE DETERMINATION OF HFIR TARGET CAPSULES USING DILATOMETRIC ANALYSIS OF SILICON CARBIDE MONITORS –** 94

T. Hirose, N. Okubo, H. Tanigawa (Japan Atomic Energy Agency), Y. Katoh, A.M. Clark, J.L. McDuffee, D.W. Heatherly, R.E. Stoller (Oak Ridge National Laboratory)

The irradiation temperatures of the HFIR target capsules JP-26 and JP-27 were determined by dilatometric analysis of silicon carbide passive temperature monitors. The monitors from holders for SSJ3 tensile specimens demonstrated good agreement with the design temperatures derived from finite element model (FEM) analysis and were consistent with post-irradiation hardness of F82H. Although the irradiation temperatures for some bend-bar (PCCVN and DFMB) holders were higher than FEM analysis, hardness tests on irradiated F82H implied that actual irradiation temperatures were close to the design temperatures.

TABLE OF CONTENTS

7.2	ESTIMATION OF HELIUM PRODUCTION BY THE NICKEL FOIL IMPLANTER TECHNIQUE FOR BEND STRESS RELAXATION TESTS IN THE TITAN PHASE II RABBIT IRRADIATION CAMPAIGN –	100
	K. Ozawa, Y. Katoh, L.L. Snead (Oak Ridge National Laboratory), T. Yamamoto (University of California, Santa Barbara), T. Hinoki (Kyoto University), A. Hasegawa (Tohoku University)	
	<p>He profiles in bend stress relaxation specimens from the thin Ni foil implanter technique were calculated for the TITAN Phase II Campaign. The calculations revealed that the distribution of the implanted transmuted helium is uniform at 2.1, 15 and 21 appm He/dpa to a depth of 11 μm for the case of a 2 μm-thick implanter foil for irradiation to 1, 10 and 20×10^{25} n/m^2 ($E > 0.1$ MeV), equivalent to 1, 10, and 20 dpa-SiC in the HFIR-PTP. It is noted that the He/dpa ratio is strongly fluence dependent, since natural Ni was used for the implanter foil and hence the He is produced by a two neutron capture sequence.</p>	
8.0	IRRADIATION EXPERIMENTS AND TEST MATRICES	
8.1	OPERATING CONDITIONS AND IRRADIATION HISTORY FOR EXPERIMENT MFE-RB-15J –	110
	J. McDuffee, D. Heatherly (Oak Ridge National Laboratory)	
	<p>The MFE-RB-15J experiment was designed to irradiate steel specimens at 300 and 400°C for 10 cycles in the RB* irradiation facility in HFIR. The irradiation vessel was divided into three subcapsules. The specimen regions of the upper and lower subcapsules were about 7.7 cm long, located ± 14 cm from the reactor midplane, and designed to operate at 300°C. The specimen region of the middle subcapsule was about 11.5 cm long, centered at the reactor midplane, and designed to operate at 400°C.</p>	
	<p>Each subcapsule was filled with lithium, which became molten during operation and solidified during reactor outages. Thermocouples were located at the centerline of each subcapsule and extended upward through part of the axial length of the subcapsule.</p>	
	<p>Because of concerns over the potential for a volatile reaction between the lithium and water in the event of a containment failure, the specimen-containing subcapsules were housed inside two outer containments. There were small gas gaps between the primary and secondary containments and between the secondary containment and the subcapsules. The outer gas gap was filled with helium. The inner gas gap was filled with a mixture of helium and neon, and the relative concentrations of the two were controlled to provide the gas conductivity necessary to achieve the desired temperatures. The gas compositions for each of the three subcapsules were controlled separately, although not completely independently.</p>	
8.2	DESIGN OF THE JP30 AND JP31 EXPERIMENTS –	115
	J. McDuffee, D. Heatherly, N. Cetiner (Oak Ridge National Laboratory)	
	<p>Two experiments, JP30 and JP31, have been designed to place various stainless steel specimens in the flux trap of the High Flux Isotope Reactor (HFIR). These designs are very similar to other experiments irradiated previously in HFIR (e.g., JP26, JP27, JP28, JP29).</p>	

TABLE OF CONTENTS

The JP30 and JP31 experiments are designed to irradiate F82H specimens of various sizes and types in the flux trap of HFIR at temperatures in the range of 300 to 650°C. The specimens are typically contained within holders of either DISPAL (dispersion-strengthened aluminum) or a vanadium alloy (V-4Cr4Ti). The primary outer containment is an Al-6061 tube with an outer diameter of 1.27 cm. Helium is used as the fill gas inside the experiment. The specimen temperature is controlled by the size of the gap between the holder and housing. This report summarizes the work described in the design and analysis calculation for this project.

8.3 HFIR IRRADIATION EXPERIMENTS – December 31, 2010 – 134 F. W. Wiffen (ORNL)

Summary of recent, current, and planned Fusion Materials Program Experiments in the High Flux Isotope Reactor (HFIR).

1.1 TEM Observation of Dual Ion Beam Irradiated F82H mod.3 and MA957 –T. Yamamoto, Y. Wu, G. R. Odette (University of California Santa Barbara), K. Yabuuchi, A. Kimura (Kyoto University)

OBJECTIVE

The objective of this work is to characterize cavity evolution under Fe^{3+} and He^+ dual ion beam irradiation in two fusion reactor candidate structural alloys: a normalized and tempered martensitic steel, (TMS) F82H mod.3: and, a nanostructured ferritic alloy (NFA), MA957. The dpa and He/dpa ratio varied with the depth in the sample, but at intermediate locations were ≈ 10 dpa and ≈ 40 appm He/dpa, respectively. The irradiation temperature was 480°C . The dual ion results are compared to in situ He injection experiments in HFIR for similar irradiation conditions, but at a much lower dpa rate.

SUMMARY

TEM microstructures of TMS F82H mod.3 and NFA MA957 have been characterized after dual ion beam (Fe^{3+} and He^+) irradiation to a nominal condition of 10 dpa and 400 appm He at $\approx 480^\circ\text{C}$. The irradiations were performed at dual beam facility, DuET, located at Kyoto University in Japan. Helium bubbles were found at depths greater than 300 nm in F82H mod.3. The average bubble diameter was larger and the number density comparable to or lower than for those observed following in situ He implanter (ISHI) irradiations in the HFIR JP26 experiment at 500°C at similar dpa and He levels (9 dpa and 380 appm He), but at much lower dpa rates. A few larger cavities, that are likely voids, were observed following the DuET irradiation. However, a bimodal bubble and void size distribution was less apparent in the DuET case, compared to the ISHI results. No He bubbles were observed in MA957 following DuET irradiation to a condition similar to that for the JP26 ISHI experiment where bubbles were observed. Bubbles were only visible at DuET conditions of > 15 dpa and He > 550 appm, and they were less numerous than found in the ISHI irradiation at lower damage and He levels.

PROGRESS AND STATUS

Introduction

Predicting and mitigating the effects of a combination of large levels of transmutant He and displacement damage (dpa), produced by high energy neutrons, on the dimensional stability and mechanical properties of structural materials is one of the key challenges in the development of fusion energy [1]. The fundamental overriding questions about He-dpa synergisms include: a) What are the basic interacting mechanisms controlling He and defect transport, fate and consequences, and how are they influenced by the starting microstructure and irradiation variables (dpa rate, He/dpa ratio, temperature and applied stress); and, b) how can the detrimental effects of He-dpa synergisms be mitigated and managed by proper microstructural design?

We have previously demonstrated that in situ He implantation (ISHI) in mixed spectrum fission reactor irradiations provides a very attractive approach to assessing the effects of He-dpa synergisms, while avoiding most of the confounding effects associated with Ni- or B-doping type experiments [1-8]. Another approach to study He-dpa synergism is to use multiple ion beams to simultaneously implant He and create displacement damage with heavy ions [1,9-12]. In spite of an apparent similarity, the two techniques have many differences that include the dpa rate, the spatial distribution of damage and He and the proximity of a free surface. Thus comparing the microstructural evolutions in the same alloys for

the two different irradiation conditions is an important objective and provides a basis to inform, calibrate and validate predictive models.

Experimental Procedure

The alloys studied here are a TMS F82H mod.3 and a NFA MA957. The F82H series is the most widely used TMS alloys for variety of studies including the He effects [1,3,7,11-17]. In the case of F82H mod.3, the base composition of F82H-IEA (nominally, 7.5%Cr 2%W 0.2%V 0.1%C 0.1%Si 0.02%Ta 60ppmN) was modified to reduce N and Ti to 14 ppm and 0.001%, respectively, and to add 0.1% Ta [13]. The steel was austenitized at 1040°C for 30 min, normalized (air-cooled), and tempered at 740°C for 1.5 h. F82H mod.3 has a fine prior-austenite grain size (ASTM 9.5) along with a finer scale lath structure formed in the process of martensitic transformation [13]. MA957 is a representative NFA that is gaining growing interest for the radiation resistance especially with a good He management as well as the good high temperature mechanical properties [1,5,8,18,19]. As-extruded MA957 has a fine scale elongated grain structure with nano-meter scale oxide features (NF) dispersed as strengthening obstacles. The typical grain size is about 1 and 5 μm in the transverse and axial directions, respectively. More details of the materials including the chemical compositions and microstructure are given elsewhere [5,13,18,19].

Two 3 mm diameter disks of the alloys were mechanically ground to a nominal 200 μm thickness were cut into small sections to fit into the ion beam specimen holder. The surface of the section was electro-polished before irradiation. Dual ion beam irradiation was performed in DuET facility in the Institute of Advanced Energy, Kyoto University (Kyoto, Japan), where Fe^{3+} ions accelerated to 6.4MeV by a tandem accelerator and He^+ ions accelerated to 1MeV by a single end accelerator were simultaneously induced to the specimens held in a temperature control stage [20]. The He^+ ion beam was passed through a rotating beam energy degrader that results in He^+ ions in four energy intervals resulting a broader uniform He deposition profile.

Figure 1 shows depth profile of the displacement damage and He deposition calculated with SRIM 2006 code. The irradiation was performed so that the nominal conditions of 10 dpa and 400 appm He were achieved at the location 600 nm from the specimen surface. The implantation covers a range of He, He/dpa ratios, dpa and dpa rates. The region between ≈ 400 to 1000 nm has an approximately constant 40 ± 5 appm He/dpa ratio, and the region between ≈ 400 and 700 nm accumulated a net dose of $\approx 10\pm 2$ dpa. The corresponding dpa rate was ≈ 3 to 6×10^{-4} dpa/s. The specimen temperature was controlled at $\approx 480^\circ\text{C}$. More generally, the dpa increase to a peak at ≈ 32 dpa at 1600 nm, while the He and He/dpa decrease with increasing depth greater than 1000 nm, approaching 0 at about 1500 nm. Thus, in principle, the DuET irradiation provides a basis to evaluate the effects of a range of irradiation variables, including high dpa with no He as well as undamaged regions.

A FEI HELIOS Focused Ion Beam (FIB) tool was used to micromachine < 100 nm thick electron transparent lift-outs ≈ 5 μm wide and 5 μm deep. Post irradiation TEM was performed on the 200 keV FEI T20 instrument in the UCSB microstructure and microanalysis facility. Through focus bright field imaging used to characterize the cavities. The cavity images were manually marked for location and size and the image analysis software package Image-J was used to determine cavity area number densities and size distributions. The foil thickness, needed to compute volume number densities, was confirmed by convergent beam electron diffraction measurements.

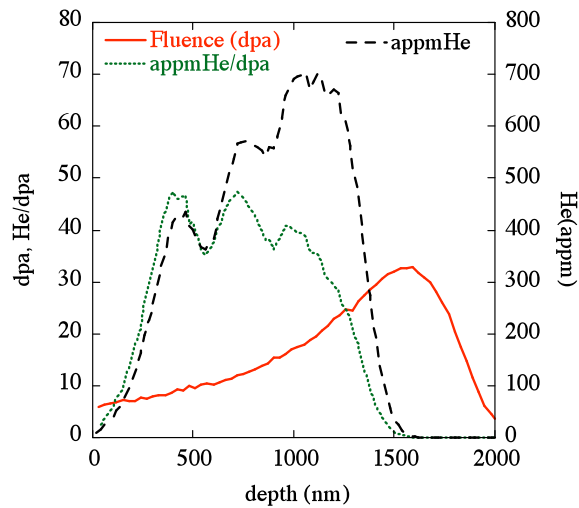


Figure 1. Depth profile of displacement damage and He deposition in the specimens in the DuET dual ion beam irradiation calculated with SRIM 2006 code.

Results and Discussion

Microstructure of dual ion beam irradiated F82H mod.3

Figure 2 shows the low magnification TEM image of the dual ion beam irradiated F82H mod.3 at under-focus condition. Cavities were observed only at the locations between ≈ 300 and 1500 nm from the surface. The 1500 nm corresponds to the He implantation depth. Figure 3 and Figure 4 show high magnification cavity images covering the depths between about 500 to 1000 nm and 1000 to 1500 nm, respectively. The bubbles are strongly associated with dislocations, boundaries and precipitates. The string of pearls arrangements of the bubbles indicate the strong dislocation association. The bubbles on boundaries and precipitates are smaller and more numerous than those formed on dislocations. Significant homogeneous bubble nucleation in the matrix is not observed. The overall bubble sizes are roughly similar in the two regions. A small number of larger faceted cavities with diameters > 7 nm, that are likely voids, are found in the deeper region, corresponding to higher dpa and lower He concentrations and He/dpa ratios.

Figure 5 shows the average diameter and number density as a function of depth. These analyses were performed for the areas sectioned in 100 nm steps so that, for example, the data for 400 nm represents the area at a depth from 400 to 500 nm. The significant “scatter” is largely due to variations in the local microstructure. There is a slight general trend to a decrease in the average diameter of the bubbles with depth that may be due to the irradiation conditions. The average diameter of the bubble at a depth of 600 nm is ≈ 4 nm. The corresponding number densities are lower up to about 700 nm with values of $\approx 4.5 \pm 1 \times 10^{22}/\text{m}^3$, followed by a peak density of $\approx 1.2 \times 10^{23}/\text{m}^3$ at 800 nm that is then followed by a decrease at greater depths up to the end of the He deposition range.

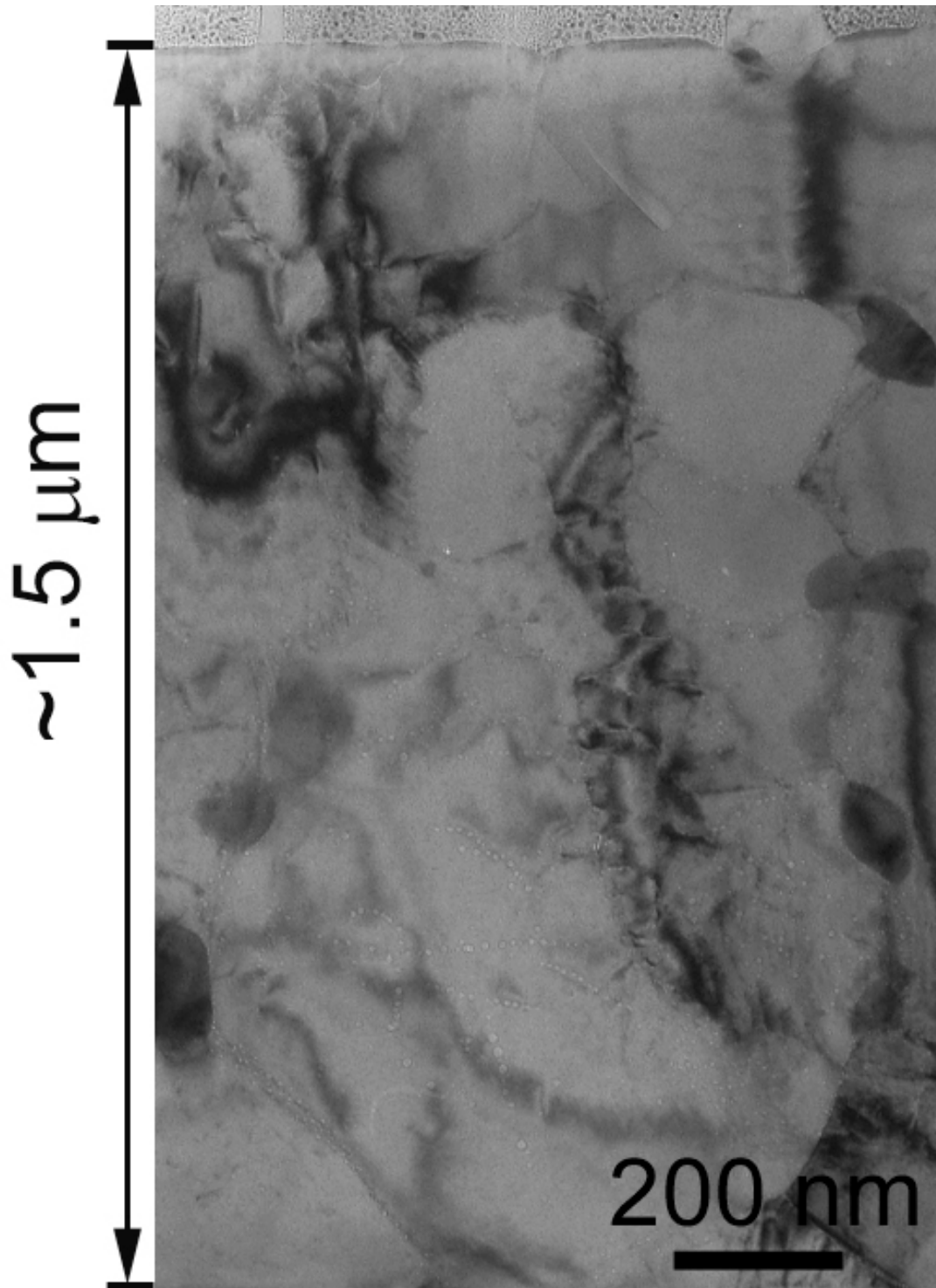


Figure 2. Low magnification under-focused TEM image showing He bubbles in F82H mod.3 after dual beam irradiation over the He deposition zone.

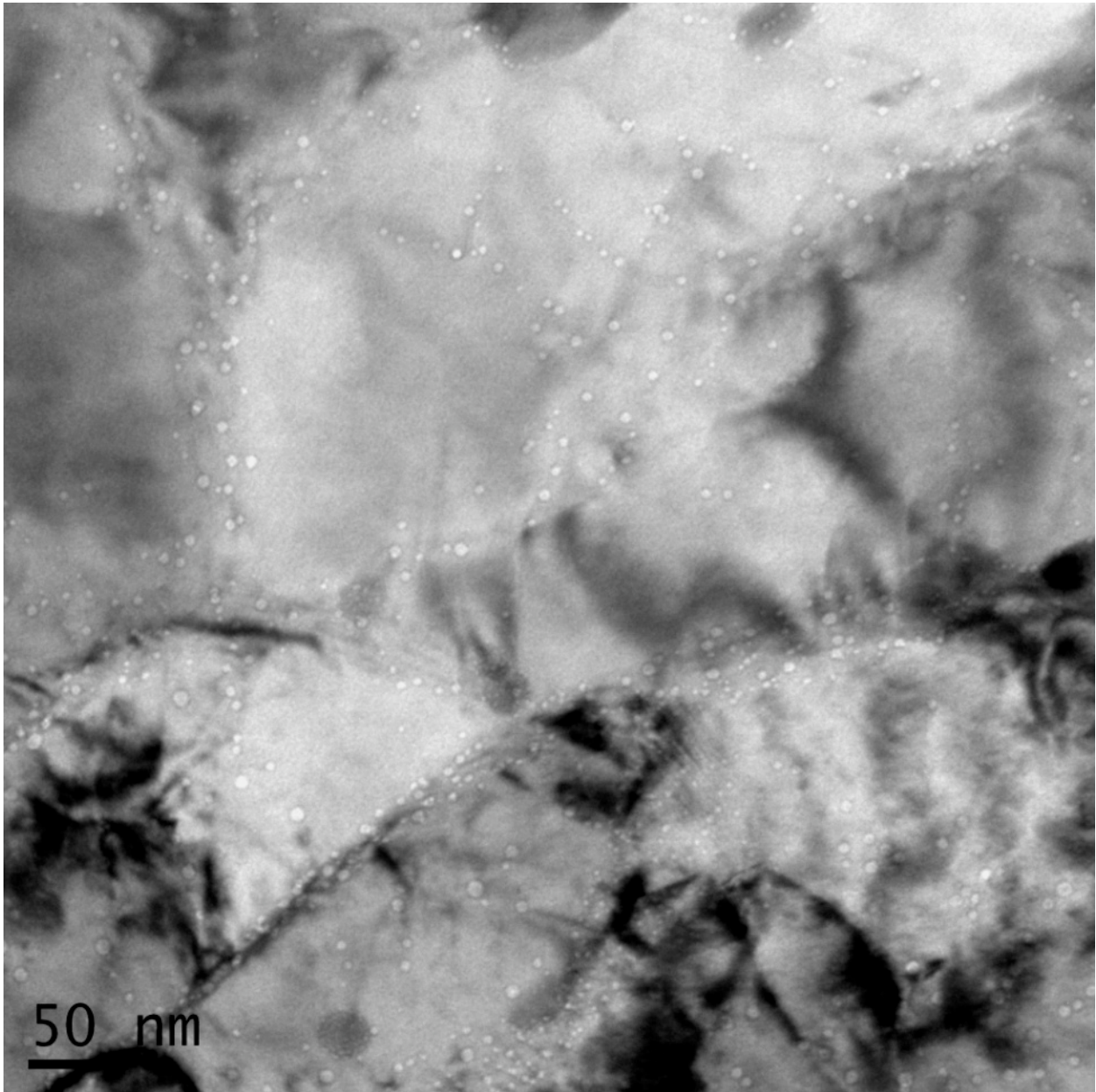


Figure 3. High magnification under-focused cavity image showing He bubbles in F82H mod.3 after dual ion beam irradiation in the area located from ≈ 0.5 to ≈ 1.0 μm deep from the surface.

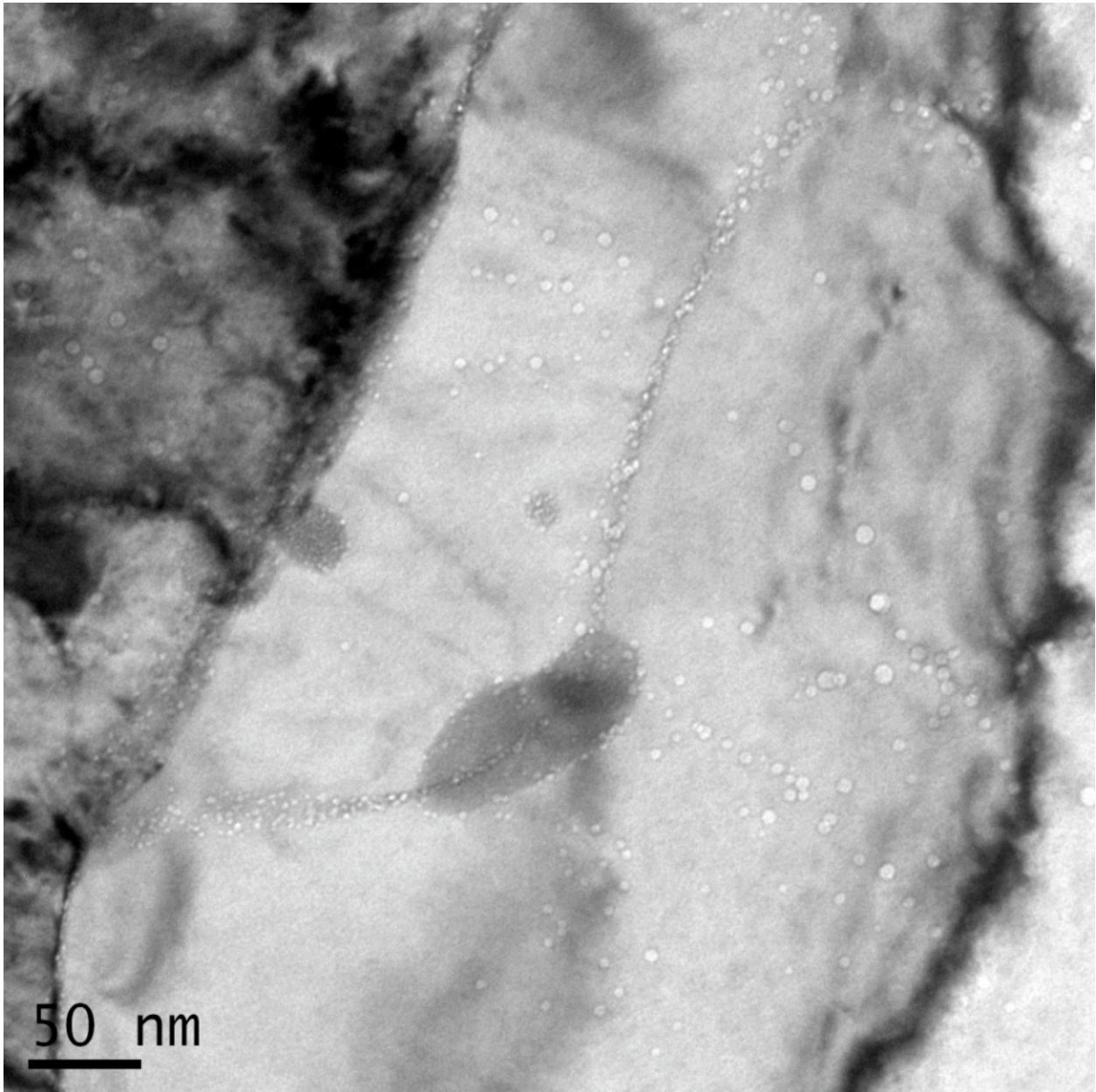


Figure 4. High magnification under-focused cavity image showing He bubbles in F82H mod.3 after dual ion beam irradiation in the area located from ≈ 1.0 to ≈ 1.5 μm deep from the surface.

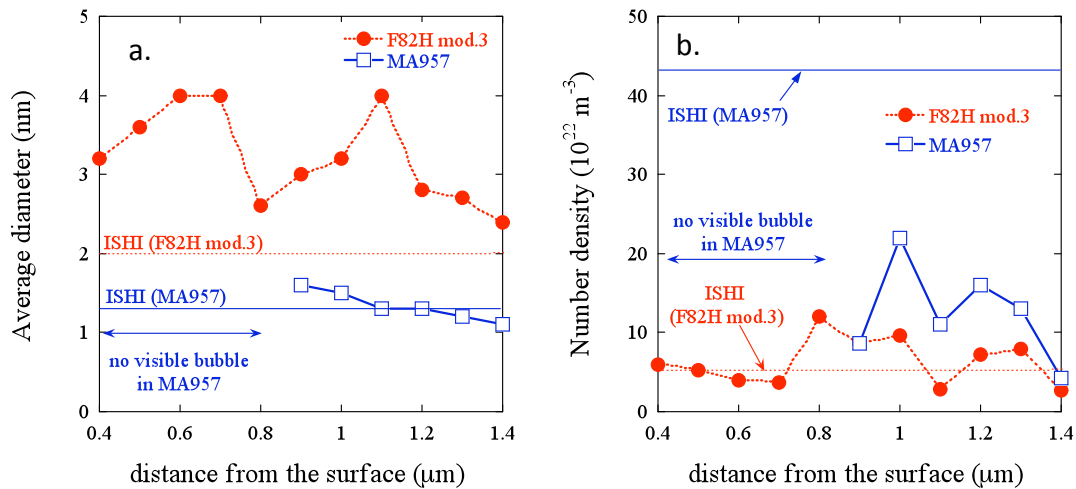


Figure 5 (a) Average diameter and (b) number density of He bubbles as a function of the distance from the surface for F82H mod.3 and MA957 after DuET irradiation. Analyses were conducted for the areas sectioned by 0.1 μm step so that, for example, 0.4 μm distance analysis covers the area from 0.4 to 0.5 μm in the distance. Thin horizontal lines show the results from ISHI experiments for the alloys.

TEM observation of the same alloy irradiated in the ISHI HFIR irradiation to approximately same dpa and He condition (9 dpa, 380 appm He) nominally at 500 $^{\circ}\text{C}$, showed a somewhat smaller average cavity size that has been reported to range from ≈ 2 to 3.4 nm [6,7, THIS STUDY], compared to that observed at 400-600 nm in the DuET irradiation condition of $\approx 3.7 \pm 0.3$ nm. The corresponding nominal ISHI number densities of $5.3 \times 10^{22} \text{ m}^{-3}$, are similar to that for the DuET irradiation at 600 nm $\approx 4.5 \pm 0.5 \times 10^{22}$ [5]. However, these comparisons require a caveat. The ISHI and DuET studies were carried out at different times and by different researchers, using somewhat different techniques. Thus it will be important to repeat the characterization of the cavity structures for the ISHI conditions using methods that are identical to those used for the DuET irradiations. Further, the characterization must develop metrics that account for the local microstructural-bubble associations and the corresponding variations noted above.

Indeed the comparison of ISHI and DuET cavity structures shown in Figure 6 suggest more significant differences that described above. In both cases, the regions examined are dominated by dislocation-associated bubbles. The ISHI irradiation clearly has a higher density of smaller (see Figure 6a) bubbles compared to the DuET irradiation condition. Further, a bimodal cavity distribution composed of small bubbles and large voids is observed in the ISHI condition, while the distribution is more unimodal for the DuET irradiation.

Microstructure of the DuET irradiated NFA MA957

As shown in Figure 5, bubbles are not observed in the DuET irradiation condition of MA957 at a depth of less than 800 nm. Figure 7a and b show under-over focus TEM images of the DuET irradiated MA957 from ≈ 900 to ≈ 1100 nm. A high density ($\approx 1.5 \times 10^{23} / \text{m}^3$) of small bubbles with average diameter of ≈ 1.4 nm were observed; and larger faceted voids were entirely absent in this case. As shown in Figure 7c the bubbles in MA957 are much smaller than in F82H mod.3. The dpa at this depth is ≈ 15 to 20 dpa. While

the sizes are similar, the bubble number density in the DuET irradiation ($\approx 1.5 \times 10^{23}/\text{m}^3$) is about a factor of 3 lower than for the ISHI condition ($4.3 \times 10^{23}/\text{m}^3$).

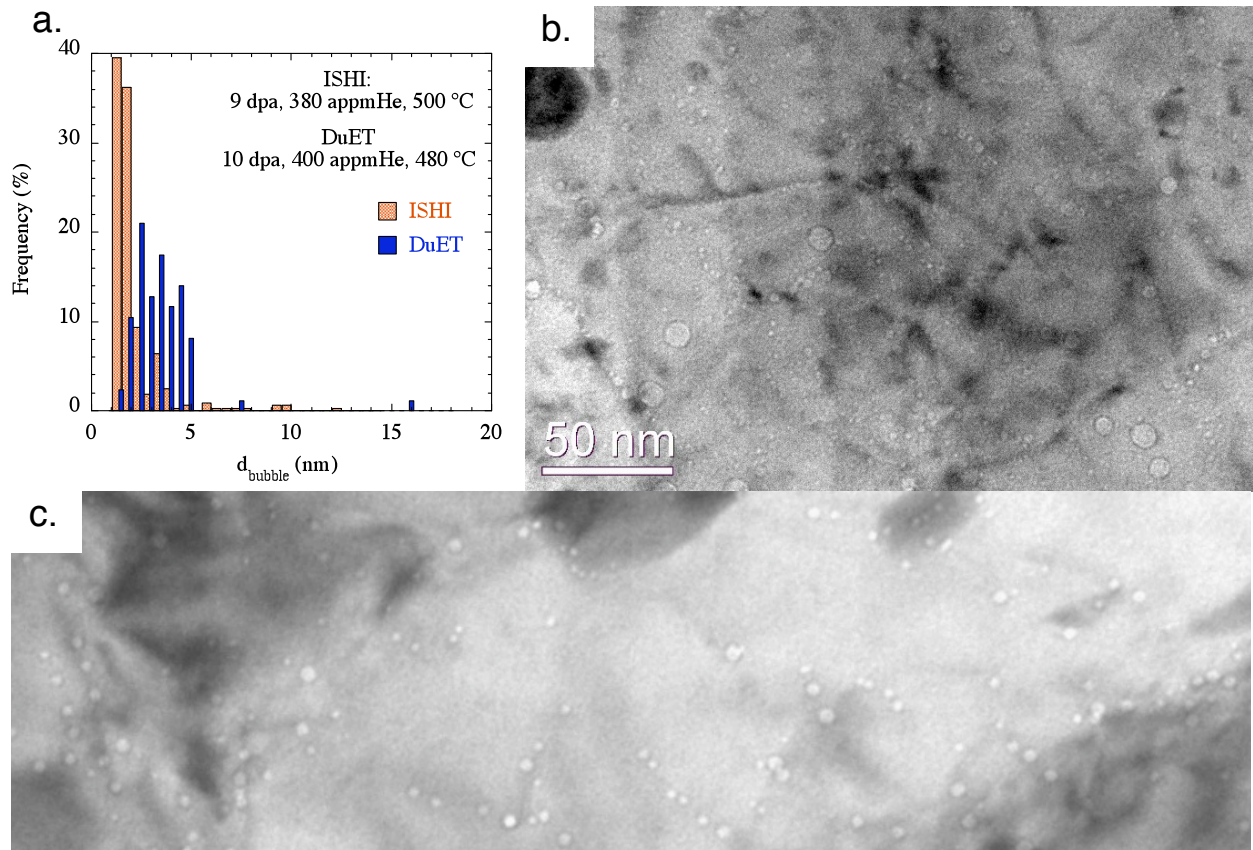


Figure 6. (a) Comparison of the He bubble size distributions in F82H mod. 3 specimens irradiated and He implanted in ISHI experiment vs. DuET facility; and corresponding bubble microstructure images in (b) ISHI and (c) DuET irradiation. Two TEM images are at the same magnification.

Future Research

Work during the current reporting period will include continued evaluation of the cavity and other microstructures in both the DuET and ISHI irradiation conditions. Further, the nominal comparative dpa in the DuET irradiations will be extended to ≈ 25 dpa and 1000 app He. ISHI specimens irradiated to a similar peak dpa and He content from the HFIR JP27 experiment will also be examined.

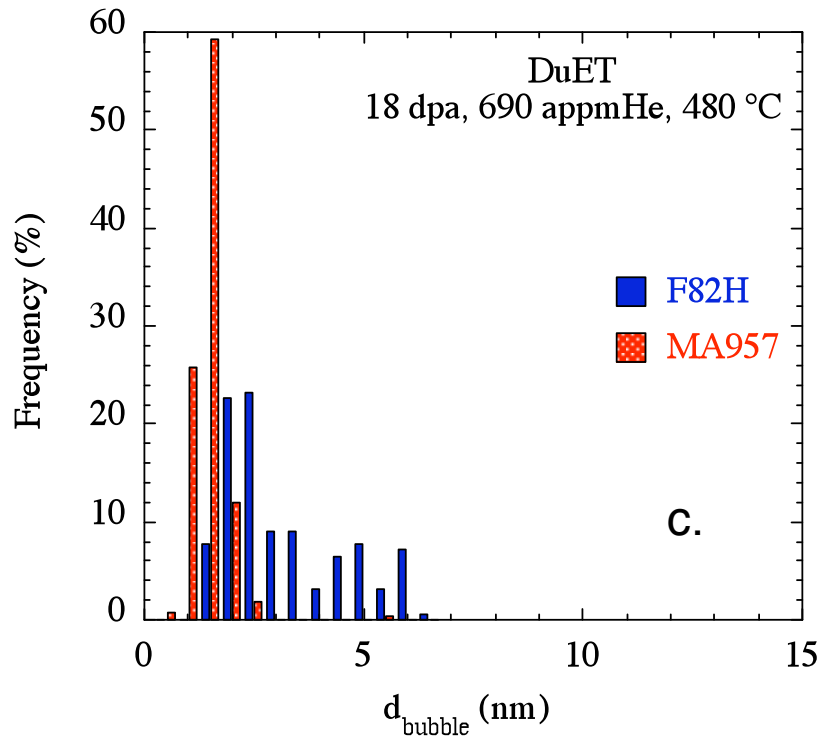
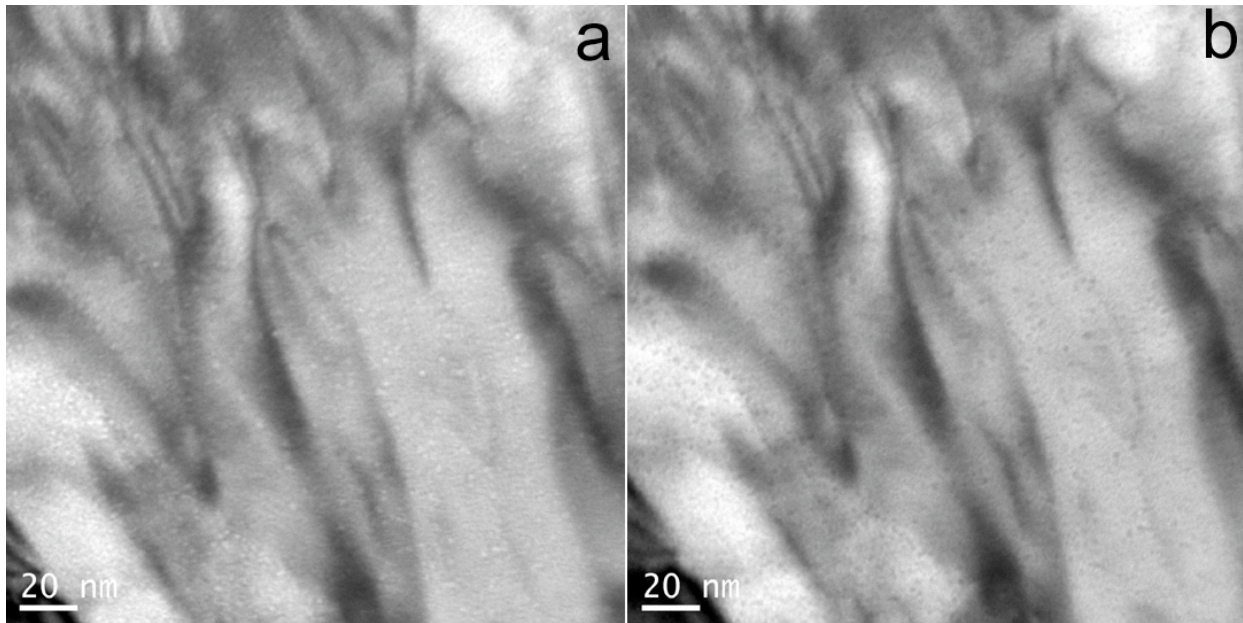


Figure 7. (a) an under focus and (b) an over focus TEM images of MA957 irradiated and He implanted in DuET irradiation over the depth range about 0.9-1.1 μm . (c) bubble size distributions over the depth range 1.0 - 1.1 μm in MA957 and F82H mod.3.

Acknowledgements

This work has been conducted as a part of the TITAN program for US DOE- Japan MEXT collaboration for fusion energy research. The work performed at UCSB was supported by the U. S. Department of Energy, Office of Fusion Energy Sciences, under contract DE-FG03-94ER54275.

References

- [1] Y. Dai, G.R. Odette, T. Yamamoto, *The Effects of helium on irradiated structural alloys (2011) in press.*
- [2] T. Yamamoto, G. R. Odette, L. R. Greenwood, *Fusion Materials Semiannual Report 1/1 to 6/30/2005* DOE/ER-313/38 (2005) 95.
- [3] T. Yamamoto, G. R. Odette, P. Miao, D. T. Hoelzer, J. Bentley, N. Hashimoto, H. Tanigawa, R. J. Kurtz, *J. Nucl. Mater.* 367 (2007) 399.
- [4] R. J. Kurtz, G. R. Odette, T. Yamamoto, D. S. Gelles, P. Miao, B. M. Oliver, *J. Nucl. Mater.* 367-370, 417 (2007).
- [5] G. R. Odette, M. J. Alinger, B. D. Wirth, *Annu. Rev. Mater. Res.* 38 (2008)471.
- [6] T. Yamamoto, G. R. Odette, P. Miao, D. J. Edwards, R. J. Kurtz., *J. Nucl. Mater.* 386-388 (2009) 338.
- [7] D. J. Edwards, R. J. Kurtz, G. R. Odette, T. Yamamoto, *Fusion Materials Semiannual Report 12/31/2009* DOE/ER-313/47 (2010) 59.
- [8] G. R. Odette, P. Miao, D. J. Edwards, T. Yamamoto, R. J. Kurtz, Y. Tanigawa, *J. Nucl. Mat.* (2011) in press.
- [9] E. H. Lee, J. D. Hunn, T. S. Byun, L. K. Mansur, *J. Nucl. Mater.* 280 (2000) 18.
- [10] H. Kishimoto, K. Yutani, R. Kasada, A. Kimura, *Fusion Eng. Des.* 81 (2006) 1045.
- [11] R. Kasada, H. Takahashi, H. Kishimoto, K. Yutani, A. Kimura, *Materials Science Forum 654-656* (2010) 2791 ([doi:10.4028/www.scientific.net/MSF.654-656.2791](https://doi.org/10.4028/www.scientific.net/MSF.654-656.2791)).
- [12] A. Kimura, R. Kasada, A. Kohyama, H. Tanigawa, T. Hirose, K. Shiba, S. Jitsukawa, S. Ohtsuka, S. Ukai, M. A. Sokolov, R. L. Klueh T. Yamamoto, G. R. Odette, *J. Nucl. Mater.* 367-370 (9007) 60.
- [13] K. Shiba, M. Enoeda, S. Jitsukawa, *J. Nucl. Mater.* 329-333 (2004) 243.
- [14] A. Kimura, R. Kasada, K. Morishita, R. Sugano, A. Hasegawa, K. Abe, T. Yamamoto, H. Matsui, N. Yoshida, B. D. Wirth, T. D. de la Rubia, *J. Nucl. Mater.* 307-311 (2002) 521-526.
- [15] G. R. Odette, T. Yamamoto, H. J. Rathbun, M. Y. He, M. L. Hribernik, J. W. Rensman, *J. Nucl. Mater.* 323 (2003) 313.
- [16] T. Yamamoto, G. R. Odette, H. Kishimoto, J-W. Rensman, P. Miao, *J. Nucl. Mater.* 356 (2006) 27.
- [17] Z. Tong, Y. Dai, *J. Nucl. Mater.* 385 (2009) 258.
- [18] M. L. Hamilton, D. S. Gelles, R. J. Lobsinger, M. M. Paxton, W. F. Brown, "Fabrication Technology for ODS Alloy MA957," PNL-13165, Pacific Northwest Laboratory (2000).
- [19] Y. Wu et al. to be published.
- [20] A. Kohyama, Y. Katoh, M. Ando, K. Jimbo, *Fusion Eng. Des.* 51-52 (2000) 789.

1.2 Further Atom Probe Tomography Studies of Nanostructured Ferritic Alloy MA957 in Three Conditions

Nicholas J. Cunningham, G. Robert Odette and Erich Stergar, University of California Santa Barbara

Objective

The objective of this work is to characterize the size distributions, number densities, microstructural associations, compositions, structures and thermal stability of the Y-Ti-O nanostructures (NFs) in ferritic nanostructured alloys (NFA).

Summary

We report on atom probe tomography (APT) studies on nano-structured ferritic alloys (NFAs) that contain an ultrahigh density of nm-scale Y-Ti-O nanostructures (NFs). A local electrode atom probe (LEAP) was used to characterize the NFs in both as-extruded bar (US) and thick walled tube (French) heats of MA957. APT was also carried out on the US MA957 following long-term thermal aging (LTTA) at 1000°C for 19 kh. The as-extruded US MA957 was found to contain $\approx 3.2 \times 10^{23}$ NFs/m³ with an average diameter of ≈ 2.4 nm. The French MA957 tubing contained an average of 6.1×10^{23} NFs/m³ with an average diameter of ≈ 2.8 nm. The average Y/Ti/O ratio of $\approx 13/47/40$ was similar in both heats. The NFs coarsen under 1000°C LTTA, with average number densities and diameters decreasing to 7×10^{22} NFs/m³ and increasing to ≈ 2.8 nm, respectively. The NF composition in the aged condition is relatively unchanged with only a slight increase in the Y/Ti ratio.

Introduction and Background

Nano-structured ferritic alloys (NFA) have high tensile and creep strength permitting operation up to 800°C, manifest remarkable resistance to radiation damage and can manage a high concentration of He [1]. These outstanding properties derive from an ultrahigh density of Ti-Y-O enriched nano-structures (NF) that provide dispersion strengthening, help stabilize dislocation and fine grain structures, reduce excess concentrations of displacement defects and trap He in fine bubbles [1]. Here we further characterize the NF in NFA MA957 in various conditions.

Material and Methods

The following report describes atom probe tomography (APT) data acquired from three conditions of the alloy MA957. This new data is compared to and combined with APT data previously reported on the same materials. The base MA957 is as-extruded 1150°C, 25mm diameter round bar acquired from Pacific Northwest National Laboratory and referred to as US-MA957. A 9 mm thick, 65 mm outer diameter tube fabricated by center drilling the bar of base material followed by hot extrusion is referred to as Fr-MA957. This heat was acquired from CEA Saclay in France via Oak Ridge National Laboratory. The third variation is the US-MA57 after long-term thermal aging (LTTA) at 1000°C for 19kh. This sample was wrapped in high Cr stainless steel foil during aging to reduce the loss of this element. Approximately two millimeters of the sample surface was removed to avoid the effect of near surface effects.

APT was performed using an Imago Local-Electrode Atom Probe (LEAP) 3000X HR. Samples are prepared by either electropolishing or micromachining using an FEI Helios 600 focused ion beam (FIB). Electropolished samples were made from $\sim 0.5 \times 0.5 \times 20$ mm bars using the two stage process described by Miller [2]. FIB sample preparation used the trench method described by Thompson [3]. Each sharpened tip is cleaned to remove Ga damage first using a 5 KeV and then a final 2 KeV beam at 28 pA. The LEAP samples were examined in voltage or laser mode with 200kHz laser or voltage pulse repetition rate, 0.5% or 1% evaporation rate, and a 34 K to 60 K temperature range. In the voltage mode the pulse fraction was either 20 or 25% while in laser mode green ($\lambda = 532$ nm) laser pulse energies varied from 0.13 nJ to 0.15 nJ. The Imago Interactive Visualization and Analysis Software (IVAS) package was used for reconstruction and analysis of the LEAP data. The average number densities of the NF are weighted with the total atoms collected, and the NF size and composition averages are weighted based on NF count.

Results

US-MA957

Eight US-MA957 runs carried out in the UCSB LEAP were reported previously [4]. The corresponding results for 2 additional FIBed needles are presented here. The new measurements of the NF sizes (d) and compositions are generally similar to the previous results.

Table 1 shows the average APT composition for all sample runs and the bulk chemistry of MA957 measured in another study [5]. Including the new datasets, the average size of the NF is $\langle d \rangle = 2.4$ nm. The overall number densities (N) of NFs varied from ≈ 0.7 to $7.1 \times 10^{23}/\text{m}^3$, averaging $3.2 \times 10^{23}/\text{m}^3$. The N for the new measurements is higher than the overall average, ranging from ≈ 3.8 to $7.1 \times 10^{23}/\text{m}^3$. This large variability reflects the heterogeneous distribution of the NFs, from the nanometer to micron length scales, as well as the small APT volumes analyzed. The overall average nominal Y/Ti/O ratio of the US-MA957 is 14.4/45.6/39.9. The average N and $\langle d \rangle$ are shown in Table 2.

Figure 1 shows a subset of the data from one of the newly analyzed samples. This sample contained the highest N for any of the US-MA957 runs. No grain boundaries were observed and all the NFs were relatively small ($d < 4$ nm). The previous samples with lower N typically contained larger (some >10 nm diameter) precipitates that were not uniformly present through the sample and were probably associated with grain boundaries.

Table 1. Bulk composition of US MA957

At%	Bulk Chemistry	APT US-MA957
Fe	82.97	83.29
Cr	14.32	14.76
Ti	1.123	0.868
Mo	0.170	0.144
Y	0.128	0.084
O	0.786	0.365
Ni	0.089	0.157
Al	0.183	0.042
Mn	0.065	0.098
Si	0.059	0.066
C	0.073	0.008
Cu	0.009	0.008
B	-	0.023
Co	-	0.049
V	-	0.054
Nb	-	0.005

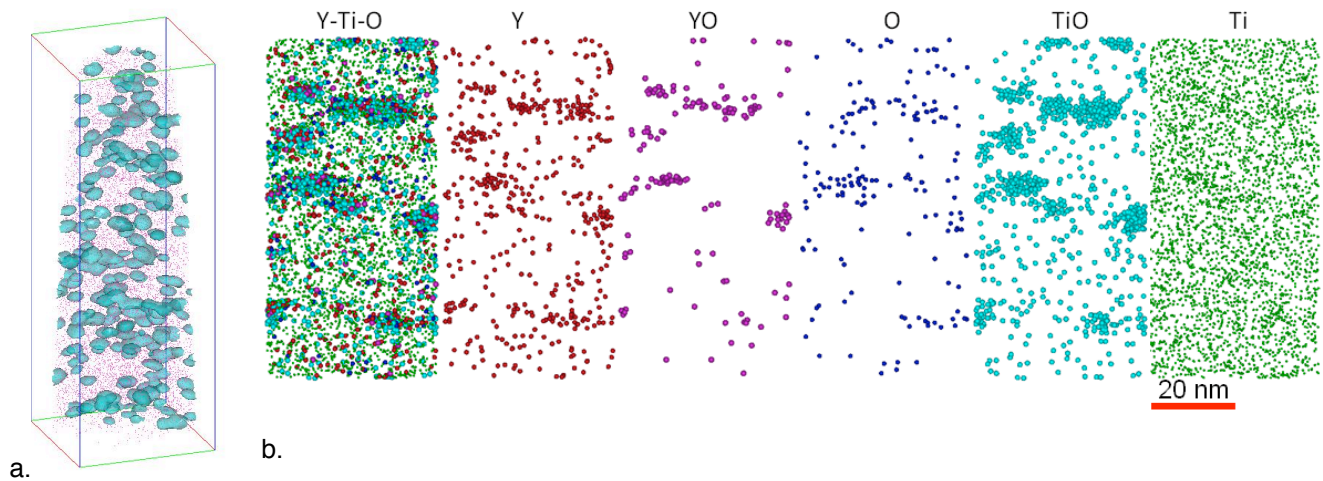


Figure 1. a) 3% Y-Ti-O isoconcentration surfaces in MA957 sample with high number density of NFs; b) $20 \times 20 \times 40 \text{ nm}^3$ volumes of Y, Ti, and O ions in data set.

A small sample run of approximately 1.5 million ions contained a grain boundary near the edge of the data set. Atom maps of Cr overlaid with specific ions are shown in Figure 2 for this sample. Many solute ions segregate to the grain boundaries including Cr, Ti, Mo, B, and P.

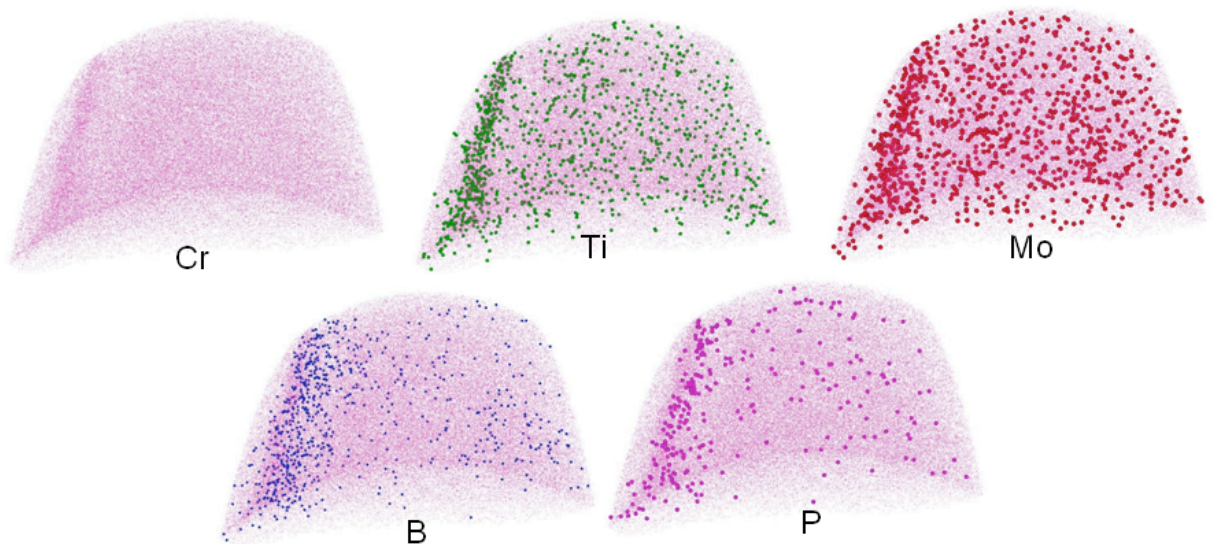


Figure 2. a) Atom maps of MA957 showing segregation to the grain boundary.

Fr-MA957

Two new Fr-MA957 samples were prepared by electropolishing and run in either laser mode or voltage mode with four and five million ions detected, respectively. In a previous report only one Fr-MA957 data set was available for comparison with the US-MA957 [4]. Figure 3 shows Y-Ti-O isoconcentration surfaces for a subset of the voltage mode run where only small NFs were observed. The laser mode run consisted mostly of small NFs, but a

large, Ti-rich, precipitate was also observed on the edge of the dataset. The Y/Ti/O ratio for an observed fraction of the larger precipitate was 1.1/32.6/66.3.

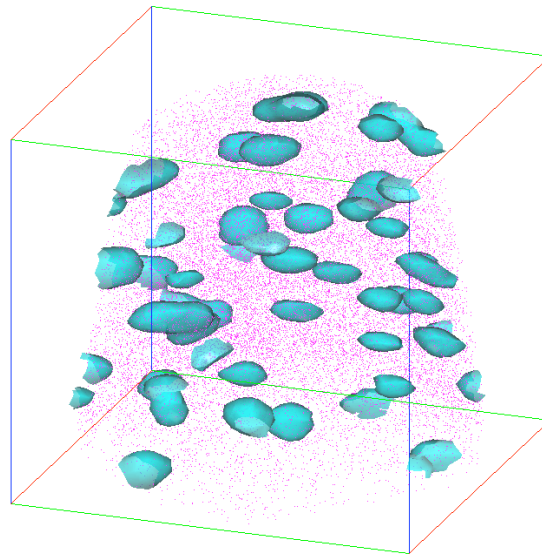


Figure 3. Atom map of Fr-MA957 with 3.5% Y-Ti-O isoconcentration surfaces.

Combining all Fr-MA957 sample data to date gives a number density range from $N = 3.1$ to $7.8 \times 10^{23} \text{ m}^{-3}$, with an overall average for the Fr-MA957 of $6.1 \times 10^{23} \text{ m}^{-3}$. The previous Fr-MA957 run had slightly larger NFs with $\langle d \rangle \sim 3.1$ nm compared to the newer data sets with $\langle d \rangle$ between 2.0 and 2.4 nm, and with an overall average of 2.4 nm. The overall average Y/Ti/O ratio for the Fr-MA957 is 12.5/47.0/40.4. The compositions were similar between the previous and new voltage run, but the laser run with the large Ti-rich phase had a Y/Ti/O ratio of 16.1/37.5/46.3, excluding the Ti-rich phase. The overall average number density and diameter for the Fr-MA957 is given in Table 2.

US-MA957 LTTA

It has been previously found that NFs are unaffected by long-term thermal aging up to 900°C. At 950°C slight coarsening occurs, while at 1000°C more significant coarsening is observed. The grain sizes, however, remain relatively unchanged as shown in Figure 4. Here the grain structure of the as-extruded US heat of MA957 and LTTA MA957 perpendicular to the extrusion direction are compared. The as-extruded MA957 has a uniform, fine grain structure with aspect ratio about 5:1. This structure is largely unchanged after 19 kh at 1000°C aging. Higher magnification still shows the presence of small precipitates in the MA957 after LTTA.

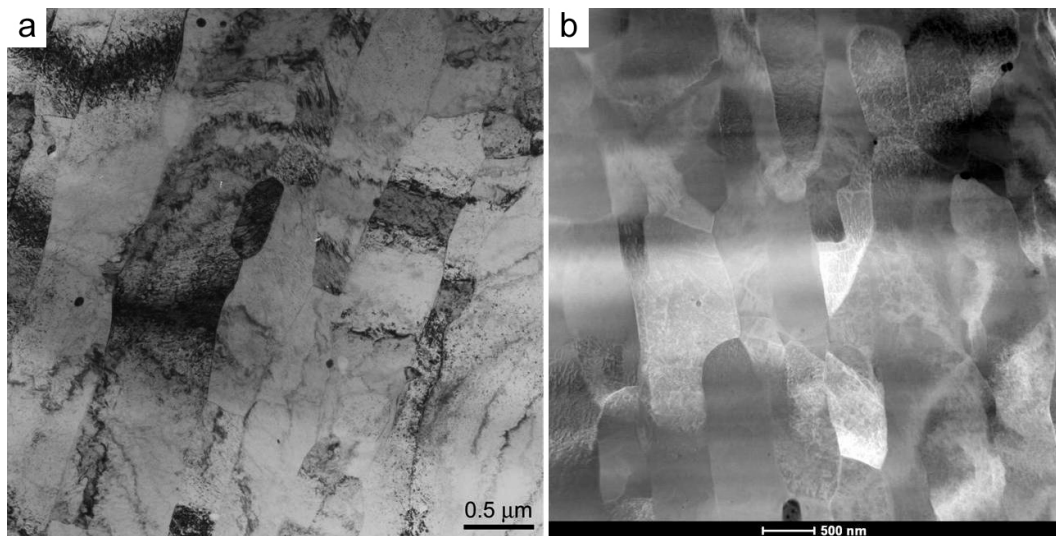


Figure 4. TEM micrographs perpendicular to extrusion direction a) As-received MA957 using bright field image, b) STEM imaging of 1000°C, 19 kh aged MA957.

Table 2. MA957 NF size and number density comparison (add compositions)

NF Parameter	US-MA957	Fr-MA957	LTTA US-MA957
Average diameter <d> (nm)	2.4	2.8	2.8
Number density N (10^{23} m^{-3})	3.2	6.1	0.7

The previous APT revealed a decrease in the number density and a slight increase in the NF size for the 1000°C LTTA sample. In addition, the total Ti content of the MA957 was reduced from nominal levels of ≈ 1.1 to 0.22 at%. Most of the residual Ti was found to be associated with the precipitates, while the balance was missing from the matrix. However, the composition of the NFs is only modestly affected, with a slight decrease in Ti level. One APT sample contained a grain boundary along its entire length. The Cr, B, Mo, and P segregation to the boundary was similar to the un-aged MA957; no Ti segregation was observed. The Cr content of the bulk sample was found to be ≈ 18 at% which is significantly higher than the ~ 14.8 at% observed in the un-aged MA957. This increase in Cr is not understood. Additional APT measurements performed on the 1000°C LTTA confirmed the previous measurement of ≈ 18 at% Cr. They also showed a lower number of larger NF. The overall average Y/Ti/O ratio for all MA957 LTTA samples is 17.7/34.2/48.1. The Y/Ti ratio is higher than the un-aged material. The size and number density is compared to the US-MA957 and the Fr-MA957 APT results in Table 2 below.

References

1. G. R. Odette, M. J. Alinger, and B. D. Wirth, Annual Review of Materials Research, Vol. 38, (2008).
2. M. K. Miller, *Atom Probe Tomography: Analysis at the Atomic Level*, Kluwer Academic/Plenum Publishers, New York (2000).
3. K. Thompson, D. Lawrence, D. J. Larson, J. D. Olson, Kelly, T. F., and B. Gorman, Ultramicroscopy, 107 (2007) 131.

4. N. J. Cunningham, A. Etienne, Y. Wu, E. M. Haney and G. R. Odette, Fusion Semiannual Progress Report for period ending June 30, 2010 (DOE-ER-0313/48).
5. H. L. Hamilton, D. S. Gelles, R. J. Lobsinger, G. D. Johnson, W. F. Brown, M. M. Paxton, R. J. Puigh, C. R. Eiholzer, C. Martinez, and M. A. Blotter, "Fabrication Technological Development of the Oxide Dispersion Strengthened Alloy MA957 for Fast Reactor Applications," Technical Report PNL-13168 (1991).

2.1 TITAN TASK 2-3 SILICON CARBIDE BEND STRESS RELAXATION CREEP STUDY: PHASE-II EXPERIMENT — Y. Katoh, K. Ozawa (Oak Ridge National Laboratory), and T. Hinoki (Kyoto University)

OBJECTIVE

This report provides a brief outline of the technical planning and progress of the Phase-II irradiation experiment for the Task 2-3 on Dynamic Deformation of Fusion Materials, US/Japan TITAN collaboration on fusion materials and blanket technology.

SUMMARY

A study of irradiation creep behavior of silicon carbide ceramics and composites is part of Task 2-3 of the US/Japan TITAN collaboration on fusion materials and blanket technology. In the Phase-I experiment, low fluence irradiation creep behavior of monolithic silicon carbide ceramics was studied using the bend stress relaxation (BSR) technique. The objective of the Phase-II experiment is to gain understanding of the stress relaxation and creep behavior of silicon carbide ceramics, fibers, and composites under neutron irradiation to higher fluences at elevated temperatures. The neutron irradiation will be performed using the fixed rabbit facilities of the High Flux Isotope Reactor. The Phase-II program will irradiate 13 rabbit capsules; 8 for monolithic and composite samples and 5 for fiber samples. Target irradiation temperatures are 300, 500, 800, and 1200°C. The present schedule assumes the initiation of irradiation in early 2011.

PROGRESS AND STATUS

Introduction

Irradiation creep is an important irradiation effect phenomenon for materials for services in high radiation environments, because it is a major contributor to potential dimensional instability of materials under irradiation at such temperatures that thermal creep is not strongly anticipated.^[1] Although irradiation creep often determines irradiated lifetime of metallic structural components, it may also be beneficial for inherently brittle materials like ceramics for functional applications, because creep may relax or redistribute the stresses.^[2] For silicon carbide (SiC)-based nuclear components, the latter function of irradiation creep may be important, in particular when a significant temperature gradient exists and the secondary stresses developed by differential swelling can be severe. Flow channel insert in liquid metal blankets of fusion energy systems is an example of such applications.^[4]

Studies on neutron irradiation creep of SiC have so far been extremely limited and insufficient. Price published the result of the irradiation creep study on chemically vapor-deposited (CVD) SiC in 1977.^[6] In that work, elastically bent strip samples were irradiated in a fission reactor, and the linear-averaged creep compliance was estimated to be in the order of 10^{-38} [Pa·n/m² (E > 0.18 MeV)]⁻¹, or 10^{-7} [MPa·dpa]⁻¹, in a temperature range 780 - 1130°C. This result may involve very significant uncertainty because stresses in some of the samples appeared to have been completely relaxed at the end of irradiation. However, the experimental method of estimating the creep parameters based on the stress relaxation in elastically bent strip samples developed by Price was later adopted to examine the thermal creep behavior of refractory ceramic fibers and was named bend stress relaxation (BSR) method by Morscher and DiCalro.^[5]

In more recent work, Katoh et al. applied it for studying the irradiation creep of high purity, stoichiometric CVD SiC, demonstrating the applicability of the BSR technique to determine the irradiation creep parameters.^[3] They also revealed that the creep strains SiC were dominated by transient creep at

temperatures below $\sim 950^{\circ}\text{C}$ whereas steady-state creep may operate at higher temperatures with a compliance of $1.5 \pm 0.8 \times 10^{-6} [\text{MPa}\cdot\text{dpa}]^{-1}$ with the initial flexural stress magnitude ~ 100 MPa. However, fundamental aspects of the irradiation creep, including the effect of stress magnitude on the creep strain rate, the correlation of irradiation creep and swelling, and the responsible physical mechanism, remain to be understood.

Based on the previous demonstration of the experimental technique and the recognized importance of the irradiation creep, a more detailed study on the BSR irradiation creep of SiC ceramics and composites was planned as the main focus of Task 2-3 on dynamic deformation of fusion materials in the US Department of Energy /Japan MEXT (Ministry of Education, Culture, Sports, Science and Technology) TITAN Collaboration. In the Phase-I study, understanding of the transient creep and stress relaxation behavior of various SiC ceramics, including high purity, polycrystalline beta-phase SiC, monocrystalline alpha SiC, and liquid phase-sintered SiC, during neutron irradiation was obtained. The Phase-I study also demonstrated that the rapid stress relaxation in SiC at the onset of irradiation is very substantially suppressed when the as-grown defects are annealed by pre-irradiation heat treatment, with large fractions of the initial stress remaining after low fluence irradiation. This result indicates that the crystalline SiC with sufficiently low as-grown defect density makes an exceptionally radiation-resistant spring material. Moreover, it indicates that the stress relaxation technique may be used for experiments to higher fluences. The Phase-II study is intended to explore the irradiation creep or stress relaxation behavior of monolithic SiC, SiC fibers, and SiC composites.

Technical Plan Details

Irradiation Matrix

The Phase-II irradiation program consists of irradiation of 13 rabbit capsules including 8 rabbits for monolithic and composite materials and 5 rabbits for fiber specimens. The irradiation matrix is shown in [Table 1](#).

Table 1 – Irradiation conditions planned for Phase-II SiC irradiation creep.

Capsule ID in Titan	Capsule Type	Target Temperature ($^{\circ}\text{C}$)	Target Dose ($\times 10^{25}$ n/m ² fast)	Materials	Facility
T10-01J	Titan-BSR1	300	1	Monolithic and Composites	PTP or TH
T10-02J	Titan-BSR1	300	10		
T10-03J	Titan-BSR1	300	20		
T10-04J	Titan-BSR1	500	10		
T10-05J	Titan-BSR1	500	20		
T10-06J	Titan-BSR1	800	10		
T10-07J	Titan-BSR1	800	20		
T10-08J	Titan-BSR1	1200	10		
T10-09J	Titan-BSR2	500	1	Fibers	PTP or TH
T10-10J	Titan-BSR2	500	10		
T10-11J	Titan-BSR2	500	20		
T10-12J	Titan-BSR2	1200	1		
T10-13J	Titan-BSR2	1200	10		

Irradiation Capsules

The standard “SiC Bend Bar” type capsule housing configurations are employed, using the existing HFIR capsule design X3E020977A325. Inside the standard sleeve, which holds two ceramic bend bar samples in the standard configuration, a rectangular casing (denoted “coffin” hereafter) is accommodated for the Titan-BSR1 configuration. Both the sleeves and the coffins were made of molybdenum. In the Titan-BSR2 configuration, ceramic fiber specimens are accommodated in fixture made of nuclear grade graphite.

Each coffin for the Titan-BSR1 configuration consists of a straight rectangular tube with end pillars on both ends, Fig. 1. The end pillars are for 1) fixing the internal parts and specimens in appropriate positions, and 2) retaining the internal parts and specimens during the capsule disassembly process until right before the specimen examination in the post-irradiation examination facility. The end pillars are made of the same material with the tube.

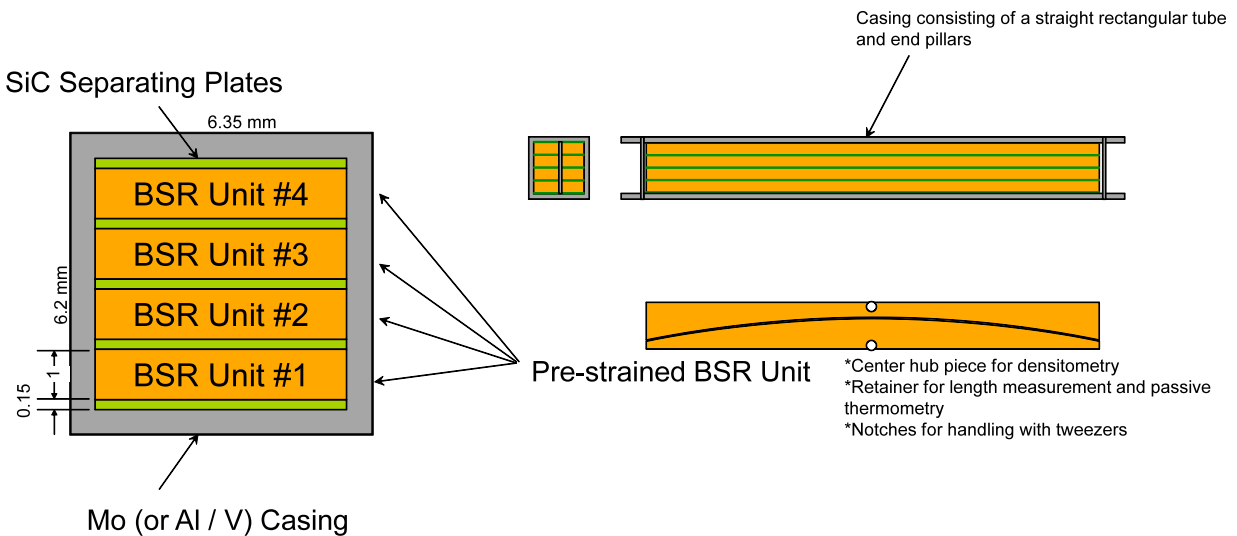


Fig. 1 – Schematic illustration of monolithic/composite SiC ceramics BSR fixture and loading into coffin.

Thin strip specimens of monolithic ceramics and ceramic composites are loaded into fixture, making an individual BSR unit. The fixture, once held in the coffin, keeps the specimens uniformly bent to the pre-determined curvatures, which are typically 100 mm radius for the monolithic specimens and 200 mm radius for the composite specimens. Fig. 2 shows the specimens in fixture, held in an assembly tool, along with the specimens and nickel foils used for in-situ helium injection (as described in the next section).

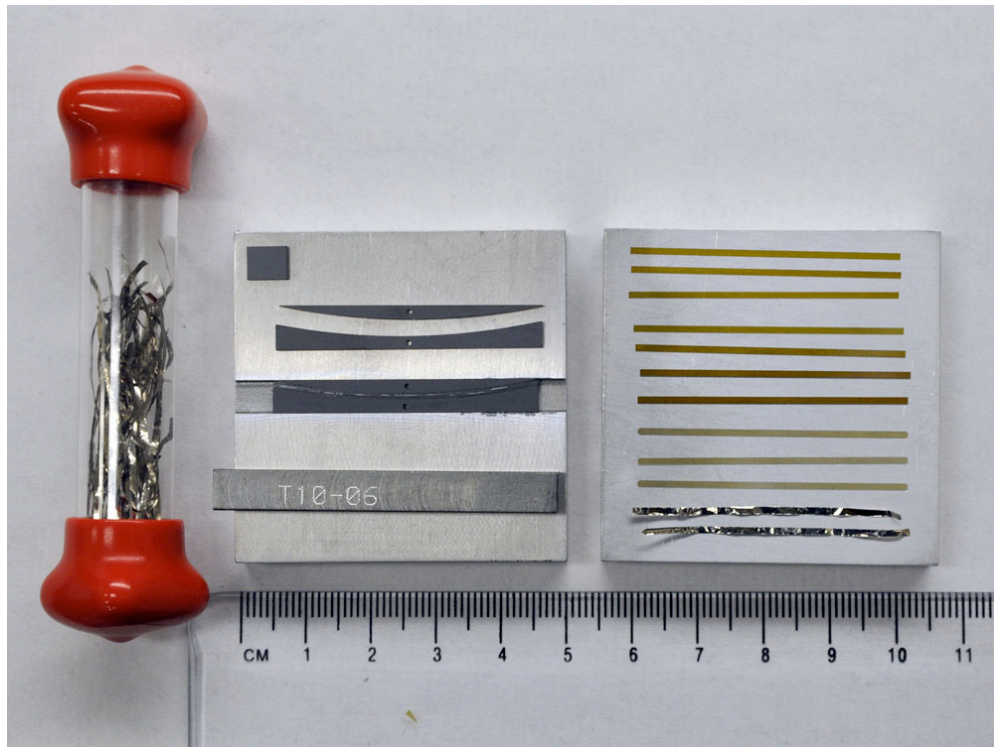


Fig. 2 – CVD SiC BSR fixture with specimens loaded in assembly tool (middle), monolithic ceramic specimens before loading (right), and nickel foil strips (left) for in-situ helium injection.

Four pre-strained BSR units are accommodated in each coffin. Each unit is of size approximately 48 mm x 5.1 mm x 1 mm. The BSR assembly units are stacked together with CVD SiC liners/seperator plates at the top, bottom, and between the units, Fig. 3. The CVD SiC liners/separators prevent potential undesirable reaction between the samples and the metallic parts or fixture, as well as help aligning the BSR assembly units in proper positions.

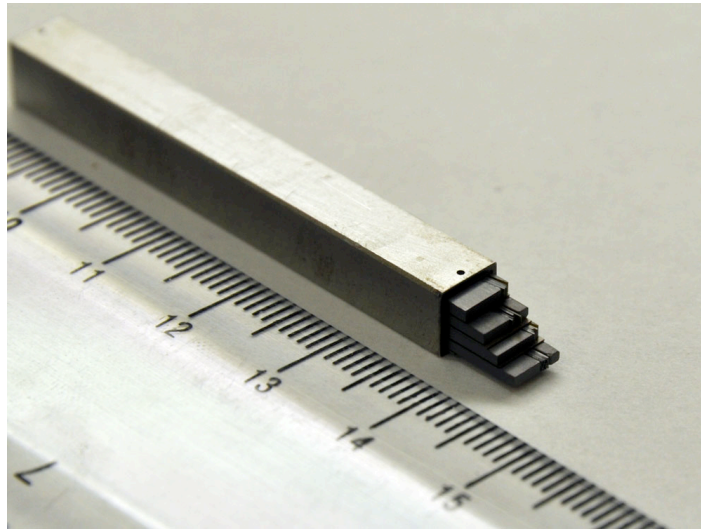


Fig. 3 – Photograph showing a set of four monolithic/composite SiC ceramic BSR units being loaded, separated by SiC sheets, into a molybdenum coffin.

In the Titan-BSR2 configuration, instead of the coffin, a pair of fiber BSR units are accommodated in the sleeve. Each assembled unit measures 25 mm x 6.35 mm x 6.22 mm and holds fibers in two separate bundles. The fiber bundles are elastically bent to three different curvatures as shown in Fig. 4. The unit is held together by a graphite pin penetrating throughout the fixture length with help by the spring force of the fiber samples. Appearance of the assembled fiber BSR unit is shown in Fig. 5.

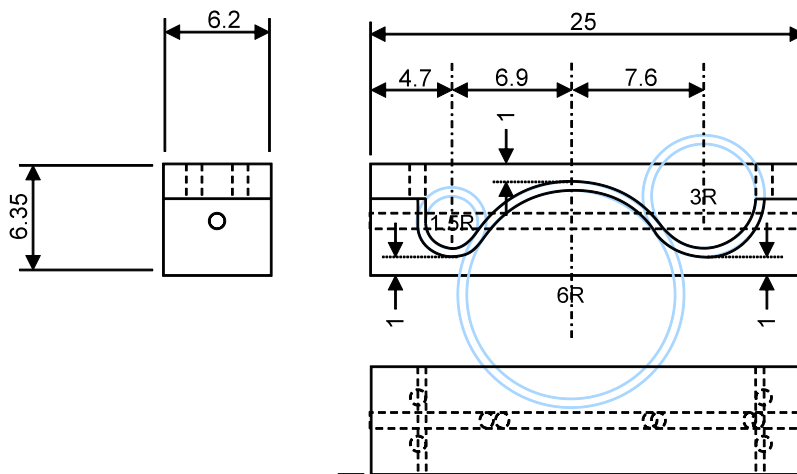


Fig. 4 – Graphite fixture for fiber BSR irradiation creep.

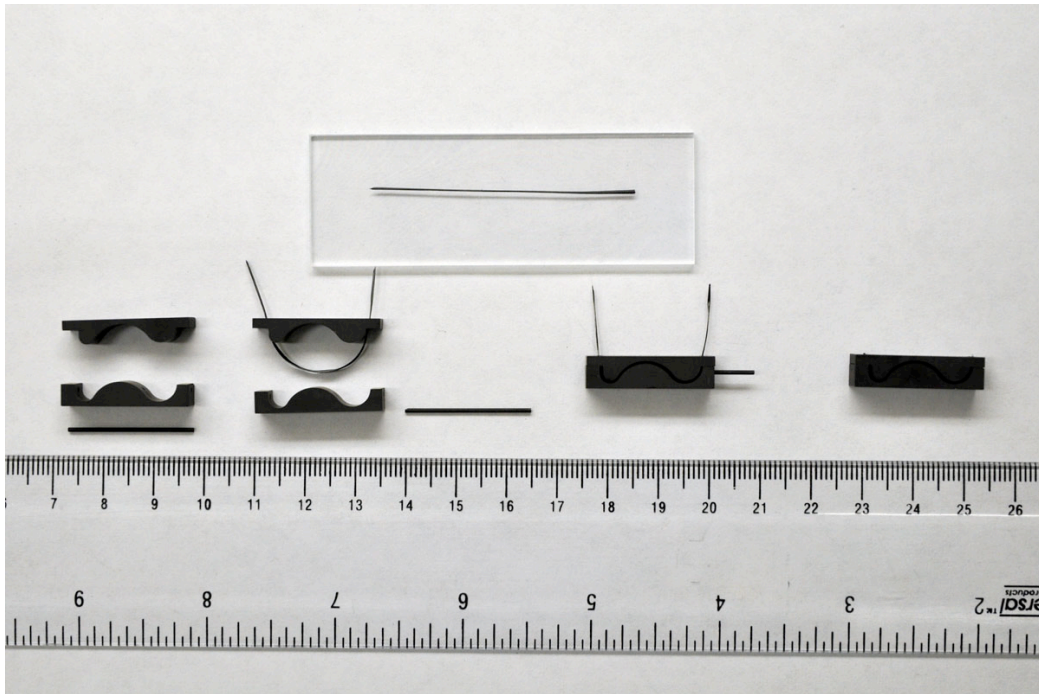


Fig. 5 – Photograph showing assembly process for fiber BSR unit (top) and magnified view of assembled unit (bottom).

Materials and Specimens

Monolithic and composite materials to be studied and the specimen loading to each rabbit are summarized in [Table 2](#). The Cree 4H single crystal samples were machined for the surface parallel with {0001} and the length parallel with <1120>.

The dimensions of the BSR creep specimens are 40 mm (l) x 1 mm (w) x varied thickness. Some of the materials were machined into slightly reduced width for materials identification. The thickness was varied to allow determination of the effect of stress magnitude. Typical initial flexural stresses for the specimen thicknesses 0.05, 0.1, and 0.15 mm are ~100, ~200, and ~300 MPa, respectively, for monolithic samples. Typical initial flexural stresses for the composite specimens are ~100 and ~200 MPa for thicknesses 0.1 and 0.2 mm, respectively. Some of the sample strips are loaded with thin nickel foils on both faces or one face for the purpose of in-situ helium injection. The inclusion of nickel foils was limited to capsules for irradiation at below 500°C to avoid reaction with the SiC samples.

Table 2 – SiC materials and specimens for the BSR creep experiment.

Material ID	Material	Specimen Thickness (mm)	Typical # of specimens in a rabbit
RH	R&H CVD-SiC, polycrystalline beta SiC	0.05	2
		0.10	4
		0.15	4
CT	Coorstek CVD SiC polycrystalline beta SiC	0.05	1
		0.10	1
		0.15	1
SX	Cree 4H SiC, W4NRF0X-0D00, Lot# FX0778-28/161430	0.05	1
		0.10	1
		0.15	1
NT1	NITE matrix material, standard	0.075	1
		0.10	2
		0.15	1
NT2	NITE matrix material, reduced additives	0.05	2
NITE	NITE SiC/SiC composite, uni-directional	0.10	2
		0.20	2
RH with Ni	R&H CVD-SiC, in contact with nickel 2 micron-thick foil(s)	0.05	3
CT with Ni	Coorstek CVD-SiC, in contact with nickel 2 micron-thick foil(s)	0.05	3

The ceramic fiber materials to be studied and the specimen loading to each rabbit are given in [Table 3](#). The fibers are bent to three different nominal curvature radii, namely 6, 3, and 1.5 mm. The anticipated flexural stresses for typical SiC fibers with 0.01 mm-diameter and Young's modulus 400 GPa are 333, 667, and 1333 MPa, respectively, ignoring Poisson effect. An example of the actually measured curvature profile is presented in [Fig. 6](#).

Table 3 – Materials for the fiber BSR creep experiment.

Material ID	Material	Fiber Diameter (micron)
HNLS	Hi-Nicalon™ Type-S	~11
SA3	Tyranno™-SA3	~7.5
Syl-B11	Experimental Sylramic	~10
Syl-iB11N	Experimental Sylramic-iBN	~10

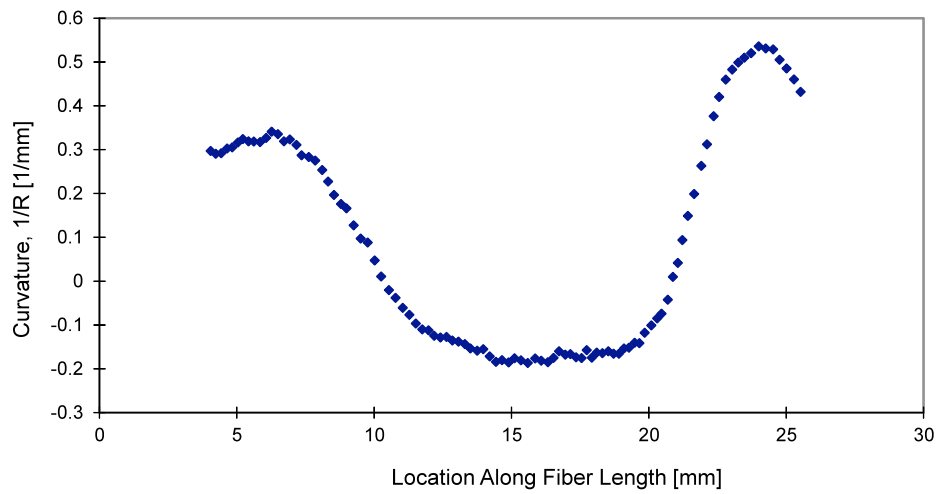


Fig. 6 – An example curvature profile of a SiC fiber specimen loaded in fiber BSR fixture.

References

- [1] K. Ehrlich, *Journal of Nuclear Materials* 100 (1981) 149-166.
- [2] Y. Katoh, S. Kondo, and L.L. Snead, *Journal of Nuclear Materials* 382 (2008) 170-175.
- [3] Y. Katoh, and L.L. Snead, *Ceramic Engineering and Science Proceedings* 26 (2005) 265-272.
- [4] N.B. Morley, Y. Katoh, S. Malang, B.A. Pint, A.R. Raffray, S. Sharafat, S. Smolentsev, and G.E. Youngblood, *Fusion Engineering and Design* 83 (2008) 920-927.
- [5] G.N. Morscher and J.A. DiCarlo, *Journal of the American Ceramic Society* 75 (1992) 136-40.
- [6] R.J. Price, *Nuclear Technology* 35 (1977) 320-336.

2.2 Low Activation Joining of SiC/SiC Composites for Fusion Applications¹ – C. H. Henager, Jr., R. J. Kurtz (Pacific Northwest National Laboratory², Richland, WA 99336, USA), and M. Ferraris, (Politecnico di Torino, Torino, Italy)

OBJECTIVE

This work discusses the latest developments in TiC + Si displacement reaction joining at PNNL based on mechanical property test results from miniature torsion joints.

SUMMARY

The use of SiC composites in fusion environments may require joining of plates using reactive joining or brazing. One promising reactive joining method is the use of solid-state displacement reactions between Si and TiC to produce $Ti_3SiC_2 + SiC$. We continue to explore the processing envelope for this type of joint for the TITAN collaboration to produce the best possible joints to undergo irradiation studies in HFIR. The TITAN collaboration has designed miniature torsion joints for preparation, testing, and irradiation in HFIR. As part of that project PNNL synthesized 40 miniature torsion joints and several were tested for shear strength prior to irradiation testing in HFIR. The resulting tests indicated that joint fixture alignment problems cause joint strengths to be lower than optimal but that several joints that were well aligned had high shear strengths and promising mechanical properties. High joint strengths cause non-planar shear fracture and complicate strength analysis for these miniature torsion joints.

PROGRESS AND STATUS

Introduction

SiC is an excellent material for fusion reactor environments, including first wall plasma facing materials and breeder-blanket modules. It is low-activation, temperature-resistant, and radiation damage tolerant compared to most materials. In the form of woven or braided composites with high-strength SiC fibers it has the requisite mechanical, thermal, and electrical properties to be a useful and versatile material system for fusion applications, especially since microstructural tailoring during processing allows control over the physical properties of interest [1-6]. However, it is difficult to mechanically join large sections of such materials using conventional fasteners so the analog of welding is being pursued for these ceramic materials [2,4-15]. Such methods include metallic brazes [8,16], glass ceramics [7,17], preceramic polymers [15], and displacement reactions [2,6]. This paper reports on the current status of SiC and SiC-composite joining for fusion applications based on displacement reactions between Si and TiC. This has been used to produce bulk composite material consisting of $SiC-Ti_3SiC_2$, with small amounts of TiC determined by the phase equilibria conditions [18].

Experimental Procedures

Joints are made using a tape calendaring process using organic binders and plasticizers together with a mixture of TiC and Si powders, with 99.99% purity, average diameters less than $45 \mu m$, and a TiC:Si ratio of 3:2. The flexible tapes were $200 \mu m$ thick and were cut to a disk shape and applied between two CVD SiC miniature torsion specimens as shown in Figure 1. These green joints were placed within a graphite joining fixture shown in Figure 2 that allows for alignment of the torsion joints and for applied compressive force during heating in an inert gas furnace enclosure. Joints were formed by heating the torsion coupons in argon to 1698K at 10K/min and holding for 2 hours at 40 MPa applied pressure. The resulting joints were dense and approximately $15 \mu m$ thick. They were prepared for optical and scanning electron microscopy using standard ceramographic cutting, grinding, and polishing methods. However, the SEM results have not yet been obtained for these joints. However, several prototype joints having slightly different total thickness dimensions were fabricated at PNNL and tested at ambient temperature in torsion

¹ Partly based on oral presentation given at the 2010 IEA SiC workshop held in Osaka, Japan as part of ICC3.

² PNNL is operated for the U.S. Department of Energy by Battelle Memorial Institute under Contract DE-AC06-76RLO 1830.

at the Politecnico di Torino, Torino, Italy by Dr. Ferraris' group and characterized there using SEM of the fracture surfaces.

Results

Figure 1 shows the torsion specimen drawing and a fabricated joint at PNNL prior to any testing. Figure 2 shows the joints placed into the graphite alignment fixture prior to processing in argon at 1698K for 2 hours. Some slight misalignment can be observed in some of the processed joints as shown in Figure 3. An improved graphite alignment fixture has been designed based on these initial processing results, but many of the processed joints are nearly perfectly aligned as shown in Fig. 1b and these were sent to HFIR for irradiation testing and for pre- and post-test strength testing.

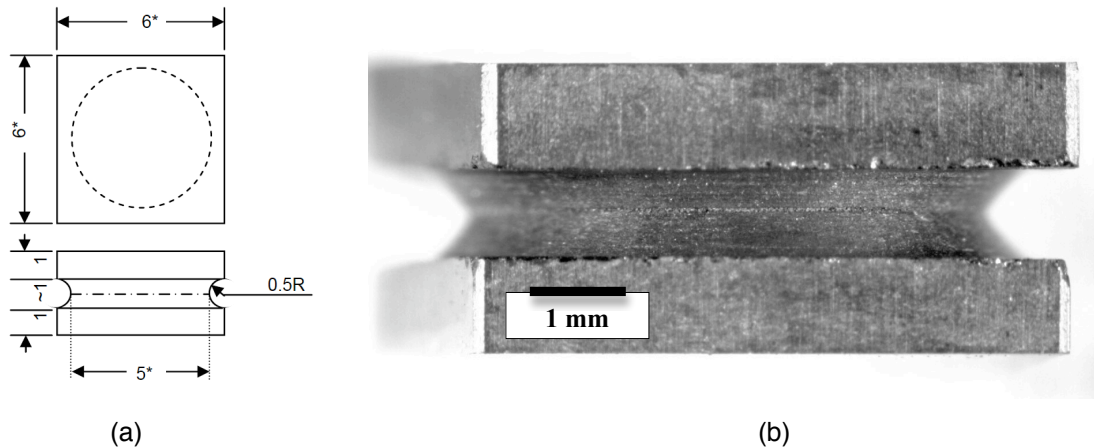


Figure 1. (a) Drawing of miniature torsion joining specimen for HFIR irradiation. Dimensions are shown in mm in (a). Shown in (b) is a photomicrograph of a PNNL fabricated torsion specimen. The joint line is visible along the specimen horizontal centerline.

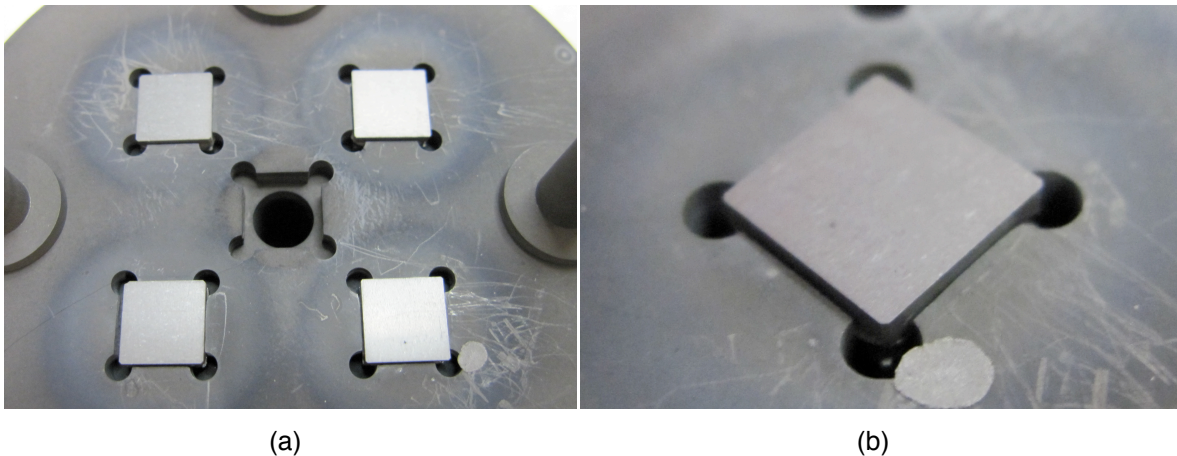


Figure 2. (a) Photomicrograph of graphite joining fixtures with 4 torsion joints ready for processing. The central hole in this photo allows an alumina-sheathed thermocouple to be placed close to the joints during processing. Shown in (b) is a close-up photomicrograph of a single joint held in place prior to processing. The torsion joints are 6-mm square and slightly less than 3-mm in height.

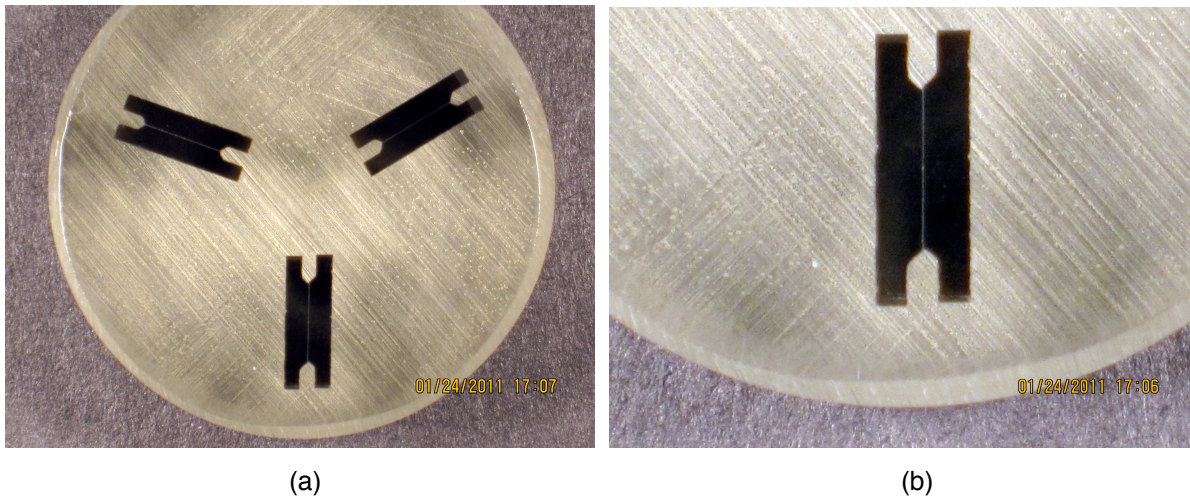


Figure 3. (a) Three sectioned joints mounted in epoxy for joint photomicrography and for checking joint alignment. The vertically oriented joint in the lower portion of the photo can be seen to be slightly misaligned and this is seen more clearly in (b).

Several joints were tested in Torino and the results of those tests are shown in Figure 4. The focus here is the large discrepancy between the high strength and low strength joints. The main findings in this study are that well made joints, i.e., those that are aligned and fully dense have high strengths in torsion but otherwise do not, as shown in Figure 5. The highest torsion strengths measured here exceed the target strength of 50 MPa and agree reasonably well with strengths measured using other joint strength measurements [2]. Shear lap joint tests with similarly processed joints between Hexoloy SiC bars were measured at 50 MPa shear strength in this previous study. Additionally, optical photomicrography results on recently processed joints, shown in Figure 6, show similar dense regions with typical SiC/Ti₃SiC₂ interpenetrating microstructures with strong bonding to the CVD SiC coupon surfaces. Some residual porosity is observed due to binder gas release during joint processing.

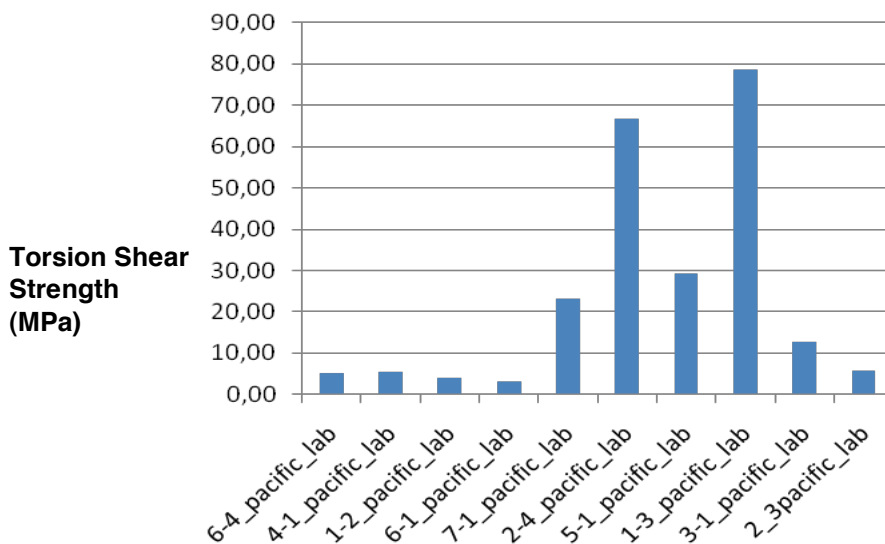


Figure 4. Bar graph of joint strengths measured in MPa of torsion shear strength. The strengths are distributed basically in two groups: those less than 30 MPa and those greater than 60 MPa. The high strength joints are of interest for irradiation testing.

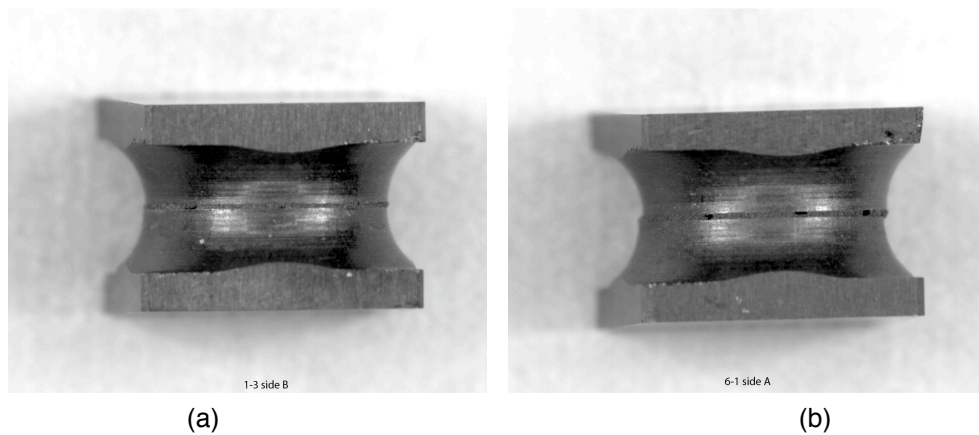
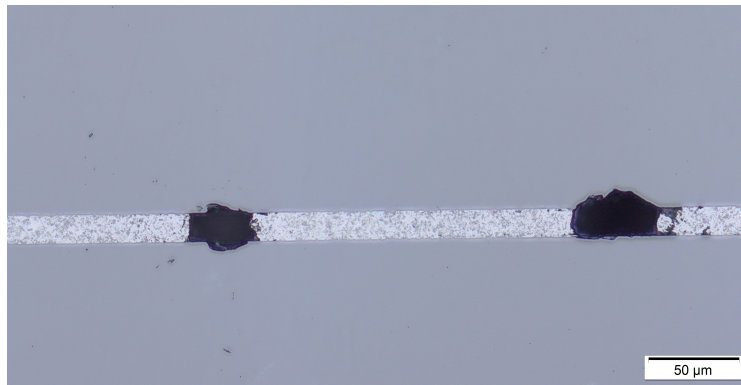
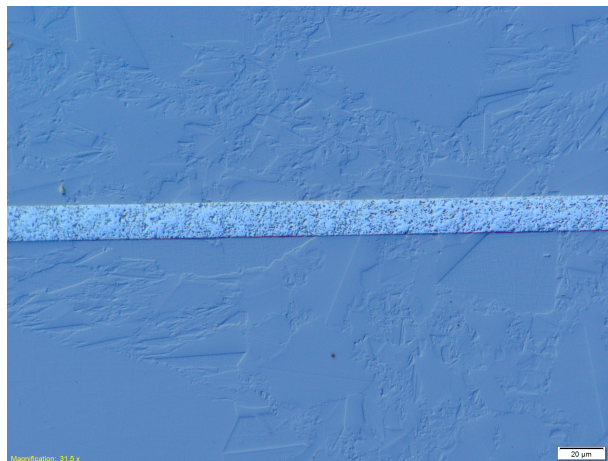


Figure 5. Side-by-side comparisons of two processed joints tested in torsion at Politecnico di Torino. The joint 1-3 in (a) on the left is well aligned and is a thin, dense joint. The joint 6-1 in (b) on the right is not well aligned and the joint region is thick and not fully dense. The shear strengths were 79 MPa for joint 1-3 in (a) and 3 MPa for joint 6-1 in (b).



(a)



(b)

Figure 6. Photomicrographs of a polished cross-section torsion joint as seen in Figure 3. Shown in (a) is a bright-field reflected image of a joint region showing dense joint region and porosity in the joint. The porosity is thought to arise from gas release from the binder during joint processing. In (b) is a differential interference contrast (DIC) image under conditions that reveal the CVD SiC grain structure and the joint interpenetrating two-phase structure is also highlighted by this technique.

Several of the fractured joints were examined at Politecnico via SEM. Specimen 6-1, a low strength joint (3 MPa) fractured along the torsion joint in shear as shown in Figure 7. Fractography reveals that this joint was weak due to poor bonding to the CVD SiC surface and due to the porosity of the joint. However, joint 1-3, which was a high strength joint (79 MPa) is imaged in Figure 8. A non-planar fracture in the joint region is observed and at higher magnifications it can be seen that surface damage to the CVD SiC has occurred due to strong joint bonding. Further, although these images do not reveal that explicitly, the joining materials imaged on the joint fracture surface are dense compared to those seen in Figure 7. Therefore, both joint alignment and proper processing are observed to play a role in joint strength in these preliminary torsion shear tests. Recent joints sent to ORNL for HFIR irradiation testing were handpicked for alignment and much care was taken in proper processing conditions for those joints to ensure that the proper joining pressure was applied during processing. Joint regions should be less than 20 μm in thickness as shown in Figure 6 to ensure proper densification has occurred.

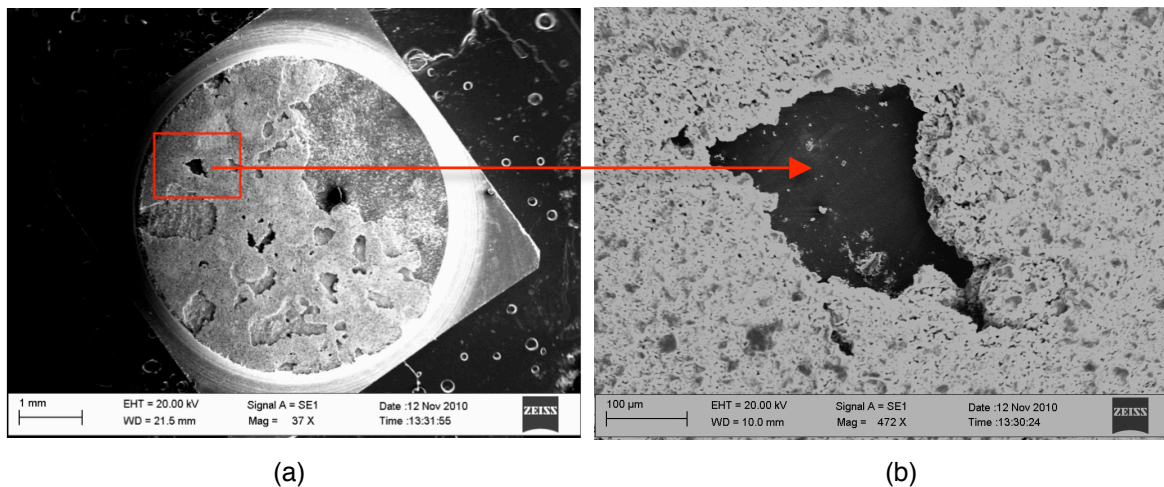


Figure 7. Low magnification SEM micrograph in (a) reveals a planar fracture surface for specimen 6-1, which had a 3 MPa shear strength measurement. The higher magnification photo in (b) indicates that regions of unbonded SiC are observed and that the joint material is highly porous.

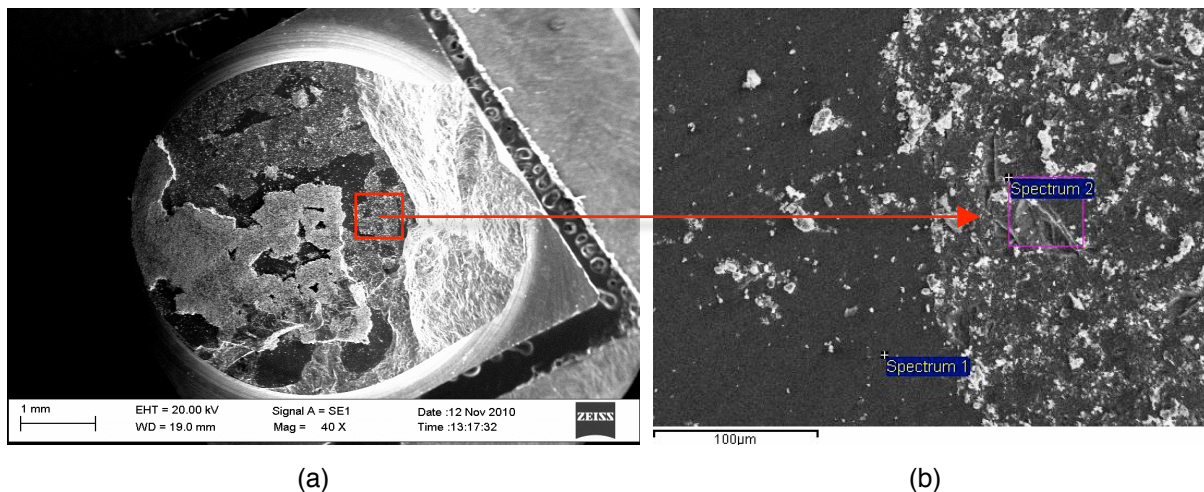


Figure 8. Low magnification SEM micrograph in (a) reveals a non-planar fracture surface for specimen 1-3, which had a 79 MPa shear strength. The higher magnification photo in (b) indicates that regions of severe surface damage in the CVD SiC can be observed where the fracture path was presumably located at the joint/SiC interface. In addition, although it is not shown here, the joint material was observed to be denser on the fracture surface of 1-3 as compared to 6-1.

References

1. Katoh, Y., L.L. Snead, C.H. Henager Jr., A. Hasegawa, A. Kohyama, B. Riccardi, and H. Hegeman, "Current status and critical issues for development of SiC composites for fusion applications," *J. Nucl. Mater.*, **367-370 A** (2007) 659-671.
2. Henager, C.H.J., Y. Shin, Y. Blum, L.A. Giannuzzi, B.W. Kempshall, and S.M. Schwarz, "Coatings and joining for SiC and SiC-composites for nuclear energy systems," *J. Nucl. Mater.*, **367-370** (2007) 1139-43.
3. Yvon, P. and F. Carre, "Structural materials challenges for advanced reactor systems," *J. Nucl. Mater.*, **385** (2009) 217-222.
4. Nozawa, T., T. Hinoki, A. Hasegawa, A. Kohyama, Y. Katoh, L.L. Snead, C.H. Henager Jr, and J.B.J. Hegeman, "Recent advances and issues in development of silicon carbide composites for fusion applications," *J. Nucl. Mater.*, **386-388** (2009) 622-627.
5. Jung, H.-C., Y.-H. Park, J.-S. Park, T. Hinoki, and A. Kohyama, "RD of joining technology for SiC components with channel," *J. Nucl. Mater.*, **386-388** (2009) 847-851.
6. Henager C.H, J. and R.J. Kurtz, "Low-activation joining of SiC/SiC composites for fusion applications," *J. Nucl. Mater.*, **in press** (2011)
7. Ferraris, M., P. Appendino, V. Casalegno, F. Smeacetto, and M. Salvo, "Joining of ceramic matrix composites for fusion application," *Adv. Sci. Technol.*, **33** (2003) 141-152.
8. Riccardi, B., C.A. Nannetti, T. Petrisor, and M. Sacchetti, "Low activation brazing materials and techniques for SiCf/ SiC composites," *J. Nucl. Mater.*, **307-311** (2002) 1237-1241.
9. Jones, R.H., L. Giancarli, A. Hasegawa, Y. Katoh, A. Kohyama, B. Riccardi, L.L. Snead, and W.J. Weber, "Promise and challenges of SiC_f/SiC composites for fusion energy applications," *J. Nucl. Mater.*, **307-311** (2002) 1057-1072.
10. Bruce, R.L., S.K. Guharay, F. Mako, W. Sherwood, and E. Lara-Curzio, "Polymer-derived SiCf/SiCm composite fabrication and microwave joining for fusion energy applications," *IEEE/NPSS Symposium on Fusion Engineering*, (2002) 1078-8891.
11. Zucchetti, M., M. Ferraris, and M. Salvo, "Safety aspects of joints and coatings for plasma facing components with composite structures," *Fusion Engineering and Design*, **58-59** (2001) 939-943.
12. Raffray, A.R., R. Jones, G. Aiello, M. Billone, L. Giancarli, H. Golfier, A. Hasegawa, Y. Katoh, A. Kohyama, S. Nishio, B. Riccardi, and M.S. Tillack, "Design and material issues for high performance SiC_f/SiC-based fusion power cores," *Fusion Engineering and Design*, **55** (2001) 55-95.
13. Lewinsohn, C.A., R.H. Jones, T. Nozawa, M. Kotani, Y. Katoh, A. Kohyama, and M. Singh, "Silicon carbide based joining materials for fusion energy and other high-temperature, structural applications," *Ceram. Engr. Sci. Proc.*, **22** (2001) 621-625.
14. Lewinsohn, C.A., M. Singh, T. Shibayama, T. Hinoki, M. Ando, Y. Katoh, and A. Kohyama, "Joining of silicon carbide composites for fusion energy applications," (2000) Colorado Springs, CO, USA: Elsevier.
15. Colombo, P., B. Riccardi, A. Donato, and G. Scarinci, "Joining of SiC/SiC_f ceramic matrix composites for fusion reactor blanket applications," *J. Nucl. Mater.*, **278** (2000) 127-135.
16. Riccardi, B., C.A. Nannetti, T. Petrisor, J. Woltersdorf, E. Pippel, S. Libera, and L. Pilloni, "Issues of low activation brazing of SiC_f/SiC composites by using alloys without free silicon," (2004) Kyoto, Japan: Elsevier, Amsterdam, Netherlands.
17. Katoh, Y., M. Kotani, A. Kohyama, M. Montorsi, M. Salvo, and M. Ferraris, "Microstructure and mechanical properties of low-activation glass-ceramic joining and coating for SiC/SiC composites," *J. Nucl. Mater.*, **283-287** (2000) 1262-6.
18. Radhakrishnan, R., C.H. Henager, Jr., J.L. Brimhall, and S.B. Bhaduri, "Synthesis of Ti₃SiC₂/SiC and TiSi₂/SiC composites using displacement reactions in the Ti-Si-C system," *Scripta Materialia*, **34** (1996) 1809-1814.

2.3 CHARACTERIZATION BY SEM OF THE PYROCARBON FIBER COATING IN 2D-SiC/CVI-SiC - G. E. Youngblood (Pacific Northwest National Laboratory¹)

OBJECTIVE

The primary objectives of this task are: (1) to assess the properties and behavior of SiC_f/SiC composites made from SiC fibers (with various SiC-type matrices, fiber coatings and architectures) before and after irradiation, and (2) to develop analytic models that describe these properties as a function of temperature and dose as well as composite architecture. Recent efforts have focused on examining the electrical conductivity properties of SiC_f/SiC composites considered for application in flow channel insert (FCI) structures in support of the U.S. dual-coolant lead-lithium (DCLL) fusion reactor blanket concept.

SUMMARY

The previous report examined electrical conductivity (EC) data from RT to 800°C for several forms of two-dimensional silicon carbide composite made with a chemical vapor infiltration (CVI) matrix (2D-SiC/CVI-SiC), an important quantity needed for the design of an FCI. We found that both in-plane and transverse EC-values for 2D-SiC/CVI-SiC strongly depended on the total thickness of the highly conductive pyrocarbon (PyC) fiber coating and the alignment of the carbon coating network. Furthermore, the transverse EC depended on the degree of interconnectivity of this network. For our EC-modeling efforts we used either “nominal” coating thickness values provided by the composite fabricator or we made thickness estimates based on a limited number of fiber cross-section examinations using SEM. Because of the importance of using a truly representative coating thickness value in our analysis, we examined numerous new SEM cross-sectional views to reassess the reliability of our limited number of original coating thickness measurements as well as to obtain an estimate of the variation in thickness values for different composite configurations.

PROGRESS AND STATUS

Introduction

A clear demonstration of how important the total PyC coating thickness is in determining the EC of a 2D-SiC/CVI-SiC is illustrated in Figure 1 (Fig. 1 is Fig. 2 from the previous FMSPR report [1]).

The in-plane EC(T)-curves in Fig. 1 appear to separate into four groupings with parallel curves, in which each group exhibits similar temperature dependence. The major observation is the marked decrease in EC-values as the total “nominal” PyC fiber coating thickness of each group decreases from 310 nm down to 50 nm. In fact, the relative decrease in magnitude of the EC-values is almost linearly proportional to the decrease in the coating thickness values. This behavior of the in-plane EC is due to its dependence primarily on conduction through the thin PyC fiber coatings with little dependence on the conductivity of the majority SiC matrix or fiber components. A somewhat similar dependence on coating thickness was observed for the transverse EC(T)-curves (see Fig. 5 in [1]). However, for 2D-SiC/CVI-SiC the transverse EC exhibits some dependence on conductivity through the SiC matrix and fiber components as well as through the PyC fiber-coating network, as indicated by the generally lower magnitude of the EC and its overall temperature dependence. Most importantly, the transverse EC also depends on the degree of interconnectivity of the fiber coating network within the fiber bundles as well as between the fabric layers.

¹PNNL is operated for the U.S. Department of Energy by Battelle Memorial Institute under Contract DE-AC06-76RLO 1830.

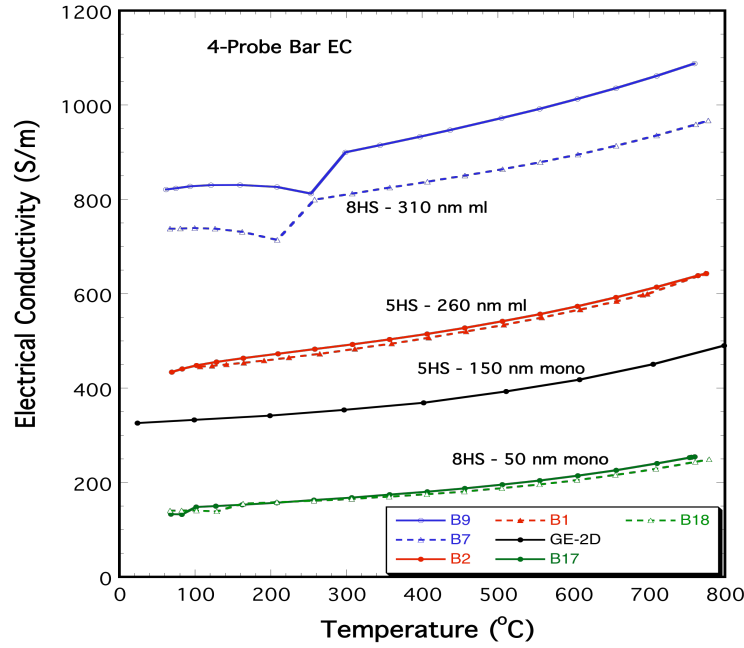


Figure 1. In-plane EC(T)-values for representative 2D-SiC/CVI-SiC bar samples with 0/90 weave and different total “nominal” PyC fiber coating thickness. The four groupings (two samples each) are labeled according to their total PyC coating thickness in descending order: 310 nm (multilayer), 260 nm (multilayer), 150 nm (monolayer), and 50 nm (monolayer).

In Ref. [1], a simple “series layer” model was introduced that described the transverse EC(T) of a 2D-SiC/CVI-SiC plate in terms of the interior carbon-networked, fabric-layered region EC (EC_{int}) in series with outer “seal coat” layers of densely adherent, single phase CVD-SiC of EC (EC_{sc}):

$$EC(T) = EC_{int}[1 - 2f(1 - R)]^{-1} \quad [1]$$

In Eq. [1], T is temperature, $f = t/L$ where t is the average thickness of a seal coat layer, L is the composite plate thickness (including the seal coat layers). Values of EC_{int} are determined by making EC measurements on a disc sample with the seal coat layers removed by grinding each surface down well into the fabric-layered interior region. Also, R is the ratio EC_{int}/EC_{sc} , where in our case EC_{sc} was calculated for a CVD-SiC seal coat using values of EC measured for representative samples of pure, monolithic CVD-SiC. Because f in Eq. [1] is relatively small, the magnitude of the overall transverse EC(T)-values, especially in the moderate 200-700°C temperature range, depends primarily on the electrical conduction of the carbon-networked interior region of a 2D-SiC/CVI-SiC composite through EC_{int} . In turn, EC_{int} depends on the amount of relatively high conductivity carbon (even though it is only a few per cent of the total volume) and on the interconnectivity of the carbon network within this interior region.

In reference [2], Katoh, et al, presented a method to quantify the degree of interconnectivity in the interior region of a 2D-SiC/CVI-SiC composite. The authors defined a “through-thickness interphase bypass efficiency” $\eta = 2\sigma_t/f_i\sigma_i \approx \sigma_t/\sigma_{ip}$, where they considered that $\sim 1/2$ of the interphase film contributes to in-plane conduction in one of the 0/90 fiber directions. In this expression, σ and f are electrical conductivity and volume fraction; and the subscripts t, ip and i denote through-thickness (transverse), in-plane and interphase, respectively. They stated that η -values should be dependent on interphase thickness and packing density of the SiC fabrics. For two types of monolayer interphase composites and a multilayered

composite, they measured η -values of 1.2–1.7%, and ~2.8%, respectively. They stated that the η -values of multilayered composites should exceed that of monolayer composites because in a multilayered composite the different layers have a higher chance of transverse bridging over multiple fibers since the outer PyC layers tend to envelope multiple fibers.

This report will examine in more detail how to determine the actual amount and thickness of the PyC fiber coating and will determine the degree of the PyC network interconnectivity calculated according to the “Katoh” method for four types of 2D-SiC/CVI-SiC, two with multilayered and two with monolayer PyC fiber coatings.

Materials and Procedures

Four of the 2D-SiC/CVI-SiC samples examined in the previous report were selected for reexamination here. They contained either multilayer (nominally a relatively thick ~200 nm PyC layer covered by four alternating 100-nm SiC layers/20-nm PyC layers) or a single ~150 nm or ~50 nm monolayer PyC coating. The samples were fabricated by CVI in a similar manner by Hyper-Therm, HTC or GE Power Systems Composites using Hi-Nicalon™ type S fabrics [1]. The “50-nm” PyC monolayer composite was made by Hyper-Therm specifically to satisfy the desired FCI-application goal of having a total transverse EC <20 S/m for all temperatures up to 800°C.

Sample cross-sections were cut and mounted in resin plugs, and polished smooth to 1- μ m diamond followed by a final colloidal silica polish. Each sample plug was examined in a field emission SEM (FEI Helios Nanolab FIB, Hillsborough, OR). For each sample, the fiber-coating interphase configuration and dimensions were examined in views of ~30 different surface locations at low (~x5000) and high (x80,000 to x250,000) magnifications. To statistically determine a representative fiber PyC coating thickness and its variation, ~10 thickness measurements were made at different locations on each view for ~300 or more total measurements for each sample. To reduce electron beam spreading and improve resolution a low energy electron beam (5 KeV) was used. A backscatter electron detector at 3.2-mm working distance produced sufficient atomic number contrast to clearly define the SiC matrix or fiber components and PyC fiber coatings at the cross-section surfaces.

Results

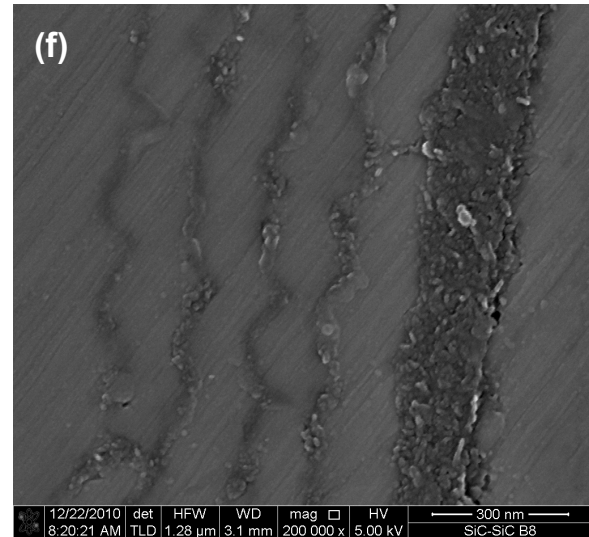
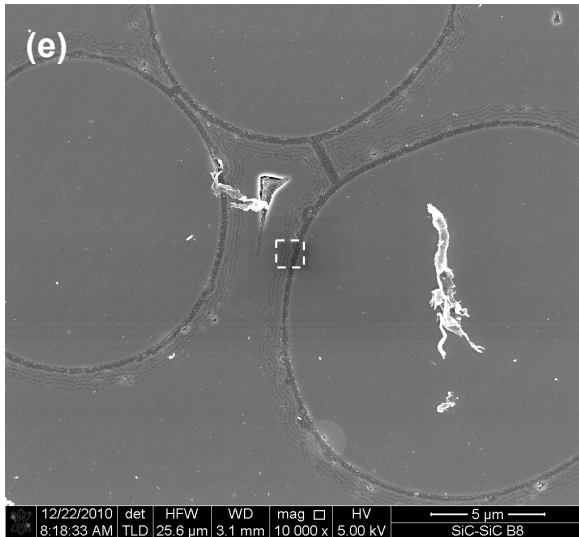
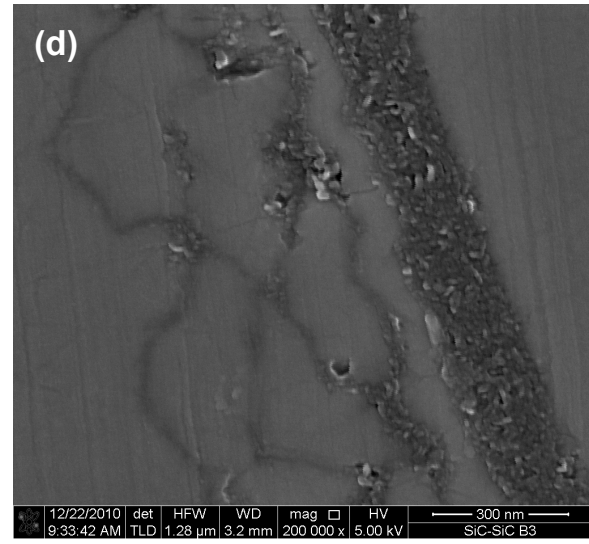
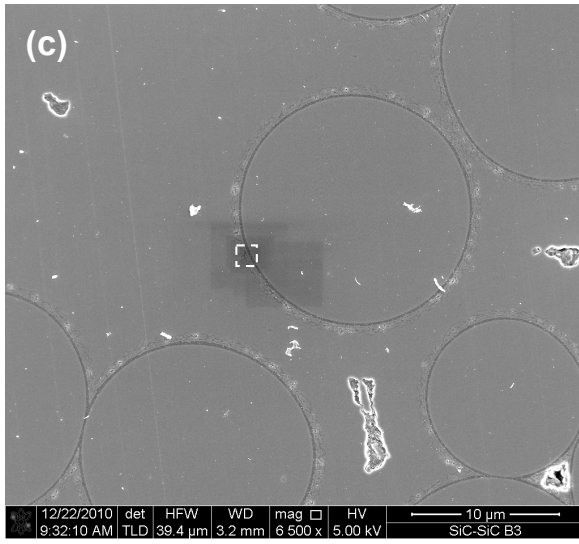
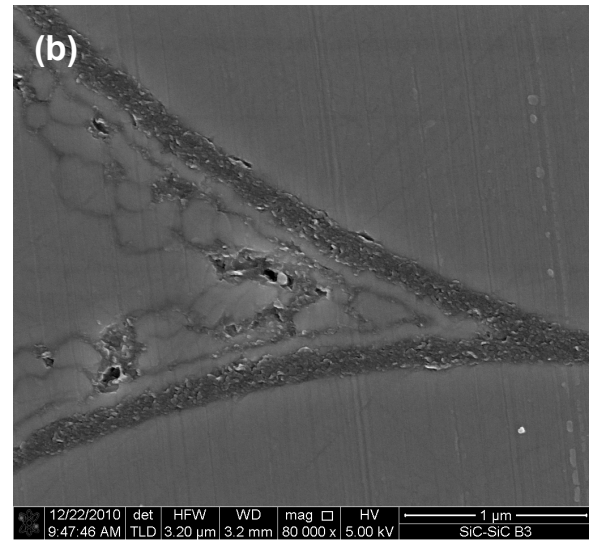
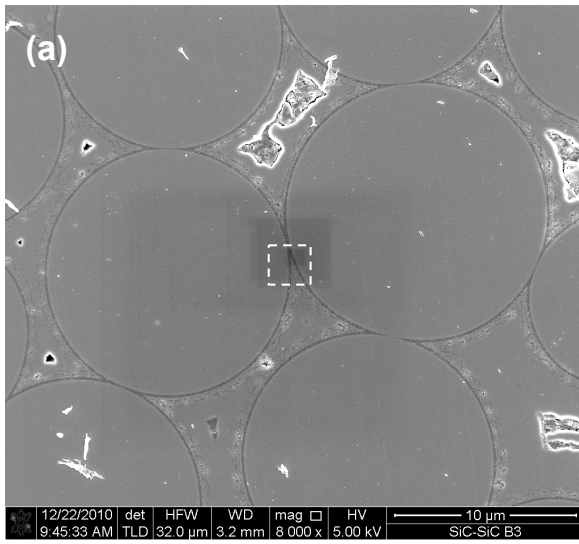
In Table 1, the measured in-plane and transverse EC-values and the estimated transverse bypass efficiencies (using Katoh’s method) for the four examined samples are given along with their weave types (either five or eight harness satin, 5HS or 8HS, respectively) and nominal multilayer (ml) or monolayer (mono) PyC coating thickness(es).

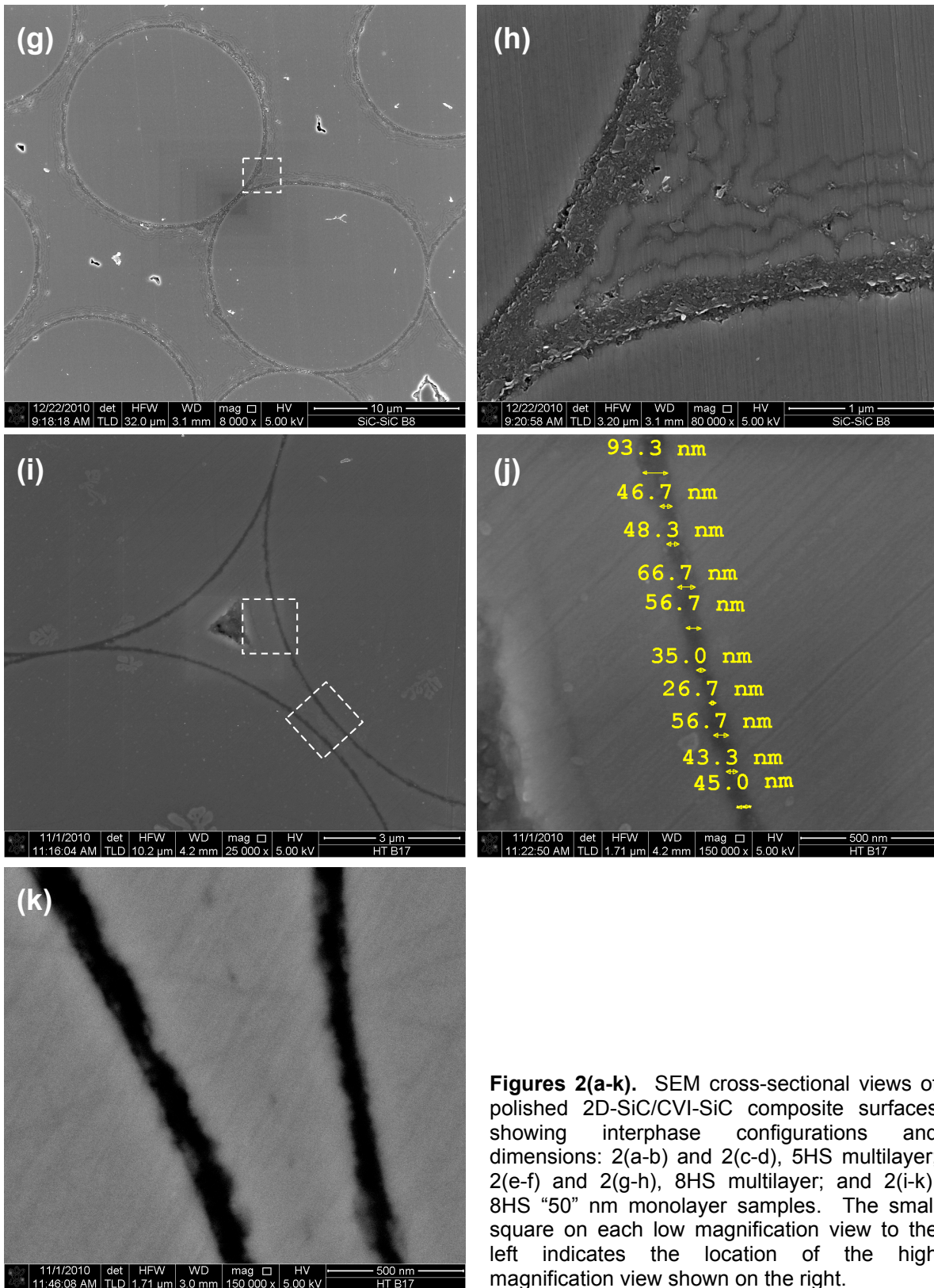
Table 1. Bypass efficiency estimates for four 2D-SiC/CVI-SiC sample types

Weave – PyC thickness (nm)	σ_{ip} @ 30°C (S/m)	σ_t @ 30°C (S/m)	$\eta \approx \sigma_t/\sigma_{ip}$ (%)
5HS -180 + 4(20), ml	440 ± 10 (2 samples)	10.0	2.3
8HS -230 + 4(20), ml	770 ± 40 (“ “)	12.5	1.6
5HS -150 mono	325 ± 10 (“ “)	2.6	0.8
8HS -50 mono	150 ± 10 (“ “)	1.2	0.8

At this point, general agreement with Katoh’s findings was found. That is, the by-pass efficiency η for the composites with multilayer coatings was approximately twice the values for the composites with a monolayer coating. Also, the η -magnitudes were in reasonable agreement (1.6 – 2.3 compared to 2.8 ml, and 0.8 compared to 1.2 – 1.7 for mono, respectively).

In Figures 2(a-k), representative SEM views of the PyC fiber coatings for three of the four sample types are given. The views for the 5HS-150 nm monolayer sample were not ready in time for this report.





Figures 2(a-k). SEM cross-sectional views of polished 2D-SiC/CVI-SiC composite surfaces showing interphase configurations and dimensions: 2(a-b) and 2(c-d), 5HS multilayer; 2(e-f) and 2(g-h), 8HS multilayer; and 2(i-k), 8HS “50” nm monolayer samples. The small square on each low magnification view to the left indicates the location of the high magnification view shown on the right.

In these views the SiC matrix or fiber components appear light grey, and the PyC coatings appear dark grey by atomic number contrast. Several cross-sections of needle-shaped pores lying parallel and between individual fiber filaments also are observed. In Table 2, a summary of the fiber coating thickness measurements is compared to their nominal values given by the fabricator. When possible, the standard deviations were calculated for ~60 different coating thickness measurements and are included in the table in parenthesis. The typical scatter in coating thickness measurements is illustrated in Fig. 2(j) for ten measurements made on one a representative of the 8HS-“50-nm” PyC monolayer sample surface.

Table 2. Summary of PyC/SiC fiber coating thickness measurements

Weave type	Nominal dimensions (nm)	Measured dimensions (nm)
5HS, ml	180 PyC + 4[100 SiC/20 PyC]	183 (± 15) PyC + 60 (± 8) SiC/22 (± 18) PyC +3[?/?]
8HS, ml	230 PyC + 4[100 SiC/20 PyC]	226 (± 40) PyC + 4[118 (± 9) SiC/32 (± 6) PyC]
8HS, mono	50 PyC	61 (± 10) PyC

Analysis and discussion

Fortuitously, the newly determined thickness values of the inner PyC fiber coating for each multilayer sample agree very well with the previous “nominal” thickness values, values that had been based on only a few random thickness measurements. However, the thickness of the so-called nominal “50-nm” PyC monolayer actually is 61 ± 10 nm. Based on these newly determined PyC coating thickness values, for these high quality 2D-SiC/CVI-SiC composites all the conclusions previously reached concerning the dependence of the in-plane and the transverse EC-values on the total PyC fiber coating thickness are still valid [1].

The largest uncertainty in the coating thickness values appears to be in the values determined for the alternating SiC/PyC multilayers that cover the relatively thick initial PyC layer, especially for the 5HS sample. For this material the initial PyC layer is well defined as is the initial SiC layer (Figs. 2(a-d)), although the initial SiC layer is somewhat thinner (60 ± 8 nm) than the designed 100-nm layer. However, the three following PyC/SiC layers appear to intersect numerous times so that a consistently separated layer pattern did not result from the processing conditions. From previous detailed TEM examinations of a CVI-SiC fiber/matrix interface [3], columnar SiC growth texture may lead to rough, nodular surfaces; thus an inconsistent SiC/PyC layer pattern may result, as observed in Figs. 2(b) and 2(d). Obviously, the PyC network for the 5HS material is well interconnected, at least within a fiber bundle. However, the rough, inconsistent texture of the PyC/SiC multilayers is not so evident for the 8HS multilayer sample. For this material, consistent thickness measurements were possible for the alternating SiC/PyC multilayers, and they agreed fairly well with the nominal design dimensions. This observable microstructural difference between the 5HS and 8HS multilayer composites likely led to the calculated differences in their η -values, 2.3 versus 1.6, respectively.

Even though a low 5 KeV energy electron beam was used to reduce beam spreading, there was sufficient scattering at the PyC/SiC interfaces to make distinct thickness measurements difficult. Therefore, for our modeling efforts we continue to use the nominal value of 20 nm provided by the fabricator for the thin PyC layer thicknesses.

An effort was made to discern any preferred deposition rates in regions of tight or open fiber packing. However no trends were observed, so we assume that the deposition rates were similar throughout during the CVI processing of these relatively thin (~3 mm) plate composites. However, the degree of infiltration and the deposition rates definitely depend on thickness for thicker plates, as observed in a microstructural study performed on a 12.0-mm thick plate made by forced chemical vapor infiltration (FCVI) [4].

CONCLUSIONS

A detailed examination by high magnification, field emission SEM of the PyC coating configurations for several 2D-SiC/CVI-SiC composites with either PyC/SiC multilayer or PyC monolayer fiber coatings was performed. Previous coating thickness values generally were confirmed, and all the conclusions based on these measurements concerning the dependence of the in-plane and the transverse EC-values on the total PyC fiber coating thickness still apply [1]. However, it is wise to perform a quality control examination of composite structures rather than accepting nominal design parameters for use in performing further analysis.

REFERENCES

- [1] G.E. Youngblood, E. Thomsen and R.J. Shinavski, "The electrical conductivity of SiC/SiC – Effects of pyrocarbon fiber coating thickness and contact resistance," pp 12-21 in Fusion Materials Semiannual Progress Report (FMSPR) for period ending June 30, 2010 (DOE/ER-0313/48).
- [2] Y. Katoh, S. Kondo and L.L. Snead, "DC electrical conductivity of silicon carbide ceramics and composites for flow channel insert applications," J. Nucl. Mater. 386-388 (2009) 639-642.
- [3] D.S. Gelles and G.E. Youngblood, "Microstructural examination of SiC/SiC woven fiber composites," pp 19-25 in FMSPR for period ending June 30, 2008 (DOE/ER-0313/44).
- [4] G.E. Youngblood, D.J. Senior, R.H. Jones and Yutai Katoh, "Modeling the thermal conductivity of 2D-SiC/SiC composites with woven architectures," pp. 36-42 in SiC/SiC Ceramic Composites for Fusion Energy Application, 5th international Energy Agency Workshop, April 12-13, 2002, San Diego, CA.

2.4 EVALUATION OF DAMAGE TOLERANCE OF ADVANCED SiC/SiC COMPOSITES AFTER NEUTRON IRRADIATION—K. Ozawa, Y. Katoh, L.L. Snead (Oak Ridge National Laboratory),

T. Nozawa (Japan Atomic Energy Agency), T. Hinoki (Kyoto University)

OBJECTIVE

The main objective of this study is to determine the neutron irradiation effects on damage tolerance of SiC/SiC composites with near-stoichiometric fibers and two different matrix types. In the current study, we applied non-linear fracture mechanics, based on actual crack increment measurements.

SUMMARY

The effect of neutron irradiation on damage tolerance of two nuclear grade SiC/SiC composites (plain-woven Hi-Nicalon™ Type-S fiber-reinforced, CVI SiC matrix composites with a multilayer interphase and unidirectional Tyranno™-SA3 fiber-reinforced, NITE matrix with a carbon mono-layer interphase) was evaluated by means of miniaturized single-edged notched-beam test. No significant changes in crack extension behavior and in the load-loadpoint displacement characteristics such as the peak load and hysteresis loop width were observed after irradiation to 5.9×10^{25} n/m² ($E > 0.1$ MeV) at 800°C and to 5.8×10^{25} n/m² at 1300°C. The global energy balance analysis based on non-linear fracture mechanics estimated the energy release rate contributed by macro-crack initiation to be 3 ± 2 kJ/m² for both the unirradiated and irradiated composites. The effects of neutron irradiation on fracture resistance of these composites appeared insignificant for the conditions examined.

PROGRESS AND STATUS

Introduction

Silicon carbide fiber reinforced silicon carbide matrix (SiC/SiC) composites are attractive candidate materials for structural and functional components in fusion energy systems due to the good radiation stability coupled with inherently low induced radioactivity and after-heat [1, 2]. For the new class of “nuclear grade” SiC/SiC composites, determining fracture resistance is one of the most important issues to be investigated. However, this has been challenging because composites consist of several constituents and hence the fracture resistance of composites with non-uniform properties cannot be determined by applying common methods for the linear-elastic plane-strain fracture toughness determination (such as ASTM E-399) or the compliance method based on linear-elastic fracture mechanics (LEFM) for a homogeneous material. Since no full-consensus test standards are available for damage tolerance determination of ceramic continuous fiber reinforced ceramic matrix composites, even though some ASTM standards for polymer composites (D 5528 for Mode I Interlaminar toughness and D 6671 for Mixed I and II Mode) are available, various methods of experiments and analyses have been proposed by researchers [3-8]. Moreover, there are no published results on the effects of irradiation on damage tolerance, while there have been extensive efforts to study the irradiation effects in the SiC/SiC composite system [9-13]. There has been a report on fracture toughness of Hi-Nicalon™ Type-S fiber reinforced SiC matrix composites after neutron irradiation to 4.3×10^{24} n/m² at 40°C, unfortunately with no detailed information disclosed [14]. The main objective of this study is to determine the neutron irradiation effects on fracture toughness of SiC/SiC composites with near-stoichiometric fibers and the matrices. In the current study, we attempted to apply non-linear fracture mechanics, based on actual crack increment measurements.

Experimental

Hi-Nicalon™ Type-S plain-woven fabric-reinforced CVI matrix composites with (PyC₂₀/SiC₁₀₀)₅ multilayer interphase composite (HNLS-CVI-ML) and unidirectional Tyranno™-SA3 reinforced with 500 nm PyC mono-layer interphase and nano-infiltration and transient eutectic-phase (NITE) SiC composite (TySA-NITE) were prepared. Detailed information about the composites is given elsewhere [15, 16]. The materials were machined into miniature single-edged notched-beam (SENB) specimens for in-plane

mode-I fracture behavior evaluation. Effects of the test specimen size on the fracture behavior have been studied and are discussed elsewhere [17, 18]. Neutron irradiation was conducted in the High Flux Isotope Reactor (HFIR) at the Oak Ridge National Laboratory as a part of RB*-18J campaign. The peak neutron fluence and the nominal irradiation temperature were $\sim 5.9 \times 10^{25} \text{ n/m}^2$ ($E > 0.1 \text{ MeV}$) at 800°C and $\sim 5.8 \times 10^{25} \text{ n/m}^2$ at 1300°C . An equivalence of one displacement per atom (dpa) = $1 \times 10^{25} \text{ n/m}^2$ ($E > 0.1 \text{ MeV}$) is assumed. The SENB tests were conducted at room-temperature using an electromechanical testing machine with a load capacity of 1 or 10 kN. Test specimens were loaded using a three-point bend fixture with a support span of 16 mm under a constant crosshead displacement rate of 0.05 mm/min. Loadpoint displacement was measured using a clip-on crack opening gauge. The unloading-reloading sequences were applied to evaluate the damage accumulation behavior during testing. Crack length at each loading-unloading cycle was evaluated by optical microscope observations of the replica films. Detail experimental procedure is given elsewhere [19].

Results and Discussion

Typical load-loadpoint displacement (P - u) curves of the composites before/after neutron irradiation are reproduced in Figure 1. Both composites exhibited typical quasi-ductile behavior. No significant changes in various features of the P - u curves such as peak load and hysteresis loop width following neutron irradiation were observed for either composite type.

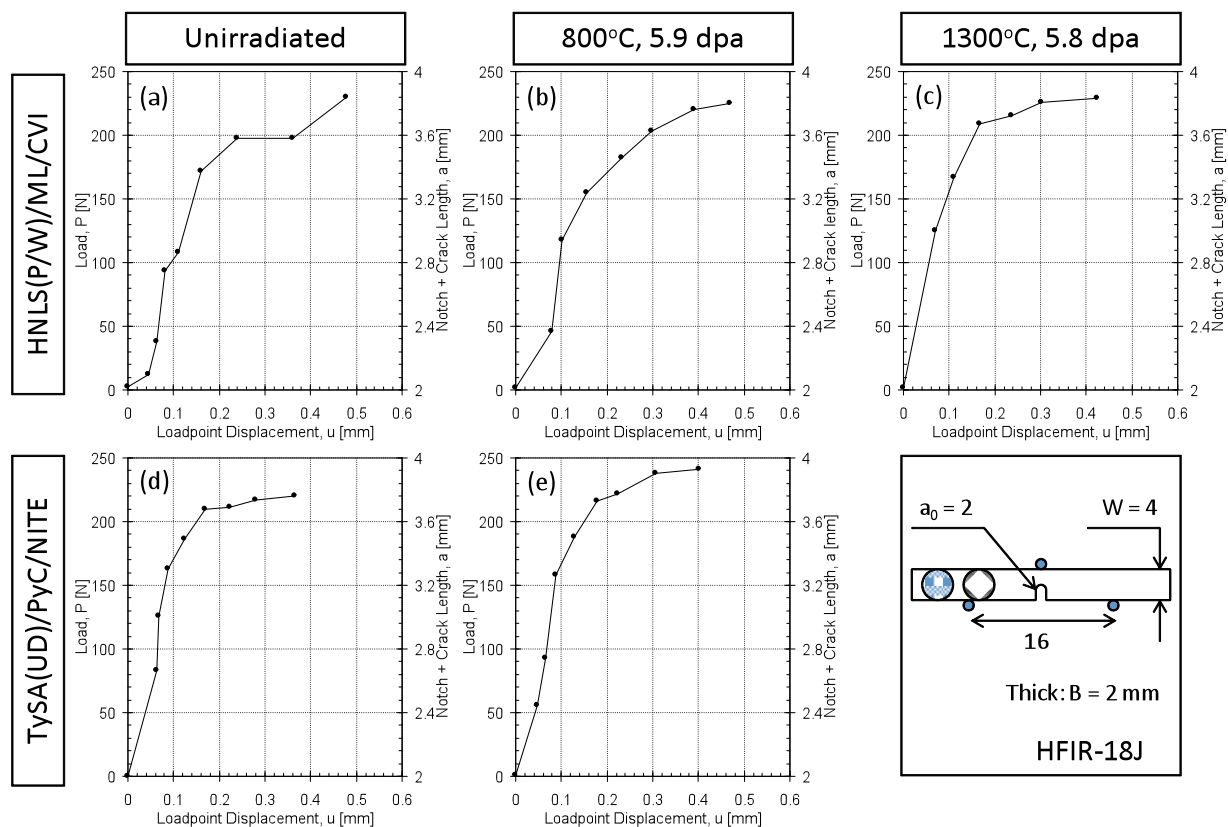


Figure 1. Typical load-loadpoint displacement curves for the unirradiated and irradiated HNLS-CVI-ML and TySA-NITE composites.

Because of the apparent quasi-ductility of the composites, application of an analytical model based on non-linear fracture mechanics [20, 21] for determining fracture resistance is considered suitable. In the present work, the analytical method developed by Nozawa *et al.* [17, 18] has been applied. The definition of each energy is shown in Figure 2 and the detailed analytical procedure is given elsewhere [19]. In brief,

the apparent fracture resistance (G_{total}) and energy release rate for micro-crack formation (G_{micro}) were calculated from the following equations:

$$G_{total} \equiv \frac{1}{B} \frac{\partial \Gamma_{total}}{\partial a} = \frac{1}{B} \frac{\Delta \Gamma_{total}}{\Delta u} \frac{\Delta u}{\Delta a} \tag{1}$$

$$G_{micro} \equiv -\frac{1}{B} \frac{\Delta \Gamma_{micro}}{\Delta a} \equiv \frac{1}{WB} \sum_{i=1}^n i C_i \left(1 - \frac{a}{W}\right)^{i-1} \tag{2}$$

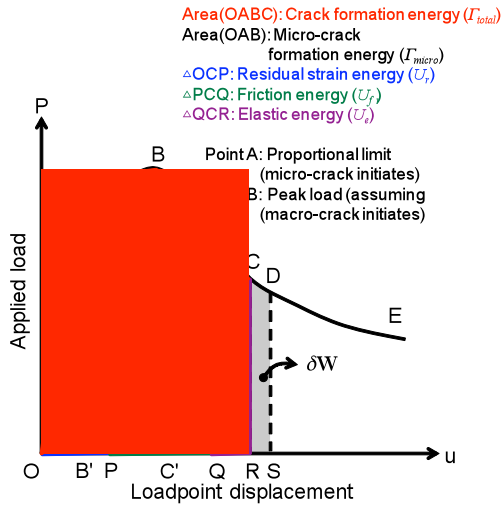


Figure 2. Schematic illustration of P - u curve and definition of each energy.

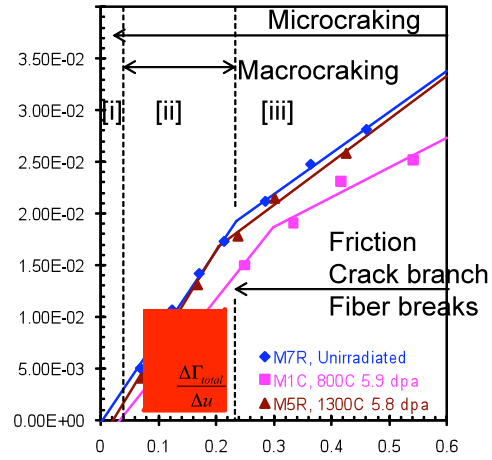


Figure 3. Total crack formation energy (Γ_{total}) and definition of $\Delta \Gamma_{total}/\Delta u$.

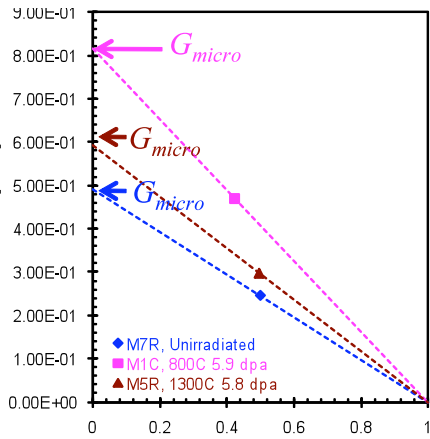


Figure 4. G_{micro} determination.

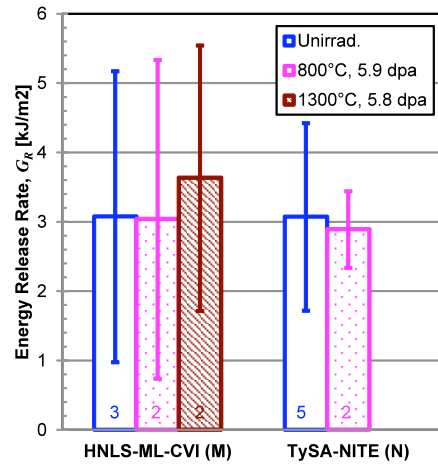


Figure 5. Non-linear energy release rate of unirradiated and irradiated (a) HNLS-CVI-ML and (b) TySA-NITE composite. Error bars, and numbers in each bar denote one standard deviation, and the number of valid tests.

with Γ_{total} being the apparent surface crack formation energy, Γ_{micro} the micro-crack formation energy, a the crack length, B the specimen thickness, W the specimen width, u the loadpoint displacement, C_i the constants. The $\Delta\Gamma_{total}/\Delta u$ values were obtained from the slope of $\Gamma_{total}-u$ graph at the stage [ii], corresponding to the macro-crack extension, as shown in Figure 3. The $\Delta u/\Delta a$ values were measured from the plots of the actual crack length change in the stage [ii] in Figure 1. The G_{micro} value in Eq. (2) was obtained by linear-fitting (Figure 4). The actual energy release rate was given by $G_{macro} = G_{total} - G_{micro}$. Eventually, the energy release rate contributed only by macro-crack initiation of 3 ± 2 kJ/m² was estimated for either type of composite before and after irradiation (Figure 5).

Significant scatter was observed in the energy release rate analysis, likely due to the limited specimen dimensions as compared to the weave unit cell size. However, the damage tolerance properties of these composites did not appear to have changed remarkably, based on the present result on the energy release rate analysis. The previous results of the tensile tests after neutron irradiation and the hysteresis loop analysis estimating the interfacial properties further support this conclusion [16,22]. As shown in Figure 6, no significant changes in tensile stress-strain curves was observed for either type of composite irradiated in identical conditions. In addition, it is previously pointed out by Droillard *et al.* that energy release rate can be strongly influenced by interfacial sliding stress (and hence matrix crack density) from the viewpoint of frontal process zone size [7]. Since sliding stress was not directly measured, it was estimated by the interfacial sliding stress parameter at around same matrix damage parameter proposed by Katoh *et al.* [23] for qualitative comparison. From the result in Figure 6, almost no change or the tendency of slight increasing “effective” sliding stress was also estimated (except NITE 1300°C, 5.8 dpa for which evaluation is underway). Hence, it is concluded that the effect of neutron irradiation on fracture resistance of the SiC/SiC composites is not significant for the conditions studied.

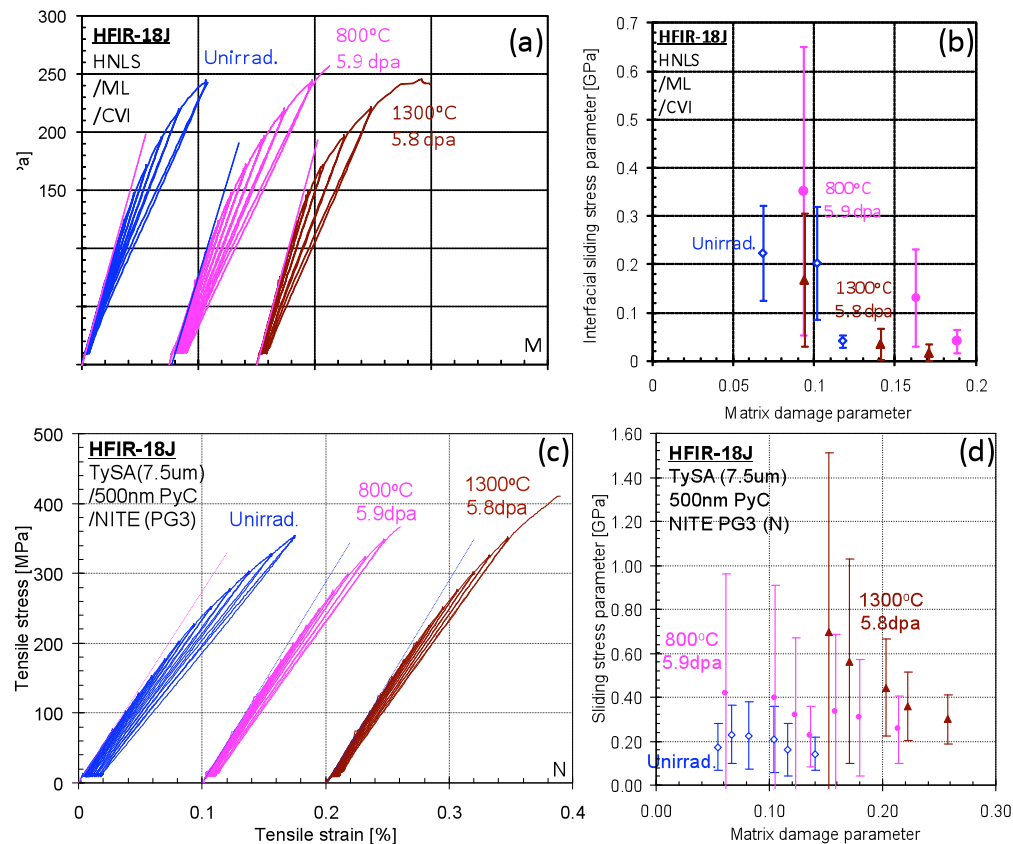


Figure 6. Tensile stress-strain curves for (a) HNLS-CVI-ML [16] and (c) TySA-NITE composite [22], and interfacial sliding stress parameter for (b) HNLS-CVI-ML and (d) TySA-NITE composite.

Conclusions

The effect of neutron irradiation on damage tolerance of the nuclear grade SiC/SiC composites was evaluated by means of miniaturized single-edged notched-beam test. No significant changes in crack extension behavior and the load-loadpoint displacement characteristics such as the peak load and hysteresis loop width were observed after irradiation to 5.9×10^{25} n/m² ($E > 0.1$ MeV) at 800°C and to 5.8×10^{25} n/m² at 1300°C. The global energy balance analysis based on non-linear fracture mechanics estimated the energy release rate contributed by macro-crack initiation to be 3 ± 2 kJ/m² for both the unirradiated and irradiated composites. According to this analytical result, it was included that the tensile properties, and the hysteresis loop analysis of the tensile tests, the effects of neutron irradiation in conditions studied on fracture resistance of these composites are insignificant.

Acknowledgement

The authors would like to thank Ms. A.M. Williams, Ms. P.S. Tedder, Mr. L.E. Reid, Ms. S.G. Beck and Ms. B.D. Johnson for the post-irradiation experiments. Irradiation was carried out in the Department of Energy High Flux Isotope Reactor User Facility. This research was sponsored by the Office of Fusion Energy Sciences, US Department of Energy under contract DE-AC05-00OR22725 with UT-Battelle, LLC. This study was also a part of TITAN US Department of Energy/Japanese Ministry of Education, Culture, Sports, Science and Technology (MEXT) collaboration for fusion material system research.

Reference

- [1] T. Nozawa, T. Hinoki, A. Hasegawa, A. Kohyama, Y. Katoh, L.L. Snead, C.H. Henager Jr, J.B.J. Hegeman, *J. Nucl. Mater.* 386-388 (2009) 622.
- [2] Y. Katoh, L.L. Snead, C.H. Henager Jr, A. Hasegawa, A. Kohyama, B. Riccardi, H. Hegeman, *J. Nucl. Mater.* 367-370 (2007) 659.
- [3] C. Droillard, P. Voisard, C. Heibst, J. Lamon, *J. Am. Ceram. Soc.* 78 (1995) 1201.
- [4] Y.W. Mai, M.I. Hakeem, *J. Mater. Sci* 19 (1984) 501.
- [5] M. Gomina, D. Themines, J.L. Chermant, F. Osterstock, *Int. J. Fract.* 34 (1987) 219.
- [6] M. R'Mili, D. Rouby, G. Fantozzi, *Compos. Sci. Technol.* 37 (1990) 207.
- [7] C. Droillard, P. Voisard, C. Heibst, J. Lamon, *J. Am. Ceram. Soc.* 78 (1995) 1201.
- [8] C. Droillard, J. Lamon, *J. Am. Ceram. Soc.* 79 (1996) 849.
- [9] T. Nozawa, Y. Katoh, L.L. Snead, *J. Nucl. Mater.* 384 (2009) 195.
- [10] T. Nozawa, K. Ozawa, S. Kondo, T. Hinoki, Y. Katoh, L.L. Snead, A. Kohyama, *J. ASTM Int.* 2 (2005) 12884.
- [11] K. Ozawa, T. Hinoki, T. Nozawa, Y. Katoh, Y. Maki, S. Kondo, S. Ikeda, A. Kohyama, *Mater. Trans.* 47 (2006) 207.
- [12] K. Ozawa, T. Nozawa, Y. Katoh, T. Hinoki, A. Kohyama, *J. Nucl. Mater.* 367-370 (2007) 713.
- [13] Y. Katoh, T. Nozawa, L.L. Snead, T. Hinoki, *J. Nucl. Mater.* 367-370 (2007) 774.
- [14] G. Vekinis, K. Mergia, G. Xanthopoulou, *Abstracts of International Symposium on New Frontier of Advanced Si-Based Ceramics and Composites* (2004) 25.
- [15] Y. Katoh, K. Ozawa, L.L. Snead, Y.B. Choi, T. Hinoki, A. Hasegawa, *Fusion Mater.* DOE/ER-0313/45 (2008) 21.
- [16] Y. Katoh, K. Ozawa, T. Hinoki, Y.B. Choi, L.L. Snead, A. Hasegawa, *J. Nucl. Mater.* doi:10.1016/j.jnucmat.2011.02.006 (2011).
- [17] T. Nozawa, T. Hinoki, A. Kohyama, H. Tanigawa, *Preprints of the 22nd IAEA Fusion Energy Conference* (2008) FT/P2.
- [18] T. Nozawa, H. Tanigawa, J.S. Park, A. Kohyama, *Ceram. Eng. Sci. Proc.* 30 (2009) 65.
- [19] K. Ozawa, Y. Katoh, T. Nozawa, L.L. Snead, *Effect of Neutron Irradiation on Fracture Resistance of Advanced SiC/SiC Composites*, *Proceedings of ICFRM-14*, to be published in *J. Nucl. Mater.*
- [20] V. Kostopoulos, Y.P. Markopoulos, Y.Z. Pappas, S.D. Peteves, *J. Eur. Ceram. Soc.* 18 (1998) 69.
- [21] M. Sakai, K. Urashima, M. Inagaki, *J. Am. Ceram. Soc.* 66 (1983) 868.

- [22] T. Hinoki et al., "Irradiation Effects on Mechanical Properties of NITE-SiC/SiC Composites," presented at ICFRM-14.
- [23] Y. Katoh, T. Nozawa, L.L. Snead, *J. Am. Ceram. Soc.* 88 (2005) 3088.

3.1 THERMO-MECHANICAL DAMAGE OF TUNGSTEN SURFACES EXPOSED TO RAPID TRANSIENT PLASMA HEAT LOADS —T.Crosby and N.M. Ghoniem (University of California, Los Angeles)¹

OBJECTIVE

The objective of this work is the development of a computational model to determine the relation between the thermo-mechanical loading conditions and the onset of damage and failure of tungsten surfaces.

SUMMARY

Tungsten (W) has one of the highest melting points of any metallic material, and for this reason, it is used in applications where extreme heat fluxes and thermo-mechanical conditions are expected. Recently, international efforts have focused on the development of tungsten surfaces that can intercept energetic ionized and neutral atom and heat fluxes in the divertor region of magnetic fusion confinement devices, and as armor in chamber wall applications in inertial confinement fusion energy systems. The combination of transient heating and local swelling due to implanted helium and hydrogen atoms has been experimentally shown to lead to severe surface and sub-surface damage. The thermo-mechanical model is based on elasticity, coupled with a reaction-diffusion model of material swelling and grain boundary degradation due to helium and deuterium bubbles resulting from the plasma flux. This material state is also coupled with a transient heat conduction model for temperature distributions following rapid thermal pulses. The multi-physics model includes contact cohesive elements for grain boundary sliding and fracture. Results of the computational model are compared to experiments on tungsten bombarded with energetic helium and deuterium particle fluxes.

PROGRESS AND STATUS

Introduction

In nuclear fusion reactors, the plasma facing components (PFC) (e.g. divertor) are subjected to high fluxes of energetic neutrons, hydrogen and helium ions. The impingement of these energetic atom fluxes leads to rapid and transient surface heating.

Bombardment by helium isotopes leads to helium-induced damage accompanying micro-structural evolution, such as material swelling and the formation of blisters [1], dislocation loops and helium holes or bubbles [2]. Several recent experiments (see references [3] and [4]) have shown that the damage in the surface region and inside the material may degrade the thermo-physical properties as well as the optical reflectivity of Tungsten.

The divertor in fusion reactors are subjected to transient plasma events characterized with high thermal energy for a short time. One of these transient events is the Edge localized modes (ELMs) which are highly nonlinear magneto-hydrodynamic events and which are accompanied by a periodic expulsion of particles and high thermal energy (3-10% of the core thermal energy). ELMs energies deposited at the divertor plates are usually higher than the plasma energy content in it. Typical values for ELM energies are 0.1-0.5 (MJ/m²) for JET and 1-5 (MJ/m²) for ITER. The duration of the ELMs events are relatively short, 0.1-1 ms, causing material damage like melting, ejections of clusters and droplets and release of Hydrogen isotopes. ELMs events have also long-term effects such as degradation of thermo-physical properties due to the cyclic heat loading [5], [6].

¹Formatted from the original paper “**THERMO-MECHANICAL DAMAGE OF TUNGSTEN SURFACES EXPOSED TO RAPID TRANSIENT PLASMA HEAT LOADS**,” T. Crosby and N. M. Ghoniem, to be published in “International Journal of Interaction and Multiscale Mechanics.”

Experimental observations of cracks developing in Tungsten subjected to transient heat loads exist in the literature, for example [7] and [8], an example of this experimental work is shown in Fig [1].

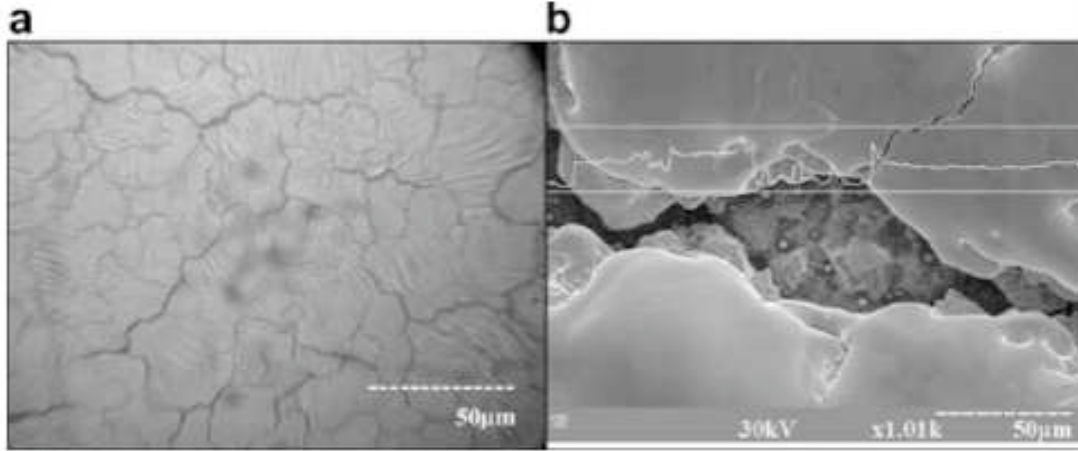


Figure [1]. Cracks on the Tungsten surface after 80 and 310 plasma pulses 0.75 MJ/m² [8].

Recently Tungsten has become a primary candidate material for Plasma-Facing Components (PFC) because it has good thermo-physical properties, a high melting point, a low sputtering rate, and a low tritium inventory [9].

Models that describe and study the change in Tungsten structure and the damage that occurs inside it are critical in determining the limits for its operating conditions in environments with extreme heat flux. The main objective of this paper is to develop a computational model for the development of thermo-mechanical damage in W under energetic ion bombardment conditions. Recent experiments have shown that under helium and hydrogen ion bombardment conditions, some near-surface grains are observed to be ejected from the bulk to the surface region [10].

Coupled thermal and mechanical models

In Tokamak-type plasma applications, such as in JET and ITER, the divertor is subjected to transient high heat loads that propagate inside the divertor material by heat conduction. This is described with the heat equation that takes the general form:

$$\rho C_p \frac{\partial T}{\partial t} + \nabla \cdot (-k \nabla T) = Q - \rho C_p \mathbf{u} \cdot \nabla T \quad (1)$$

where Q is a heat source, and k is the thermal conductivity.

To simulate transient conditions of the plasma, the tungsten surface is subjected to a heat flux from one side on the form of:

$$-\mathbf{n} \cdot \mathbf{q} = q_o + h(T_o - T) \quad (2)$$

where q_o is the inward heat flux normal to the boundary and \mathbf{q} is the total heat flux vector :

$$\mathbf{q} = -k \nabla T + \rho C_p \mathbf{u} T \quad (3)$$

In order to perform thermo-mechanical analysis, a boundary value problem (BVP) is formulated for an elastic material response. The BVP is constructed by substituting the constitutive equation for linear elasticity:

$$\sigma_{ij} = C_{ijkl}(\epsilon_{kl}^e + \epsilon_{kl}^{\theta}) \quad (4)$$

into the strong form of the equilibrium equation:

$$\sigma_{ij,j} + f_i = 0 \quad (5)$$

where σ is the symmetric stress tensor and f is body force, ϵ_{kl}^e is the elastic strain tensor, and ϵ_{kl}^{θ} is the strain tensor due to thermal expansion.

The result of this substitution is Navier's equation:

$$(\lambda + \mu)u_{j,j} + \mu u_{i,ii} + f_i - (3\lambda + 2\mu)\alpha\theta_{,i} = 0 \quad (6)$$

where μ and λ are the lame constants, along with the boundary conditions:

$$\begin{cases} \sigma_{ij}n_j = t_i \text{ on } \partial\beta_i \\ u_i = \bar{u}_i \text{ on } \partial\beta_u \end{cases} \text{ s.t. } \partial\beta_u \cup \partial\beta_i = \beta, \quad \partial\beta_u \cap \partial\beta_i = \emptyset \quad (7)$$

Damage crack formation model

Grain boundary sliding and motion result in stress concentrations along grain boundaries, which are generally weak regions in the material susceptible to crack initiation and propagation, we consider here a crack equilibrium model to describe crack damage formation along weak grain boundaries. From force equilibrium on the crack faces and using a stress equation for the field similar to that of a dislocation, an expression for the crack length is found to be:

$$2L = \frac{F^2(1-\nu^2)}{\pi\mu E} \quad (8)$$

As a simple constitutive damage model, we take the grain boundary thermally induced forces in the crack surface as simply proportional to the internal strain at the grain boundary during the transient:

$$F = \alpha E \Delta T \quad (9)$$

where ΔT is the temperature difference between an assumed relaxed and stress-free state take to be at room temperature, to a thermally- and mechanically- stressed state at the current temperature. The thermal force exhibits spatial and time dependence, as a result of the spatial dependence and time dependence of the temperature field and locality of grain boundaries.

Computational model

A multiphysics computational model has been developed within a finite element framework in order to investigate the synergistic effects of transient high heat loads and helium ion irradiation. The implementation of the model utilizes the capabilities of the COMSOL multiphysics platform in which a transient heat conduction analysis, coupled with a large deformation quasi-static elastic structural

mechanics analysis with contact elements along the grain boundaries were solved in a segregated fashion. The simulated model is a 10 mm x 10 mm, two-dimensional block, which was divided into a random distribution of grains using an algorithm based on the Voronoi diagram as shown in Fig [2].

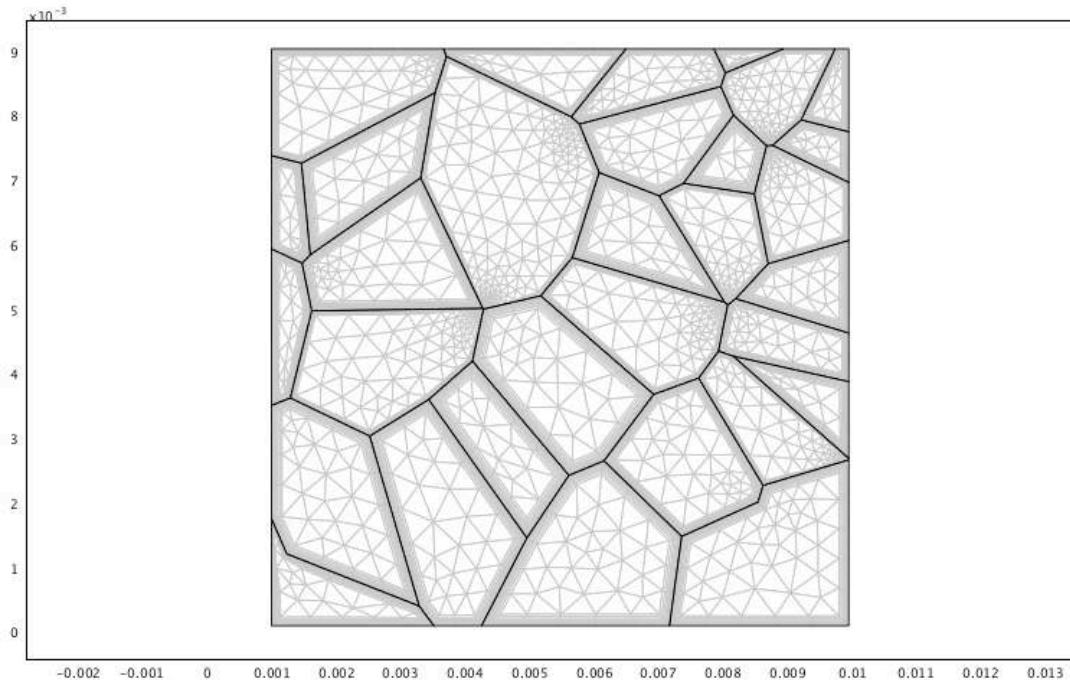


Figure [2]. Initial configuration of the random distribution of grains with boundary layer mesh.

The grain boundaries were replaced with cohesive contact elements to better simulate sliding and opening between the grains, as a result of He bubble formation along grain boundaries causing the grains to open up and form micro-cracks. A boundary layer mesh was utilized along the grain boundaries, as can be seen in the figure.

Thermal boundary conditions were prescribed as an inward heat flux, q_w , on the left side. The heat flux pulse was taken to be 10×10^3 , 2×10^3 , 1×10^3 (MW/m^2), for the duration of 0.1, 0.5 and 1 ms, respectively, as shown schematically in Fig [3]. These heat flux profiles are similar to conditions expected in the ITER design during ELM transient heat loads. A convective heat flux boundary condition was applied on the other side of the W plate, representing helium cooling. The mechanical boundary conditions were taken as free surface on the left side, while the right side was fixed. Periodic boundary conditions for both the displacement and the temperature field were used on the top and bottom boundaries of the model. The simulation duration was taken to be 0.1 s, with time steps of 0.1 ms using a segregated solver that combines transient thermal analysis with the quasi-static mechanical analysis.

Results

The high heat flux applied to the surface of W causes the temperature on the surface of the material and inside it to increase, causing thermal expansion and contraction during thermal transients, forcing the grains to slide relative to each other. This relative motion between the grains leads to separation between them, forming inter-granular micro-cracks. The cracks propagate inside the material, forming networks of cracks of different resolutions, which can be categorized into primary (relatively larger) cracks, and secondary (relatively smaller) cracks. Typical results at the end of the simulation that show the onset of cracks of different sizes are shown in Figs [4], [5], and [6].

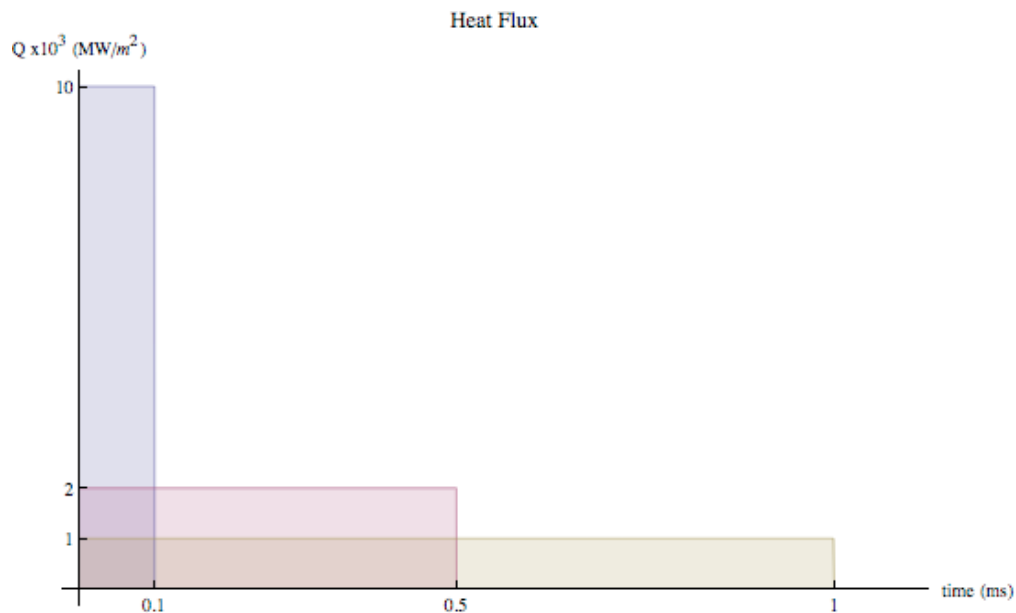


Figure [3]. Inward heat flux profile: values of the heat flux (MW/m²) vs. duration of application (ms) for the three cases considered.

It's noted that the temperature rises to very high values exceeding the melting point for the case when the heat flux is 1×10^4 (MW/m²). Our model doesn't directly address the ensuing evaporation of W from the surface in such severe conditions, as experimentally observed, for example in references [11] and [12]. The temperature of the surface at the end of the simulation is shown in Fig [7].

We note the difference in the distribution and in the size of cracks for the different applied heat fluxes, so we see from the results that the cracks have larger sizes for the case when the heat flux was 1×10^4 (MW/m²), but they are more close to the surface, while for the case when the heat flux was 1×10^3 (MW/m²), the cracks are smaller in size and there cracks formed at deeper distances from the surface of Tungsten, this is due to the difference in heat propagation for the different heat fluxes profiles.

Another aspect of the W surface damage is grain ejection which has been experimentally observed in Tungsten subjected to He irradiation [10]. When the W surface is subjected to He and D⁺ bombardment at high temperature, Helium and vacancies diffuse to the grain boundaries forming grain boundary bubbles. When the surface is subsequently subjected to a transient heat load, He bubbles grow and expand rapidly along grain boundaries, causing substantial pressure on grain faces. When the pressure exceed a critical value greater than the cohesive forces on grain boundaries, causing the grains to completely separate resulting in the phenomena called grain ejection.

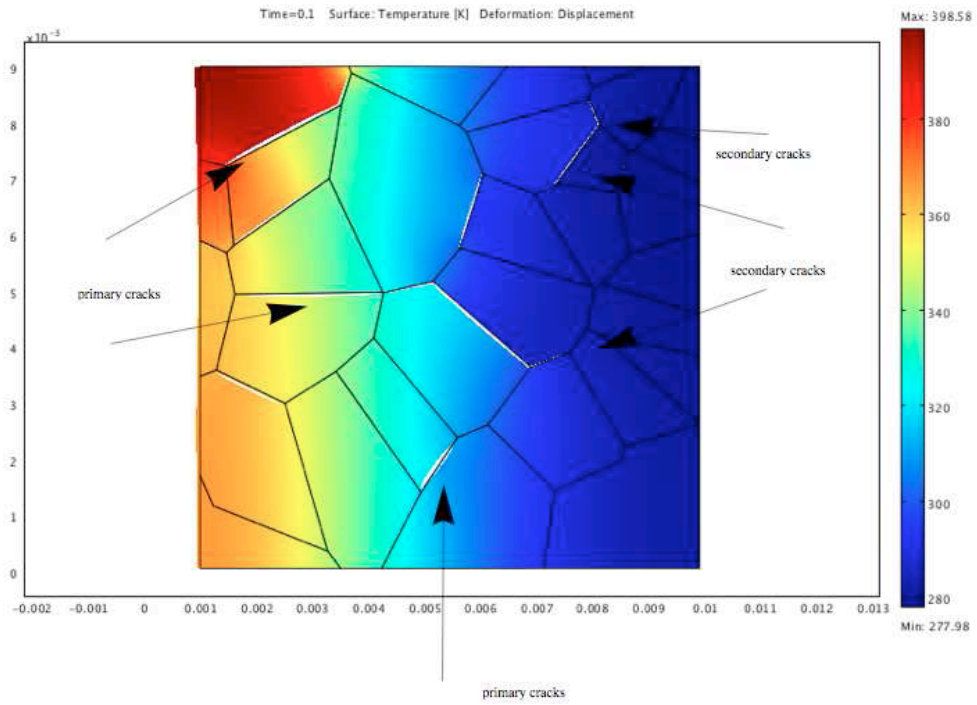


Figure [4]. Temperature and damage distribution in [K] and Tungsten grain boundary damage due to differential thermal expansion/contraction and crack formation when subjected to $Q = 1 \times 10^3$ (MW/m²).

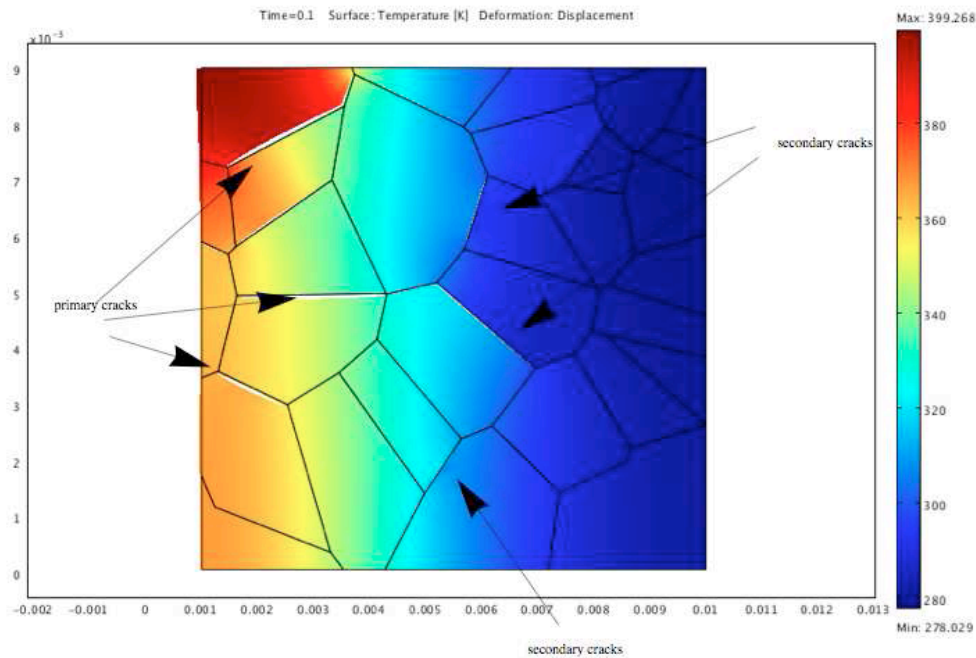


Figure [5]. Temperature and damage distribution in [K] and Tungsten grain boundary damage due to differential thermal expansion/contraction and crack formation when subjected to $Q = 2 \times 10^3$ (MW/m²).

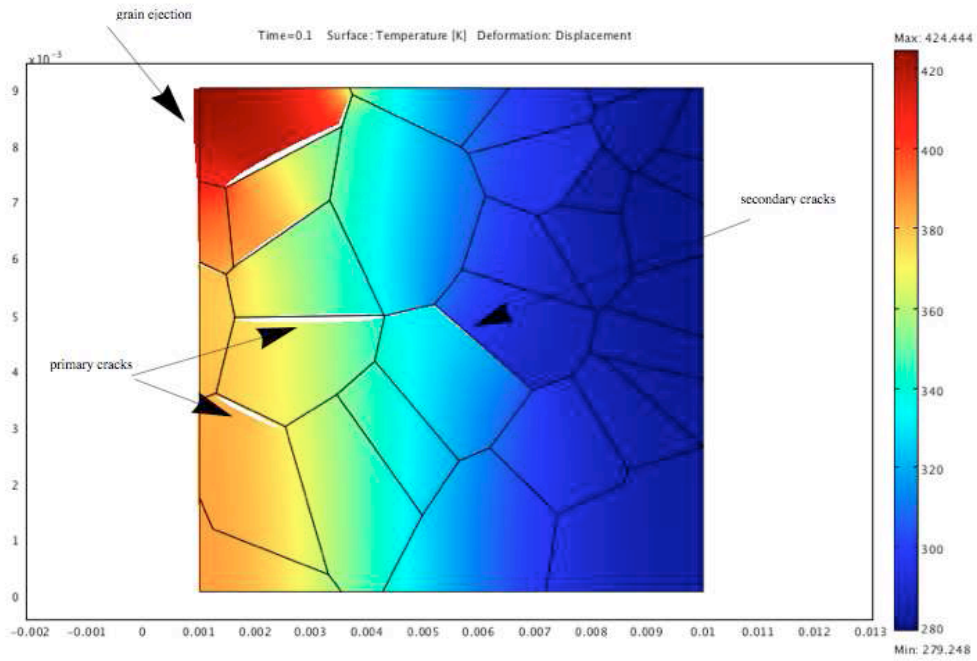


Figure [6]. Temperature and damage distribution in [K] and Tungsten grain boundary damage due to differential thermal expansion/contraction and crack formation when subjected to $Q = 10 \times 10^3$ (MW/m²).

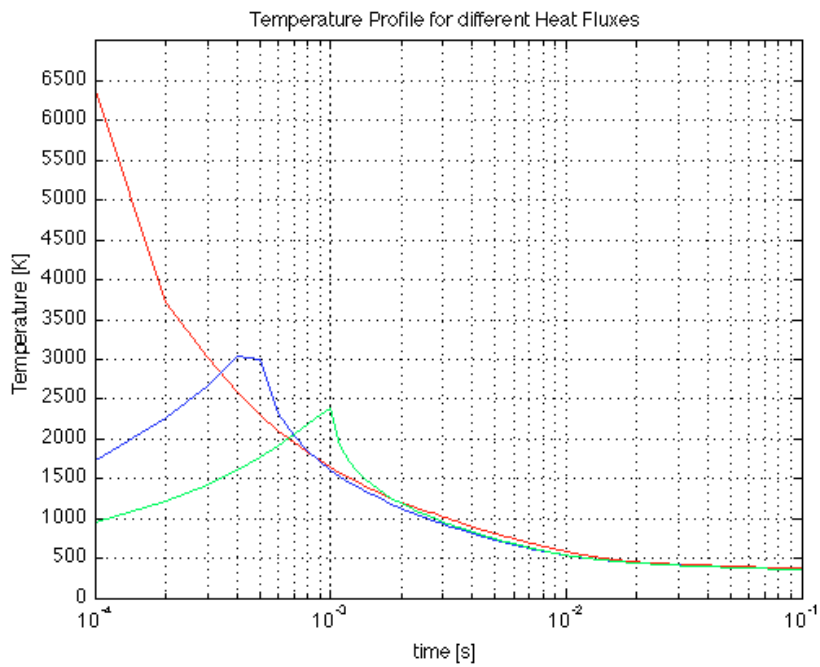


Figure [7]. Transient temperature profiles of the Tungsten surface at different heat fluxes.

Conclusion

The effect of transient plasma heat loads, such as edge localized modes (ELMs), on Tungsten thermal and mechanical properties was successfully studied through the development of a multi-physics model that combined mechanical and thermal transient analysis.

When the surface of tungsten is subjected to plasma ion bombardment it generates high heat fluxes that rise the temperature of the tungsten surface to temperatures close to its melting point, the thermo-mechanical model hence indicates that transient heating of W that is already containing helium bubbles will result in the evolution of sub-surface residual stresses, material swelling, grain boundary sliding, and sub-surface mechanical damage, as a consequence degradation of Tungsten properties will take place. Primary and secondary inter-granular micro-cracks are a manifestation of the surface damage, and it was observed that their size and depth from the surface vary with the heat load profile.

Another simulated type of mechanical damage was grain ejection, which happens from the complete separation between grains.

References

- [1] Q. Xu, N. Yoshida, and T. Yoshiie, *J. Nucl. Mater.* 367 (2007) 806.
- [2] H. Iwakiri, K. Yasunaga, K. Morishita, and N. Yoshida, *J. Nucl. Mater.* 283 (2000) 1134.
- [3] K. Tokunaga, *J. Nucl. Mater.* 313 (2003) 92.
- [4] K. Tokunaga, O. Yoshikawa, K. Maiske, and N. Yoshida, *J. Nucl. Mater.* 307 (2002) 130.
- [5] A. Zhitlukhin, N. Klimov, I. Landman, J. Linke, A. Loarte, M. Merola, V. Podkovyrov, G. Federici, B. Bazylev, S. Pestchanyi, V. Safronov, T. Hirai, V. Maynashev, V. Levashov, and A. Muzichenko, *J. Nucl. Mater.* 363 (2007) 301.
- [6] D. Naujoks, *Plasma-Material Interaction in Controlled Fusion*, Springer (2006).
- [7] S. E. Pestchanyi and J. Linke, *Fusion Eng. Des.* 82 (2007) 1657.
- [8] I. E. Garkusha, A. N. Bandra, O. V. Byrka, V. V. Chebotarev, I. Landman, V. A. Makhraj, S. Pestchanyi, and V. I. Tereshin, *J. Nucl. Mater.* 386 (2009) 127.
- [9] S. Kajita, N. Ohno, W. Sakaguchi, and M. Takagi, *Plasma and Fusion Research*, 4 (2009).
- [10] N. Ohno, S. Kajita, D. Nishijima, and S. Takamura, *J. Nucl. Mater.* 363 (2007) 1153.
- [11] I. E. Garkusha, A. N. Bandra, O. V. Byrka, V. V. Chebotarev, I. Landman, V. A. Makhraj, A. Marchenko, D. Solyakov, and V. I. Tereshin, *J. Nucl. Mater.* 337 (2005) 707.
- [12] B. Bazylev, G. Janeschitz, I. Landman, and S. Pestchanyi, *J. Nucl. Mater.* 337 (2005) 766.

3.2 MECHANICAL PROPERTIES OF W-1.1%TiC ALLOY - M. A. Sokolov (Oak Ridge National Laboratory)

OBJECTIVE:

The objective of this effort is to perform tensile and fracture toughness characterization of W-1.1%TiC nanostructured alloy.

SUMMARY:

A small disk of W-1.1%TiC alloy produced by Japanese researchers led by Hiroaki Kurishita was sent to ORNL for mechanical testing and characterization. The purpose of the study is to evaluate the effect of small additions of TiC in improving the performance of W-based materials designed for operation in the divertor environment. This is part of on-going efforts of the international fusion community to understand and improve the ductility and toughness of W-based materials using nano-scale microstructural modification. A test plan was developed to perform limited fracture toughness and tensile evaluation of this alloy. The results of this evaluation will be presented in the next semi-annual report.

PROGRESS AND STATUS:

A small disk of W-1.1%TiC alloy was produced by Japanese researchers led by Hiroaki Kurishita and transferred to ORNL for mechanical testing and characterization. The disk is about 22 mm in diameter and ~3 mm thick. Figure 1 illustrates the production processing for this nanostructured alloy:

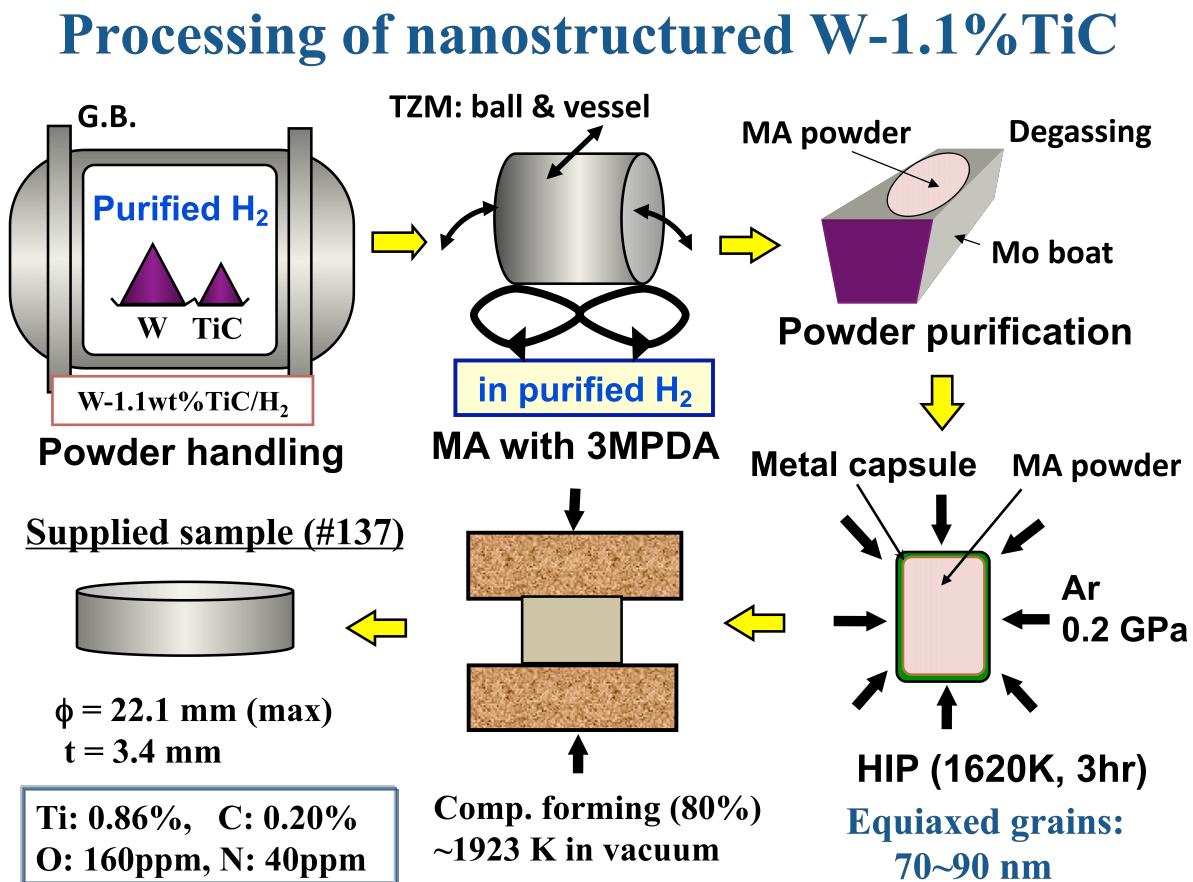


Figure 1. Processing scheme for nanostructured W-1.1%TiC alloy, produced by Prof. Kurishita.

The Vickers hardness of this alloy is $HV = 517 \pm 5$ for a load of 300gf and hold time of 20 s. A plan was developed to perform limited fracture toughness and tensile characterization of this alloy. Figure 2 shows a sketch of the layout used to machine specimen from this disk. A total of three sub-size tensile and four bend bar specimens were machined. The bend bars will be precracked and tested to determine fracture toughness. In addition, six sub-size DMFB type bend bars were also produced. Depending on precracking behavior of this material, these specimens will be tested either in impact mode or static fracture toughness mode.

The results of this evaluation will be presented in the next semi-annual report.

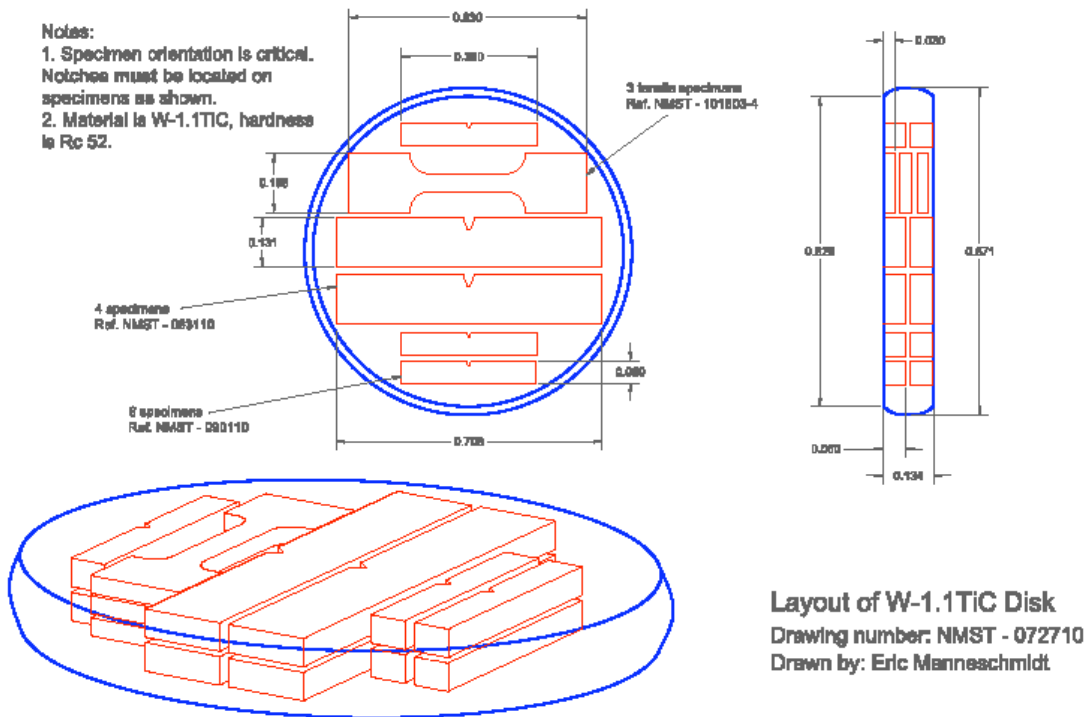


Figure 2. Layout of test specimens to characterize tensile and fracture toughness properties of W-1.1% TiC alloy.

COMPATIBILITY OF MATERIALS EXPOSED TO ISOTHERMAL Pb-Li – B. A. Pint and K. A. Unocic (Oak Ridge National Laboratory, USA)

OBJECTIVE

One proposed U.S. test blanket module (TBM) for ITER uses ferritic-martensitic alloys with both eutectic Pb-Li and He coolants at ~475°C. In order for this blanket concept to operate at higher temperatures (~700°C) for a DEMO-type reactor, several Pb-Li compatibility issues need to be addressed. Some of the issues currently being investigated are the behavior of dispersion strengthened Fe-Cr alloys compared to conventional wrought material, the performance of Al-rich coatings to inhibit corrosion and dissimilar material interaction between SiC and ferritic steel.

SUMMARY

Initial isothermal capsule experiments were conducted to compare the behavior of oxide dispersion strengthened (ODS) Fe-Cr alloys to prior results on wrought ferritic-martensitic (FM) alloys. Also, the performance of corrosion resistant, Al-rich diffusion coatings on these alloys was investigated. To further understand the performance of these coatings in Pb-Li, several experiments are in progress including a time series of experiments and a more detailed study of the unexpectedly high Al loss observed in prior experiments. New Pb-Li was cast to eliminate the prior issue of Li composition variability. Finally, to investigate any potential dissimilar material interaction between Fe and SiC, a set of capsules with SiC inner capsules is being assembled for exposures at 500°, 600° and 700°C.

PROGRESS AND STATUS

Introduction

A current focus of the U.S. fusion materials program is to address issues associated with the dual coolant Pb-Li (DCLL) blanket concept[1] for a test blanket module (TBM) for ITER and enhanced concepts for a DEMO-type fusion reactor. A DCLL blanket has both He and eutectic Pb-17 at.%Li coolants and uses reduced activation ferritic-martensitic (FM) steel as the structural material with a SiC/SiC composite flow channel insert (FCI). Thus, recent U.S. compatibility research has examined compatibility issues with Pb-Li.[2-7] Compared to Li,[8] a wider range of materials can be compatible with Pb-Li because of the low activity of Li.[9] In particular, SiC readily dissolves in Li, but not Pb-17Li.[2,4,10] However, like Pb, Pb-Li dissolves Fe, Cr and especially Ni from many conventional alloys above 500°C.[11,12] This is not a concern for a DCLL TBM operating at <500°C. However, a DCLL blanket for a commercial reactor would be more attractive with a higher maximum operating temperature, perhaps >600°C if ODS ferritic steels[13] were used. Even at 550°C, a recent study of Eurofer 97 (Fe-Cr-W) showed a very high dissolution rate in flowing Pb-Li.[12] Therefore, preliminary Pb-Li compatibility capsule experiments are being conducted at 500°-700°C in order to investigate several concepts before flowing Pb-Li compatibility tests are conducted. Recent capsule experiments have investigated (1) the effectiveness of Al-rich coatings to inhibit dissolution, (2) the effect of Fe and Ni impurities on the amount of dissolution and (3) potential dissimilar material effects between Fe and SiC. Additional capsule experiments to address the first topic are presented here and a second series of capsule experiments are being assembled to address the third topic now that chemical vapor deposited (CVD) SiC capsules have been machined.

Experimental Procedure

Static capsule tests were performed using Mo capsules and type 304 stainless steel (SS) outer capsules to protect the inner capsule from oxidation. The dissimilar materials capsules being assembled have an inner chemical vapor deposited (CVD) SiC capsule. Since this capsule cannot be sealed, it is placed

inside a Mo capsule and held shut by a Mo wire welded into the Mo capsule lid that is welded shut. A similar SS capsule was used to protect the Mo capsule in these experiments. For the Mo capsules, the specimens were ~1.5 mm thick and 4-5 cm² in surface area with a 600 grit surface finish and were held with 1 mm diameter Mo wire. (Mo can be considered to be essentially inert under these conditions.) For the SiC capsules, a CVD SiC spacer is used to hold a specimen that is ~1.5 mm thick and 2-3 cm² in surface area. The representative FM steel used in prior work was P92 (Fe-9Cr-2W) and two ODS alloys were evaluated, one from ORNL (14YWT) and the other (ODM401) from Dour Metal sro. All of the alloy compositions are shown in Table 1. Prior to aluminizing, specimens were polished to a 0.3 μm alumina finish and cleaned ultrasonically in acetone and alcohol. Aluminizing was performed in a laboratory-scale CVD reactor consisting of an inductively heated alumina tube with flowing H₂ carrying the AlCl_x vapor. The reactor has been described in detail elsewhere.[14] For the dissimilar metal experiments, unalloyed Fe specimens were used to simplify the experiment and the CVD SiC specimen was high-purity material from Rohm & Haas. For the Mo capsule results reported here, the capsules were loaded with 125g of Pb-Li in an Ar-filled glove box. To avoid recent issues with variable Li composition in the current commercial batch of Pb-Li,[7] high purity Pb and Li were placed in the capsule. For the SiC capsules, 20g of Pb-Li were loaded into the much smaller capsules. This material was cast at ORNL and chemical analysis showed a Li content of 16.5at.%Li in one stick and 15.9% in a second stick that is being used for the next series of coated specimens in Mo capsules. The Mo and SS capsules were welded shut in a glove box to prevent the uptake of impurities during the isothermal exposure. After exposure, residual Pb-Li on the specimen surface was removed by soaking in a 1:1:1 mixture of acetic acid, hydrogen peroxide and ethanol for up to 72 h. Mass change was measured with a Mettler-Toledo balance with an accuracy of 0.01 mg/cm². Characterization included x-ray diffraction (XRD), x-ray photoelectron spectroscopy (XPS), scanning electron microscopy (SEM) equipped with energy dispersive x-ray (EDX) analysis and electron microprobe analysis (EPMA) equipped with wavelength dispersive x-ray analysis.

Results and Discussion

Figure 1 shows the mass change data for both ODS alloys and aluminized alloy 401. A prior report outlined that it was not possible to aluminize the 14YWT alloy,[15] likely due to the high N content and small grain size in this batch (the prior report contained composition from a similar alloy batch whereas Table 1 contains data for the same batch as was used in these experiments). Compared to P92, the higher Cr content ODS alloys showed a similar mass loss after 1,000h at 700°C in Pb-Li and a similar improvement when aluminized. The similar mass changes are not particularly surprising since Fe and Cr are thought to dissolve in Pb-Li at a similar rate with no enrichment observed at the dissolution front of P92.

One issue that has arisen with these coatings is the unexpectedly high Al loss observed after 1,000h at 700°C.[5] The as-coated Al composition profiles reported previously has always been from representative

Table 1. Alloy chemical compositions (atomic% or ppma) determined by inductively coupled plasma analysis and combustion analysis.

Material	Fe	Ni	Cr	Al	O	C	N	S	Other
14YWT	83.3	0.03	14.1	0.04	6000	3000	5170	69	0.59W,0.12Y 0.28Ti,0.08Si
401	82.6	0.12	14.8	0.12	6560	610	1770	89	0.17Mo,0.13Y 1.2Ti,0.08Si
P92 (9Cr-2W)	87.2	0.1	9.9	0.02	80	5120	2330	87	0.55W, 0.46Mn 0.30Mo,0.32Si

< indicates below the detectability limit of <0.01% or <0.001% for interstitials

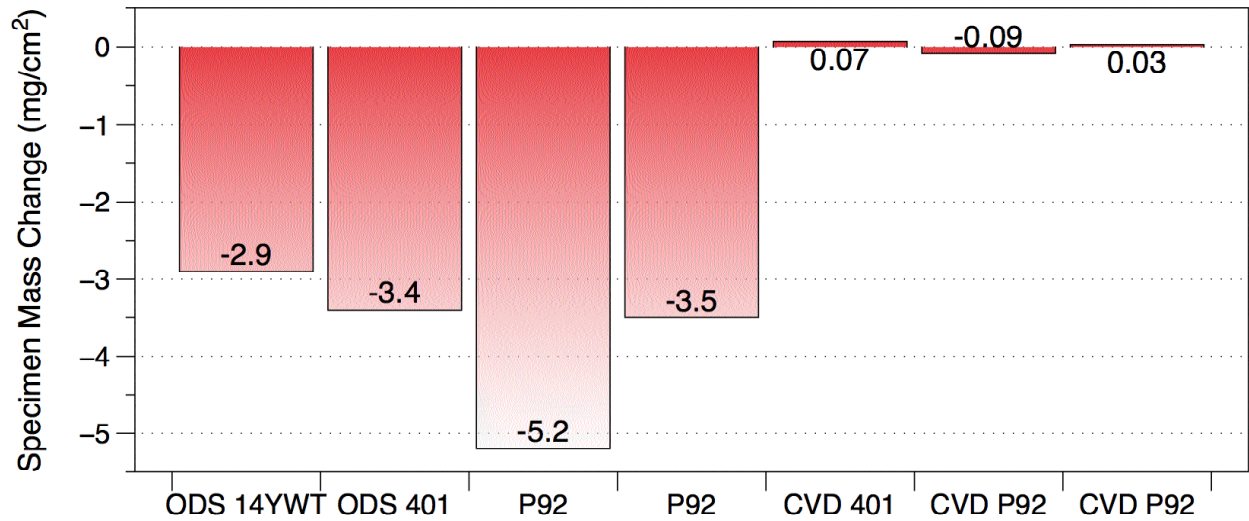


Figure 1. Mass change results after exposure for 1,000h at 700°C in Pb-Li for both wrought and ODS FeCr alloys and with and without CVD aluminide coatings.

coated specimens as coating composition could not be measured before and after exposure without cutting the specimen. In order to provide more quantitative information about the Al loss, a coated P92 specimen has been cut into three pieces. The first piece was mounted and analyzed by EPMA, Figure 2. The other pieces were pre-oxidized for 2h at 800°C in dry O₂, similar to the prior study. One piece was

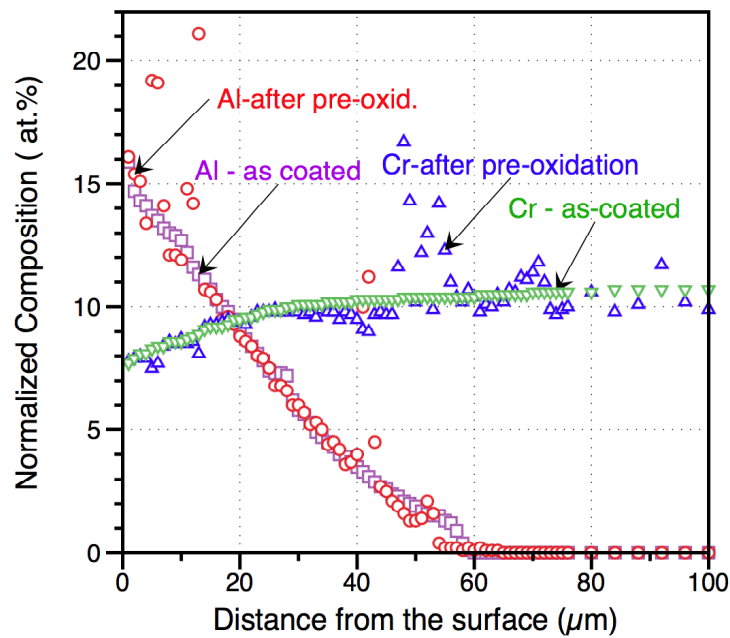


Figure 2. Specimen mass change from a series of capsule experiments with carbon steel capsules and Fe and SiC specimens exposed to Pb-Li for 1,000 h at each temperature.

mounted for analysis and the last piece is being exposed to Pb-Li for 1,000h at 700°C so that EPMA profiles can be obtained all from the same coated P92 specimen. Figure 2 shows clearly that very little Al was lost during pre-oxidation due to the formation of an Al-rich oxide on the surface or interdiffusion with the substrate. After the last piece is exposed to Pb-Li, a similar Al profile will be measured from that specimen to quantify the Al loss.

In addition to that coating experiment, three P92 specimens have been coated and will be exposed to Pb-Li for 500, 2,000 and 5,000h to measure the kinetics of Al loss and determine the effectiveness of these coatings at longer times. Those experiments all should begin in the next period and be completed in 2011.

References

- [1] M. Abdou, D. Sze, C. Wong, M. Sawan, A. Ying, N. B. Morley and S. Malang, *Fus. Sci. Tech.*, 47 (2005) 475.
- [2] B. A. Pint, *Fus. Sci. Tech.* 52 (2007) 829.
- [3] B. A. Pint and K. L. More, *J. Nucl. Mater.* 376 (2008) 108.
- [4] B. A. Pint, *Mater. Sci. Forum*, 595-598 (2008) 549.
- [5] B. A. Pint, *J. Nucl. Mater.*, in press.
- [6] B. A. Pint and K. A. Unocic, *DOE/ER-0313/47* (2009) 82.
- [7] B. A. Pint, *DOE/ER-0313/48* (2010) 102.
- [8] J. E. Battles, *Intern. Mater. Rev.* 34 (1989) 1.
- [9] P. Hubberstey, *J. Nucl. Mater.* 247 (1997) 208.
- [10] T. Yoneoka, S. Tanaka and T. Terai, *Mater. Trans.* 42 (2001) 1019.
- [11] O. K. Chopra, D. L. Smith, P. F. Tortorelli, J. H. DeVan and D. K. Sze, *Fusion Technol.*, 8 (1985) 1956.
- [12] J. Konys, W. Krauss, J. Novotny, H. Steiner, Z. Voss and O. Wedemeyer, *J. Nucl. Mater.* 386-88 (2009) 678.
- [13] S. Ukai and M. Fujiwara, *J. Nucl. Mater.* 307 (2002) 749.
- [14] Y. Zhang, B. A. Pint, K. M. Cooley and J. A. Haynes, *Surf. Coat. Tech.* 202 (2008) 3839.
- [15] A. Vande Put and B. A. Pint, *DOE/ER-0313/48* (2010) 110.

6.1 DIFFUSION OF He INTERSTITIALS AND He CLUSTERS IN α -Fe—H. Deng (Hunan University), F. Gao, H. L. Heinisch and R. J. Kurtz (Pacific Northwest National Laboratory)

OBJECTIVE

To study the diffusion properties of He interstitials and He clusters in the bulk and in grain boundaries of α -Fe with a newly developed Fe-He potential.

SUMMARY

The accumulation of He atoms in materials will significantly degrade the mechanical properties of materials; therefore, understanding the properties of He interstitials and their clusters in materials is of fundamental importance within a fusion reactor environment. The diffusion properties of single He interstitials and He clusters in the bulk and grain boundaries of α -Fe are being studied using molecular dynamics with a new Fe-He potential. It is found that the migration barrier for a single He interstitial in the bulk is very low, which is consistent with the result obtained using *ab initio* methods. Large He clusters can cause Fe self-interstitial atoms (SIA) to be formed, which can be trapped by the resulting vacancy, forming a He-vacancy complex. It is found that for He interstitials in grain boundaries (GBs), the He migration is one-dimensional in a $\Sigma 11$ GB, while it is two-dimensional in a $\Sigma 3$ GB at 600 K and three-dimensional at higher temperatures.

PROGRESS AND STATUS

Introduction

It is well known that first wall materials of a fusion power system will be exposed to a high concentration of He generated by (n, α) transmutation reactions caused by 14 MeV neutron irradiation [1]. Because of the extremely low solubility of He in materials, He atoms tend to be trapped at defects, such as vacancies, dislocations, and grain boundaries (GBs) [2, 3]. The accumulation of He atoms in materials results in the formation of He bubbles, which can lead to void swelling and produces low-temperature intergranular embrittlement, surface roughening, blistering, and premature creep rupture at high-temperatures [4]. These phenomena can significantly degrade the mechanical properties of materials, and they are strongly correlated to the diffusion of He defects and their interactions with microstructural features. Therefore, understanding of the migration and diffusion properties of He defects (single He interstitials and clusters) both in the bulk and GBs is of fundamental importance within a fusion reactor environment.

In early simulations, most studies of He behavior in Fe employed the repulsive Fe-He potential of Wilson and Johnson (WJ-potential) [6], which predicted the most stable He interstitial position to be in the octahedral configuration, in contrast to *ab initio* calculations [7–9] that demonstrated that a tetrahedral interstitial position is the most stable site. Recently, several new empirical potentials for Fe-He interaction have been developed [10–14], and all of these Fe-He potentials reproduced well the relative stability of He interstitials.

In our previous work, we have studied the diffusion properties of a He interstitial and a di-He cluster at grain boundaries in α -Fe [15–17]. Terentyev et al., also studied the migration of a He interstitial in $\langle 110 \rangle$ tilt grain boundaries in α -Fe [18], and found that the atomic structures of grain boundaries play an important role in the migration mechanism and diffusivity of He interstitials. More recently, Stewart et al., studied the formation and diffusion of He clusters and bubbles in BCC Fe [19]. However, the results obtained from these simulations are found to depend on the empirical potentials used in the Fe-He system. The details of different potentials have been described in a recent paper [20].

¹PNNL is operated for the U.S. Department of Energy by Battelle Memorial Institute under Contract DE-AC06-76RLO 1830.

Simulation Methods

In the present simulations the pair interaction and the many-body function for Fe–Fe are those of Ackland and Mendeleev [21], and the pair potential for He–He interaction is the Aziz potential [22]. The new Fe–He potential developed at PNNL is used for describing the Fe–He interaction. Similar to the many-body potential formalism, the new Fe–He potential consists of a pair potential and an embedding function, and then the total energy of a Fe–He system can be written as:

$$U = \sum_{i=1}^{N-1} \sum_{j=i+1}^N V(r_{ij}) + \sum_{i=1}^N F_s(\rho_s^i), \quad (1)$$

where the first term represents a repulsive pair potential and the second term is the many-body interaction that provides the contribution from the s-band electron density. The pair potential can be represented by a summation of cubic knot functions:

$$V(r) = \sum_{k=1}^8 a_k (r_k - r)^3 H(r_k - r), \quad (2)$$

where $H(r_k - r)$ is the Heaviside function. The many-body interaction function is

$$F_s(\rho_s) = b_1 \sqrt{\rho_s} + b_2 \rho_s^2 + b_3 \rho_s^4. \quad (3)$$

These functions are of the same forms as those for the Fe–Fe interaction [21]. For the mixed-pair density, we have employed the 1s-type and 4s-type Slater functions for He and Fe [23], respectively. The detailed fitting process and potential parameters have been described elsewhere [20]. In the ‘s-band model’, the contribution to the total energy from s-electrons is very small, but it cannot be ignored here.

The diffusion properties are obtained using molecular dynamics simulations. The positions $r_i(t)$ of all the atoms at time t are recorded and the mean-square displacement (MSD) is

$$MSD = \langle |r_i(t) - r_i(0)|^2 \rangle = \frac{1}{N} \sum_{i=1}^N |r_i(t) - r_i(0)|^2, \quad (4)$$

where N is the total atomic number and ‘ $\langle \dots \rangle$ ’ denotes averaging over all the atoms. The diffusion coefficient (D) can be obtained with the Einstein-Smoluchowski relation:

$$D = \lim_{t \rightarrow \infty} \frac{MSD}{q_i t} = \lim_{t \rightarrow \infty} \frac{1}{q_i t} \langle |r_i(t) - r(0)|^2 \rangle, \quad (5)$$

where q_i is a numerical constant that depends on the dimensionality such that $q_i = 2, 4, \text{ or } 6$ for the one-, two- or three-dimensional diffusion, respectively. The relation of the migration energy (E_m) to the diffusion coefficient D is based on the Arrhenius equation:

$$D = D_0 \exp(-E_m / k_B T). \quad (6)$$

The E_m and D can be obtained by fitting the diffusion coefficient to equation (6) over a range of temperatures.

For simulations of the diffusion of He interstitials and He-clusters in the α -Fe bulk, MD boxes of $14a_0 \times 14a_0 \times 14a_0$ with 5488 Fe and $20a_0 \times 20a_0 \times 20a_0$ with 16000 Fe atoms are used, where a_0 is the lattice constant (2.8553Å) of perfect BCC Fe. The time step is chosen to be 1 fs for the molecular dynamics (MD) simulations with the NVT ensemble. The total simulation time for a single He interstitial diffusion is about 2.85 ns, but different MD times for He clusters are used, depending on the cluster size. Two GBs ($\Sigma 3\{112\}$ and $\Sigma 11\{323\}$) have been studied, where periodic boundary conditions were imposed along the x and z directions, but nonperiodic boundary conditions were applied along the y direction [24]. The atomic structures of the two symmetric tilt GBs in α -Fe are $\Sigma 3\{112\}$ $\Theta = 70.53^\circ$ and $\Sigma 11\{323\}$ $\Theta = 50.48^\circ$ with a common $\langle 101 \rangle$ tilt axis, as shown in Fig. 1. The block size of $\Sigma 3$ is $59.35\text{\AA} \times 65.74\text{\AA} \times 56.53\text{\AA}$ with 18816 Fe atoms, and that of $\Sigma 11$ is $56.82\text{\AA} \times 65.74\text{\AA} \times 56.53\text{\AA}$ with 17976 Fe atoms.

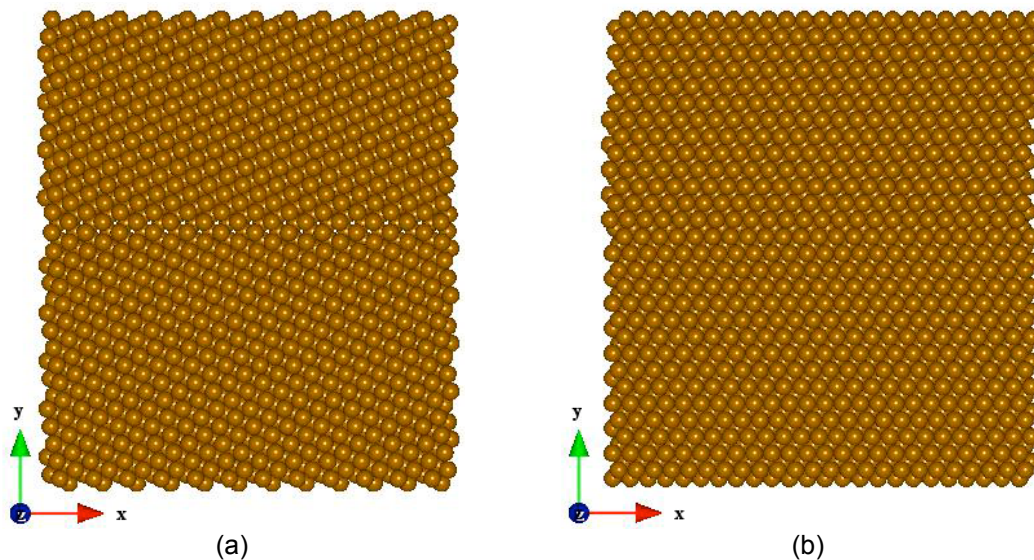


Fig. 1. Atomic structures of two GBs in α -Fe. (a) $\Sigma 11\{323\}$: $x \rightarrow [1 \ -1 \ 3]$, $y \rightarrow [-3 \ 3 \ 2]$, $z \rightarrow [110]$; and (b) $\Sigma 3\{112\}$: $x \rightarrow [1 \ -1 \ 1]$, $y \rightarrow [-1 \ 1 \ 2]$, $z \rightarrow [1 \ 1 \ 0]$.

Results and Discussion

It has been found that single He interstitials can migrate easily the Fe matrix. At a given temperature, these He interstitials are subject to a random displacement from their original positions and the trajectories can be tracked during the atomic-scale simulations. The MSD analysis can be used to extract reliable values of the diffusion coefficient D with enough simulation time, and then the migration energy can be obtained by the Arrhenius equation. In the present work, the diffusion properties of single He interstitials and He-clusters in α -Fe have been studied using classic molecular dynamics and MSD analysis, as described below. For He-clusters, the trajectories of the centers of mass were tracked. The temperatures used are different for single He interstitials and He clusters because the He_2 -cluster will dissociate, whereas the He_x -clusters ($x > 2$) will create Fe self-interstitials at high temperatures (as discussed below). For a single He interstitial, the migration behaviour is simulated at 200 ~ 700 K at 100 K intervals. As an example, the MSD of a He interstitial migrating at 500 K is shown in Fig. 2, from which it can be seen that the MSD increases with the diffusion time (as long as 2.85 ns) and shows a linear-like relation.

Single He interstitials migrate three-dimensionally along the different directions, but they can move forward or backward along one direction until they change their direction; thus the MSD is not always linear with the simulation time during a long-time diffusion process. Here the diffusion coefficients are obtained using the so-called trajectory time decomposition (TTD) technique [25], which decomposes a single long trajectory of interstitials or clusters into a sequence of short independent trajectory segments.

Based on the Arrhenius equation and the MSD calculated with the TTD technique, the migration energy and diffusion coefficient for a single He interstitial are 0.039 eV and 1.55×10^{-8} m²/s, respectively, as shown in Fig. 3 and Table 1. The migration energy is slightly smaller than the value of 0.058 eV calculated by the dimer method [20], which is in good agreement with the migration energy of 0.06 eV determined by *ab initio* calculations [8]. With different empirical Fe–Fe and Fe–He potentials, Stewart et al. [11] studied the diffusion property of single He interstitials in α -Fe, and found that the diffusion rates are similar ($2.23 \sim 9.64 \times 10^{-8}$ m²/s) and the migration energies are 0.107, 0.043, and 0.062 eV with different Fe–He potentials (Wilson potential [6], ORNL potential [10] and Juslin-Nordlund potential [12], respectively). However, the above results indicate that the migration barrier of a He interstitial in the Fe matrix is very low, and it is slightly underestimated in the dynamics simulations with the new Fe–He potential.

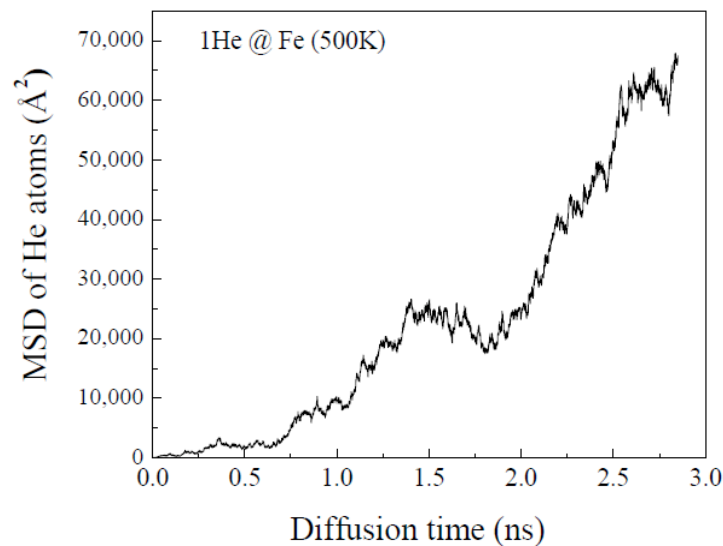


Fig. 2. MSD of a single He interstitial diffusing in Fe matrix as a function of time at 500 K

Table 1. Migration barriers and diffusion coefficients of He interstitial and clusters in α -Fe

Cluster	Migration Energy (eV)	Diffusion Coefficient (10^{-8} m ² /s)
1 He	0.039	1.55
2 He	0.090	1.47
3 He	0.097	1.10
4 He	0.103	0.45

For a He₂-cluster, it was found that the two He atoms will dissociate completely into two He interstitials when the temperature is higher than 400 K, and thus the MSDs were calculated at temperatures between 200 K and 400 K. As shown in Fig. 3 and Table 1, the migration energy and diffusion coefficient for a He₂-cluster are 0.090 eV and 1.47×10^{-8} m²/s, respectively. No SIA formation is observed for a He₂-cluster diffusing in the Fe matrix.

When the size of a He cluster is larger than 3, it is always observed that an Fe SIA is created by the He cluster at the temperatures higher than 600 K. Fig. 4 shows a typical MSD for He₃-cluster migration in an Fe matrix at 700 K. The MSD increases quickly with increasing simulation time, but remains constant when an SIA is formed. Then the He-vacancy complex appears, and the He cluster is trapped by the vacancy. It is of interest to find that although the center of mass of the He-vacancy cluster does not change with time, the He atoms rotate quickly around the vacancy. However, when the Fe SIA moves

close to the He-vacancy cluster, recombination of the SIA with the vacancy occurs. During this process, the He cluster becomes mobile again, and it can quickly migrate in the Fe matrix, leading to an increase of the MSD, as indicated by the hatched region in Fig. 4. The processes of SIA formation and recombination with the vacancy within the He-vacancy cluster occurred several times during the present simulation. The minimum temperature for creating a SIA depends on the size of He cluster, and it is found that the larger the size, the lower the formation temperature. For example, a He₃-cluster can create a SIA when the temperature is 700 K or higher; a He₄-cluster creates a SIA when the temperature is higher than 400 K; a He₇ or larger causes SIA formation even if the temperature is as low as 100 K, which suggests that the large cluster is almost immobile in the Fe matrix over the temporal scale explored in these simulations.

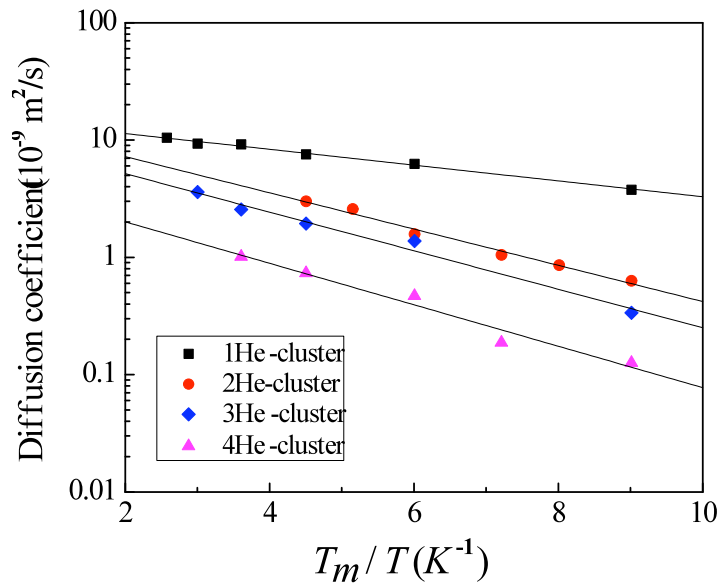


Fig. 3. Arrhenius plots for a single He atom and He clusters to diffuse in Fe matrix

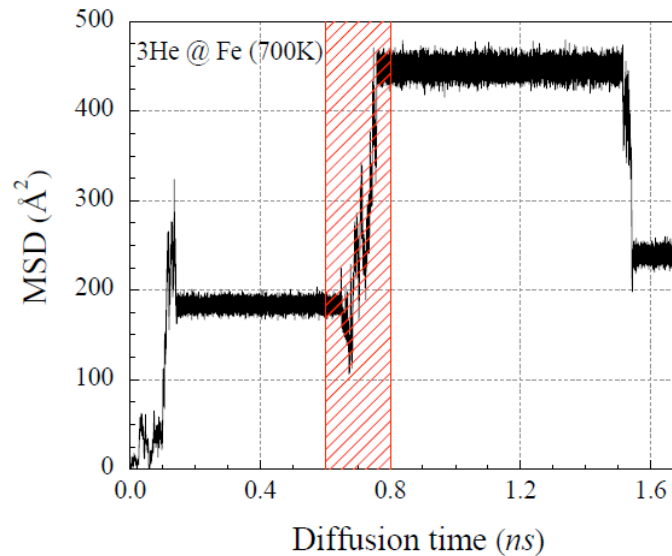


Fig. 4. MSD of a He₃-cluster diffusing in Fe matrix as a function of time at 700 K

Due to the fact that the time for creation of a SIA from a large He cluster (with more than five He atoms) at low temperature is very short (~ 5 ps), and the cluster is trapped by the vacancy, the MSDs for these large He clusters are very difficult to obtain. Considering the SIA formation temperature, the MSDs have been obtained from 200 - 600 K, or 200 - 500 K for the He_3 and He_4 clusters, respectively. The migration energies and diffusion coefficients are shown in Table 1 and Fig. 3, and they are determined to be 0.097 and 0.103 eV, and 1.10×10^{-8} and 0.45×10^{-8} m^2/s for the He_3 and He_4 cluster, respectively. In the report of Stewart et al., [19], the diffusion coefficients and migration energies of He_x -clusters ($x = 1 \sim 6$) were also calculated using the ORNL three-body potential. The diffusion coefficients are similar with those obtained in the present study, but the migration energies are slightly higher. There are also other differences between Stewart's and our results. In our calculations, for example, the He_2 -cluster will dissociate completely when the temperature is higher than 400 K, and the large He_x -cluster ($x > 4$) will create a Fe SIA in very short time (less than 100 ps) and be trapped by the vacancy even at temperatures much lower than 700 K (at which the emission of a SIA occurs in their simulations). Thus, we cannot obtain the MSDs for these clusters at this temperature.

Both $\Sigma 11$ and $\Sigma 3$ GBs have a common $\langle 110 \rangle$ tilt axis and are used to study the effect of GB structure on He diffusion. The lowest energy configurations of a single He interstitial at the GBs were determined by an annealing simulation at 1000 K for 10 ps using molecular dynamics and then, slowly cooling down to 0 K [15]. The configurations of He_x -clusters at the GBs were determined by the same method. These configurations were used as starting configurations for calculating MSDs during the diffusion of He interstitials and their clusters. The results of the MSDs for a single He interstitial to diffuse at $\Sigma 11$ and $\Sigma 3$ GBs at different temperatures (600 ~ 1000 K) are shown in Fig. 5(a) and (b), respectively.

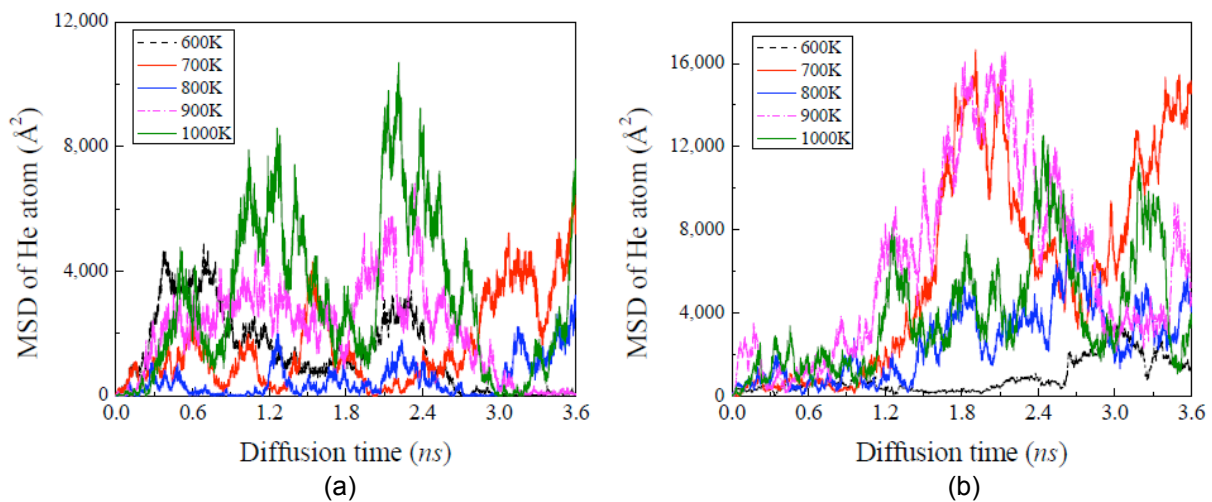


Fig. 5. The MSDs of a He interstitial diffusing along the different directions at Fe GBs as a function of time. (a): $\Sigma 11$ GB and (b) $\Sigma 3$ GB

In the $\Sigma 11$ GB it is found that He interstitial migration is mainly along the $[1\bar{1}3]$ direction, as shown in Fig. 6a, which means that the He interstitial migrates one-dimensionally. The same phenomena have been observed at all the temperatures considered here. Based on the MSDs with TTD analysis, the diffusion coefficients were determined, and they obey an Arrhenius relation (Eq. (6)), as shown in Fig. 7. The best-fit migration barrier (E_m) and pre-exponential factor (D_0) are 0.172 eV and 4.26×10^{-8} m^2/s , respectively. It is of interest to note that the present D_0 agrees well with that of our previous calculations, but the migration energy, E_m , is lower than determined previously [15, 16].

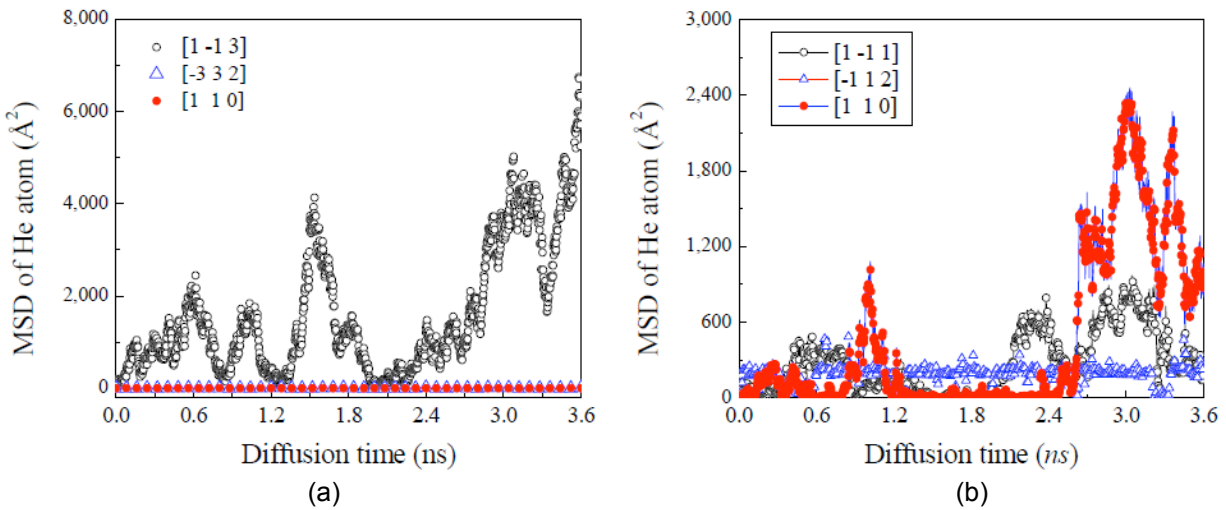


Fig. 6. The MSDs of a He interstitial diffusing along different directions; (a) $\Sigma 11$ GB at 700 K and (b) $\Sigma 3$ GB at 600 K

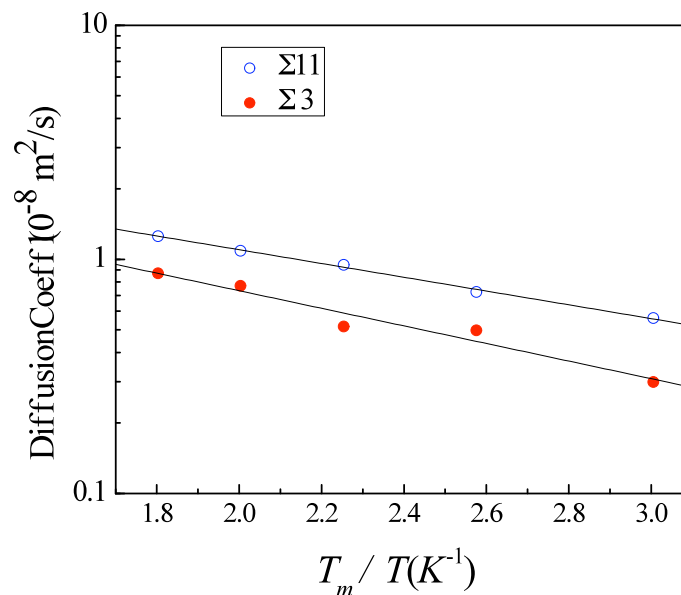


Fig. 7. Arrhenius plots for a single He interstitial diffusing at $\Sigma 11$ and $\Sigma 3$ GBs in α -Fe

In the $\Sigma 3$ GB, it is found that the He interstitial can migrate along both the $[110]$ and $[1\bar{1}1]$ directions at 600 K, as demonstrated by the MSDs in Fig. 6b, which means that He migration is two-dimensional at low temperatures. When the temperature is higher than 700 K, the migration behavior of the He interstitial changes from two-dimensional diffusion to three-dimensional diffusion. The present results agree well with those of Terentyev et al. [18] and our previous results [16] with different empirical potentials, where it was found that He atoms migrate two- and three-dimensionally at low and high temperatures, respectively. The diffusion coefficients have also been determined using MSD and TTD analysis and they obey an Arrhenius relation, as shown in Fig. 7. The best-fit E_m and D_0 are 0.224 eV and $4.14 \times 10^{-8} \text{ m}^2/\text{s}$, respectively. Also the present D_0 agrees well with those of both Terentyev et al. [18] and our previous simulations with different potentials [15, 16]; and the present E_m agrees well with that of Terentyev et al. [18], but it is slightly lower than our previous result [15, 16].

Conclusions

Based on the present calculations, it is clear that a single He interstitial in Fe has very high mobility because of a very low migration barrier. Large He-clusters will create an SIA and are trapped by the resulting He-vacancy complex. The migration energies of He interstitials in Fe GBs are higher than those of He interstitials in bulk Fe. The migration of He interstitials in $\Sigma 11$ and $\Sigma 3$ GBs is relative to the special directions in the GBs, which suggests that the GBs may provide fast diffusion paths for He migration. An He interstitial migrates one-dimensionally along the $\Sigma 11$ GB, while it migrates two-dimensionally at temperatures lower than 600 K and three-dimensionally at higher temperatures in the $\Sigma 3$ GB.

References

- [1] S. J. Zinkle, *Phys. Plas.* 12 (2005) 058101.
- [2] J. H. Evans, A. van Veen and L. M. Caspers, *Nature* 291 (1981) 310.
- [3] P. B. Johnson and D. J. Mazey, *Nature* 276 (1978) 595.
- [4] Y. Katoh, M. Ando, and A. Kohyama, *J. Nucl. Mater.* 323 (2003) 251–262.
- [5] J. Samaras, *Materials Today* 12 (2009) 46–53.
- [6] W. D. Wilson and R. A. Johnson, Rare gases in metals, in *Interatomic Potentials and simulation of Lattice Defects*, P. C. Gehlen, J. R. Beeler and R. J. Jaffee, eds., Battelle Institute Materials Science Colloquia, Columbus, Ohio, 1972, p. 375-390.
- [7] T. Seletskiaia, Y. Osetsky, R. E. Stoller, and G. M. Stocks, *Phys. Rev. Lett.* 94 (2005) 046403.
- [8] C. C. Fu and F. Willaime, *Phys. Rev. B* 72 (2005) 064117
- [9] X. T. Zu, L. Yang, F. Gao, S. M. Peng, H. L. Heinisch, X. G. Long, and R. J. Kurtz, *Phys. Rev. B* 80 (2009) 054104.
- [10] R. E. Stoller, S. I. Golubov, P. J. Kamenski, T. Seletskiaia and Yu. N. Osetesky, *Philo. Mag.* 90 (2010) 923–934.
- [11] D. M. Stewart, Yu. N. Osetesky, R. E. Stoller, S. I. Golubov, T. Seletskiaia and P. J. Kamenski, *Philo. Mag.* 90 (2010) 935–944.
- [12] N. Juslin and K. Nordlund, *J. Nucl. Mater.* 382 (2009) 143–146.
- [13] N. Gao, M. Samaras, and H. Van Swygenhoven, *J. Nucl. Mater.* 400 (2010) 240–244.
- [14] P. H. Chen, X. C. Lai, K. Z. Liu, X. L. Wang, B. Bai, B. Y. Ao, and Y. Long, *J. Nucl. Mater.* 405 (2010) 156–159.
- [15] F. Gao, H. Heinisch, and R. J. Kurtz, *J. Nucl. Mater.* 351 (2006) 133-140.
- [16] F. Gao, H. L. Heinisch, and R. J. Kurtz, *J. Nucl. Mater.* 367–370 (2007) 446–450.
- [17] F. Gao, H. L. Heinisch, and R. J. Kurtz, *J. Nucl. Mater.* 386–388 (2009) 390–394.
- [18] D. Terentyev, and X. He, *Comput. Mater. Sci.* 49 (2010) 858-864.
- [19] D. Stewart, Y. Osetskiy, and R. Stoller, *J. Nucl. Mater.*, [doi: 10.1016/j.jnucmat.2010.12.217](https://doi.org/10.1016/j.jnucmat.2010.12.217).
- [20] F. Gao, H. Q. Deng, H. L. Heinisch, and R. J. Kurtz, to be submitted.
- [21] G. J. Ackland, M. I. Mendelev, D. J. Srolovitz, S. Han and A. V. Barashev, *J. Phys.: Condens. Mater.* 16 (2004) 52629.
- [22] R. A. Aziz, A. R. Janzen, and M. R. Moldover, *Phys. Rev. Lett.* 74 (1995) 1586.
- [23] E. Clementi and C. Rostti, *Atomic Data and Nuclear Data Tables* 14 (1974) 177.
- [24] R. J. Kurtz and H. L. Heinisch, *J. Nucl. Mater.* 329–333 (2004) 1199–1203.
- [25] M. W. Cunian, R. N. Stuart, and R. J. Borg, *Phys. Rev.* 15 (1977) 699.

6.2 ATOMISTIC STUDIES OF PROPERTIES OF HELIUM IN BCC IRON USING THE NEW He–Fe POTENTIAL—David M. Stewart, Stanislav Golubov (Oak Ridge National Laboratory and the University of Tennessee), Yuri Ostersky, Roger E. Stoller, Tatiana Seletskaya, and Paul Kamenski (Oak Ridge National Laboratory)

OBJECTIVE

The objective of this work is to use molecular dynamics techniques to increase understanding of the behavior of transmutation-produced helium in reduced-activation ferritic/martensitic steels that are candidate materials for fusion reactors. As there is no suitable iron-carbon-helium interatomic potential, simulations are performed using helium in pure iron.

SUMMARY

We have performed atomistic simulations of helium bubble nucleation and behavior in iron using a new 3-body Fe–He inter-atomic potential combined with the Ackland iron potential. Updated results from ongoing large simulations examining the nucleation of helium defects are presented. When an Fe interstitial encounters a helium bubble, it can recombine with one of the vacancies in the bubble, leading to a bubble with a higher He/V ratio and hence higher pressure. We investigate how far this process can go before the bubble will not accept any more SIAs.

PROGRESS AND STATUS

Introduction

Helium produced in neutron irradiated iron affects the mechanical properties. The growth, migration and coalescence behavior of helium bubbles is very sensitive to the assumed properties of individual He interstitials and helium-vacancy clusters [1]. A new He–Fe interatomic potential has been developed at ORNL, based on extensive fitting to first-principles calculations of point defects and clusters [2–4]. This potential has been used to investigate the properties of helium, helium-vacancy clusters and helium bubbles in MD and MS simulations.

Helium diffuses very fast in the matrix, but is easily trapped in vacancies [5]. It is possible for a self-interstitial to recombine with the vacancy, knocking the helium back into an interstitial position. Previous calculations [6] showed that recombination is possible not only for a single substitutional He, but even when the vacancy contains multiple Helium atoms. The reverse process (i.e. Frenkel pair formation) can happen—an iron atom is pushed out of its lattice site, creating a He–V cluster and an SIA. As more helium joins the cluster, more Frenkel pairs are formed, creating larger defects. These mechanisms are investigated together in larger simulations [6] that examine the nucleation of He defects. Some of these simulations are ongoing, with the latest results presented here.

The He–V defects nucleated in this manner are nascent bubbles. Helium bubbles are more stable than voids and continue to grow as more helium and vacancies diffuse to the bubble. Helium bubbles of sizes 1–6 nm were studied in [6]. In order to estimate the amount of helium present from an observed bubble size distribution, it is necessary to understand the relationships between bubble size, pressure and helium content. Extensive atomistic simulations of such bubbles were compared to show effect of temperature, interatomic potentials used and helium concentration. Here we extend that by investigating the interaction of bubbles with a surplus of self-interstitial atoms. We also determine the surface energy of a bubble made up of specific crystallographic facets.

Simulation Method

For the MD simulations reported here, the general procedure followed is: Generate perfect BCC lattice. Introduce the defect(s) to be studied. Relax at constant volume using a mixture of conjugate gradient and simulated annealing, and save the atom positions in units of the lattice constant. Start the simulation.

The MD simulations used NVE (constant number of atoms, constant volume and constant energy) dynamics. The lattice constant and initial velocities were chosen to give close to zero pressure and the desired initial temperature. The boundary conditions are periodic in X, Y and Z, which are $\langle 100 \rangle$ directions. The velocity Verlet algorithm with a timestep of 0.3fs is used. As volume and temperature correction are not used, when processes that release energy are simulated the temperature and pressure both rise during the simulation.

The potentials used are the ORNL He–Fe potential [2–4], the Ackland Fe–Fe potential [7] and the Aziz He–He potential [8]

Coalescence

Previous He coalescence simulations [6,9,10] were run at four different sizes/concentrations. The smaller ones are 125 helium atoms in a $31 \times 31 \times 31$ BCC iron matrix (60,000 iron atoms) and 125 helium atoms in a $40 \times 40 \times 40$ BCC iron matrix (128,000 iron atoms). These give concentrations of 2089 and 976 appm He respectively. In addition, much larger simulations are ongoing at two concentrations: 1000 and 500 helium atoms in a $80 \times 80 \times 80$ BCC iron matrix (1,024,000 iron atoms). These give concentrations of 976 and 488 appm He respectively. All of these are simulated at 600 K and 1000 K. For all these simulations, the concentration of vacancies created is plotted as a function of time. The latest results are shown in Figure 1.

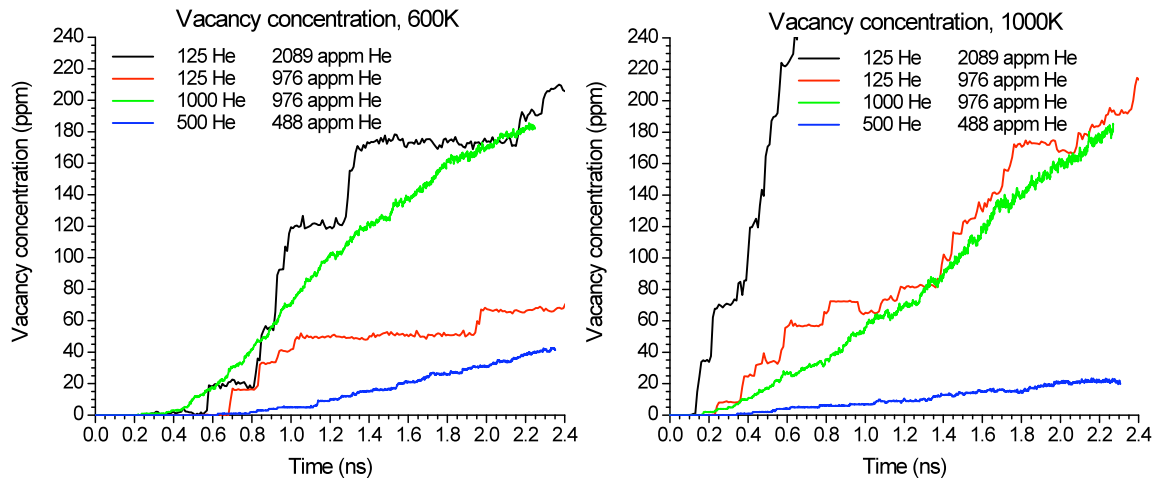


Figure 1. Coalescence for different concentrations at (a) 600 K and (b) 1000 K.

Interaction of bubble with SIAs

Self-interstitial atoms can recombine with some of the vacancies that make up a helium bubble, increasing the He/V ratio. This can lead to over-pressurized bubbles. There must be a limit to this; eventually the bubble will have to stop accepting SIAs (or invoke some other process such as ejecting helium, which seems unlikely).

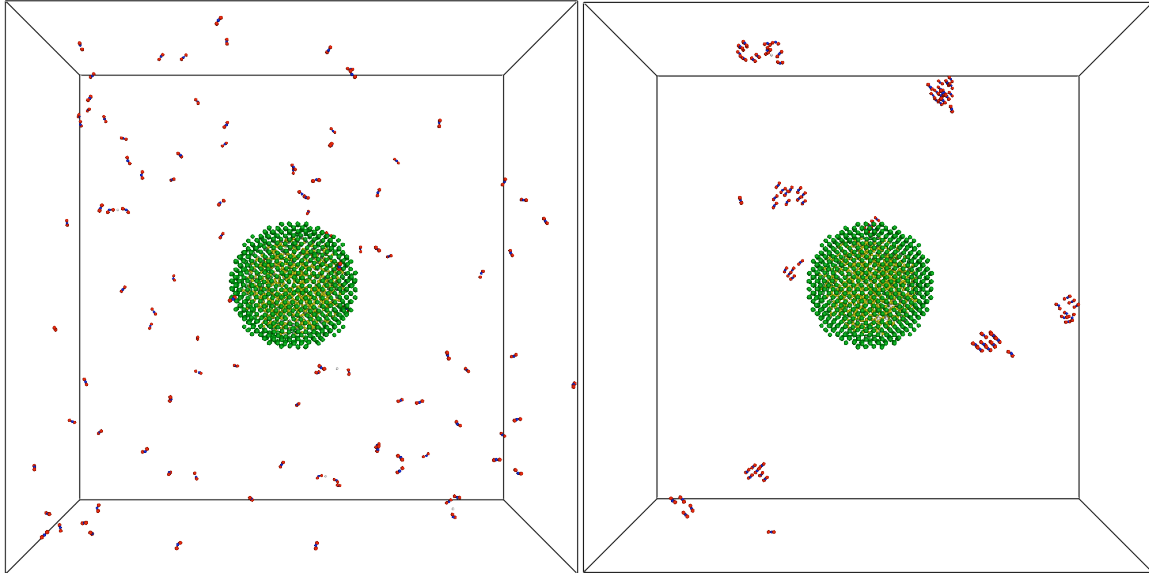


Figure 2. a) Initial condition.

b) After 1ns

In order to investigate the recombination of SIAs with a large bubble, we simulated 100 SIAs near a 4nm helium bubble. The initial configuration is shown in Figure 2a. The bubble was in the center of the 60×60×60 periodic cell, and the SIAs were placed randomly in the lattice at least 4 lattice parameters from the bubble. Figure 2b shows the situation after 1 nanosecond of simulation time. The SIAs mostly clustered with each other instead of recombining with the vacancies in the bubble.

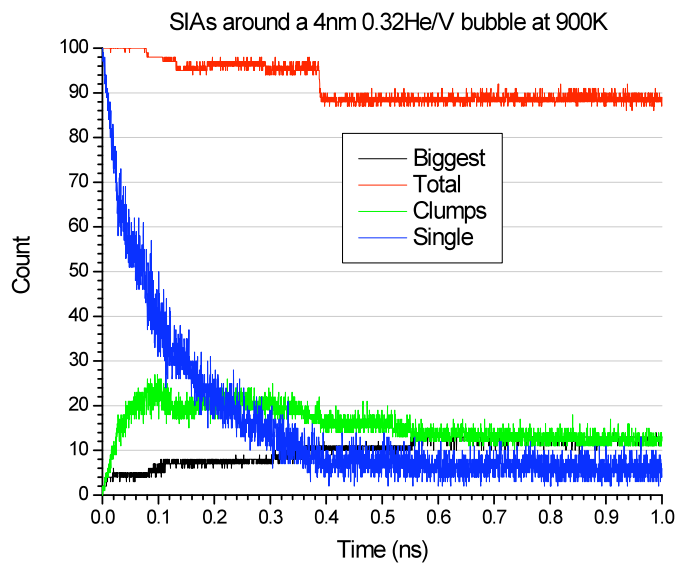


Figure 3. Recombination and clustering of SIAs around a 4 nm helium bubble. Black line: Size of largest cluster. Red: Total SIAs. Green: Clusters with 2 or more SIAs. Blue: Single SIAs.

Figure 3 shows the number of SIAs over time. In the nanosecond, 11 SIAs recombined with the bubble, 4 remained free and 85 formed 13 clusters. The biggest cluster contained 13 interstitials. SIA clusters larger than about 2 or 3 SIAs are only mobile in one dimension, which greatly reduces their chance of finding their way to the bubble. Larger SIA clusters have very little mobility at all. Eleven SIAs recombining with a bubble of 2,741 vacancies did not cause any substantial change in the bubble. Due to the clustering, it is unlikely that running the simulations longer would significantly increase the number of SIAs that recombine.

As small SIA clusters are observed to be mobile only in one dimension, a simulation that uses SIA clusters can arrange them so that they will move on a line that crosses the bubble. This allows us to set up another simulation that is better suited to testing the limit to how many SIAs the bubble will recombine with.

A 1 nm bubble was placed at the center of a $30 \times 30 \times 30$ box. An SIA cluster, consisting of seven SIAs, was placed 17 lattice parameters away in each of the eight $\langle 111 \rangle$ directions. Each cluster was oriented towards the bubble, so its only possible motion is towards the bubble or directly away from it. The bubble had 59 vacancies and different amounts of helium in each run. The clusters had a total of 56 SIAs. Figure 4 shows the starting and ending configuration for an equilibrium (23 He at 900 K) bubble.

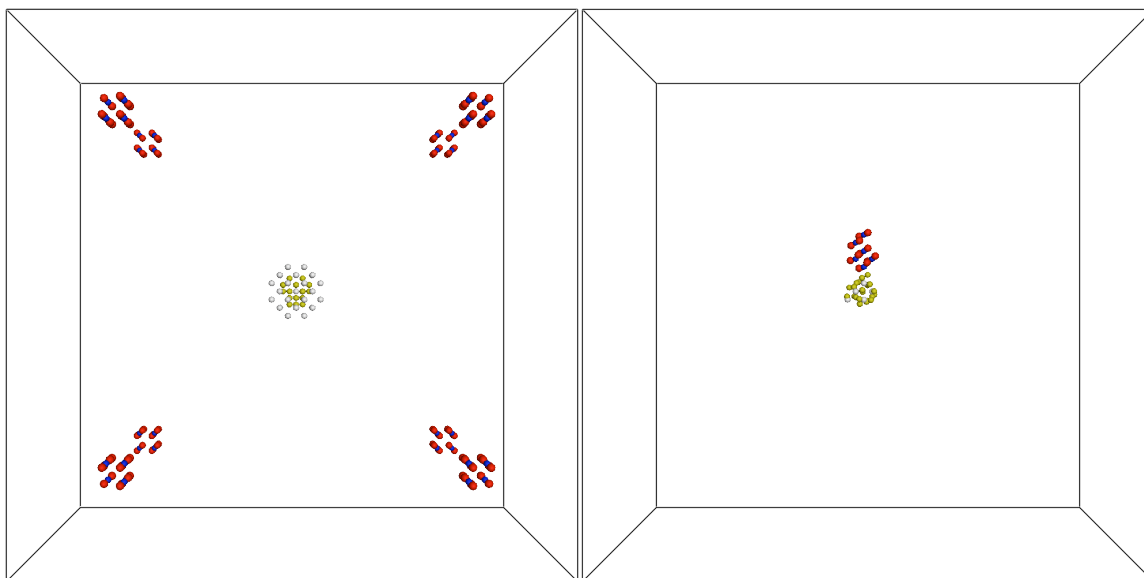


Figure 4. a) Initial condition. 23 He, 59 V

b) After 3ns

Simulations were run at 900 K for different amounts of helium in the bubble, from 5 to 95 atoms. Each SIA cluster was seen to do one of two things. It could move in and recombine with the bubble, or it could move away and merge with other clusters.

The final number of vacancies as a function of the number of helium atoms is plotted in figure 6a. For 5 He atoms, all 8 clusters recombined, leaving three vacancies.

For 10–30 He atoms, some of the clusters recombined with the bubble and the rest merged together. The merged cluster eventually collided with the bubble and partially recombined, leaving a bubble with a smaller cluster of SIAs attached. The final position for 15, 23 and 30 He atoms can be seen in figures 5a, 4b and 5b respectively.

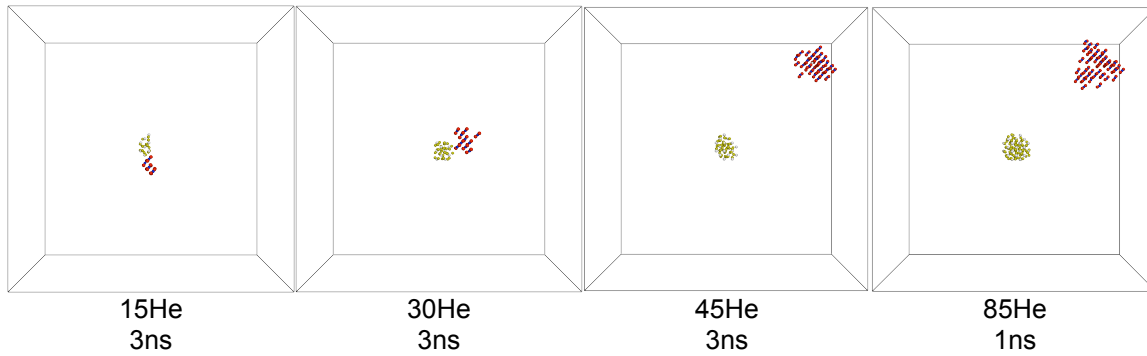


Figure 5. Final positions for different He/V ratios. All bubbles have 59 Vacancies

For 35 and more He atoms, again some of the clusters recombined with the bubble and the others merged. But this time the merged cluster did not encounter the bubble within the simulation time (1–3 ns). The final position for 45 and 85 He atoms can be seen in figures 5c and 5d respectively. Note that in figure 6a, the final number of vacancies is always 59 minus a multiple of 7, as each cluster has 7 SIAs.

The final He/V ratios as a function of the number of helium atoms is plotted in figure 6b. They have a wide range: from 1.1 to 2.3. The average is 1.66.

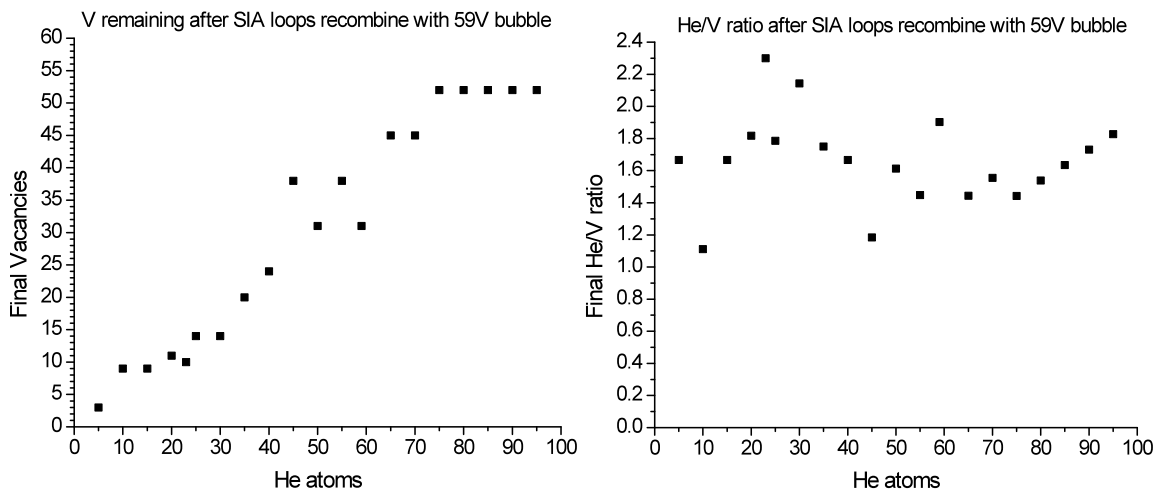


Figure 6. Final number of vacancies/Final He/V ratio in the bubble for different numbers of helium atoms. All bubbles had 59 vacancies initially.

Surface energy of voids

As different crystallographic facets have different surface energies, the shape of a void may influence the pressure of gas it can hold. The surface energy of voids of different shapes is calculated. Energy is calculated by molecular static relaxations. Surface area is calculated from the number of vacancies (i.e. the volume) using the appropriate geometric formula for the shape. A plot of energy vs. surface area is shown in figure 7.

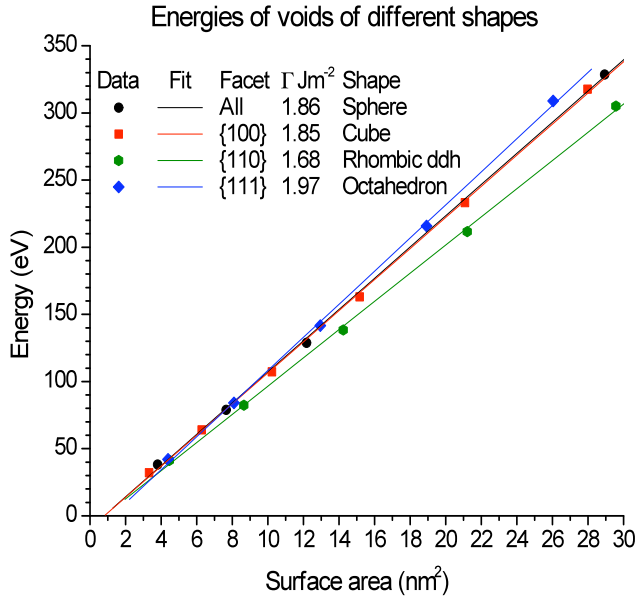


Figure 7. Energy vs surface area of different shaped voids

The four different shapes considered are shown in figure 8. The sphere has a minimum total surface area for a given volume. The cube, rhombic dodecahedron and octahedron consist of only {100}, {110} and {111} surfaces respectively. The results show that the {110} surface has the lowest energy, followed by the {100} surface and lastly by the {111} surface. As one would expect, the result from the sphere is in between as the sphere contains a mixture of different surfaces.

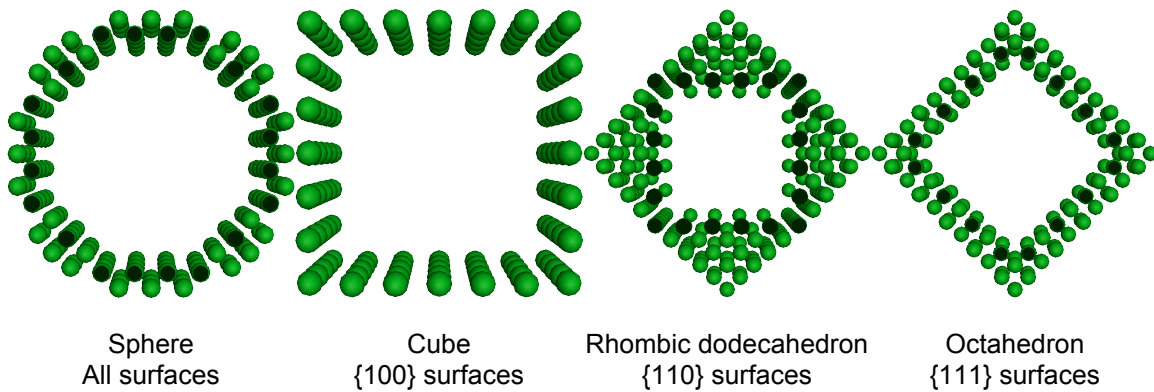


Figure 8. Cross-sections of the four different shapes of void investigated.

References

- [1] S.I. Golubov, R.E. Stoller, S.J. Zinkle, and A.M. Ovcharenko, Kinetics of coarsening of helium bubbles during implantation and post-implantation annealing, *Journal of Nuclear Materials* 361 (2007), pp. 149–159.
- [2] T. Seletskaja, Y.N. Osetsky, R.E. Stoller, and G.M. Stocks, Magnetic Interactions Influence the Properties of Helium Defects in Iron, *Physical Review Letters* 94 (2005), pp. 046403.
- [3] T. Seletskaja, Y.N. Osetsky, R.E. Stoller, and G.M. Stocks, Calculation of helium defect clustering properties in iron using a multi-scale approach, *Journal of Nuclear Materials* 351 (2006), pp. 109–118.
- [4] T. Seletskaja, Y.N. Osetsky, R.E. Stoller, and G.M. Stocks, Development of a Fe He interatomic potential based on electronic structure calculations, *Journal of Nuclear Materials* 367 (2007), pp. 355–360.
- [5] H. Trinkaus and B. Singh, Helium accumulation in metals during irradiation—where do we stand? *Journal of Nuclear Materials* 323 (2003), pp. 229–242.
- [6] D.M. Stewart, July 2010 semiannual report.
- [7] G.J. Ackland, D.J. Bacon, A.F. Calder, and T. Harry, Computer simulation of point defect properties in dilute Fe-Cu alloy using a many-body interatomic potential, *Philosophical Magazine A-Physics of Condensed Matter Structure Defects and Mechanical Properties* 75 (1997), pp. 713–732.
- [8] R. Aziz, A. Janzen, and M. Moldover, *Ab Initio* Calculations for Helium: A Standard for Transport Property Measurements, *Phys. Rev. Lett.* 74 (1995), pp. 1586–1589.
- [9] David M. Stewart, Yuri N. Osetsky and Roger E. Stoller, Atomistic studies of formation and diffusion of helium clusters and bubbles in BCC iron, In Press, *Journal of Nuclear Materials*
- [10] David M. Stewart, Yuri N. Osetsky, Roger E. Stoller, Stanislav I. Golubov, Tatiana Seletskaja and Paul J. Kamenski, Atomistic studies of helium defect properties in bcc iron: comparison of He–Fe potentials, *Philosophical Magazine*, Volume 90, Issue 7 & 8 (March 2010) pp. 935 – 944

6.3 A Multi-Scale Model of Helium Transport and Fate in Irradiated Tempered Martensitic Steels and Nanostructured Ferritic Alloys – T. Yamamoto, G.R. Odette (Department of Mechanical Engineering, University of California Santa Barbara), R.J. Kurtz (Materials Science Division, Pacific Northwest National Laboratory) and B.D. Wirth (University of Tennessee, Knoxville)

OBJECTIVE

The synergistic effects of displacement damage and He produced by high energy neutrons in the fusion reactor environment can cause severe degradation of structural materials. The objective of this research is to develop a multiscale modeling tool for exploring the transport and fate of He under fusion relevant irradiation conditions. The model development is coordinated with well-designed in situ He implanter (ISHI) experiments in HFIR that enable characterization of microstructural evolution under the simultaneous introduction of both displacement damage and He at fusion reactor relevant He/dpa ratios. This report describes the master multiscale modeling framework, as well as some details of the sub-models and comparison of model predictions with experimental observables from recent ISHI experiments.

SUMMARY

Development and application of a multiscale model of the transport and fate of He in irradiated nanostructured ferritic alloys and tempered martensitic steels are described. Model predictions for He bubble average size, size distribution and number density are in reasonably good agreement with recent observations in ISHI experiments on F82H mod.3, 12YWT and MA957.

PROGRESS AND STATUS

Introduction

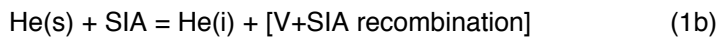
One of the challenges that fusion reactor materials development faces is to predict and mitigate the effects of transmutation He on the mechanical properties of first wall structural materials. In a typical DEMO fusion reactor design, after a year of operation at a neutron wall load of $5 \text{ MW/m}^2 \approx 500 \text{ appm He}$ will be generated in Fe-based materials, as well as displacement damage doses of $\approx 50 \text{ dpa}$. Helium bubbles form in the matrix as well as on dislocations, precipitate interfaces and grain boundaries (GB) [1]. Based on a physically motivated analysis of limited data in the literature for fracture toughness transition temperature shifts (ΔT), we previously proposed a model that predicts that irradiation hardening ($\Delta\sigma_y$) coupled with GB He embrittlement of tempered martensitic steels (TMS) produces very large ΔT at low irradiation temperatures [2,3]. Our previous predictions are in remarkably good quantitative agreement with recent spallation proton irradiation data, showing extraordinary ΔT up to $> 500^\circ\text{C}$ in TMS containing $\approx 2000 \text{ appm He}$ at $\approx 20 \text{ dpa}$ [4]. The synergistic effects of irradiation hardening and GB He embrittlement appears to emerge at He levels $> \approx 500 \text{ appm}$ corresponding to one year of operation at high wall loading. There is also a transition from transgranular cleavage to intergranular fracture [2,3]. The spallation proton data also show that high levels of He extend the range of large ΔT to above 400°C . At high irradiation temperatures matrix He may promote void swelling and He accumulation on GBs could also severely degrade creep rupture and related properties. These observations and models suggest that the temperature window for using TMS in DEMO reactor applications may be significantly narrower than previously believed, and may even close. Thus a major challenge will be to design and develop a new class of nanostructured ferritic alloys (NFA), that are dispersion strengthened by an ultra high density of Y-Ti-O enriched nanometer-scale features (NF), that can protect GBs and prevent swelling by trapping He in very small bubbles at NF interfaces [5-7]. The objective of the present research is to develop a tool to predict material performance, as a function of material and environmental variables such as microstructure, chemical composition, displacement damage (dpa), He/dpa ratio and temperature. In this report we describe the development and application of a multiscale model of the transport and fate of He in irradiated NFAs and TMS.

Multi-scale Modeling

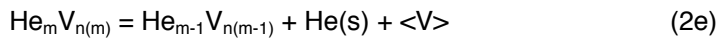
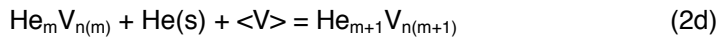
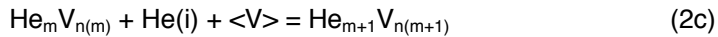
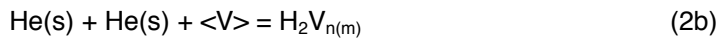
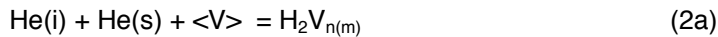
The model was built by considering the multiscale nature of the phenomena, both in time and length scales. Key elements of the basic interactions of He atoms with various features in the material microstructure as well as He migration have been atomistically modeled using molecular statics (MS), molecular dynamics (MD) and kinetic Monte Carlo (kMC) simulations. The MS simulations included the Dimer method to determine defect migration saddle point energies. Details of the atomistic models are described elsewhere [8-17]. Briefly, the interaction of He atoms, vacancies, and He-vacancy clusters with key microstructural features such as dislocations, NFs and GBs were modeled and information such as binding and migration energies were incorporated in the modified rate theory (MRT) differential equations. In some cases a type of energy (e.g. interstitial He to GB binding energy) depended on GB character [9,10,13-15]. For the calculations reported here the MRT integration code used a representative single value. Parametric studies are being performed to test the sensitivity of the model to the values we selected.

Current Integration Model Structure

The model is specifically aimed at treating intermediate to high irradiation temperatures, which are outside the low-temperature displacement damage and defect cluster dominated regime, at least for low He conditions. Reaction rate theory is used to model the transport and interactions of point defects and He, as well as He clustering, which leads to bubble formation and growth. Figure 1 shows the framework of the model. He transport and interactions in the matrix and within microstructural subregions are separately treated according to the characteristics of each region. In the matrix, point defects recombine at precipitate trap sites as well as in the matrix, or diffuse to permanent sinks such as dislocations and GBs to produce steady state concentrations of vacancy (V) and self-interstitial atoms (SIA). Helium is generated by transmutation reactions in interstitial, He(i), or substitutional, He(s), forms. These can switch form by reacting with V and SIA as follows:



The two forms of He atoms migrate at appropriate diffusivities until they meet other He atoms and Vs to create He_mV_n clusters in the matrix, or they reach sub-region sinks that are, in the current model, NF, dislocations and GBs. The He can be emitted as well as absorbed, hence He can recycle between various features and sub-regions they contain. Bubble formation and evolution is modeled using a cluster dynamics algorithm. The concentration of clusters with i He atoms and the balanced number of vacancies, $C_{\text{mxb}}(i)$ ($i > 2$), is solved by a set of rate equations considering following reactions:



Here, the $\text{H}_m\text{V}_{n(m)}$ clusters are all assumed to be stable bubbles with He gas pressure that balances the capillary pressure caused by surface tension. A hard sphere model is used for the equation of state (HSEOS), in terms of a master equation to relate ideal gas model radius to HSEOS real gas radius

developed by Stoller and Odette [18]. The master equation gives the relationship between the ideal to real gas radius ratio, $[r_{b,ideal}/r_{b,HSEOS}]$ as a function of a reduced radius, $R = r_{b,ideal}[kT/\gamma]^{1/3}$. Here, k is Boltzman's constant, T is the absolute temperature and γ is the free surface energy, typically ≈ 2.0 (J/m²) for BCC Fe. For small He clusters ($i < 20$) the He/V ratio is between 1 to 1.3 in the temperature range from 500 to 600°C. For these He/V ratios, the binding energy of He to the cluster is more than ≈ 2.5 eV according to ab initio calculations by Fu [19] and more than ≈ 4 eV in molecular dynamics calculations by Morishita et al. [20]. This suggests that, to first order, a two He atom cluster is a bubble nucleus. We plan to implement a stochastic nucleation model in the future.

He atoms captured by precipitates, dislocations, and GBs may be re-emitted back into the matrix at a rate dictated by the binding energy to that feature, or the feature subregion, the jump frequency, and the temperature. Alternately, He diffuses within the subregion until He + He reactions nucleate a bubble, or the mobile He joins He_mV_n bubbles. He atoms are also be trapped at lower energy sites within the subregion for a time that is again dictated by the binding energy. There is an increased chance of He + He \rightarrow heterogeneous bubble nucleation reaction at the low energy sites. Bubble also nucleate homogeneously on dislocation segments, in the matrix and at other features such as GB and precipitate interfaces, and bubbles that act as permanent He traps.

The local transport, trapping and interactions have been modeled according to the dimensional and energetic characteristics of the sub-region. For example, on dislocations diffusion of a He takes place one-dimensionally along the dislocation line between deeper trap sites such as bubbles, intersections and nm-scale precipitates, as shown in Figure 2a. At steady state the He concentration profile between trapping sites has a zero-gradient peak at the middle. Since there is no net He flow at the peak, the dislocation network can be represented by a distribution of isolated dislocation segments, with a trapping site at the center, as illustrated in Figure 2b. The segments are modeled as a distribution of length, $L(k)$, where $1 \leq k \leq n_{seg}$, where n_{seg} is the number of unique segment lengths. For pre-existing traps, $L(k)$ is assumed to have a log-normal distribution, with an average length $\langle L \rangle$, that is determined by the total number of the trap sites and the dislocation density, ρ . The total number of pre-existing trap sites, N_{TS} , is taken as the sum of N_{IS} for dislocation intersections and N_{PD} for precipitates on dislocations. Assuming the spacing of trapping sites on individual dislocations is $\rho^{1/2}$ and $(2 r_p N_p)^{1/2}$, N_{TS} is

$$N_{TS} = N_{IS} + N_{PD} = \rho^{3/2} + \rho (2 r_p N_p)^{1/2} \quad (3a)$$

The average segment length $\langle L \rangle$ is

$$\langle L \rangle = \rho / N_{TS} \quad (3b)$$

For example, for a typical NFA with $N_p = 6.6 \times 10^{23}/m^3$, $r_p = 1.5$ nm (or 1% volume fraction of precipitates, f_v) and $\rho = 10^{15}/m^2$, N_{IS} and N_{PD} are 3.2 and $4.6 \times 10^{22}/m^3$, respectively, resulting in an average segment length $\langle L \rangle$ of 12.9 nm. The number density, $N(k)$, of larger and smaller k -th segment, that are scaled as multiples of the Burger's vector b , is assumed to have a log normal distribution. Figure 2c shows an example of the $N(k)$ distribution as a function of $L(k)$ with distribution width parameter, $\beta_m = 0.4$. Reaction between trapped and mobile converts the site to a permanent bubble trap. Once formed the dislocation bubbles grow by collecting the He that diffuses along the dislocation segment lengths.

However, bubbles are permanent traps for He and also nucleate homogeneously in the various regions. In the case of dislocations, homogeneous bubble nucleation requires dynamic re-segmentation of the dislocation network length distribution. The reaction rate is taken to be the same as in the case of deep traps, except that the segment length is taken as $L(k)/2$ and the diffusion coefficient is doubled to $2D_{He(seg)}$. The initial segment is then partitioned into two segments with length classes of k_1 and k_2 depending on the original length class k . If k is an even number, then $k_1 = k_2 = k/2$. If k is an odd number, then

$k_1=(k-1)/2$ and $k_2=(k+1)/2$. All i He atoms at the trap are assigned to the k_1 class segment to make a segment (i, k_1) , and the new nucleus is assigned to a $(2, k_2)$ segment.

The new segments containing homogeneously nucleated He bubbles are treated site holding two He atoms in the k_2 length class. The $C_{He}^{seg(i,k)}$ on the original segment is evenly added to those of the two new segment classes, $C_{He}^{seg(i,k_1)}$ and $C_{He}^{seg(2,k_2)}$. The reason why the segment lengths were modeled to have a fixed multiple (M) Butger's vector unit length, $L_u = Mb$, is because it enables segment division without generating a new segment class that would have a different length from any existing segment class.

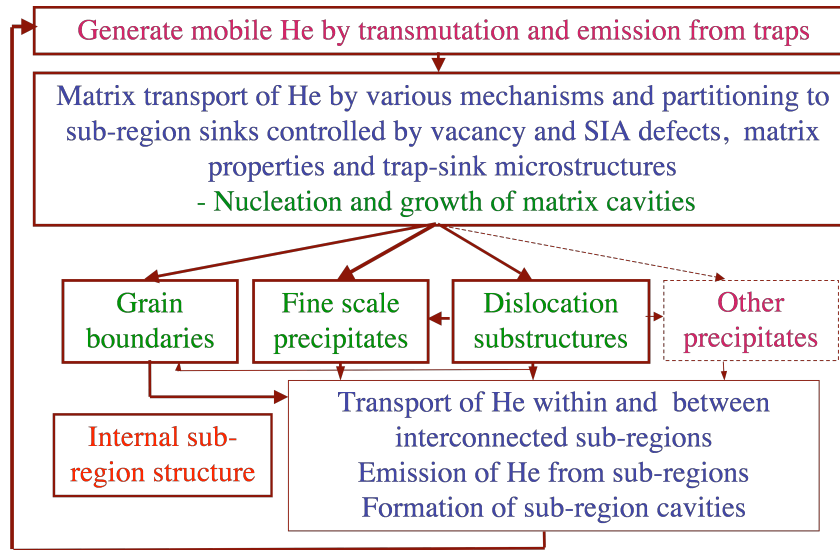


Figure 1 Master model framework showing the regions considered in the model as well as He transport between the regions.

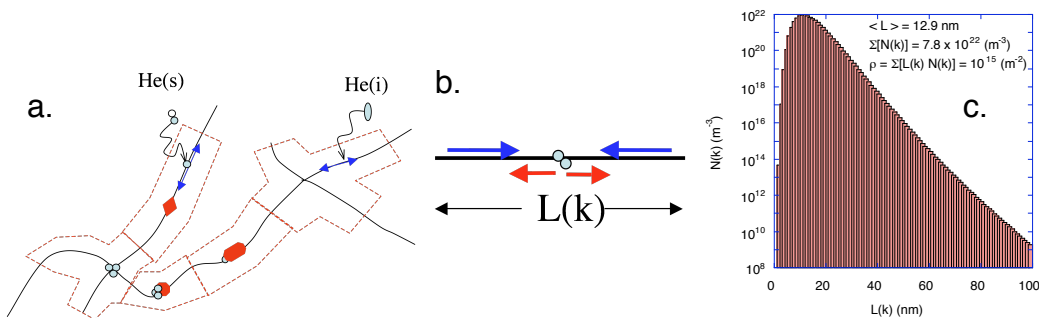


Figure 2 (a) A schematic dislocation network having intersections and precipitates as deeper He trap sites, (b) the simplest model of a part isolated at the middle points between any two of the deeper sites and (c) a modeled log-normal type distribution of the segment length with $\beta_m = 0.4$.

The rate at which He atoms on a dislocation segment are captured at the trap site is obtained by solving the one-dimensional steady-state diffusion Equation 4a. This assumes immediate capture at the surface of the trap site at $x=r_0$ so that He generation (or capture from the matrix), G_{He} , per unit length is uniform over the entire segment and should balance the net transfer of He from any location on the segment towards the trap site. Solving Equation 4a with boundary conditions shown in Equation 4b gives a

general solution shown in Equation 4c. The red solid curve in Figure 3 is an example a $C_{\text{He}}(x)$ solution for the case of a segment length of 12.9 (nm) and a capture radius of $r_o = b = 0.248$ (nm). The dashed blue line shows the average He concentration over the entire segment length, $\langle C_{\text{He}} \rangle$, which is generally given by Equation 4d. The transfer rate S_{DT} defined in $D_{\text{He}} S_{\text{DT}} \langle C_{\text{He}} \rangle = G_{\text{He}}$ is given by Equation 4e.

$$D_{\text{He}} d^2C(x)/dx^2 + G_{\text{He}} (\text{capture from the matrix}) = 0 \quad (4a)$$

$$C(x) = 0 \text{ at } x = r_o; \quad dC(x)/dx = 0 \text{ at } x = L/2 \quad (4b)$$

$$C_{\text{He}}(x) = (G_{\text{He}} L^2 / 2 D_{\text{He}}) \{ (x/L - r_o/L) - (x^2/L^2 - r_o^2/L^2) \} \quad (4c)$$

$$\langle C_{\text{He}} \rangle = (G_{\text{He}} L^2 / 2 D_{\text{He}}) (1/6 - r_o/L + 2 r_o^2/L^2 - 4/3 r_o^3/L^3) \quad (4d)$$

$$S_{\text{DT}} = G_{\text{He}} / D_{\text{He}} \langle C_{\text{He}} \rangle = 1 / \{ L^2 (1/12 - r_o/2L + (r_o/L)^2) \} \quad (4e)$$

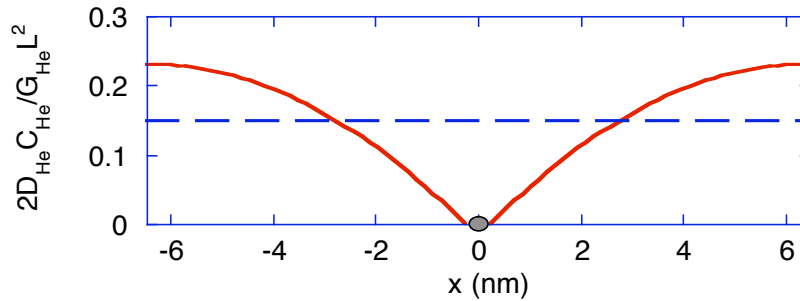


Figure 3 A steady-state He concentration profile (red solid line) on a dislocation segment with $L = 12.9$ (nm) for a uniform He generation G_{He} and capturing at a site of radius, r_o (nm), at diffusion coefficient D_{He} . Blue dashed line shows the average He concentration $\langle C_{\text{He}} \rangle$ over the entire segment.

A cluster dynamics approach is also applied to model bubble evolution on dislocation segments. For every segment length class, k , the concentration of segments holding i He atoms in the trap site, $C_{\text{seg}(i,k)}$ ($i = 0$ to n_{max}), and the concentration of untrapped He atoms (shown as the shaded regions in Figure 4), $C_{\text{He}}^{\text{seg}(i,k)}$ are modeled by a set of ordinary differential equations. The general forms for $dC_{\text{seg}(i,k)}/dt$ and $dC_{\text{He}}^{\text{seg}(i,k)}/dt$ are given by Equations 5a and 5b, respectively. Here, $S_{\text{is}(i,k)}^{\text{s}}$ is the sink strength of the trap site for the untrapped He concentration, $C_{\text{He}}^{\text{seg}(i,k)}$, in the segment, and $D_{\text{He}(s)}^{\text{seg}}$ is the diffusion coefficient of He atoms along dislocations. Equation 5a also considers He atom emission from the trap at a rate $\beta_{\text{is}}^{\text{s}}$ given by Equation 5c, where $E_{\text{b is}}^{\text{s}}$ is the binding energy of the He(s) atom to the trap site. Note that the current model allows emission of He only for $i < 2$. As has been stated previously the $\text{He}_2\text{V}_{\text{n}(2)}$ cluster is taken to be a stable bubble. A more accurate treatment of He emission from small He clusters will be included in future versions of the model. The first and second term in the Equation 5b account for He(s) or He(i) captured by the segment from the matrix, which depends on the dislocation density, and emission of He from all segment regions to the matrix at a rate $\beta_{\text{dist}}^{\text{s}}$, given in Equation 5d. The third and fourth terms account for the transfer of the previous segment to another segment class by the trap site capturing or emitting He. An integer number, $n_{\text{He}}^{\text{seg}(i,k)}$, is used to account for the number of He atoms that are being carried by the segment. The $n_{\text{He}}^{\text{seg}(i,k)}$ is taken as the $C_{\text{He}}^{\text{seg}(i,k)}/C_{\text{seg}(i,k)}$ ratio, rounded up to the nearest integer number for capture, since reactions are more likely on a segment carrying more He atoms than average, while the ratio rounded down for emission.

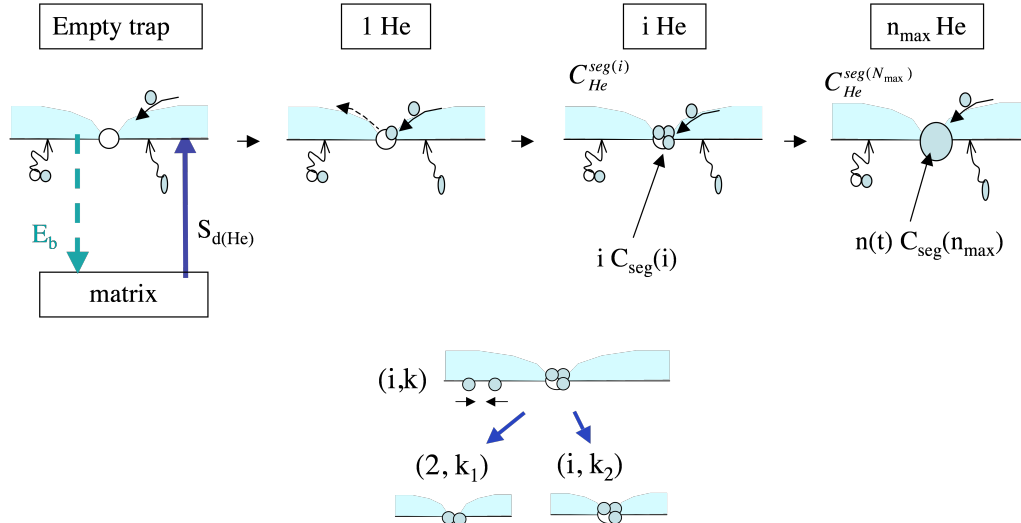


Figure 4 Schematics of a CD algorithm for He cluster formation at a trap site on a dislocation segment with a length $L(k)=kL_U$ (top) and for a treatment of homogeneous cluster nucleation other than the trap site (bottom).

$$\frac{dC_{seg(i,k)}}{dt} = S_{is(i-1,k)}^s D_{He(s)}^{seg} C_{He}^{seg(i-1,k)} - S_{is(i,k)}^s D_{He(s)}^{seg} C_{He}^{seg(i,k)} + \beta_{is}^{seg(i+1,k)} [(i+1) \cdot C_{seg(i+1,k)}] - \beta_{is}^{seg(i,k)} (i \cdot C_{seg(i,k)}) \quad (5a)$$

$$\frac{dC_{He}^{seg(i,k)}}{dt} = (S_{disl}^h D_{He(i)} C_{He(i)} + S_{disl}^s D_{He(s)} C_{He(s)}) C_{seg(i,k)} L(k) / \rho \Omega - \beta_{disl}^s C_{He}^{seg(i,k)} + S_{is(i-1,k)}^s D_{He(s)}^{seg} C_{He}^{seg(i-1,k)} (n_{He}^{seg(i-1,k)} - 1) - S_{is(i,k)}^s D_{He(s)}^{seg} C_{He}^{seg(i,k)} (n_{He}^{seg(i,k)} - 1) + \beta_{is}^{seg(i+1,k)} [(i+1) \cdot C_{seg(i+1,k)}] (n_{He}^{seg(i+1,k)} + 1) - \beta_{is}^{seg(i,k)} (i \cdot C_{seg(i,k)}) (n_{He}^{seg(i,k)} + 1) \quad (5b)$$

$$\beta_{is}^{seg(i,k)} = D_{He(s)}^{seg} \exp(-E_{bis}^s / kT) / b^2 \quad (5c)$$

$$\beta_{disl}^s = D_{He(s)}^{mtx} \exp(-E_{bdisl}^s / kT) / b^2 \quad (5d)$$

$$\frac{dC_{seg(i,k)}^{nucl}}{dt} = -S_{is(i,k)}^{s,nucl} 2D_{He(s)}^{seg} C_{He}^{seg(i,k)} [C_{He}^{seg(i,k)} / C_{seg(i,k)}] \quad (5e)$$

As noted previously, bubbles also homogeneously nucleate by He + He reactions on dislocation segments. The rate of nucleation is given by Equation 5e.

The original $C_{He}^{seg(i,k)}$ on segment before a new bubble nucleates is evenly divided between the two new segments. Homogeneously nucleated bubbles also grow by the diffusion of He along the dislocation segments as well as He fluxes from the matrix in the same way as bubbles formed on traps.

He bubble formation in GBs is modeled similarly accounting for both the trap site and homogeneous nucleation mechanisms. The entire GB area is divided into circular regions with area, A_{trap} , for each trap site. The concentration, $C_{gt}(i)$, carrying i He atoms is tracked using the cluster dynamics method for two-dimensional He diffusion in A_{trap} . For simplicity, homogeneously nucleated $He_2V_{n(2)}$ clusters are combined with the $C_{gt}(2)$ trap formed He bubble nuclei class. The A_{trap} is updated based on the total number of the

trap sites, including new homogeneously nucleated bubbles. Flow of He atoms in a GB to the trap site is found by solving the two dimensional diffusion equation, analogous to that for He fluxes from the matrix to dislocations. This involves replacing the dislocation density with $1/A_{\text{trap}}$ and the core radius with the trap site (or bubble) radius. The governing equations are given by:

$$S_{GBT(i)}^s = \ln[R_{\text{trap}}/r(i)](1/A_{\text{trap}}) \quad (6a)$$

$$\begin{aligned} dC_{GBT(i)}/dt = & S_{GBT(i-1)}^s D_{He(s)}^{GB} C_{He}^{GB} - S_{GBT(i)}^s D_{He(s)}^{GB} C_{He}^{GB} \\ & + \beta_{GBT}^s [(i+1)C_{GBT(i+1)}] - \beta_{GBT}^s (i \cdot C_{GBT(i)}) \end{aligned} \quad (6b)$$

$$\beta_{GBT}^s = D_{He(s)}^{GB} \exp(-E_{bGBT}^s/kT)/b^2 \quad (6c)$$

He cluster formation on NFs have been also modeled by cluster dynamics algorithm. In the current version of the model each NF has a maximum of one bubble with i He atoms, Helium is trapped on and emitted from the NFs at a rate specified by a binding energy $E_{\text{bnf}}^{\text{He}(s)}$. Bubble nucleation is treated by assuming that a second He atom reaching a NF with a previously trapped He atom immediately forms a bubble. Vacancies and interstitials are also trapped at NFs, which also act as recombination centers. NFs trap He and point defects by three dimensional diffusion mediated by the matrix composition of and the NF-bubble sink strength given by,

$$S_{NF(j)}^s = 4\pi r_{NF(j)} C_{NF(j)} (1 + r_{NF(j)} \sqrt{S_t}) / \Omega \quad (7a)$$

$$\begin{aligned} dC_{NF(j)}/dt = & S_{NF(j-1)}^{s,h} (D_{He(i)} C_{He(i)} + D_{He(s)} C_{He(s)}) - S_{NF(j)}^{s,h} (D_{He(i)} C_{He(i)} + D_{He(s)} C_{He(s)}) \\ & + \beta_{NF(j+1)}^s C_{NF(j+1)} - \beta_{NF(j)}^s C_{NF(j)} \end{aligned} \quad (7b)$$

$$\beta_{NF(j)}^s = D_{He(s)}^{mx} \exp(-E_{bNF(j)}^s/kT)/b^2 \quad (7c)$$

The preceding thumbnail sketch of the model does not include all the details of the formulation of the complex code containing 3000 to 8000 equations, that will be further described in future reports.

Companion HFIR Experiments using He-implanter Technique

The model calculations are compared with our systematically designed and carefully controlled experiments in the HFIR, a mixed spectrum reactor. While the details are given elsewhere [5-7,21-23], the so-called in-situ He-implantation (ISHI) experiments utilize NiAl coating that is deposited on TEM samples of TMS, NFA and model Fe-based alloys. The isotope, ^{58}Ni , which is about 60% of the natural Ni in the NiAl coating reacts with thermal neutrons to emit He as α -particles with 4.71 MeV energy. Depending on the thickness of the coating, He is implanted uniformly over an ≈ 6 to 8 μm thick layer from the sample surface adjacent to the coating. The He-to-dpa ratio ranges from ≈ 5 to 50 appm He/dpa, depending on the coating thickness. Our recent results clearly showed differences in He precipitation behavior between TMS alloys F82H and Eurofer versus NFA MA957 and 12YWT[5-7,22-23].

Model calculations have been performed for the typical TMS and NFA microstructural parameters shown in Table 1. The corresponding values of the thermodynamic parameters used in the model are shown in Table 2. The examples shown here are for a He/dpa ratio of 40 at 500°C and a dpa rate of 10^{-6} dpa/s

Table 1 Microstructural Parameters

Model	ρ (m ⁻²)	Grain size	Sink strength (m ⁻²)		
			NF	Dislocation	GB
TMS-1	3×10^{14}	20 μm	-	$\approx 10^{14}$	$\approx 10^{13}$
TMS-2	1×10^{15}	20 μm	-	$\approx 10^{15}$	$\approx 10^{13}$
TMS-3	1×10^{15}	2 μm	-	$\approx 10^{15}$	$\approx 10^{14}$
NFA-1	1×10^{15}	20 μm	$\approx 10^{16}$	$\approx 10^{15}$	$\approx 10^{13}$
NFA-2	1×10^{15}	2 μm	$\approx 10^{16}$	$\approx 10^{15}$	$\approx 10^{14}$

Table 2 Model Thermodynamic Parameters

Parameter		Value
Binding energy of He (s)	To dislocations (disl.)	0.9 eV
	To nm-scale features (NF)	0.59 eV
	To grain boundary (GB)	0.5 eV
	To disl. Intersection vs. disl.	0.6 eV
	To NF on disl. vs. disl.	0.6 eV
	To deep trap on GB vs. GB	0.6 eV
Binding energy of V	To NF	0.6 eV
Migration energy of	He(i) in matrix	0.08 eV
	He(s) in matrix	2.35 eV
	V in matrix	1.40 eV
	SIA in matrix	0.08 eV
	He(s) on dislocations	1.18 eV
	He(s) on GB	1.18 eV
Formation energy of	Vacancy	1.6 eV

Results and Discussion

Bubble nucleation of dislocations accompanied by division of the segments

The model predicts that dislocations play a dominant role in bubble formation. Figure 5a shows an example of the change in the dislocation segment length distribution as a function of dpa for the TMS model. The change in the distribution to a larger number of shorter segments becomes significant above about 10^{-3} dpa. Figure 5b shows the total number of segments, the number of segments carrying bubbles and the number of homogeneously nucleated bubbles plotted as a function of dpa for both the TMS and NFA models. In the TMS case, most of the bubbles nucleated homogeneously on dislocations at damage levels less than ≈ 0.01 dpa. The increase in the number of segments corresponds to the number of homogeneously nucleated bubbles. The number of segments increases by a factor of ≈ 3 saturating at ≈ 0.2 dpa. The bubbles formed by heterogeneous nucleation at a trap sites are reflected by the difference between the total bubble number density and of the number density of homogeneously nucleated bubbles,

which becomes moderately significant above ≈ 0.01 dpa. Figure 5c shows the bubble nucleation rates plotted as a function of dpa. Clearly, homogeneous nucleation is the dominant mechanism for bubble formation on dislocations. As shown in Figures 5b and d, similar behavior is observed in the NFA. However, in this case the dpa are shifted up by about an order of magnitude than for the TMS, and bubble nucleation continues up to several dpa. The delay in the dislocation bubble formation in NFA is largely due to the effect of He trapping by NFs, which are described in more detail in the following section.

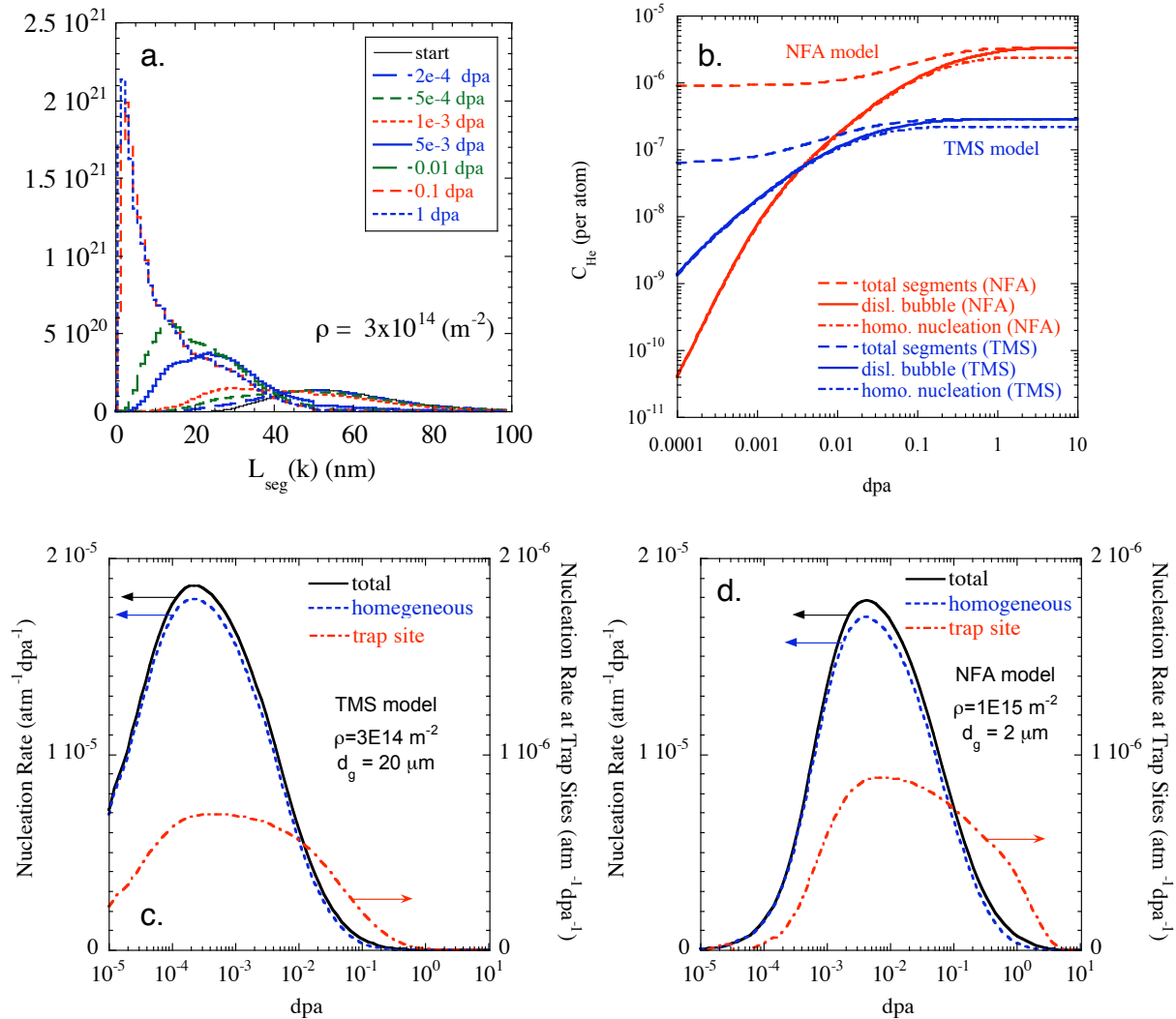


Figure 5 (a) Evolution of the dislocation segment length distribution, through 1 dpa of neutron irradiation with He generation at 10 appm He/dpa, in a TMS model with dislocation density of $3 \times 10^{14} \text{ m}^{-2}$, and (b) total number density of dislocation segments as well as that of He cluster carrying segments for both of TMS ($\rho = 3 \times 10^{14} \text{ m}^{-2}$) and NFA ($\rho = 1 \times 10^{15} \text{ m}^{-2}$) models.

He partitioning and bubble formation in the TMS models

Figure 6 shows He partitioning into subregions, represented in terms of both the He concentration per total number of atoms (Figure 6a, c, e) as well as per the number of atoms in the subregion (Figure 6b, e, f), which we refer to as “coverage” below, for TMS models with various dislocation densities (ρ) and grain diameters (d_g). Figures 6a-b, c-d and e-f show the results for $\rho = 3 \times 10^{14} \text{ m}^{-2}$ and $d_g = 20 \mu\text{m}$, $\rho = 10^{15} \text{ m}^{-2}$

and $d_g = 20 \mu\text{m}$, and $\rho = 10^{15} \text{ m}^{-2}$ and $d_g = 2 \mu\text{m}$, respectively. For this range of parameters, the He largely partitions to dislocations. Starting at a dose and He level lower than 10^{-5} dpa and 4×10^{-4} appm He, essentially all of the He partitions to dislocations, as shown by the red solid lines in Figures 6a, c, e. Most the He is in the form of single atoms spread over dislocation segments up to a dose of $\approx 2 \times 10^{-5}$ and 5×10^{-5} dpa, respectively, for $\rho = 3 \times 10^{14} \text{ m}^{-2}$ and $\rho = 10^{15} \text{ m}^{-2}$. Dislocation bubbles nucleate both homogeneously and heterogeneously at higher doses. Both the He_s and He_i reach a quasi-steady state concentration after $\approx 10^{-5}$ dpa at $\approx 10^{-10}$ and 10^{-20} , respectively.

Matrix bubble nucleate at a low rate by $\text{He}_s + \text{He}_s$ reactions. In rough proportion the total He in both cases. He_i is immediately partitioned to all the subregions and bubble sites. He partitioning to GBs is strongly affected by grain size. In the case of $d_g = 20 \mu\text{m}$, the partitioning to GBs is roughly constant up to ≈ 0.01 dpa, followed by a gradual increase. For the $d_g = 2 \mu\text{m}$ case, He partitioning increases more rapidly above 10^{-4} dpa, so that about 10^3 times more He accumulates at GBs than for the case with $d_g = 20 \mu\text{m}$. As shown below in the bubble size and number density trends, the rapid increase in partitioning to GB is due to by bubble nucleation and growth as early as 0.001 dpa for the case with $d_g = 2 \mu\text{m}$, due to the fact that bubbles are permanent traps for He. The resulting saturation GB He coverage are $\approx 10^{-7}$ and $\approx 10^{-5}$ for $d_g = 20 \mu\text{m}$ and $d_g = 2 \mu\text{m}$, respectively.

Figure 7 summarizes the number density and average size (radius) of the bubbles in each sub-region as a function of dpa for all the TMS models. The plots also include the measurements from He implanter experiments performed for F82H mod.3 in both the as tempered and 20% cold worked conditions. The bubble number density and average size in the model for low and high dislocation density shows reasonably good agreement with the experimental data obtained for both of these conditions. The dominance of bubble nucleation on dislocations predicted by the model is also consistent with experimental observations.

While the overall agreement between model and experiment is reasonably good, GB He bubble formation in the model somewhat underestimates the bubble formation observed on lath boundaries in the experiments. Changing the grain size in the model to the experimental lath size was a first-order approximation that demonstrated that the GB bubbles start forming and growing at very low dose. The 10^{-5} He coverage corresponds to one bubble containing ≈ 10 He atoms ($r_b = 0.3 \text{ nm}$) in every $\approx 4 \times 10^4 \text{ nm}^2$. The bubble density on boundaries have not been quantified, but appears to be qualitatively larger than the model predictions. The predicted size of the bubbles is smaller than those that are observed. Future refinements of our model will include more appropriate treatment of the lath boundaries.

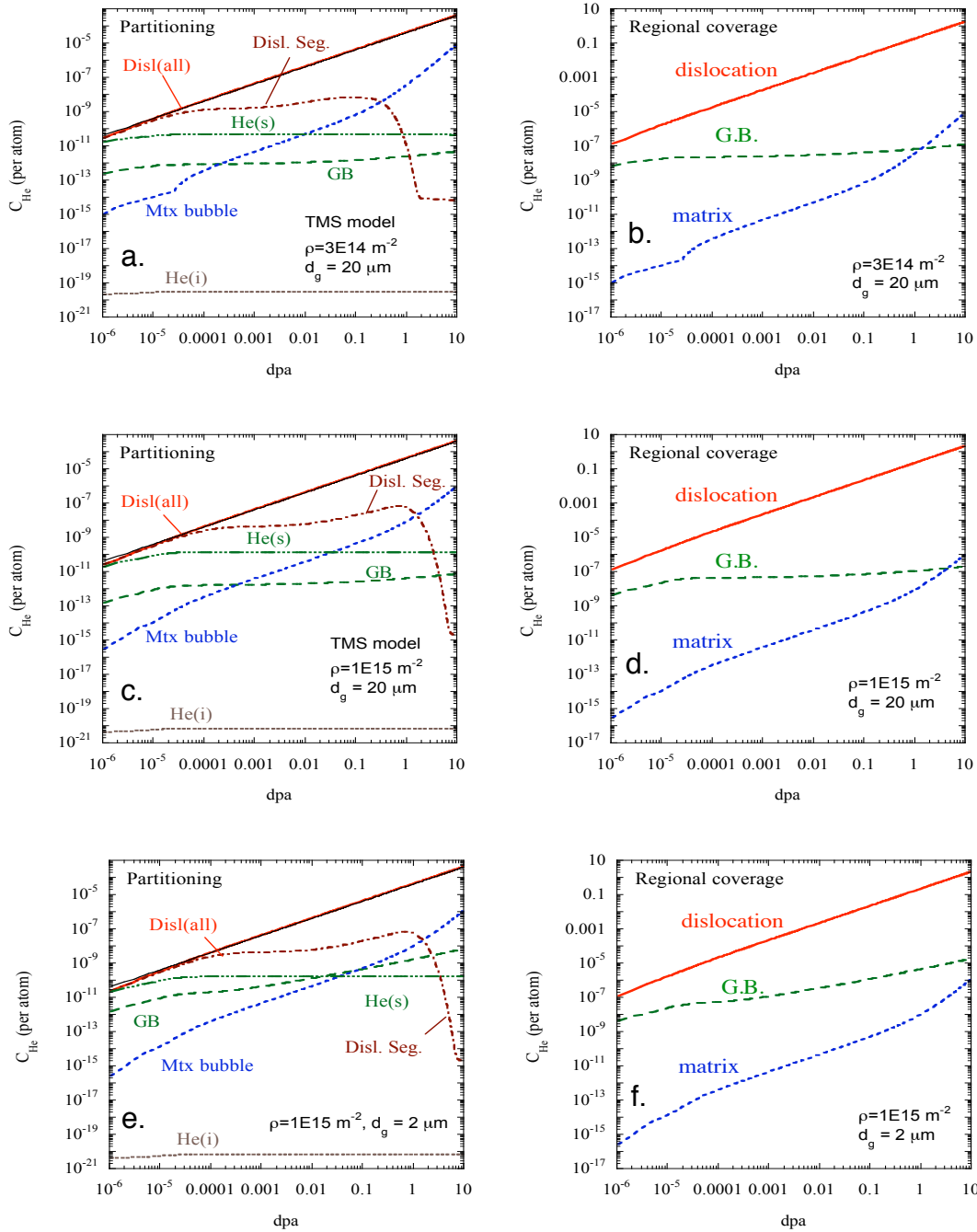


Figure 6 He partitioning into subregions, in terms of He concentration per total atoms ((a), (c) and (e)) as well as per subregion atoms ((b), (d), and (f)), referred as “coverage”, for TMS models with various dislocation densities (ρ) and grain diameters (d_g). (a) and (b) for $\rho = 3 \times 10^{14} \text{ m}^{-2}$ and $d_g = 20 \text{ }\mu\text{m}$, (c) and (d) for $\rho = 10^{15} \text{ m}^{-2}$ and $d_g = 20 \text{ }\mu\text{m}$, and (e) and (f) for $\rho = 10^{15} \text{ m}^{-2}$ and $d_g = 2 \text{ }\mu\text{m}$.

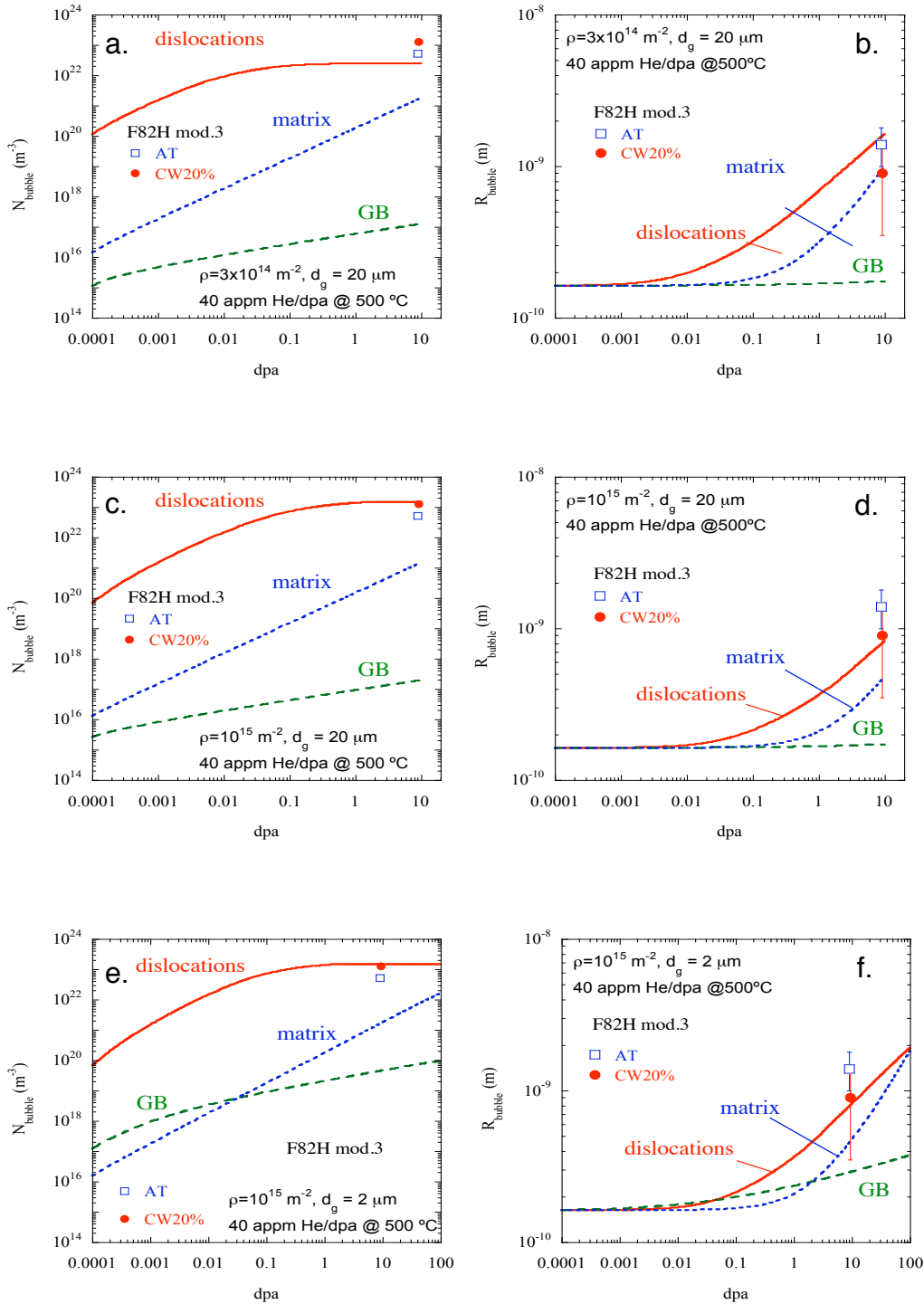


Figure 7 He bubble number density and average size (radius) in various sub-regions as a function of dpa for TMS models with various dislocation densities (ρ) and grain diameters (d_g). (a) and (b) for $\rho=3 \times 10^{14} \text{ m}^{-2}$ and $d_g = 20 \text{ }\mu\text{m}$, (c) and (d) for $\rho = 10^{15} \text{ m}^{-2}$ and $d_g = 20 \text{ }\mu\text{m}$, and (e) and (f) for $\rho=10^{15} \text{ m}^{-2}$ and $d_g = 2 \text{ }\mu\text{m}$, compared with the observation in He-implanter experiments on F82H mod.3 at as-tempered (AT) and 20% cold worked (CW20%) conditions.

He partitioning and bubble formation in the NFA models

Figure 8 shows He partitioning to and coverage of sub-regions in NFA models. Figures 8a-b and 8c-d are for coarse (20 μm) and fine (2 μm) grain size cases, respectively. The same NF size (radius), $r_{\text{NF}} = 1.5 \text{ nm}$ and number density, $N_{\text{NF}} = 7 \times 10^{23} \text{ m}^{-3}$ corresponding to a 1% NF volume fraction was used in all cases. In all the NFA models the NFs, are the highest density sink with a strength of $\approx 10^{16} \text{ m}^{-2}$. The NF play a significant role in collecting He. Up to $\approx 10^{-4}$ dpa the NFs collect $\approx 100 \%$ of the He, but at this point the He is mostly in the form of single atoms that are loosely bound and are emitted back to the matrix at a rate dictated by the binding energy of $E_{\text{bnf}} = 0.6 \text{ eV}$. The corresponding matrix He(s) and He(i) build up to the peak values of $\approx 10^{-9}$ and 10^{-21} , respectively, balancing the emission of trapped He from the NFs. The matrix He continues to flow to dislocations, matrix bubbles and GB subregions. Accelerated He collection starts once bubble formation becomes significant in these regions. Dislocations become the primary He collector around 10^{-3} dpa after both homogeneous and heterogeneous bubble nucleation have begun as shown in Figure 5d. Helium build-up in the other features slows down, and dislocations continue to collect most of the He up to ≈ 1 dpa. He bubbles start forming on NFs, which leads to accelerated He partitioning to that region around 0.01 dpa. He partitioning to NF catches up to dislocations at ≈ 10 dpa. Helium partitioning to matrix bubbles is low ($\approx 10^{-3}$ of the total He) because the other microstructural features more effectively collect He. Helium partitioning to GB is strongly affected by grain size, so that in the 2 μm grain size case partitioning to GBs is $\approx 3 \times 10^{-5}$ of the total He, which is $\approx 10^3$ times more than for the 20 μm grain size model. The resulting GB He coverage is $\approx 2 \times 10^{-5}$ and the average GB bubble radius is $\approx 0.25 \text{ nm}$. This suggests such a small, subvisible He bubbles in exist every $\approx 2 \times 10^4 \text{ nm}^2$.

Figure 9 shows the number density and radius of He bubbles formed in various sub-regions as a function of dpa. At 10 dpa, $\approx 72\%$ of the total bubbles formed on dislocations homogeneously as well as at trap sites that include dislocation intersections and NFs trapped on dislocations. About, $\approx 27\%$ of the bubbles formed on NFs in the matrix, and $\approx 1\%$ of the bubbles formed homogeneously in the matrix. A further break down for the dislocation bubbles are: $\approx 52\%$ as homogeneous; $\approx 12\%$ on NFs; and $\approx 8\%$ at intersections. Both NFs in the matrix and on dislocations assisted are sites for $\approx 39 \%$ of the bubble formation. Due to the high dislocation and the NF number densities, the He bubble number density was $\approx 4 \times 10^{23} \text{ m}^{-3}$ and the average bubble radius was $\approx 0.6 \text{ nm}$. The results for the NFA models are in very good agreement with the results obtained from the He implanter experiments.

Bubble Size Distribution

Figure 10a shows the bubble size distributions obtained from a TMS model with $\rho = 10^{15} \text{ m}^{-2}$ and $d_g = 20 \mu\text{m}$. The figure also shows experimental results for F82H mod.3 in the AT and 20%CW conditions. The microstructural parameters in this model better correspond to the 20%CW case. The results give only a single mode distribution since the current model does not include bubble to void transformation, whereas the experimental results shows a bimodal distribution with a lower number of larger voids. Nevertheless, the agreement of the model with the bubble part of the experimental results in the 20%CW case is excellent. Note that, the experimental TEM observations are only valid for bubbles larger than $\sim 1 \text{ nm}$ in diameter. Figure 10b shows the corresponding bubble distribution comparison for the NFA model with $\rho = 10^{15} \text{ m}^{-2}$ and $d_g = 2 \mu\text{m}$ and the experimental results for NFA MA957 and 12YWT at the corresponding condition. With no bubble to void transformation observed in these alloys, the model shows even better agreement with experiment.

First Order Estimates of Void Growth in the TMS model

While the current model does not include an algorithm to deal with bubble-to-void transformation, the experimental bubble distribution shown in Figure 10a, after 5 dpa of irradiation, includes a population of large bubbles exceeding the critical size, which assures their continued growth by absorbing excess vacancies. The large bubbles were manually separated from the distribution obtained at 1 dpa, and

grown as voids at a rate dictated by the excess vacancy flux in the model. Figure 11 shows the results of the void growth and estimation of swelling of the F82H mod.3 steel. This result suggests that a few percent swelling may occur in a TMS steel at 100 dpa with the assistance of He. Future models will directly incorporate the critical bubble void nucleation and growth.

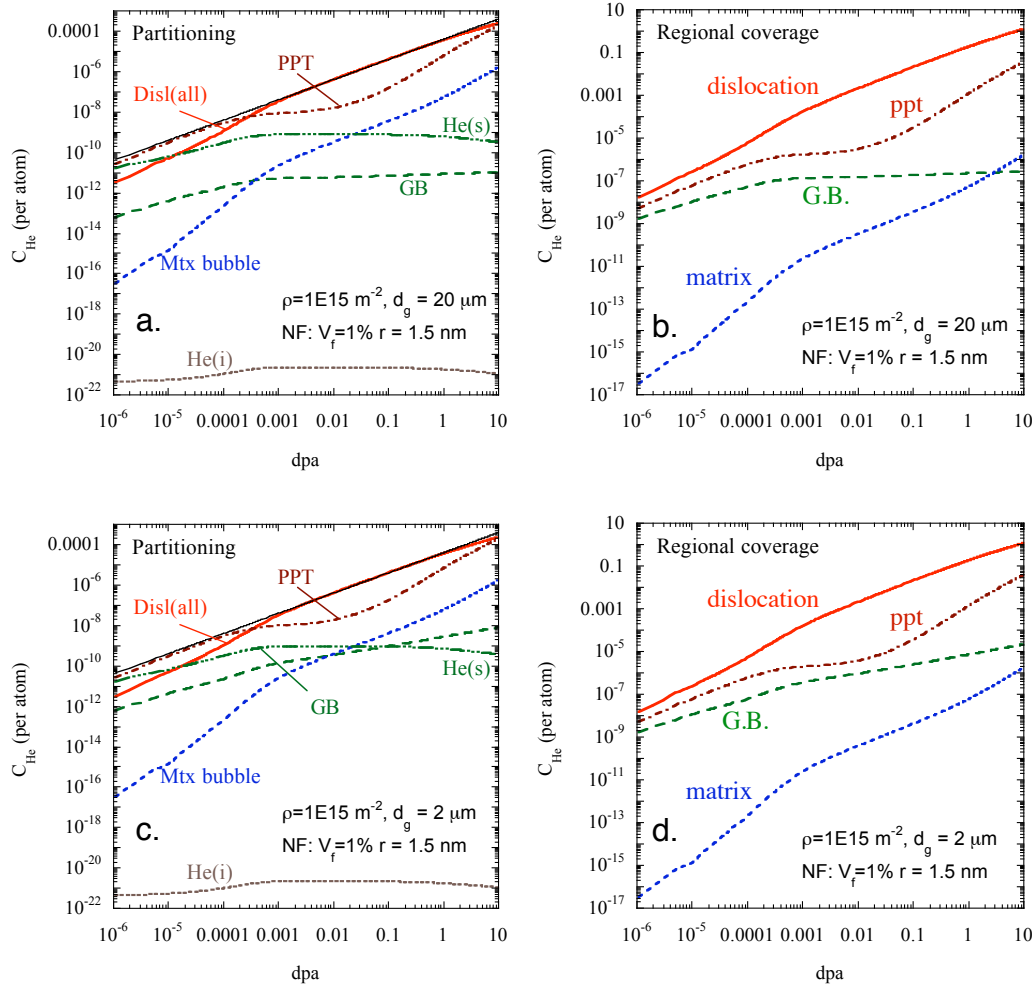


Figure 8 He partitioning and He coverage of subregions for NFA models with two grain sizes, $d_g = 20 \mu\text{m}$ (a, b) and $d_g = 2 \mu\text{m}$ (c, d).

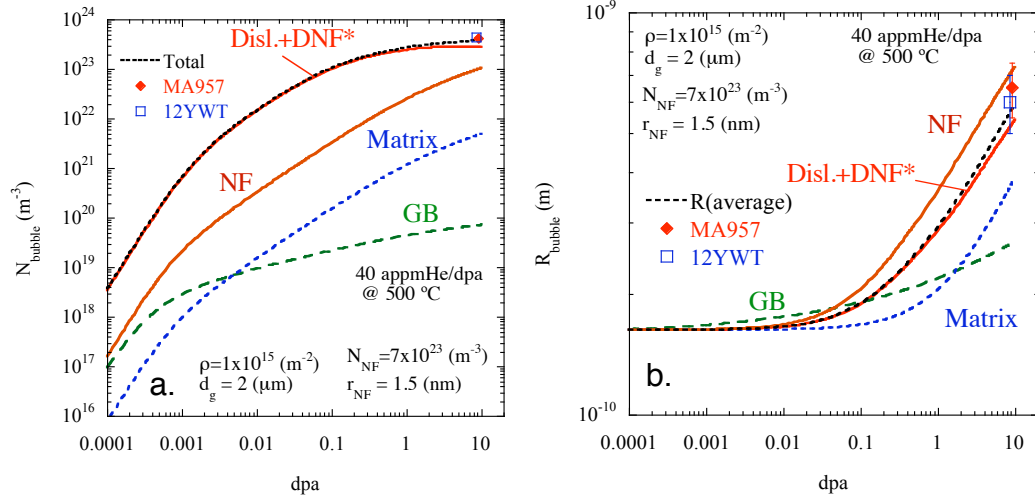


Figure 9 Number density and size of He bubbles in the NFA model with grain size of $d_g = 2 \mu\text{m}$, compared with the observation in He-implanter experiments on two NFAs, MA957 and 12YWT.

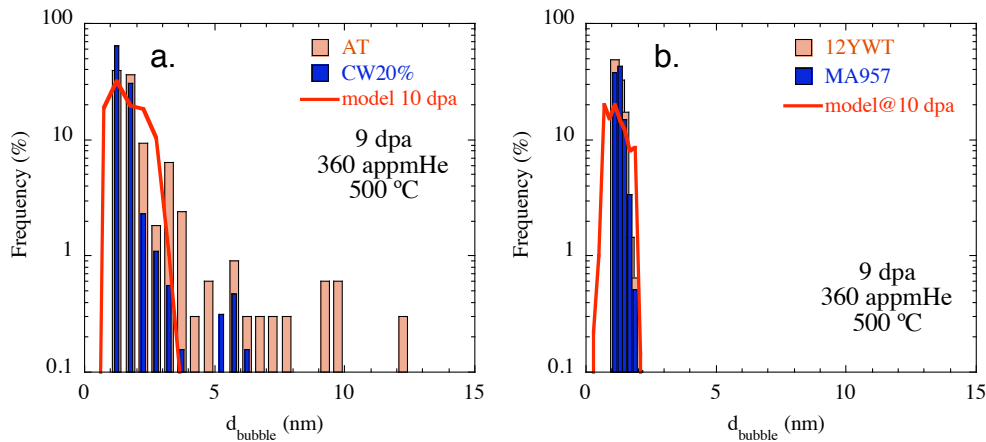


Figure 10 Bubble size distributions by TMS and NFA models with experimental observations in comparable alloy and irradiation conditions.

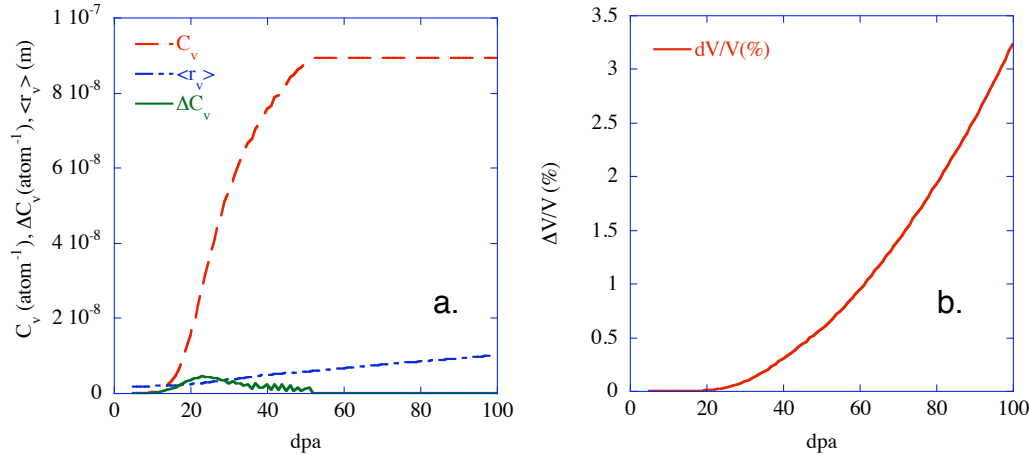


Figure 11 First order estimates of void growth in the TMS model with $\rho=10^{15} \text{ m}^{-2}$ and $d_g = 2 \text{ }\mu\text{m}$; (a) void number density, C_v , nucleation, ΔC_v , and average radius, $\langle r_v \rangle$, and (b) swelling as a function of dpa.

Future Research

Refinement of the model to treat lath boundaries and to integrate bubble to void conversion and void growth models will be carried out during the current reporting period.

References

1. Y. Dai, G. R. Odette, T. Yamamoto, *The Effects of helium on irradiated structural alloys (2011) in press.*
2. T. Yamamoto, G.R. Odette, H. Kishimoto, J-W. Rensman, P. Miao, *J. Nucl. Mater.* **356** (2006) 27.
3. G.R. Odette, T. Yamamoto, H.J. Rathbun, M.Y. He, M.L. Hribernik, J.W. Rensman, *J. Nucl. Mater.* **323** (2003) 313.
4. T. Yamamoto, Y. Dai, G. R. Odette, M. Salston, P. Miao, *Trans. American Nuclear Society*, 98 (2008) 1111.
5. T. Yamamoto, G.R. Odette, P. Miao, D. T. Hoelzer, J. Bentley, N. Hashimoto, H. Tanigawa, R. J. Kurtz, *J. Nucl. Mater.* 367 (2007) 399.
6. G.R. Odette, M.J. Alinger, and B.D.Wirth, *Annu. Rev. Mater. Res.* 38 (2008)471.
7. G.R. Odette, P. Miao, D.J. Edwards, T. Yamamoto, R. J. Kurtz, Y. Tanigawa, *J. Nucl. Mat.* (2010) in press.
8. B.D. Wirth, G.R. Odette, J Marian et al., *J. Nucl. Mater.* 329-333 (2004) 103
9. R.J. Kurtz and H. L. Heinisch, *J. Nucl. Mater.* 329-333 (2004) 1199-1203.
10. R.J. Kurtz, H.L. Heinisch and F. Gao, *J. Nucl. Mater.* 382 (2008) 134.
11. H. L. Heinisch, F. Gao, R.J. Kurtz, E. A. Le, *J. Nucl. Mater.* 351 (2006) p141-148.
12. H. L. Heinisch, F. Gao, R.J. Kurtz, *Phil. Mag.* 90 (2010) 885.
13. F. Gao, H. L. Heinisch, R. J. Kurtz, *J. Nucl. Mater.* 351(2006) 133-140.
14. F. Gao, H. L. Heinisch, R. J. Kurtz, *J. Nucl. Mater.* 367-370(2007) 446-450.
15. F. Gao, H. L. Heinisch, R. J. Kurtz, *J. Nucl. Mater.* 386-388 (2009) 390-394.

16. L. Ventelon, B. Wirth, C. Domain, *J. Nucl. Mater.* 351 (2006) 119–132.
17. Jae-Hyeok Shim, Sang Chul Kwon, Whung Whoe Kim, Brian D. Wirth, *J. Nucl. Mater.* 367-370 (2007) 292-297.
18. R.E. Stoller, G.R. Odette, *J. Nucl. Mater.* 131 (1985) 118.
19. C. C. Fu, F. Willaime, *Phys Rev. B* 72, 064117(2005).
20. K. Morishita, R. Sugano, B.D. Wirth, T. D. de la Rubia, *Nuclear Instruments and Methods in Physics Research B* 202 (2003) 76–81.
21. T. Yamamoto, G. R. Odette, L. R. Greenwood, *Fusion Materials Semiannual Report 1/1 to 6/30/2005* DOE/ER-313/38 (2005) 95.
22. R.J. Kurtz, G.R. Odette, T. Yamamoto, D.S. Gelles, P. Miao, B.M. Oliver, *J. Nucl. Mater.* 367-370, 417 (2007).
23. T. Yamamoto, G.R. Odette, P. Miao, et al., *J. Nucl. Mater.* 386-388 (2009) 338.

6.4 FIRST-PRINCIPLES INVESTIGATION OF THE INFLUENCE OF ALLOYING ELEMENTS ON THE ELASTIC AND MECHANICAL PROPERTIES OF TUNGSTEN— G. D. Samolyuk, Y. N. Osetskiy, and R. E. Stoller (Oak Ridge National Laboratory)

OBJECTIVE

The objective of this research is to support possible approaches to the design of ductile tungsten alloys through the use of relevant *ab initio* electronic structure calculations.

SUMMARY

The equilibrium lattice parameter, elastic constants and phonon dispersions were calculated for a set of binary $W_{1-x}Tm_x$ alloys with different transition metal, Tm, concentrations within the local density approximation of density functional theory. Reasonable agreement between results obtained using conventional super-cell and virtual crystal approximation approaches has been demonstrated. Alloying W with transition metals with larger number of d-electrons changes the symmetry of the core of a dislocation from symmetric to asymmetric and reduces the value of the Peierls barrier.

PROGRESS AND STATUS

Introduction

The alloys of W with Re have been studied extensively using both experiment [1, 2] and theory [3, 4, 5]. Adding Re has the effect of ductility improvement of the tungsten. In [5] it was demonstrated using first principles calculations that addition of Re in tungsten modifies the symmetry properties of $\frac{1}{2}\langle 111 \rangle$ screw dislocations and reduces the value of the Peierls barrier. In the present research we investigate the properties of screw dislocations in binary $W_{1-x}Tm_x$ using first-principles electronic structure calculations for a set of transition metals, (Tm). This result will be used in a future search for alloying elements causing changes in tungsten alloys properties similar to the effects of Re.

Formalism

We calculated the electronic structure within the local density approximation of density functional theory (DFT) using the quantum espresso package [6]. The calculations have been done using a plane-wave basis set and ultrasoft pseudo-potential. The Brillouin zone (BZ) summations were carried out over a $24 \times 24 \times 24$ BZ grid for the system with one unit cell and $16 \times 16 \times 16$ grid for the supercell, representing $2 \times 2 \times 2$ unit cells, with Gaussian boarding of 0.02 Ry. The plane wave energy cut off at 42 Ry allows accuracy of 0.2 mRy/atom. As a realization of VCA for the pseudo potential method we used the scheme proposed in Ref. [7]. The elastic constants were calculated from the total energies obtained for the set of unit cell deformations [8].

A periodic quadrupole arrangement of $\frac{1}{2}\langle 111 \rangle$ screw dislocation was used to describe the core structure and Peierls barrier. Two dislocations with opposite Burgers vectors were placed in a super cell containing 135 atoms with lattice vectors $\mathbf{b}_1=9(\mathbf{u}_1+\mathbf{u}_2+\mathbf{u}_3)/2$, $\mathbf{b}_2=5\mathbf{u}_2$ and $\mathbf{b}_3=\mathbf{u}_3$, where vectors $\mathbf{u}_1=\langle 112 \rangle$, $\mathbf{u}_2=\langle 110 \rangle$ and $\mathbf{u}_3=\langle 111 \rangle/2$. The BZ summations were carried out over a $1 \times 1 \times 3$ BZ grid. It was demonstrated that the increase of BZ grid to $1 \times 2 \times 6$ changes the value of the Peierls barrier by 7%. The Peierls barrier in $W_{1-x}Tm_x$ was obtained by moving a $\frac{1}{2}\langle 111 \rangle$ dislocation from easy to hardcore configurations. The alloying was modeled using the virtual crystal approximation (VCA).

Results

The applicability of the virtual crystal approximation to $W_{1-x}Re_x$ binary alloys was verified in our previous research, see [9]. Also, it was demonstrated that the so called rigid band approximation can be applied. Thus, all dilute tungsten based alloys with the same number of electrons per atom (e/a) have the same elastic constants. The concentration of different alloying elements which give the same (e/a) value can be calculated through the simple expression

$$x = \frac{(e/a)}{Z - Z_W}, \quad (1)$$

where Z is the number of valence electrons of the alloying transition metal atom and Z_W of tungsten. The calculated elastic properties reproduce experimental data for the $W_{1-x}Re_x$ alloy within 10% accuracy; see [9] and results presented in Table 1.

The result for elastic constants and lattice parameter calculated in both supercell and VCA approaches are summarized in Table 1 and Figure 1. As the d band is filled by addition of the transition metal, the lattice parameter decreases and elastic anisotropy $A=C_{44}/C'$ increase [10], see Figure 1.

Table 1. Experimental (first row) and calculated lattice parameter (a) in a.u., bulk modulus (B), elastic constants (C_{ij}) in GPa in alloy $W_{1-x}Tm_x$, where Tm – transition metal and x is concentration.

Tm	x	a	B	C'	C_{44}	C_{11}	C_{12}
experiment [2]							
W	0.0	5.9827	314.0	164.0	163.0	533.0	205.0
calculated, virtual crystal approximation (VCA)							
Re	0.0	6.0288	307.1	160.4	141.1	520.9	200.2
	0.03	6.0244	306.1	156.0	142.0	514.0	202.1
	0.05	6.0218	305.5	153.1	142.9	509.6	203.4
	0.0625	6.0201	305.2	151.3	143.5	506.9	204.3
	0.10	6.0152	303.8	146.0	144.6	498.5	206.5
	0.30	5.9883	296.0	130.0	155.6	469.3	209.4
Zr	1.00	5.9181	338.3	-30.3	162.9	298.0	358.5
	0.025	6.0650	291.0	160.9	135.6	506.9	204.3
Ta	0.0625	6.0650	278.8	152.9	1.387	482.7	176.9
	0.0625	6.0370	306.1	161.2	136.4	521.0	198.7
Fe	0.05	6.0350	305.0	161.8	137.2	520.7	197.2
	0.025	6.0186	293.0	148.0	135.5	490.3	194.4
Ru	0.0625	6.0103	273.3	131.8	128.3	449.0	185.4
	0.025	6.0180	302.2	152.8	141.3	505.9	200.3
Os	0.0625	6.0040	298.0	142.4	142.2	487.9	203.1
	0.025	6.0210	305.3	153.1	142.8	509.4	203.3
Rh	0.0625	6.0110	306.0	143.3	146.3	497.0	210.5
	0.0167	6.0180	301.7	152.6	140.9	505.2	200.0
Ir	0.0625	5.9923	287.9	135.4	141.2	478.5	207.7
	0.0167	6.0186	304.3	153.5	143.2	509.0	201.9
	0.0625	5.9973	294.6	147.3	148.1	478.3	202.7
calculated, super cell (SC) 2x2x2							
W_{16}	0.00	6.0275	300.1	156.6	139.1	511.8	202.9
$W_{15}Ta$	0.0625	6.0402	305.0	156.5	135.0	498.2	185.1
$W_{15}Re$	0.0625	6.0205	305.5	149.9	143.1	498.9	199.1
$W_{15}Fe$	0.0625	5.9934	299.0	139.5	132.0	484.9	206.0
$W_{15}Zr$	0.0625	6.0616	311.6	150.4	126.9	512.1	211.3

The agreement between elastic constants calculated within VCA and super cell approaches is quite reasonable, with the largest difference observed for C_{44} in alloy with concentration 0.0625 of Zr. For the other elements the agreement is within 15%.

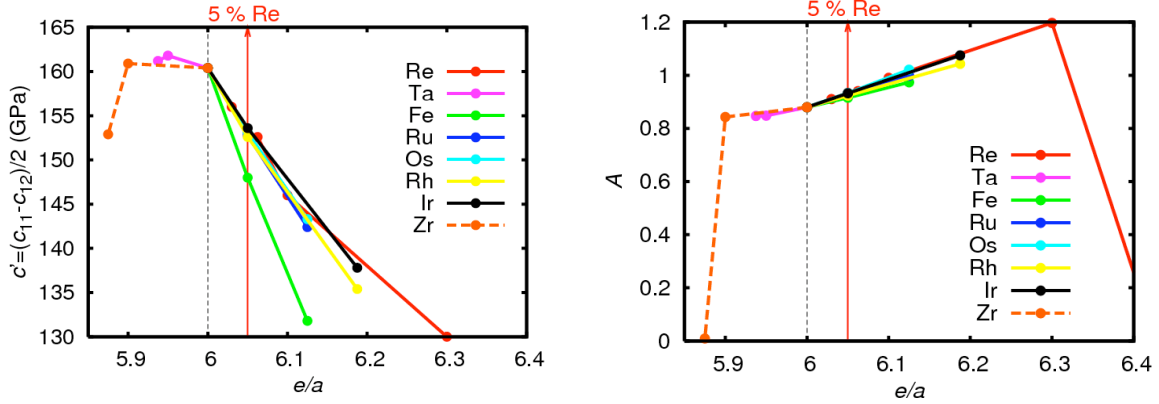


Figure 1. Elastic constant C' and elastic anisotropy, A , calculated by VCA for the set of transition metals as a function of number of electrons per atom.

As it can be seen the C' and A values demonstrate very close dependence on concentration if they are plotted as a function of (e/a), the number of electrons per atom. This similarity supports conclusion that the main effect of alloying W with transition metals with larger number of d electrons is related to d band filling. The alloying with Zr or Ta gives a reduction of (e/a) value and this increases values of C' .

The calculated structure of the easy core configuration of a $1/2\langle 111 \rangle$ dislocation is shown on Figure 2 for pure W, $W_{0.9}Re_{0.1}$ and $W_{0.95}Fe_{0.05}$, where concentrations of transition metals were chosen to give the same (e/a) value. The circles on Fig. 2 represent W atoms looking in the $\langle 111 \rangle$ direction and the structure of dislocation is illustrated by differential displacement maps [11]. It should be mentioned that for tungsten alloys with other Tm with the same (e/a) value the core configurations are the same as for Re and Fe alloys but are not shown here. As was demonstrated in [5] for W a symmetric core is obtained, i.e. the dislocation expands equally along the six $\langle 112 \rangle$ directions.

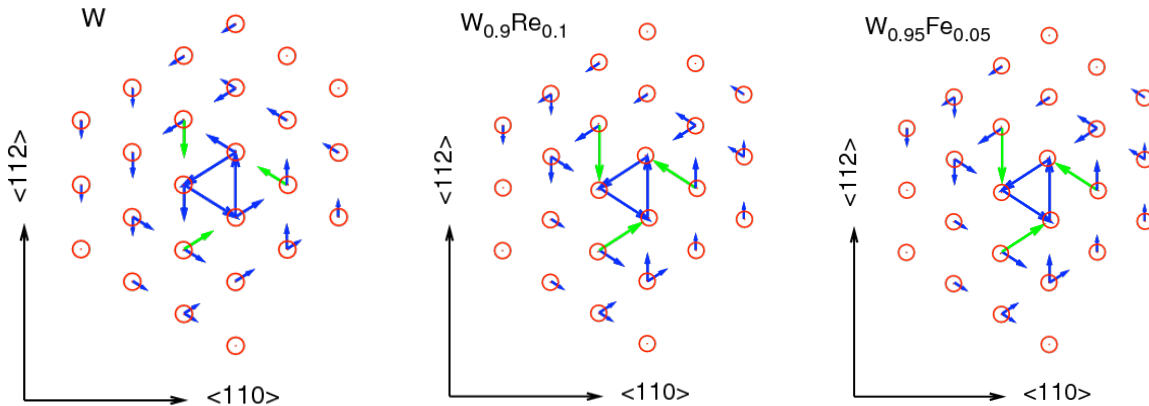


Figure 2. The easy core dislocation structure in $W_{1-x}Tm_x$ calculated in VCA.

Alloying with Re or any other Tm with the same value of (e/a) leads to change from a symmetric core structure to an asymmetric structure. We observed this core symmetry transition for Re concentration starting at 10 %, whereas Ref. [5] reported this transition at larger concentrations. As was mentioned in Ref [5], the transition from symmetric to asymmetric cores changes the dislocation slip plane. The symmetric core dislocations move uniformly on $\{110\}$ planes; asymmetric ones move in a zigzag manner [12] and the slip plane changes to $\{112\}$.

Along with the change of core symmetry the value of the Peierls barrier changes, see Fig. 3. As can be seen, alloying with Re, Os, Ir, Ru, or Rh with concentration which corresponds to (e/a)=6.05 reduces the barrier by 10%. Fe reduces the Peierls barrier even more significantly, whereas Zr increases the barrier and makes the tungsten alloy more brittle.

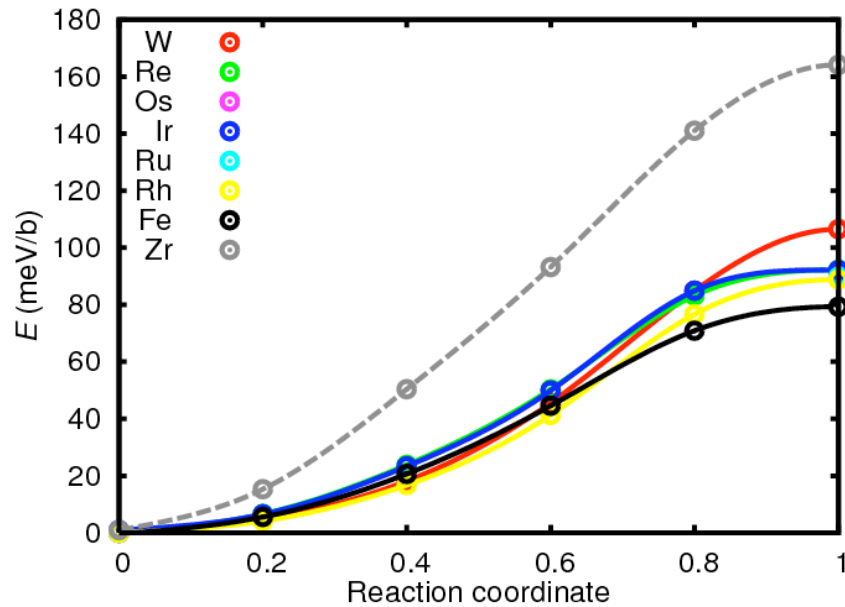


Figure 3. Calculated Peierls barrier in $W_{1-x}Tm_x$.

Thus it may be concluded that alloying tungsten with any group VIIA to VIIIA elements leads to similar modifications of dislocation core structure and reduction of the Peierls barrier.

References

- [1] S. J. Zinkle, "Thermomechanical Properties of W-Re Alloys & Initial Survey of Molten Tin Corrosion Data," presented at APEX Study Meeting UCLA, November 2-4, 1998.
- [2] R. A. Ayres, G. W. Shanette, and D. F. Stein, "Elastic Constants of Tungsten-Rhenium Alloys from 44 to 298 K," *J. Appl. Phys.* 46, 1528, 1974.
- [3] K. Persson, M. Ekman, and G. Grimvall, "Dynamical and Thermodynamical Instabilities in the Disordered Re_xW_{1-x} System," *Phys. Rev. B* 60, 9999, 1999.
- [4] M. Ekman, K. Persson, and G. Grimvall, "Phase Diagram and Lattice Instability in Tungsten-Rhenium Alloys," *J. Nucl. Mater.* 278, 273, 2000.
- [5] L. Romaner, C. Ambrosch-Draxl, and R. Pippan, "Effect of Rhenium on the Dislocation Core Structure in Tungsten," *Phys. Rev. Lett.* 104, 195503, 2010.
- [6] P. Giannozzi, S. Baroni, N. Bonini, "QUANTUM ESPRESSO: A Modular and Open-Source Software Project for Quantum Simulations of Materials," *J. Phys.: Condens. Matter* 21, 395502, 2009.
- [7] N. J. Ramer and A. M. Rappe, "Virtual-Crystal Approximation that Works: Locating a Compositional Phase Boundary in $Pb(Zr_{1-x}Ti_x)O_3$," *Phys. Rev. B* 62, R743, 2000.
- [8] M. J. Mehl, et al., *Phys. Rev. B* 41, 10311, 1990.
- [9] R. A. Ayres, G. W. Shannette, and D. F. Stein, *J. Appl. Phys.* vol. 46, p. 1526 (1976).
- [10] G. D. Samolyuk, Y. N. Osetskiy, and R. E. Stoller, "First-Principles Investigations of the Influence of Alloying Elements on the Elastic and Mechanical Properties of Tungsten," Fusion Materials Semiannual report, June 30, 2010, pp. 96-101.
- [11] V. Vitek, *Cryst. Lattice Defects* 5, 1, 1974.
- [12] J. P. Hirth and J. Lothe, *Theory of Dislocation* (Wiley-Interscience, New York, 1982).

7.1 IRRADIATION TEMPERATURE DETERMINATION OF HFIR TARGET CAPSULES USING DILATOMETRIC ANALYSIS OF SILICON CARBIDE MONITORS

— T. Hirose, N. Okubo, H. Tanigawa (Japan Atomic Energy Agency), Y. Katoh, A.M. Clark, J.L. McDuffee, D.W. Heatherly, R.E. Stoller (Oak Ridge National Laboratory)

OBJECTIVE

The objective of this work is to determine the irradiation temperatures of the HFIR target capsules JP-26 and JP-27, which were conducted under the Collaboration on Fusion Materials between Japan Atomic Energy Agency and the US DOE.

SUMMARY

The irradiation temperatures of the HFIR target capsules JP-26 and JP-27 were determined by dilatometric analysis of silicon carbide (SiC) passive temperature monitors. The monitors from holders for SSJ3 tensile specimens demonstrated good agreement with the design temperatures derived from finite element model (FEM) analysis and were consistent with post-irradiation hardness of F82H. Although the irradiation temperatures for some bend-bar (PCCVN and DFMB) holders were higher than FEM analysis, hardness tests on irradiated F82H implied that actual irradiation temperatures were close to the design temperatures.

PROGRESS AND STATUS

Introduction

Previous work demonstrated that dilatometry-based passive thermometry is invaluable to determine irradiation temperature as well as the more commonly used resistivity-based passive thermometry [1]. This method was employed to determine the irradiation temperature, T_{irr} of non-instrumented target capsules JP-26 and JP-27 irradiated in the flux trap region of the HFIR reactor. These experiments were carried out within the framework of the JAEA- US DOE Collaboration on Fusion Materials, Annex I, which was started in its fourth phase [2, 3, 4]. In that phase, four target capsules, JP-26, JP-27 JP-28 and JP-29 were developed to evaluate irradiation response of reduced activation ferritic/martensitic steel. Specimen holders for these capsules have the common design and have been irradiated at the same T_{irr} with several dose levels. It is an important objective of these experiments to evaluate effects of heat treatment and additional minor elements on irradiation hardening, which strongly depends on T_{irr} , in reduced activation ferritic/martensitic steel, F82H. Therefore it is necessary to determine the T_{irr} to clarify the effects of the modifications. Since irradiation hardening has been evaluated for F82H irradiated in JP-26 and JP-27, the T_{irr} from the dilatometric analysis is discussed along with the hardening [5].

Experimental Procedure

The material of the temperature monitor was chemically-vapor-deposited (CVD) SiC manufactured by Rohm & Haas Advanced Materials. The SiC passive temperature monitor has rectangular shape and its dimensions are summarized in Table 1. The passive temperature monitor was irradiated in the target capsule JP-27. JP-27 consists of sixteen specimen holders designed to accommodate six types of specimens and irradiate them at 300, 400 and 500°C. Specimen holders have common design, and the details are presented elsewhere [2, 3]. The target capsule JP-26 was irradiated in the target region of the HFIR from cycle 398 to 402, and JP-27 was from cycle 400 to 412. The irradiation of JP-27 was interrupted for 1.5 year between cycle 407 and 409 due to installation of cold neutron source. The dilatometry was conducted up to 1000°C at a constant ramp rate of 2.5°C /minute using Workhorse TM I dilatometer system, Anter Corporation. The temperature monitor was placed in an upright position between a stage and a dilatometer probe made of silica. The shorter monitors, SSJ3 and DFMB were

placed on an extra spacer of aluminum oxide. Difference between initial heating and cooling curves were calculated to clarify inflection due to defect annealing.

Table 1: Dimensions of SiC passive temperature monitors.

Specimen type	Thickness (mm)	Width (mm)	Length (mm)
SSJ3	0.482	2.99	15.1
PCCVN	0.482	3.11	35.8
DFMB	0.482	3.11	18.1

The irradiation temperature, T_{irr} was defined as an intersection of trend lines before and after deflection. Otherwise, it was defined as the point the slope in the derivative of the differential turned negative.

Results and Discussions

Typical length-temperature plots of SSJ3 type temperature monitor are shown in [Figure 1](#). The temperature monitor exhibited a deflection around the T_{des} due to defect annealing. The slope (black cross), defined as derivative of the differential length change, decreased and approached $-5 \times 10^{-6} / ^\circ\text{C}$. The T_{irr} and the onset of defect annealing were 317°C , which was very close to the T_{des} , 314°C . [Figure 2](#) shows a result of length-temperature plots of PCCVN type temperature monitor. As shown in this figure, it is difficult to determine a linear fitting after recovery due to gradual deflection. Therefore T_{irr} was determined as the point where the slope turned negative. This gradual deflection was observed in most of monitors for PCCVN. [Figure 4](#) shows hardness distribution over the length of PCCVN bend-bar specimen irradiated in JP-27. The length of PCCVN is 36 mm and it is much longer than the others. The hardness has a peak at the middle of the length in most of specimen, though neutron flux decreases with a distance from the reactor midplane. It implies lowest T_{irr} at the middle, where is analyzed using FEM. Therefore the inhomogeneous hardness distribution is due to temperature distribution. From these results, it is considered the gradual deflection was caused by temperature distribution over the length of the holder.

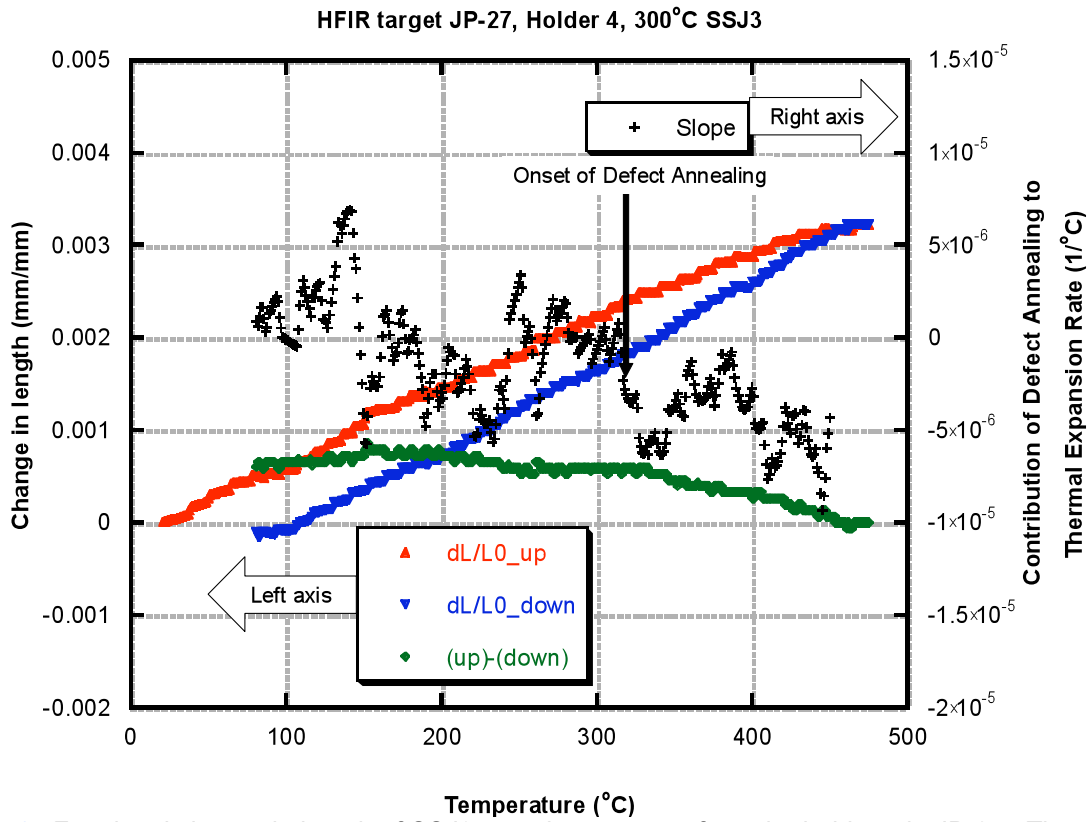


Figure 1. Fractional change in length of SSJ3 type thermometer from the holder 4 in JP-27. The nominal T_{irr} is 300°C.

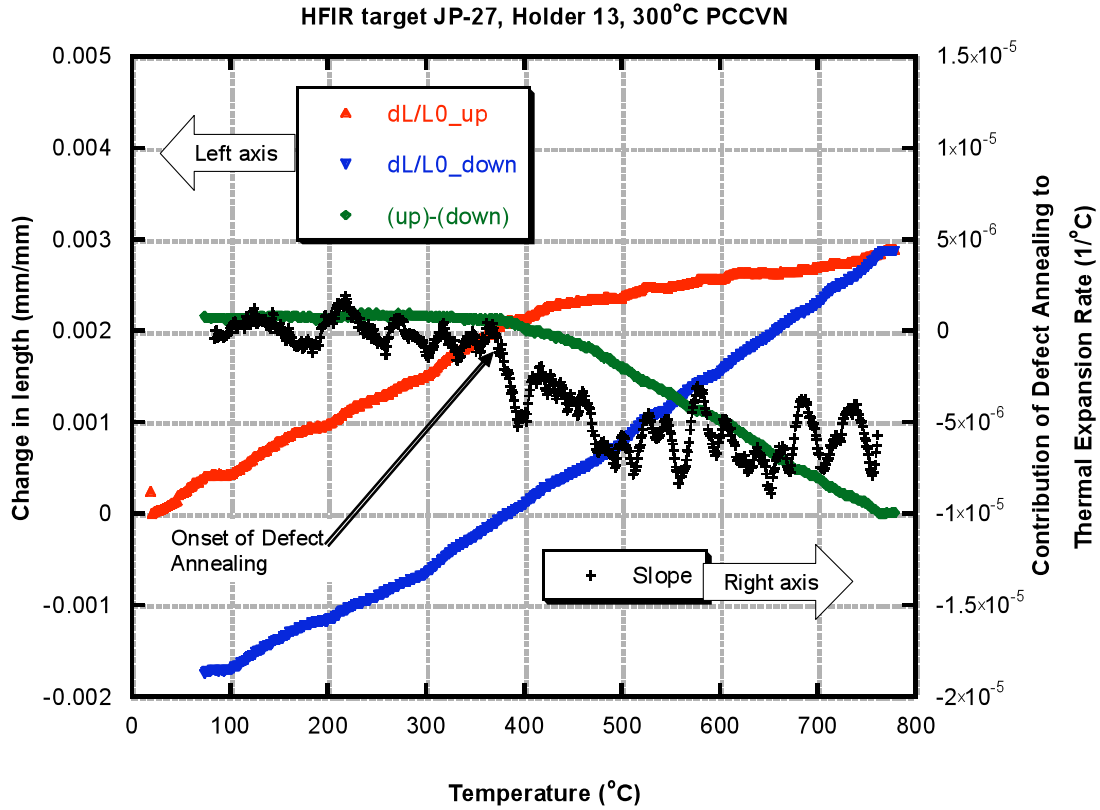


Figure 2. Fractional change in length of PCCVN type thermometer from the holder 13 in JP-27. The nominal T_{irr} is 300°C.

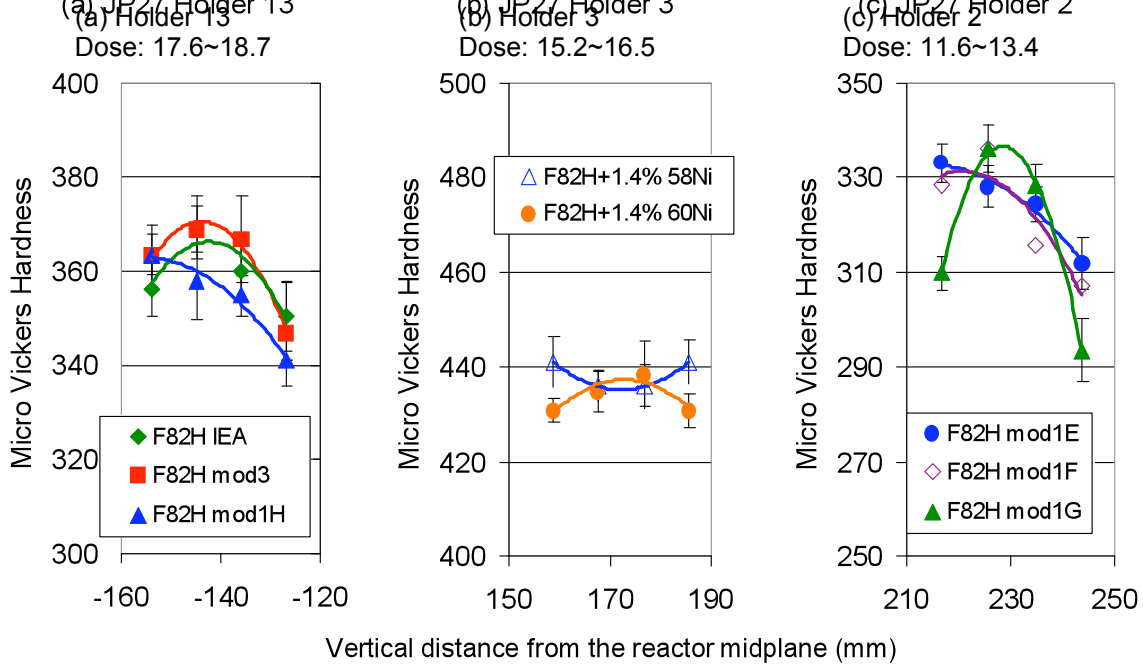


Figure 4. Hardness distribution over length of PCCVN specimen of F82H irradiated in the holder 13 in JP-27. (a) holder 13, (b) holder 3 and (c) holder 2. The nominal T_{irr} is 300°C.

The results of dilatometer analysis are summarized in Table 2. A couple of measurements were conducted on the holder 4, 6 and 11 in JP-27, and the results demonstrated good reproducibility. It is considered that the results are consistent with the design temperature, because it is anticipated that $\pm 20^{\circ}\text{C}$ of error range is included in determining irradiation temperature using dilatometric analysis [1]. The temperature monitors from SSJ3 holders showed good agreement with the T_{des} for various T_{irr} and dose levels. However, it is obvious that the T_{irr} of PCCVN holder has large uncertainty. T_{des} of PCCVN holder was defined at the vertically middle position. Therefore it is considered that this uncertainty is due to temperature gradient in its length direction. Figure 5 shows micro Vickers hardness of F82H and its variants irradiated at nominal $T_{\text{irr}} = 300^{\circ}\text{C}$ in JP-27. The specimens were prepared from the same materials, and the difference in hardness simply depends on the T_{irr} . It is reported that irradiation hardening of F82H-IEA irradiated in holder 4 showed good agreement with some reference work [5, 6]. Therefore it is assumed that T_{irr} of holder 4 was close to the T_{des} . A dilatometry on holder 3 demonstrated 40°C higher T_{irr} than T_{des} . Nickel doped F82H irradiated in holder 3 demonstrated less hardening than that in holder 4, and it is consistent with the dilatometric analysis. In contrast, an inconsistency was found between holders 4 and 13. Dilatometry on holder 13 showed 45°C higher T_{irr} . However, F82H-IEA and mod3 irradiated in the holders 4 (SSJ3) and 13 (PCCVN) showed very similar hardness. It is considered that these holders were irradiated at similar temperature, and the dilatometry overestimated T_{irr} . From these results, it is considered that JP-26 and JP-27 were successfully irradiated at the design temperature.

Table 2. Summary of irradiation temperature of HFIR target capsules, JP-26 and JP-27.

Holder	Specimen	Dose (dpa)	Nominal T_{irr} ($^{\circ}\text{C}$)	Design temp. at SiC monitor location, T_{des} ($^{\circ}\text{C}$)	T_{irr} from SiC monitor, T_{meas} ($^{\circ}\text{C}$)	$T_{\text{meas}} - T_{\text{des}}$ ($^{\circ}\text{C}$)
JP26-4	PCCVN	6.3	300	320	342	22
JP26-5	SSJ3	7.5	300	314	315	1
JP26-6	SSJ3	8.1	400	422	449	27
JP26-14	DFMB	6.6	300	327	348	21
JP27-2	PCCVN	12.5	300	315	301	-14
JP27-3	PCCVN	15.8	300	320	357	37
JP27-4	SSJ3	18.4	300	314	317	3
					332	18
JP27-5	SSJ3	20.2	400	416	440	24
JP27-6	SSJ3	21.4	400	422	432	10
					438	16
JP27-7	PCCVN	21.9	400	430	417	-13
JP27-10	DFMB	21.7	400	426	442	16
JP27-11	PCCVN	20.9	400	426	383	-43
					396	-30
JP27-12	DFMB	19.7	300	327	358	31
JP27-13	PCCVN	18.0	300	325	370	45
JP27-14	SSJ3	15.5	300	314	332	18
JP27-15	SSJ3	12.3	300	308	313	5

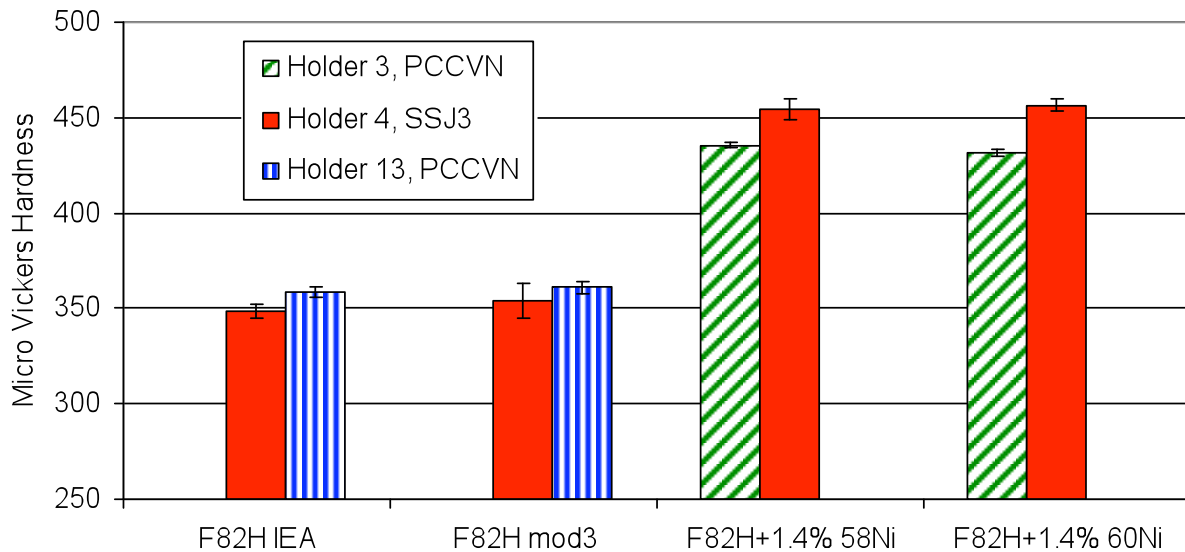


Figure 5. Micro Vickers hardness of F82H and its variants irradiated in JP-27. The nominal T_{irr} is 300°C.

References

- [1] Y. Katoh, A. Clark, K. Ozawa, "Dilatometry of irradiated silicon carbide as a method for determination of irradiation temperature," Fusion Materials Semi-annual Progress Report DOE/ER/0313/48, (June 2010) 158.
- [2] D. K. Felde, K. R. Thoms, D. W. Heatherly, S. H. Kim, R. G. Sitterson, R. E. Stoller, H. Tanigawa, "Assembly of the US-Japan JP-27 experiment and start of irradiation in the HFIR," Fusion Materials Semi-annual Progress Report DOE/ER/0313/36, (June 2004) 124.
- [3] K. R. Thomas, D. W. Heatherly, S. H. Kim, R. G. Sitterson, R. E. Stoller, H. Tanigawa, "Assembly of the US-Japan JP-26 experiment and start of irradiation in the HFIR," Fusion Materials Semi-annual Progress Report DOE/ER/0313/35, (December 2003) 250.
- [4] D. K. Felde, D. W. Heatherly, S. H. Kim, R. G. Sitterson, R. E. Stoller, C. Wang, M. Ando, H. Tanigawa, "Assembly of the US-JAPAN JP-28 and JP-29 experiments and start of irradiation in the HFIR," Fusion Materials Semi-annual Progress Report DOE/ER/0313/38, (June 2005) 164.
- [5] T. Hirose, N. Okubo, H. Tanigawa, M. Ando, M. A. Sokolov, R. E. Stoller, G. R. Odette, Journal of Nuclear Material (in press), doi:10.1016/j.jnucmat.2010.12.044
- [6] B. V. Schaaf, C. Petersen, Y. De Carlan, J. W. Rensman, E. Gaganidze, X. Averty, "High dose, up to 80 dpa, mechanical properties of Eurofer 97," J. Nucl. Mater. 386-388 (2009) 236-246.

7.2 ESTIMATION OF HELIUM PRODUCTION BY THE NICKEL FOIL IMPLANTER TECHNIQUE FOR BEND STRESS RELAXATION TESTS IN THE TITAN PHASE II RABBIT IRRADIATION CAMPAIGN—K. Ozawa, Y. Katoh, L.L. Snead (Oak Ridge National Laboratory), T. Yamamoto (University of California, Santa Barbara), T. Hinoki (Kyoto University), A. Hasegawa (Tohoku University)

OBJECTIVE

This report aims to estimate helium production in the bend stress relaxation test specimens by the nickel foil implanter technique, used in the Phase II campaign of the US-Japan Joint Research TITAN Project.

SUMMARY

He profiles in bend stress relaxation specimens from the thin Ni foil implanter technique were calculated for the TITAN Phase II Campaign. The calculations revealed that the distribution of the implanted transmuted helium is uniform at 2.1, 15 and 21 appm He/dpa to a depth of 11 μm for the case of a 2 μm -thick implanter foil for irradiation to 1, 10 and 20 $\times 10^{25}$ n/m² ($E > 0.1$ MeV), equivalent to 1, 10, and 20 dpa-SiC in the HFIR-PTP. It is noted that the He/dpa ratio is strongly fluence dependent, since natural Ni was used for the implanter foil and hence the He is produced by a two neutron capture sequence.

PROGRESS AND STATUS

Introduction

In the TITAN Phase I irradiation campaign, transient irradiation creep properties of silicon carbide (SiC) have been investigated and engineering important experimental results have been revealed about stress exponent ($n = 1$), linear swelling-creep relationship, and effects of microstructural features such as grain size, grain boundary and crystal structure on irradiation creep [1]. Subsequently, a Phase II irradiation campaign is planned and this focuses on both steady-state irradiation enhanced creep and helium effects for relatively high dose conditions, in order to understand the whole irradiation creep phenomena.

Regarding He effect study, ingenuity is required to simulate fusion relevant He production in fission reactor neutron irradiation experiments, because the neutron spectrum is completely different from 14 MeV fusion spectrum and He production is generally low. For He effects studies of SiC using neutron irradiation, some researchers have used boron-sintered SiC to simulate fusion, since B has a large (n, α) cross section and is easily transmuted to He by nuclear reaction. However, the physical properties of SiC have been totally changed by B assisted sintering and the helium production was not estimated precisely and quantitatively.

One of the solutions for these issues is foil implanter technique, which utilizes $^{59}\text{Ni}(n, \alpha)$ nuclear reaction to inject transmuted He to a specimen from a Ni foil attached on it. The base concept has been originally derived by Gould [2], and suggested for the fusion study by Odette [3]. In practical, the He flow property of the fusion relevant alloys in the HFIR irradiations (JP-26, -27 and -28/29 campaigns) was reported by Yamamoto et al. [4].

This report aims to estimate He production in the bend stress relaxation (BSR) test specimens by nickel foil implanter technique, associated with the Phase II campaign in the US-Japan Joint Research Project.

Table I. Test matrix for the TITAN Phase 2 Campaign. Only the specimens related to this report have been excerpted. Other monolithic SiC, SiC/SiC composites and advanced SiC fibers without Ni foils will be irradiated at the same time. (This table continues on the next page.)

Capsule ID	Irrad. Temp.	DPA	Unit ID	Curv. [mm]	Mat.	Thick. [μm]	Initial Stress [MPa]	Note
T10-01J	300	1	21P3	R 200	RH	50	56	
					RH	50	56	(i)
					Ni	2	-	
					RH	50	56	(ii)
					Ni	2	-	
					RH	50	56	(iii)
					RH	100	113	
					RH	100	113	
					RH	150	169	
					RH	150	169	
					CT	50	56	(i)
					Ni	2	-	
					CT	50	56	(ii)
					Ni	2	-	
CT	50	56	(iii)					
T10-02J	300	10	22P3	R 100	RH	50	113	
					RH	50	113	(i)
					Ni	2	-	
					RH	50	113	(ii)
					Ni	2	-	
					RH	50	113	(iii)
					RH	100	225	
					RH	100	225	
					RH	150	338	
					RH	150	338	
					CT	50	113	(i)
					Ni	2	-	
					CT	50	113	(ii)
					Ni	2	-	
CT	50	113	(iii)					
T10-03J	300	20	23P3	R100	RH	50	113	
					RH	50	113	(i)
					Ni	2	-	
					RH	50	113	(ii)
					Ni	2	-	
					RH	50	113	(iii)
					RH	100	225	
					RH	100	225	
					RH	150	338	
					RH	150	338	
					CT	50	113	(i)
					Ni	2	-	
					CT	50	113	(ii)
					Ni	2	-	
CT	50	113	(iii)					
T10-04J	500	10	24P3	R100	RH	50	113	
					RH	50	113	(i)
					Ni	2	-	
					RH	50	113	(ii)
					Ni	2	-	
					RH	50	113	(iii)
					RH	100	225	
RH	100	225						

					RH	150	338	
					RH	150	338	
					CT	50	113	(i)
					Ni	2	-	
					CT	50	113	(ii)
					Ni	2	-	
					CT	50	113	(iii)
T10-05J	500	20	25P3	R100	RH	50	113	
					RH	50	113	(i)
					Ni	2	-	
					RH	50	113	(ii)
					Ni	2	-	
					RH	50	113	(iii)
					RH	100	225	
					RH	100	225	
					RH	150	338	
					RH	150	338	
					CT	50	113	(i)
					Ni	2	-	
					CT	50	113	(ii)
					Ni	2	-	
					CT	50	113	(iii)
T10-06J	800	10	26P3	R100	RH	50	113	
					RH	50	113	(iv)
					RH	50	113	(iv)
					RH	50	113	(iv)
					RH	100	225	
					RH	150	338	
					RH	150	338	
					CT	50	113	(iv)
					CT	50	113	(iv)
					CT	50	113	(iv)
T10-07J	800	20	27P3	R100	RH	50	113	
					RH	50	113	(iv)
					RH	50	113	(iv)
					RH	50	113	(iv)
					RH	100	225	
					RH	100	225	
					RH	150	338	
					RH	150	338	
					CT	50	113	(iv)
					CT	50	113	(iv)
					CT	50	113	(iv)
T10-08J	1200	10	28P3	R100	RH	50	113	
					RH	50	113	(iv)
					RH	50	113	(iv)
					RH	50	113	(iv)
					RH	100	225	
					RH	100	225	
					RH	150	338	
					CT	50	113	(iv)
					CT	50	113	(iv)
					CT	50	113	(iv)

Irrad. Temp.: Irradiation temperature, Curv.: radius of curvature of the fixture, Mat.: material, RH: Roam & Haas CVD-SiC, CT: CoorsTek CVD-SiC, Ni: Ni foil for implanter, Thick.: specimen thickness. (i) He on the compression side. (ii) He on both tension and compression sides. (iii) He on the tension side. (iv) No He effect.

Materials and Specimen Loading

The test matrix for this irradiation plan is listed in [Table I](#). Chemically vapor deposited (CVD) monolithic silicon carbide (SiC) manufactured by Roam & Haas and CoorsTek with thickness of 50-200 μm were used. It is noted that only specimens related to this report have been excerpted. Other SiC materials (CVD-SiC by Roam & Haas and CoorsTek, single crystal 6H-SiC by Cree, and SiC/SiC composites processed by nano infiltration method) and advanced SiC fibers (Hi-Nicalon™ Type-S, Tyranno™-SA3, experimental Sylramic™ and experimental Sylramic™-iBN) without Ni foils will be irradiated at the same time. The details of the full test matrix are given elsewhere [\[5\]](#).

Consideration of appropriate nuclei for achieving (n,α) reactions with high energy, radiation activity of specimens after neutron irradiation, and machinability of a implanter foil, led to selection of 2 μm -thick nickel foils manufactured by Goodfellow Cambridge Limited (Huntingdon, England). The purity of Ni in the foil is 99.95% and other major impurities are given in the manufacturer's catalogue [\[6\]](#). The Ni foils, specimens and fixtures are shown in [Figure 1](#). The Ni foils were cut with a fine wire saw to $40 \times 1 \times 0.002$ mm and were located adjacent to the SiC specimen using water lubrication when loading the specimen holders for the irradiation experiment.

Neutron irradiation to 1, 10, 20 dpa-SiC at 300-1200°C is planned, as shown in [Table I](#). However, Ni foils were not used with the specimens to be irradiated at 800, 1000 and 1200°C, since a strong interaction between Si and Ni is a concern. For example, it has been reported that reaction layer between SiC and Ni was formed when annealed above 800°C [\[7\]](#).

The initial stage bend stress (σ) was calculated by the following simple equation,

$$\sigma = \varepsilon E = \frac{t}{2R} E \quad (1)$$

where ε is the strain, E the elastic modulus, t the specimen thickness and R the radius of curvature of the fixture. The Young's modulus of CVD-SiC was assumed to be 450 GPa. A more complete description of the BSR experimental technique is given elsewhere [\[8\]](#).

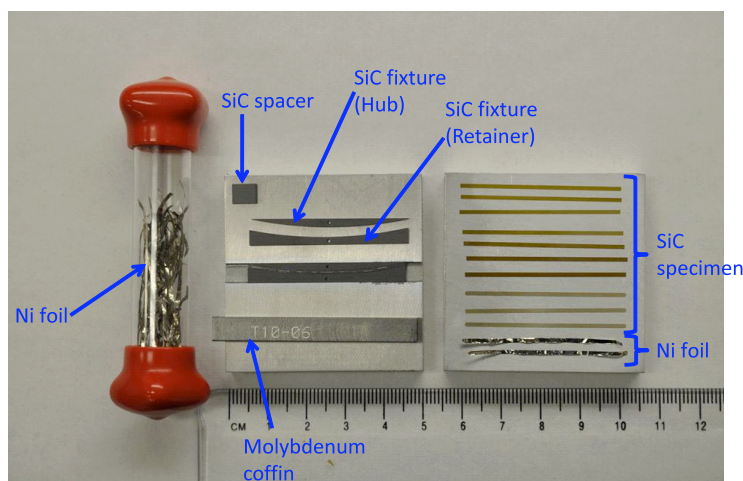


Figure 1. Specimens, Ni foils and SiC fixtures.

Analysis

He Production of the Ni foil [9]

He is transmuted from Ni through the following $^{58}\text{Ni}(n,\gamma)^{59}\text{Ni}(n,\alpha)^{56}\text{Fe}$ reactions;



The energy of α -particles from this reaction sequence is $5.09 \times 4/(56+4) = 4.75$ [MeV]. The production of helium (i.e. He concentration in the foil: C_f) from nickel by the sequential nuclear reactions with this energy is calculated as follows,

$$C_f = \frac{N(\text{He})}{N_0(^{58}\text{Ni})} = \frac{\sigma_\alpha [\sigma_T (1 - \exp(-\sigma_\gamma \phi t)) - \sigma_\gamma (1 - \exp(-\sigma_T \phi t))]}{\sigma_T (\sigma_T - \sigma_\gamma)} \quad (4)$$

Where

- $N(\text{He})$ = Helium atoms produced at time t
- $N_0(^{58}\text{Ni})$ = Initial number of ^{58}Ni atoms
- σ_α = $^{59}\text{Ni}(n,\alpha)$ cross section
- σ_T = ^{59}Ni total absorption cross section
- σ_γ = $^{58}\text{Ni}(n,\gamma)$ cross section
- ϕ = Total flux
- t = Irradiation time

All cross sections should be averaged over the neutron energy spectrum. Total helium production from nickel includes not only the low-energy production given in Eq. (3), but also fast neutron production from both ^{58}Ni and ^{60}Ni . However, the helium production by fast neutrons was ignored in this estimation because the contribution to the total helium production seems to be very small (<0.05%). Figure 2 shows the calculated result for He production by this calculation, plotted against total neutron fluence. Parameters used were listed in Table II. It is noted that the cross section values in the HFIR Peripheral Target Position (PTP) in the CTR-32 campaign [9] were used in the calculation.

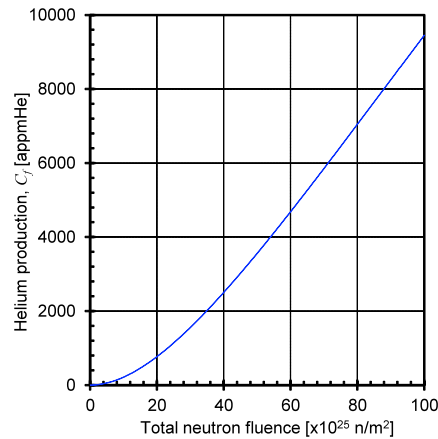


Figure 2. Calculated result of He production plotted against total neutron fluence in the HFIR-PTP.

Table II. Parameters used in the Ni foil implanter design in this study. Subscript *f* and *S* denote “foil” and “specimen.”

Symbol	Description	Value	Unit	Ref.
σ_α	Spectral averaged $^{59}\text{Ni}(n,\alpha)$ cross section	4.33	$\text{b} (\times 10^{-28} \text{ m}^2)$	[9]
σ_T	Spectral averaged ^{59}Ni total absorption cross section	34.29	$\text{b} (\times 10^{-28} \text{ m}^2)$	[9]
σ_γ	Spectral averaged $^{58}\text{Ni}(n,\gamma)$ cross section	1.63	$\text{b} (\times 10^{-28} \text{ m}^2)$	[9]
$^{58}\text{Ni}/^{70}\text{Ni}$	Relative isotopic abundance of ^{58}Ni	0.683	-	[10]
E_{He}	^4He nucleation energy	4.75	MeV	
$R_f (R_{\text{Ni}})$	Helium injection average range for Ni	8.66	μm	[11]
$R_S (R_{\text{SiC}})$	Helium injection average range for SiC	14.6	μm	[11]
$d_f (d_{\text{Ni}})$	Density of Ni	8.91	g/cm^3	-
$d_S (d_{\text{SiC}})$	Density of SiC	3.21	g/cm^3	-
$M_f (M_{\text{Ni}})$	Atomic mass of Ni	58.69	g/mol	-
$M_S (M_{\text{SiC}})$	Atomic mass of SiC	41.4	g/mol	-
$\rho_f (\rho_{\text{Ni}})$	Molar density of Ni	0.152	$\text{g-atom}/\text{cm}^3$	-
$\rho_S (\rho_{\text{SiC}})$	Molar density of SiC	0.155	$\text{g-atom}/\text{cm}^3$	-
$\phi'_{\text{t}}/\phi_{\text{t}}$	Ratio of thermal ($E < 0.5 \text{ eV}$) to total neutron fluence	0.414	-	[12]
$\phi''_{\text{t}}/\phi_{\text{t}}$	Ratio of fast ($E > 0.1 \text{ MeV}$) to total neutron fluence	0.268	-	[12]

He Implantation Profiles [4]

The ^{59}Ni isotope in the implanter foil produces an α -particle with characteristic energy and corresponding range in the foil and sample of R_f and R_S , respectively. Assume that the foil thickness is larger than the implanted He range in the specimen, as shown in Figure 3a (thick foil case). The α -particles emitted from the foil under neutron irradiation are implanted in the specimen to the depth of R_S . All calculations in this section assume the area (y, z) dimensions of the implanter foil-specimen are much larger than R_f , hence, edge effects can be neglected. For simplicity, first assume $R_f = R_S = R$ and ignore α -particle straggling. The He concentration, C_{He} , at a depth x ($x < R$) in the specimen should be proportional to the area fraction, $f(x)$, of the spherical shell in the implanter foil of radius, R , centered on x , as shown in Figure 4. The $f(x)$ is expressed as;

$$f(x) = \int_0^{\theta_{\max}} 2\pi R \sin \theta R d\theta / 4\pi R^2 = \frac{1}{2} \left(1 - \frac{x}{R} \right) \quad (5)$$

where θ is the angle between the radial vector R and the normal to the specimen surface and θ_{\max} occurs at the implanter foil/specimen boundary. The resulting He concentration profile is linear with $f(x)$ decreasing from 1/2 at $x = 0$ to 0 at $x = R_S$. Therefore the He concentration in the specimen (C_{He}) can be described as follows:

$$C_{\text{He}}(x) = \frac{C_f \rho_f R_f}{2 \rho_S R_S} \left(1 - \frac{x}{R_S} \right) \quad (6)$$

where

C_f = volumetric concentration of He in the implanter foil which is the same as the bulk concentration for a given implanter foil composition and neutron dose (The

corresponding molar (or atomic) concentration c_f must be adjusted by multiplying C_f by the ratio of the foil/specimen atomic densities (N , N_f/N_s).

R_f, R_s = Helium injection average range for the foil and specimen, respectively, calculated using TRIM-98 code as the average of 99999 4.75 MeV He ions [11].

ρ_f, ρ_s = molar density of the foil and the specimen, respectively.

It is noted that both differences 1) in the α -particle ranges between the foil and the specimen (R_f and R_s), and 2) in the molar densities (ρ_f and ρ_s), should be accounted for by ratio factors of R_f/R_s and ρ_f/ρ_s . In summary, the schematic illustration of the He distribution for the thick foil case was shown in Figure 3b.

Using the result of the thick foil case described above, the result for the thin foil case ($t_f < R_s$, shown in Figure 3c), can be calculated. The profile of the thin foil case (red bold line in Figure 3d) could be simply obtained by subtracting the missing contribution from the (n, α) reactions further from the interface (blue dotted line), from the thick-foil profile (black solid line). Therefore, in the thin foil case where $R_f \neq R_s$ and $x_m = R_f(1-t_f/R_s)$, the He concentration vs. position x can be described as follows:

$$C_{He}(x) = \begin{cases} \frac{C_f \rho_f t_f}{2 \rho_s R_s} & : 0 < x < R_s(1-t_f/R_f) \\ \frac{C_f \rho_f R_f}{2 \rho_s R_s} \left(1 - \frac{x}{R_s}\right) & : R_s(1-t_f/R_f) < x < R_s \\ 0 & : R_s < x \end{cases} \quad (7)$$

Results

Figure 5 illustrates the calculated results for neutron irradiation to 1, 10 and 20 dpa-SiC at the HFIR PTP with different Ni foil thickness ($t_f = 1, 2, 3$ and $8.66 \mu\text{m}$). In this calculation, 1 dpa-SiC = $1 \times 10^{25} \text{ n/m}^2$ ($E > 0.1 \text{ MeV}$) = $3.74 \times 10^{25} \text{ n/m}^2$ (total fluence), is assumed. This assumption is based on Ref. [12], but similar ratios of thermal or fast to total fluence at the target positions is confirmed (Table III). The calculations show that a uniform He/dpa ratio of 2.1, 15 and 21 appm/dpa is achieved to a depth of $x_m = 11 \mu\text{m}$ for the case of $t_f = 2 \mu\text{m}$ with 1, 10 and 20 dpa irradiation. When x_m is greater than $11 \mu\text{m}$, the ratio decreased proportionally with x , resulting in $C_{He} = 0$ at $x = 14.5 \mu\text{m}$. It is noted that the He/dpa ratio is strongly fluence dependent, since natural Ni was used for the implanter foil and hence the He is produced by a two neutron capture sequence.

Table III. Neutron fluence at the HFIR target positions in previous irradiation experiments, calculated by Greenwood et al. [12-15]

Campaign	Position	Cycles	Neutron Fluence [$\times 10^{22} \text{ n/cm}^2$]				Ratio		Ref.	
			Total	Thermal < 0.5 eV	0.5 eV - 0.1 MeV	Fast > 0.1 MeV	> 1 MeV	Thermal /Total		Fast /Total
JP-23	Target, G6	322-326	4.39	1.92	1.36	1.12	0.565	0.437	0.255	[13]
JP-9, 12, 15	Target	289-324	26.3	10.9	8.39	7.06	3.67	0.414	0.268	[12]
JP-20	Target	322-326	4.19	1.84	1.32	1.05	0.519	0.439	0.251	[14]
CTR-62, 63	Target	335-341	6.91	3.15	2.08	1.68	0.85	0.456	0.243	[15]

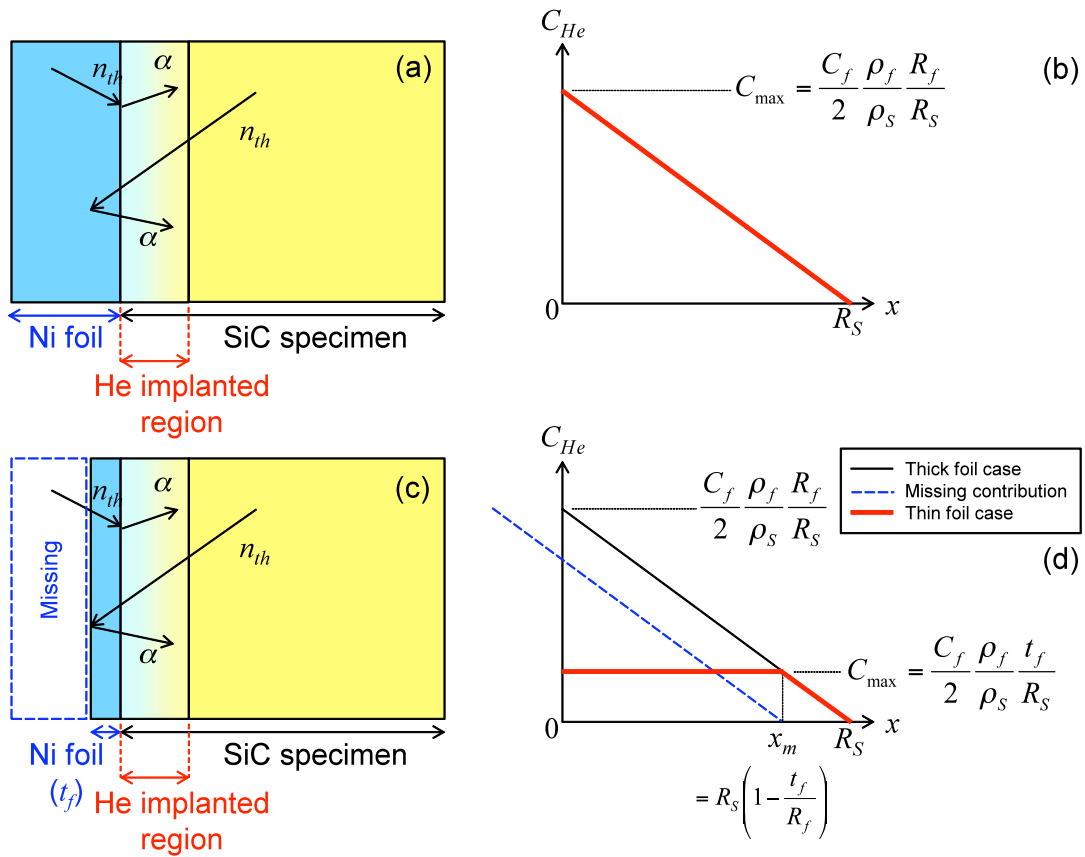


Figure 3. Schematic illustration of Ni foil implanter concept from one side of a specimen: (a) Thick foil case, where the foil thickness is larger than the He implanted average range. (b) He profile for the thick foil case. (c) Thin foil case, where the thickness is smaller than the He range. (d) He profile for the thin foil case.

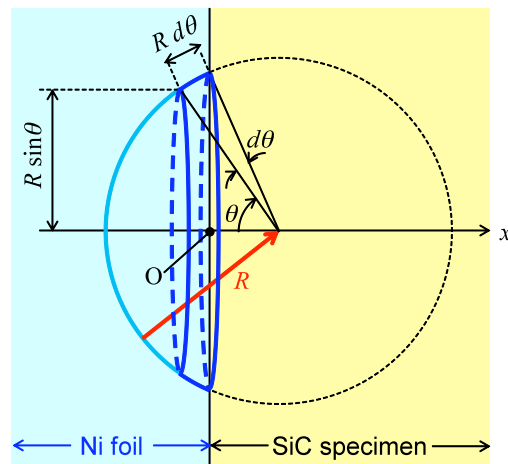


Figure 4. The implanter source volume for He deposited at a depth x in the specimen.

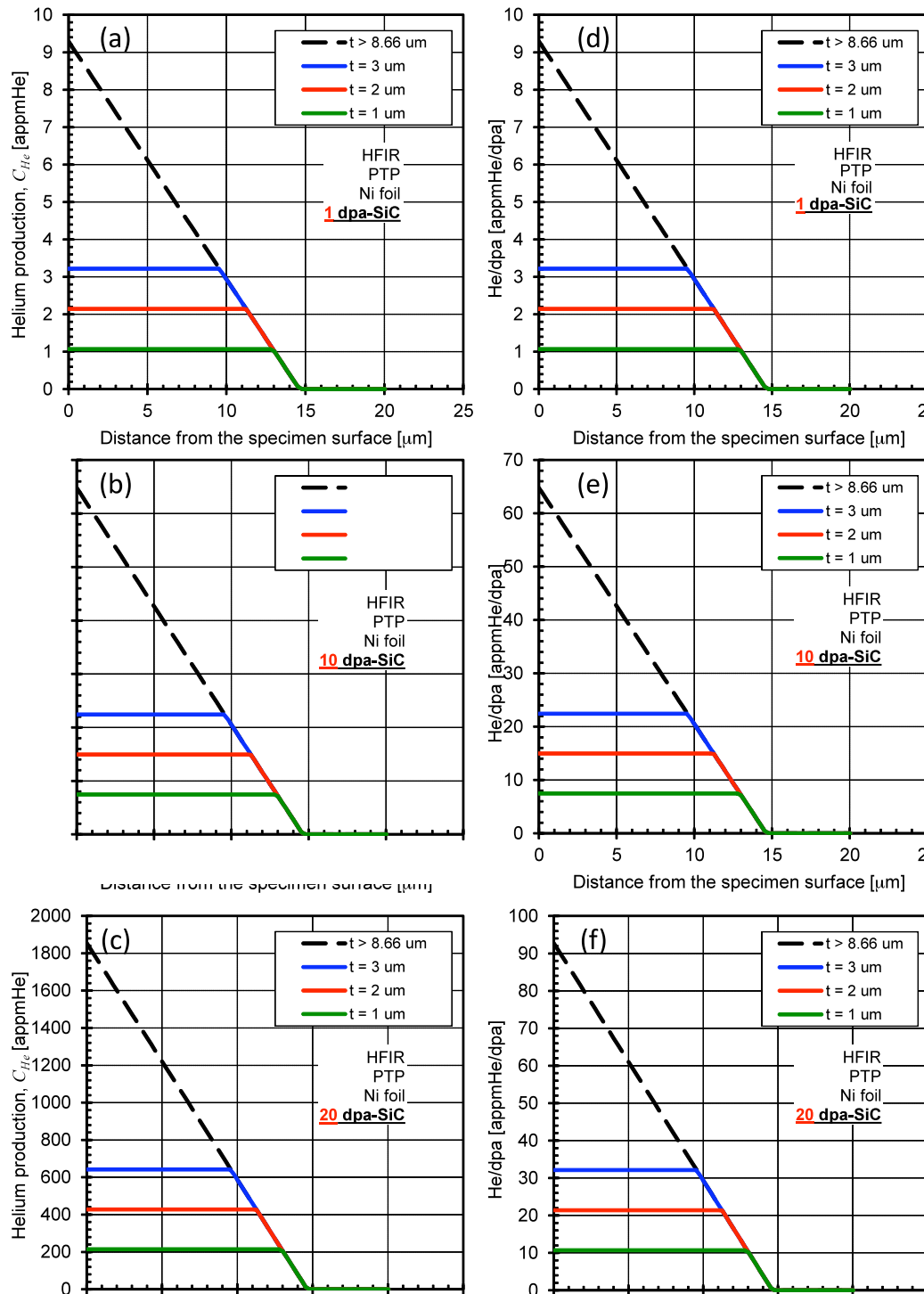


Figure 5. He production profiles in SiC specimens for (a) 1, (b) 10 and (c) 20 dpa conditions corresponding HFIR Target 2 position, respectively for Ni implanter foils with $t_f = 1, 2, 3$ and $8.66 \mu\text{m}$. The corresponding He/dpa ratios are also plotted in (d)-(f).

Acknowledgement

This research is sponsored by the Office of Fusion Energy Sciences, US Department of Energy under contract DE-AC05-00OR22725 with UT-Battelle, LLC, and also a part TITAN US Department of Energy/Japanese Ministry of Education, Culture, Sports, Science and Technology (MEXT) collaboration for fusion material system research. Irradiation will be conducted in the Department of Energy High Flux Isotope Reactor User Facility starting in February 2011.

References

- [1] Y. Katoh, L.L. Snead, A. Hasegawa, S. Nogami, T. Hinoki, Y.B. Choi, "Irradiation Creep in Silicon Carbide: Experimental Results from TITAN Program and Implications to Stress Evolution in Flow Channel Inserts for Fusion Liquid Metal Blankets," ANS 19th Topical Meeting on the Technology of Fusion Energy (TOFE-19), November 7-11 2010, Riviera Hotel, Las Vegas, Nevada, USA.
- [2] T.H. Gould and W.R. McConnell, Proc. Int. Conf. on Radiation Effects and Tritium Technology for Fusion Reactors, Gatlingburg, TN, Oct. 1975, CONF-750989, V2 (1976) 387.
- [3] G.R. Odette, J. Nucl. Mater. 141-143 (1986) 1011.
- [4] T. Yamamoto, G.R. Odette, L.R. Greenwood, Fusion Mater. DOE/ER-0313/38 (2005) 95.
- [5] Y. Katoh, et al., Fusion Mater. DOE/ER-0313/49 (2011), this report.
- [6] http://www.goodfellow.com/pdf/4728_1111010.pdf
- [7] J.H. Culpin, A.A. Kodentsov, J.J. van Loo, Z. Metallkd. 86 (1995) 8.
- [8] Y. Katoh, L.L. Snead, Ceram. Eng. Sci. Proc. 26 (2005) 265
- [9] L.R. Greenwood, D.W. Kneff, R.P. Skowronski, F.M. Mann, J. Nucl. Mater. 123 (1984) 1002.
- [10] L.R. Greenwood, J. Nucl. Mater. 115 (1983) 137.
- [11] According to the TRIM-98 code: J.F. Ziegler, J.P. Biersack, U. Littmark, "The Stopping and Range of Ions in Solids," Pergamon Press, 109 (1985).
- [12] L.R. Greenwood, C.A. Baldwin, Fusion Mater. DOE/ER-0313/23 (1997) 301.
- [13] L.R. Greenwood, R.T. Ratner, Fusion Mater. DOE/ER-0313/21 (1996) 229.
- [14] L.R. Greenwood, C.A. Baldwin, Fusion Mater. DOE/ER-0313/23 (1997) 305.
- [15] L.R. Greenwood, C.A. Baldwin, Fusion Mater. DOE/ER-0313/26 (1999) 199.

8.1 OPERATING CONDITIONS AND IRRADIATION HISTORY FOR EXPERIMENT MFE-RB-15J — J. McDuffee, D. Heatherly (Oak Ridge National Laboratory)

OBJECTIVE

The objective of this summary is to describe the operating conditions (temperature & fluence) and operating history of the MFE-RB-15J experiment.

SUMMARY

The MFE-RB-15J experiment was designed to irradiate steel specimens at 300 and 400°C for 10 cycles in the RB* irradiation facility in HFIR. The irradiation vessel was divided into three subcapsules. The specimen regions of the upper and lower subcapsules were about 7.7 cm long, located ± 14 cm from the reactor midplane, and designed to operate at 300°C. The specimen region of the middle subcapsule was about 11.5 cm long, centered at the reactor midplane, and designed to operate at 400°C.

Each subcapsule was filled with lithium, which became molten during operation and solidified during reactor outages. Thermocouples were located at the centerline of each subcapsule and extended upward through part of the axial length of the subcapsule.

Because of concerns over the potential for a volatile reaction between the lithium and water in the event of a containment failure, the specimen-containing subcapsules were housed inside two outer containments. There were small gas gaps between the primary and secondary containments and between the secondary containment and the subcapsules. The outer gas gap was filled with helium. The inner gas gap was filled with a mixture of helium and neon, and the relative concentrations of the two were controlled to provide the gas conductivity necessary to achieve the desired temperatures. The gas compositions for each of the three subcapsules were controlled separately, although not completely independently.

PROGRESS AND STATUS

MFE-RB-15J Irradiation History & Fluence

The irradiation history for MFE-RB-15J is shown in Table 1. The experiment initial cycle was Cycle 415 in June of 2008. The final cycle was Cycle 424 in October 2009. The experiment total exposure was just over 20,000 MW-days, with a total of 236 effective full-power days. Assuming a dpa/fluence conversion factor of 0.000289 dpa/MWd, the total dpa for the experiment was 5.8 dpa at the reactor midplane location.

Neutron Flux Spectrum

The neutron flux spectrum is complicated for the 15J experiment because of the use of a Eu_2O_3 thermal neutron shield. The lower, middle, and upper subcapsules are all located inside the shielded region. The thermal flux inside the shield is greatly reduced due to the large thermal cross section of Eu_2O_3 . The degree of reduction depends a great deal on the accumulated fluence of the shield itself. It was originally planned to run the 15J experiment with a fresh shield. However, fabrication difficulties prevented the new shield from being completed by the beginning of the experiment. As a result, liner Eu-5, a previously used shield, was selected. Table 2 shows the lifetime of the Eu-5 shield prior to the 15J experiment.

Table 1. Experiment MFE-RB-15J irradiation history

Cycle	Start	End	Exposure (MWd)	Effective Full-Power Days	Cooling Time (days)
415	03-Jun-2008	30-Jun-2008	1992	23.44	16.1
416	16-Jul-2008	06-Aug-2008	1782	20.96	48.7
417	24-Sep-2008	18-Oct-2008	2021	23.78	25.0
418	12-Nov-2008	05-Dec-2008	1992	23.44	32.4
419	07-Jan-2009	31-Jan-2009	2047	24.08	17.8
420	18-Feb-2009	14-Mar-2009	2069	24.34	59.5
421	13-May-2009	06-Jun-2009	2070	24.35	17.5
422	24-Jun-2009	18-Jul-2009	2012	23.67	18.3
423	05-Aug-2009	29-Aug-2009	2058	24.21	45.8
424	14-Oct-2009	09-Nov-2009	2026	23.83	
Total			20069	236.10	

Table 2. Eu-5 liner operating history

Cycle	Experiment	Start	End	Exposure (MWd)	Effective Full-Power Days	Cooling Time (days)
364A	MFE-RB-10J	13-Oct-1998	23-Oct-1998	876	10.3	2.7
364B	MFE-RB-10J	26-Oct-1998	08-Nov-1998	1096	12.89	276.2
372	MFE-RB-10J	11-Aug-1999	27-Aug-1999	1378	16.21	1,704.8
400	MFE-RB-17J	27-Apr-2004	21-May-2004	2069	24.34	55.5
401	MFE-RB-17J	16-Jul-2004	09-Aug-2004	2067	24.32	50.2
402	MFE-RB-17J	28-Sep-2004	23-Nov-2004	1963	23.09	63.9
403A	MFE-RB-17J	26-Jan-2005	04-Feb-2005	765	9.00	61.2
404	MFE-RB-17J	06-Apr-2005	30-Apr-2005	1967	23.14	5.6
403B	MFE-RB-17J	05-May-2005	18-May-2005	1133	13.33	8.9
405	AI Plug	27-May-2005	20-Jun-2005	1974	23.22	8.0
406	AI Plug	28-Jun-2005	23-Jul-2005	1889	22.22	1,046.2

Figure 1 shows how the thermal flux increases as a function of irradiation time. The fast flux is essentially constant throughout the irradiation at about $4.8 \cdot 10^{14}$ n/cm²-sec, so the fast/thermal ratio changes are a reflection of the thermal flux.

The spectrum for the middle subcapsule is shown in Figure 2 for the first and last cycles for the 15J experiment. The fast flux is shown to be nearly constant in this figure. The flux spectra begin to deviate at about 1 keV.

MFE-RB-15J Operating Temperatures

Each subcapsule is fitted with a thermocouple array that extends from the bottom to some point in the middle of the subcapsule. There are three temperature measurements in each capsule, located according the drawing shown in Figure 3. The upper subcapsule is not shown, but the thermocouple locations are the same in the upper and lower subcapsules.

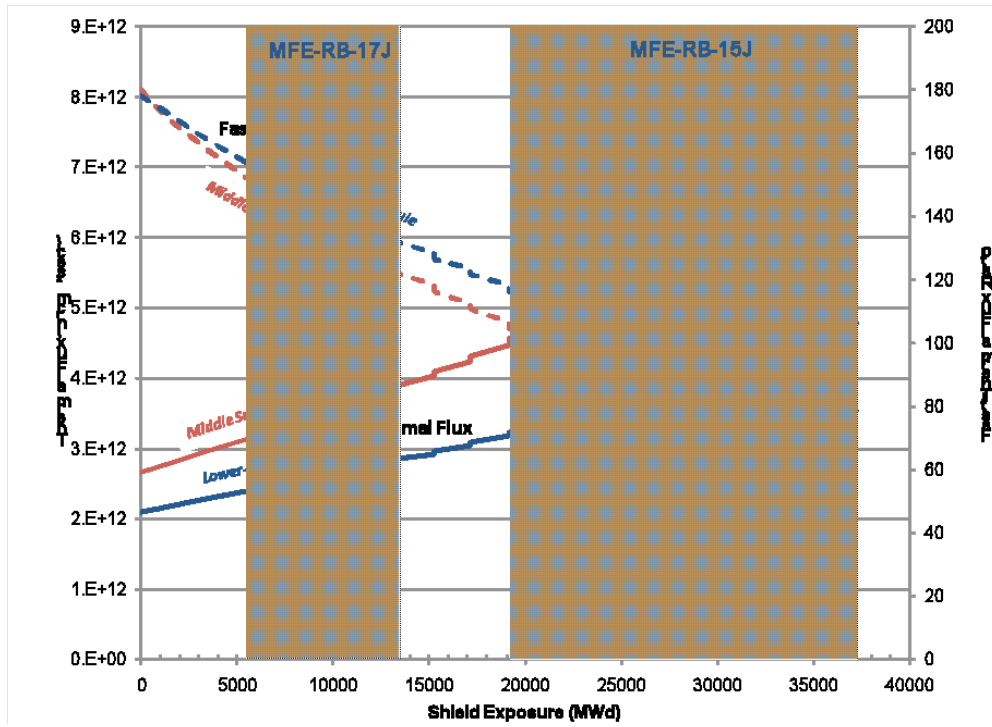


Figure 1. Thermal flux and fast/thermal ratio inside the shield as a function of irradiation time

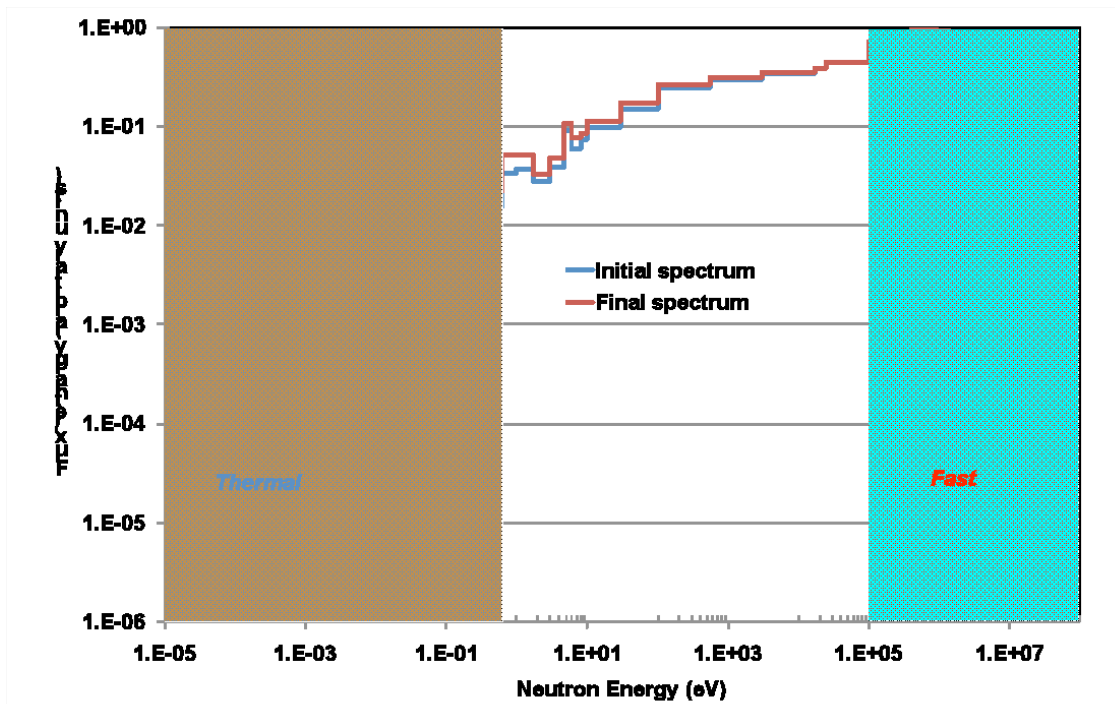


Figure 2. Flux spectra in the specimen region of the middle subcapsule for the initial and final MFE-RB-15J cycles

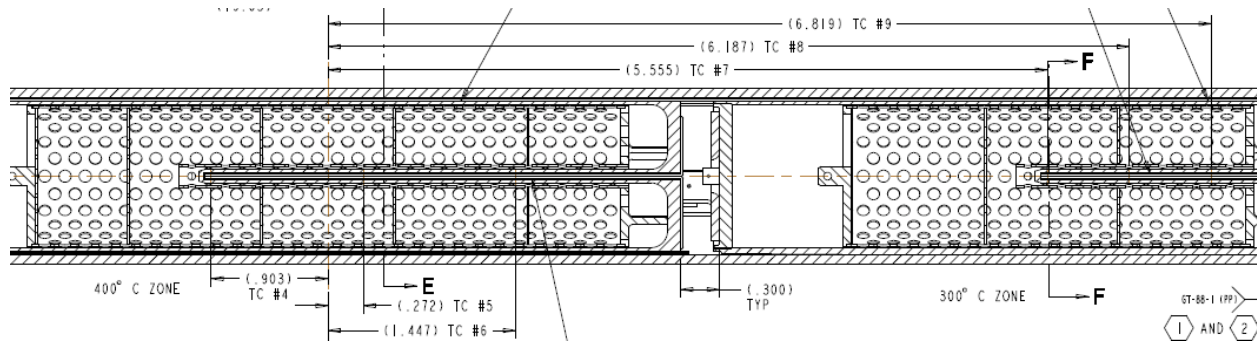


Figure 3. Thermocouple locations (inches) in each subcapsule from the reactor midplane

Table 3 summarizes the temperature measurements for all thermocouple locations through the entire experiment. For each cycle the temperature measurements at 15 minute intervals are averaged over the full cycle time where the reactor power is greater than 80 MW. Startup times where the reactor ascends to full power are typically 1 hour or less. The minimum temperatures shown in Table 3 represent the period of time just after full power attainment before the gas composition has been fully adjusted to achieve the setpoint temperature. Gas compositions are purposefully set to give too low temperatures at startup to avoid temperatures higher than desired.

Table 3. Temperature summary (°C) for the MFE-RB-15J experiment

Cycle	Upper Subcapsule			Middle Subcapsule			Lower Subcapsule		
	TE501	TE502	TE503	TE504	TE505	TE506	TE507	TE508	TE509
415	300.3	304.8	304.6	428.1	423.0	422.2	310.8	302.8	297.9
416	301.2	305.2	301.5	427.4	418.2	419.3	310.5	302.3	296.4
417	301.7	303.9	303.1	427.9	419.2	421.2	310.4	302.2	298.7
418	303.2	304.3	302.3	429.7	418.1	420.2	309.0	302.5	298.4
419	301.9	304.1	301.6	426.2	418.7	421.5	309.1	301.0	298.4
420	301.2	303.7	301.8	427.3	416.9	419.9	306.3	302.1	299.2
421	301.4	304.2	301.4	426.3	418.6	421.6	306.9	301.7	298.9
422	303.1	306.0	303.2	429.0	419.5	422.7	308.6	303.6	300.6
423	303.0	306.3	303.6	427.4	420.8	424.7	308.3	303.7	301.4
424	304.3	308.3	303.2	430.9	420.7	422.9	310.2	304.6	301.0
Average	302.1	305.1	302.6	428.0	419.4	421.6	309.0	302.6	299.1
σ	2.7	2.7	2.8	2.2	2.4	2.3	2.6	2.3	2.4
Min	245.3	243.2	241.4	372.0	362.2	362.3	256.1	249.2	244.3
Max	309.8	312.6	310.7	433.6	430.9	429.2	317.4	309.5	305.3
Average	303.3			423.0			303.6		
σ	3.0			4.3			4.8		

The temperatures shown in Table 3 are higher than the desired specimen temperatures because the thermocouple locations are at the experiment axial centerline where the temperatures are highest. There is a significant ΔT offset between the thermocouple and the average specimen temperature. Based on the design calculations, the temperature offset between the thermocouple and the average specimen temperature should be 14°C, 27°C, and 16°C for the upper, middle, and lower subcapsules, respectively. Therefore, the average specimen temperatures for each region are $289 \pm 6^\circ\text{C}$, $396 \pm 9^\circ\text{C}$, and $288 \pm 10^\circ\text{C}$ in the upper, middle, and lower subcapsules, respectively, where the \pm range represents $2 \cdot \sigma$. The experiment team realized that the temperatures in the upper and lower subcapsules were lower than desired, but it was determined that these were the maximum achievable temperatures that could be maintained consistently for the entire cycle.

Note that the standard deviations listed above refer to the variation of the measured temperatures at the experiment centerline over the course of the experiment. They provide an indication of the temperature variation over time. The design calculations show that the spatial temperature variation is $\pm 12^{\circ}\text{C}$ for the upper and lower subcapsules and $\pm 23^{\circ}\text{C}$ for the middle subcapsule, where the \pm range represents the $\frac{1}{2}$ span [$\frac{1}{2} \cdot (\text{maximum} - \text{minimum})$]. The spatial variation is primarily due to the radial temperature gradient from the centerline to the inner surface of the subcapsule housing.

8.2 DESIGN OF THE JP30 AND JP31 EXPERIMENTS – J. McDuffee, D. Heatherly, N. Cetiner (Oak Ridge National Laboratory)

OBJECTIVE

The objective of this summary is to describe the designs for the JP30 and JP31 experiments.

SUMMARY

Two experiments, JP30 and JP31, have been designed to place various stainless steel specimens in the flux trap of the High Flux Isotope Reactor (HFIR). These designs are very similar to other experiments irradiated previously in HFIR (e.g., JP26, JP27, JP28, JP29).

The JP30 and JP31 experiments are designed to irradiate F82H specimens of various sizes and types in the flux trap of HFIR at temperatures in the range of 300 to 650°C. The specimens are typically contained within holders of either DISPAL (dispersion-strengthened aluminum) or a vanadium alloy (V-4Cr4Ti). The primary outer containment is an Al-6061 tube with an outer diameter of 1.27 cm. Helium is used as the fill gas inside the experiment. The specimen temperature is controlled by the size of the gap between the holder and housing. This report summarizes the work described in the design and analysis calculation for this project [1].

PROGRESS AND STATUS

Design Drawings

Table 1 lists design drawings and titles that were modified or developed for the JP30 and JP31 experiments. Both experiments consist of a stack of individual specimen holders and specimens. Figure 1 through Figure 4 show layouts for the four specimen types taken from the design drawings in Table 1.

Table 1 JP30/31 Design Drawings

Drawing No.	Title
X3E020977A437	TEM HOLDER SUBASSY, TEM HOLDER DETAIL
X3E020977A438	M3-PCCVN HOLDER SUBASSY, M3-PCCVN HOLDER DETAIL
X3E020977A439	M5-PCCVN HOLDER SUBASSY, M5-PCCVN HOLDER DETAIL
X3E020977A441	SS-J3/APFIM HOLDER SUBASSY, SS-J3/APFIM HOLDER DETAIL
X3E020977A442	DCT SPECIMEN SUBASSY, DCT SPECIMEN DETAILS
X3E020977A443	DCT SPECIMEN MISC. DETAILS
X3E020977A444	CAPSULE SPACER ASSEMBLIES
X3E020977A445	CAPSULE SPACER DETAILS
X3E020977A446	MISC. DETAILS
X3E020977A576	JP IRRADIATION CAPSULE NO. 30 ASSEMBLY
X3E020977A577	JP IRRADIATION CAPSULE NO. 31 ASSEMBLY

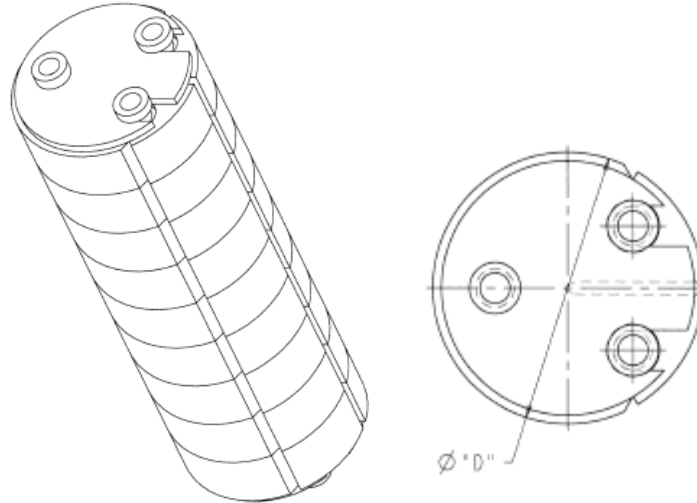


Figure 1. Specimen Layout for the DCT regions

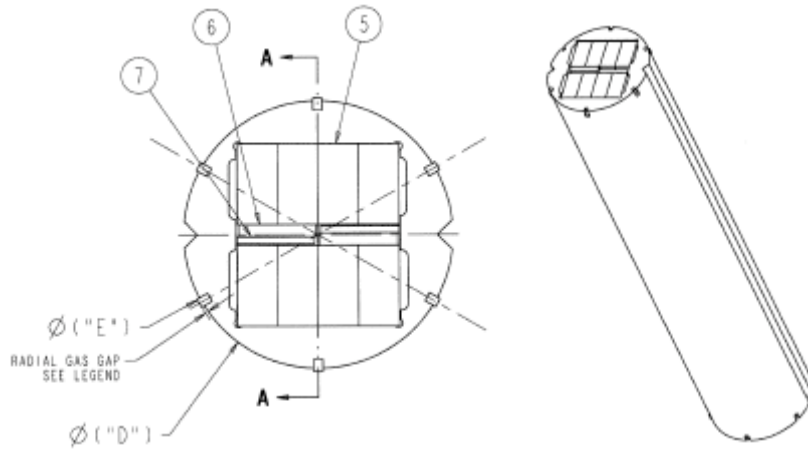


Figure 2. Specimen Layout for the PCCVN regions

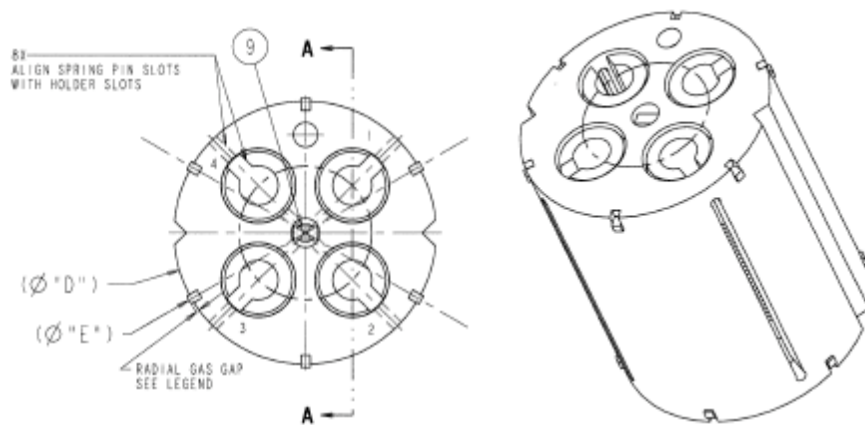


Figure 3. Specimen Layout for the TEM regions

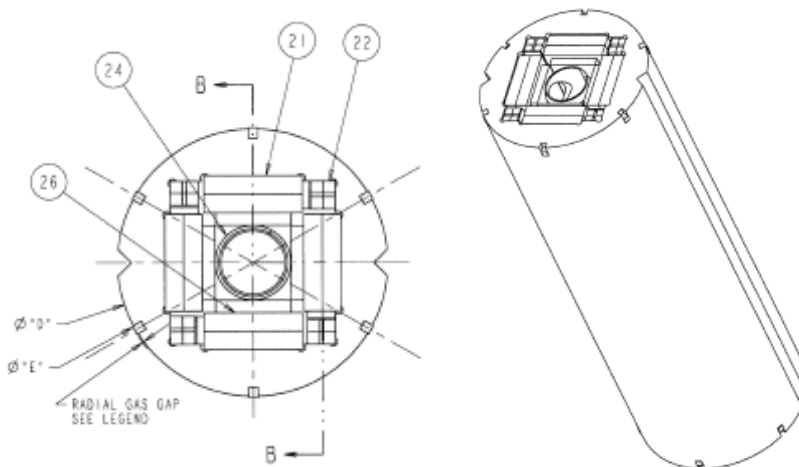


Figure 4. Specimen Layout for the SSJ3 regions

Materials of Construction

The primary outer containment is fabricated from Al6061, and specimens are all F82H or variations of this alloy. Holders are fabricated from DISPAL in the lower temperature regions and from V-4Cr4Ti in the 650C regions. Other components (e.g., spacers, centering tabs) are typically made from 300-series stainless steel.

Thermal Boundary Conditions

JP30 and JP31 are the most recent in a long series of similar experiments. Previous experiments have shown reasonably good agreement between the design temperatures and the post-irradiation analysis of experiment thermometry. Therefore, material heat generation rates, the heat transfer coefficient, and the bulk fluid temperature are all taken to be the same as that assumed for previous experiments. Table 2 summarizes the thermal boundary conditions used in this analysis. These values are taken from the design documentation associated with JP28/29 [2].

Table 2. Thermal Boundary Conditions from the JP28/29 Design

Heat transfer coefficient	48040 W/m ² .°C
Bulk fluid temperature (all regions)	60°C
Heat generation rate for AL6061, DISPAL aluminum, and silicon carbide	29.24 W/g
Heat generation rate for stainless steel	46.41 W/g

The major difference in the JP30/31 designs and previous designs is that the maximum temperature in the JP30/31 designs is 650°C rather than 500°C. All the earlier designs used holders fabricated from DISPAL aluminum, which has a melting point of about 660°C. For these new 650°C regions, a vanadium alloy (V-4Cr4Ti) is selected as the holder material which has a much larger margin to melt. The heat generation rate for this alloy is 45.1 W/g [3].

Finite Element Model

Both JP30 and JP31 have 14 regions, each with its own design temperature. The design temperatures for this experiment are 300°C, 400°C, and 650°C. Spacers are placed between regions of different temperatures to minimize axial heat flow between regions. As such, a two dimensional analysis in the R- θ plane is used for each region.

Fundamentally, there are four types of specimen regions: DCTs, PCCVNs, SSJ3s, and TEMs. The PCCVN regions may be of type M2, M3, or M5, but all of these specimen types are identical in the R-θ plane.

Figure 5 through Figure 8 show the geometrical models used for the thermal analysis for each of the specimen regions. All dimensions are shown in meters. Table 3 summarizes where each specimen region is located in the JP30/31 experiments, along with the region design temperature. Regions with a gray background in Table 3 indicate a change from the JP28/29 experiments.

Because of satisfactory results from the JP28/29 thermometry, JP30/31 specimen regions which are unchanged from the JP28/29 experiments are not redesigned. However, the JP28/29 experiments used a different extrusion stock for the housing that had a slightly different inner diameter. Specifically, the JP28/29 experiments had a housing inner diameter of 0.4413", while the JP30/31 housing stock has an inner diameter of 0.4451". In order to maintain the previous design, the JP28/29 holder design diameters were increased by 0.0038", which preserves the gas gap between the holder and housing.

Although the unchanged specimen regions are not redesigned, they are re-analyzed and reported in this calculation for completeness. Slight differences in calculated temperature are to be expected due to modeling differences.

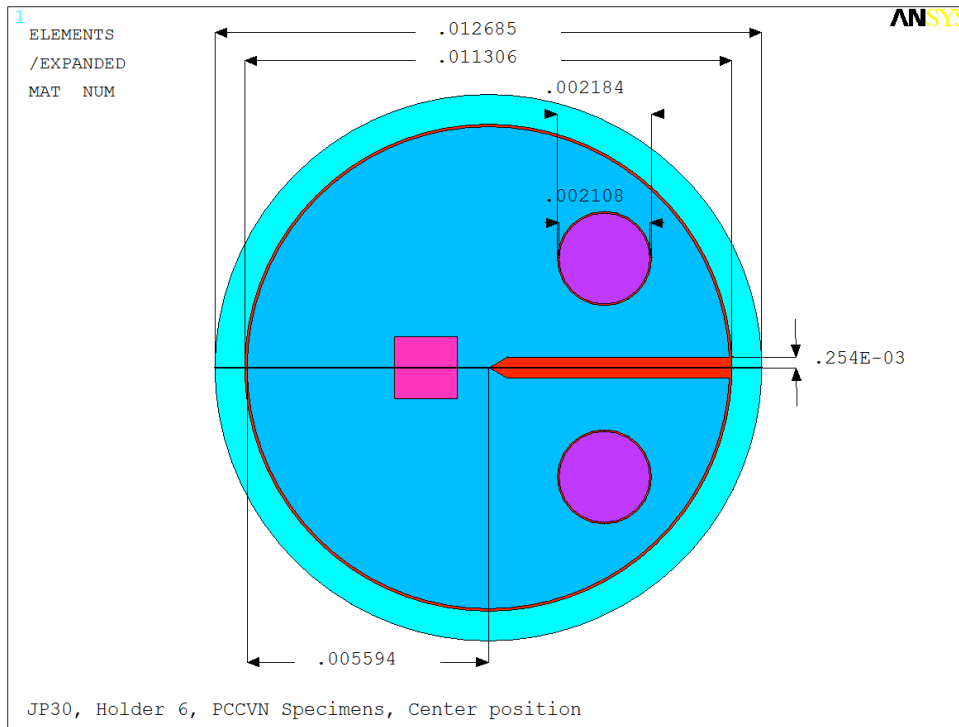


Figure 5. Geometrical Model for the DCT regions

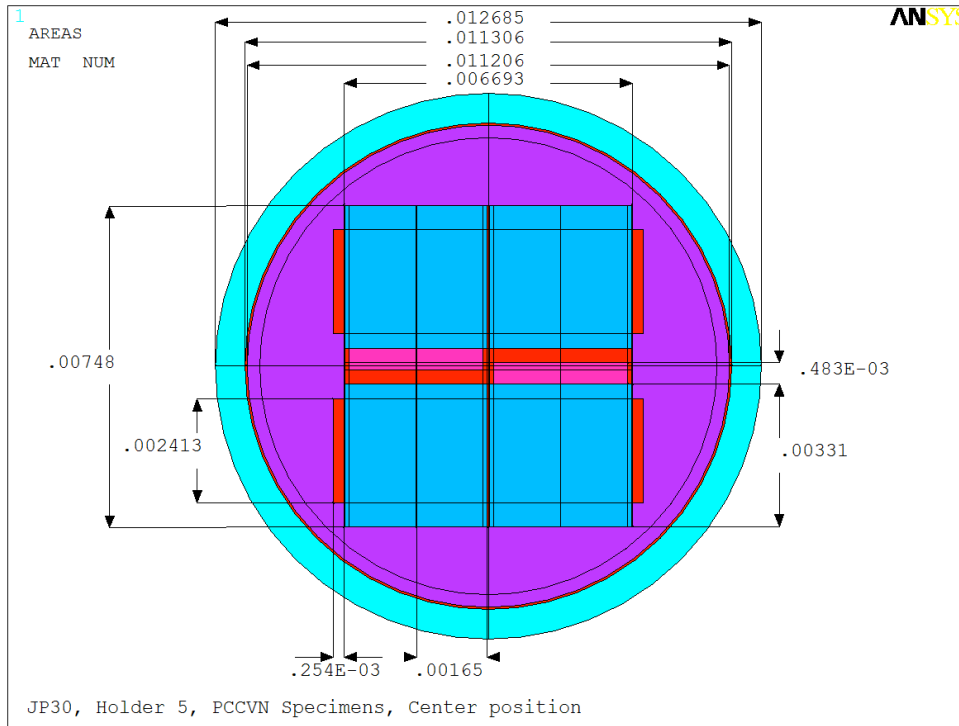


Figure 6. Geometrical Model for the PCCVN regions

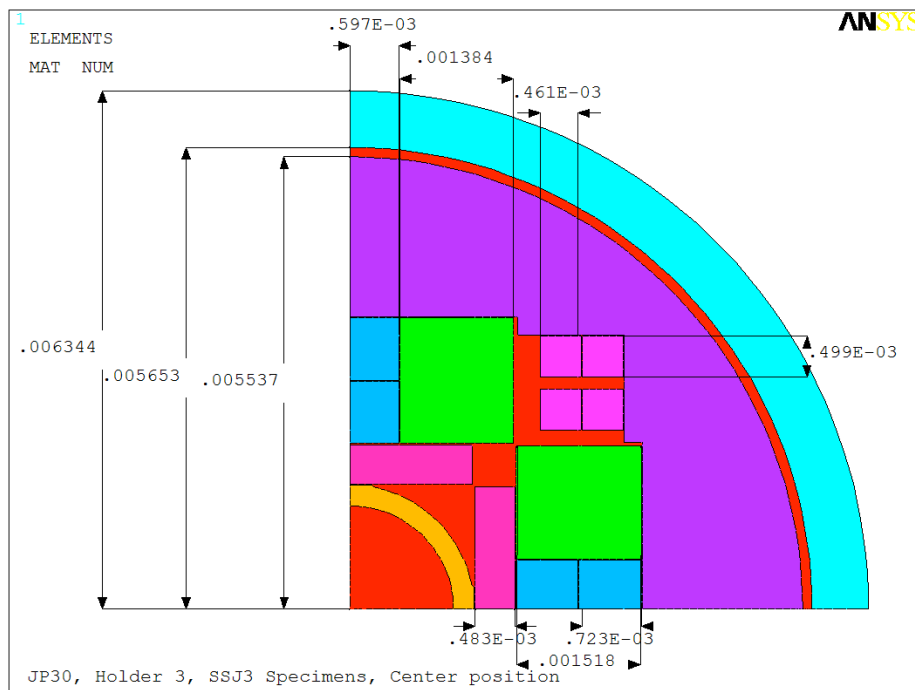


Figure 7. Geometrical Model for the SSJ3 regions

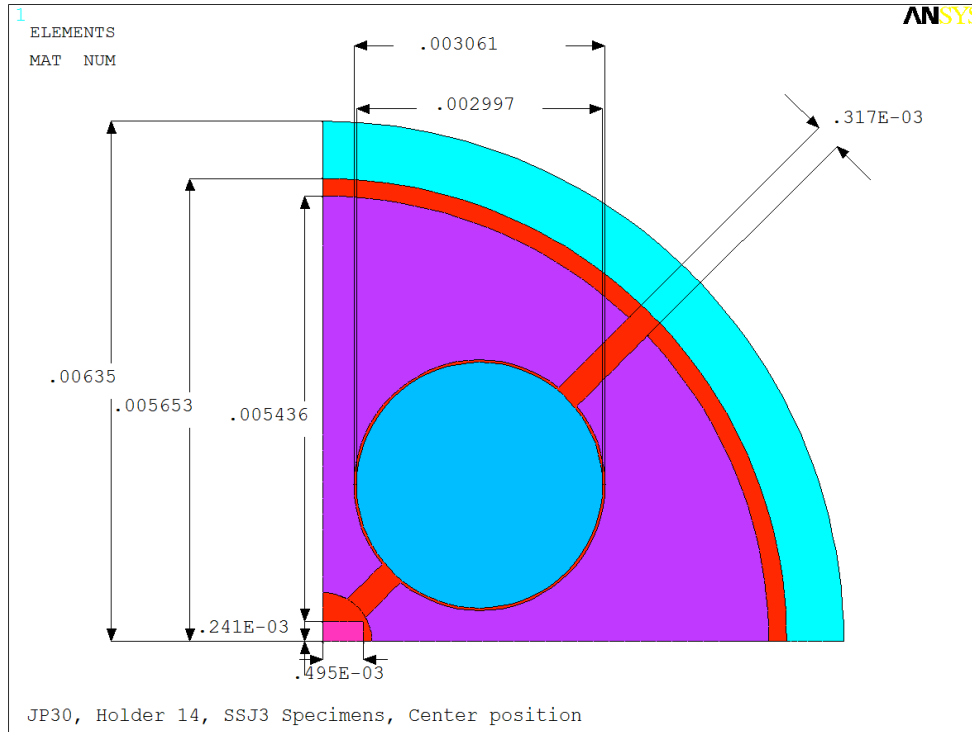


Figure 8. Geometrical Model for the TEM regions

Table 3. Design Layout for the JP30/31 Experiments

Capsule	Holder	Design Temperature (°C)	Specimen Type
JP30	1	400	SSJ3
	2	650	DCT
	3	300	SSJ3
	4	300	DCT
	5	300	M3PCCVN
	6	400	DCT
	7	400	SSJ3
	8	400	DCT
	9	650	SSJ3
	10	300	M2PCCVN
	11	300	M3PCCVN
	12	300	M3PCCVN
	13	300	M3PCCVN
	14	300	TEM

Table 3. Design Layout for the JP30/31 Experiments

Capsule	Holder	Design Temperature (°C)	Specimen Type
JP31	1	400	TEM
	2	400	SSJ3
	3	650	SSJ3
	4	300	M2PCCVN
	5	300	DCT
	6	300	M3PCCVN
	7	300	SSJ3
	8	400	M5PCCVN
	9	650	M5PCCVN
	10	300	SSJ3
	11	300	DCT
	12	300	SSJ3
	13	300	SSJ3
	14	650	TEM

Design Analysis

The sections below describe the new and repeated designs for each specimen type. The stated temperature range for each part indicates a 95% span by volume. In other words, 95% of the volume of the part will have a temperature between the endpoints of the span. The range includes segments at the top, middle, and bottom of the holder.

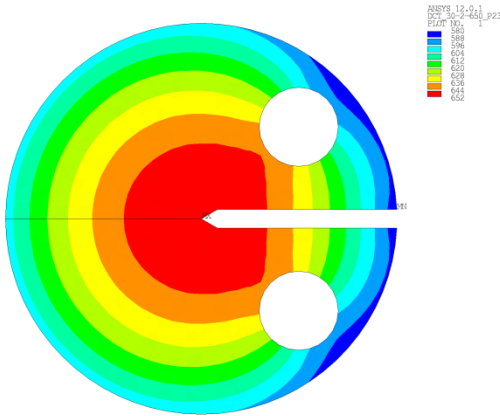
DCT New Designs

The results of the new DCT region designs are described in Table 4. Figure 9 through Figure 10 show the temperature contours for the specimens and thermometry.

Table 4. Design Summary for New DCT Regions

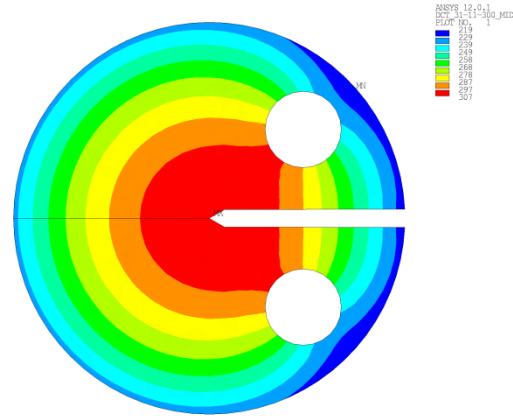
Experiment	Holder (Design Temperature °C)	Design Specimen Diameter	Part	Temperature (°C) Average (Min-Max)
JP30	2 (650°C)	10.82 mm [1-4]* (0.4257")	Housing	74 (71-76)
			DCT pin	617 (609-652)
		10.86 mm [5-9]* (0.4274")	DCT (all)	607 (571-666)
			DCT (crack region)	650 (630-666)
JP31	11 (300°C)	11.22 mm (0.4416")	Housing	77 (74-80)
			DCT pin	292 (275-307)
			DCT (all)	267 (221-314)
			DCT (crack region)	301 (287-312)

*Refers to specimen number, where 1=top and 9=bottom



JP30, Holder 2, PCDM Specimens, Initial location position

Figure 9. Contour Temperature Plot (°C) for DCT Specimens in JP30, Holder 2



JP31, Holder 11, PCDM Specimens, Center position

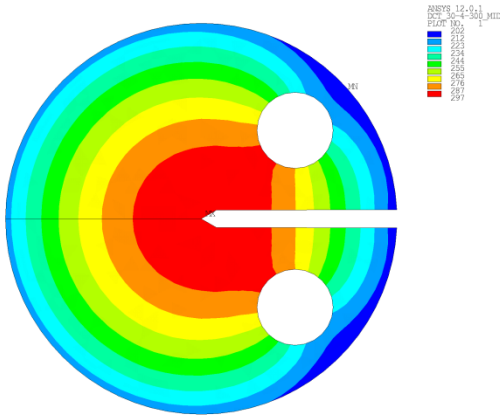
Figure 10. Contour Temperature Plot (°C) for DCT Specimens in JP31, Holder 11

DCT Repeat Designs

The results of the repeated DCT region designs are described in Table 5. Figure 11 through Figure 14 show the temperature contours for the specimens and thermometry.

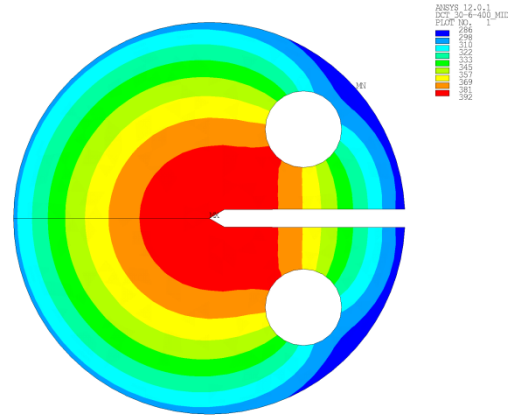
Table 5. Design Summary for Repeat DCT Regions

Experiment	Holder (Design Temperature °C)	Design Specimen Diameter	Part	Temperature (°C) Average (Min-Max)
JP30	4 (300°C)	11.23 mm (0.4423")	Housing	79 (76-82)
			DCT pin	282 (267-294)
			DCT (all)	254 (206-301)
			DCT (crack region)	290 (280-299)
JP30	6 (400°C)	11.19 mm (0.4405")	Housing	81 (78-84)
			DCT pin	371 (358-380)
			DCT (all)	344 (294-392)
			DCT (crack region)	385 (378-390)
JP30	8 (400°C)	11.19 mm (0.4405")	Housing	81 (78-84)
			DCT pin	372 (359-381)
			DCT (all)	345 (295-392)
			DCT (crack region)	386 (380-390)
JP31	5 (300°C)	11.23 mm (0.4423")	Housing	79 (76-82)
			DCT pin	282 (266-294)
			DCT (all)	253 (206-301)
			DCT (crack region)	290 (279-299)



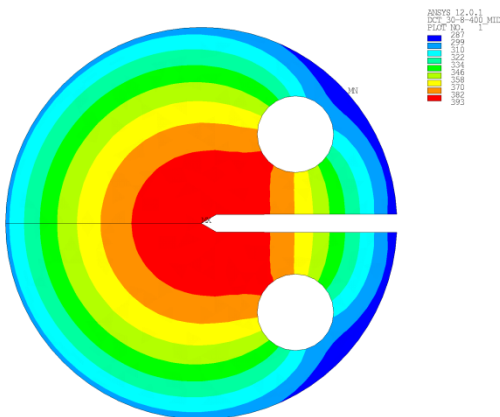
JP30, Holder 4, PCCVN Specimens, Center position

Figure 11. Contour Temperature Plot (°C) for DCT Specimens in JP30, Holder 4



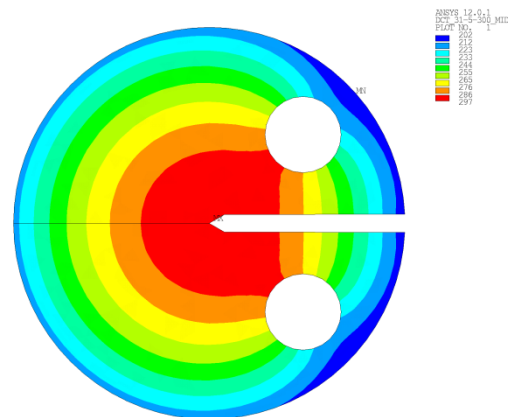
JP30, Holder 6, PCCVN Specimens, Center position

Figure 12. Contour Temperature Plot (°C) for DCT Specimens in JP30, Holder 6



JP30, Holder 8, PCCVN Specimens, Center position

Figure 13. Contour Temperature Plot (°C) for DCT Specimens in JP30, Holder 8



JP31, Holder 5, PCCVN Specimens, Center position

Figure 14. Contour Temperature Plot (°C) for DCT Specimens in JP31, Holder 5

PCCVN New Designs

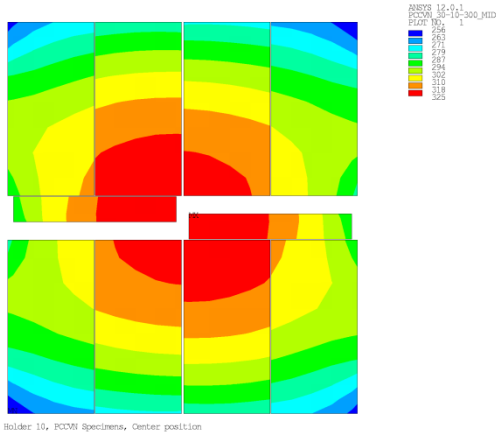
The results of the new PCCVN region designs are described in Table 6. Figure 15 through Figure 17 show the temperature contours for the specimens and thermometry.

Table 6. Design Summary for New PCCVN Regions

Experiment	Holder (Design Temperature °C)	Design Holder Diameter (mm)	Part	Temperature (°C) Average (Min-Max)
JP30	10 (300°C)	11.16 mm (0.4395")	Housing	72 (70-73)
			Holder	213 (201-228)
			Thermometry	314 (291-329)
			PCCVN Specimen	300 (267-325)
JP31	4 (300°C)	11.14 mm (0.4385")	Housing	70 (69-72)
			Holder	222 (209-237)
			Thermometry	312 (289-327)
			PCCVN Specimen	299 (268-324)

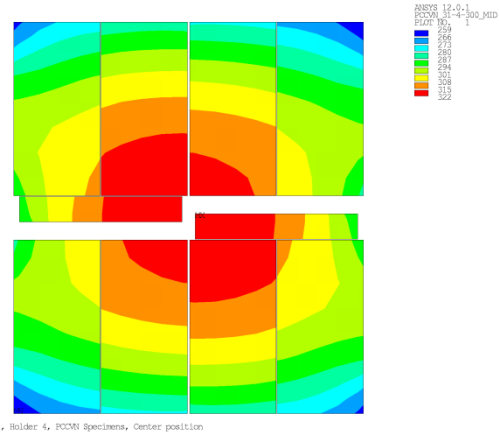
Table 6. Design Summary for New PCCVN Regions

Experiment	Holder (Design Temperature °C)	Design Holder Diameter (mm)	Part	Temperature (°C) Average (Min-Max)
JP31	9 (650°C)	10.96 mm (0.4314")	Housing	77 (75-79)
			Holder	570 (536-612)
			Thermometry	662 (639-677)
			PCCVN Specimen	650 (613-676)



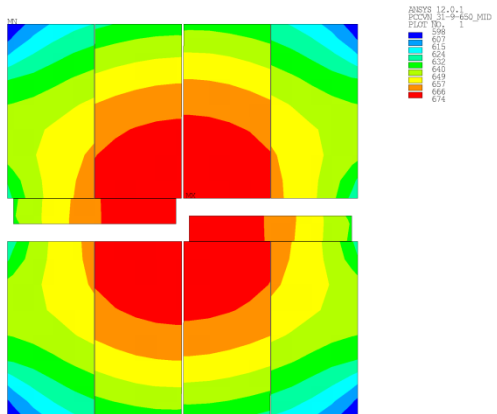
JP30, Holder 10, PCCVN Specimens, Center position

Figure 15. Contour Temperature Plot (°C) for PCCVN Specimens in JP30, Holder 10



JP31, Holder 4, PCCVN Specimens, Center position

Figure 16. Contour Temperature Plot (°C) for PCCVN Specimens in JP31, Holder 4



JP31, Holder 9, PCCVN Specimens, Center position

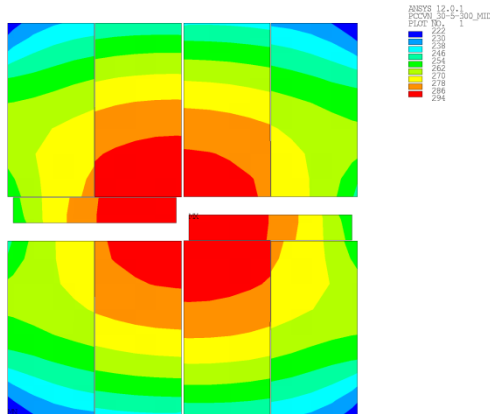
Figure 17. Contour Temperature Plot (°C) for PCCVN Specimens in JP31, Holder 9

PCCVN Repeat Designs

The results of the repeated PCCVN region designs are described in Table 7. Figure 18 through Figure 23 show the temperature contours for the specimens and thermometry.

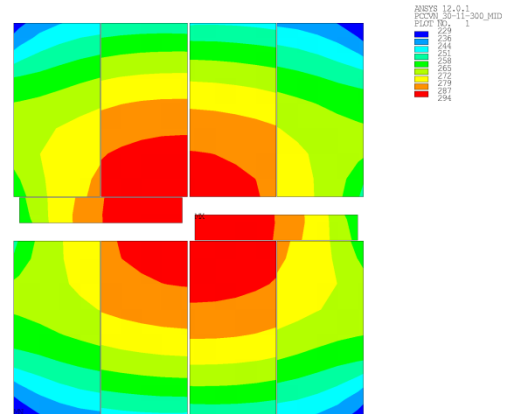
Table 7. Design Summary for Repeated PCCVN Regions

Experiment	Holder (Design Temp °C)	Design Holder Diameter	Part	Temperature (°C) Average (Min-Max)
JP30	5 (300°C)	11.21 mm (0.4412")	Housing	72 (71-74)
			Holder	177 (166-191)
			Thermometry	282 (259-296)
			PCCVN Specimen	267 (235-292)
JP30	11 (300°C)	11.18 mm (0.4402")	Housing	71 (69-72)
			Holder	189 (178-204)
			Thermometry	283 (261-298)
			PCCVN Specimen	270 (239-294)
JP30	12 (300°C)	11.12 mm [bottom] (0.4378")	Housing	69 (68-71)
		11.17 mm [top] (0.4396")	Holder	207 (184-230)
			Thermometry	289 (261-307)
			PCCVN Specimen	277 (241-305)
JP30	13 (300°C)	11.04 mm [bottom] (0.4348")	Housing	67 (66-69)
		11.12 mm [top] (0.4378")	Holder	225 (199-250)
			Thermometry	293 (264-311)
			PCCVN Specimen	283 (247-309)
JP31	6 (300°C)	11.20 mm (0.4408")	Housing	72 (71-74)
			Holder	186 (175-201)
			Thermometry	291 (269-305)
			PCCVN Specimen	276 (244-301)
JP31	8 (400°C)	11.08 mm (0.4362")	Housing	73 (71-74)
			Holder	299 (287-314)
			Thermometry	407 (387-419)
			PCCVN Specimen	391 (359-416)



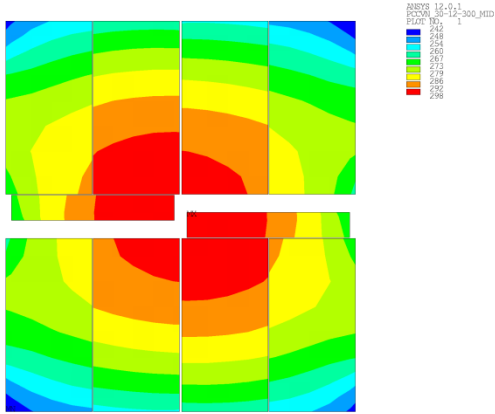
JP30, Holder 5, PCCVN Specimens, Center position

Figure 18. Contour Temperature Plot (°C) for PCCVN Specimens in JP30, Holder 5



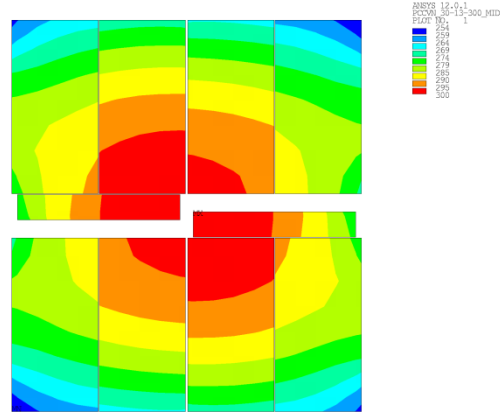
JP30, Holder 11, PCCVN Specimens, Center position

Figure 19. Contour Temperature Plot (°C) for PCCVN Specimens in JP30, Holder 11



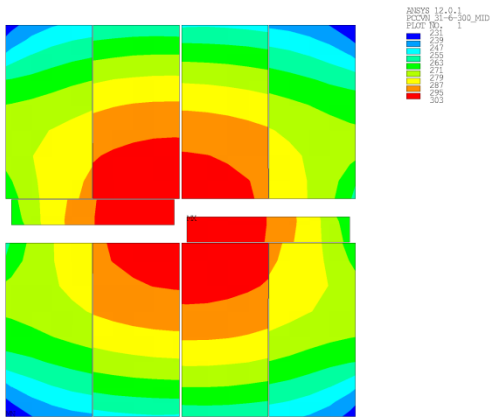
JP30, Holder 12, PCCVN Specimens, Center position

Figure 20. Contour Temperature Plot (°C) for PCCVN Specimens in JP30, Holder 12



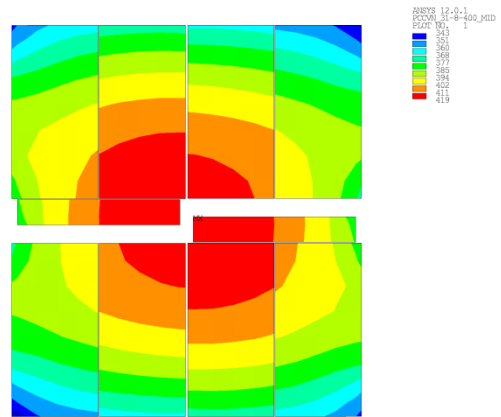
JP30, Holder 13, PCCVN Specimens, Center position

Figure 21. Contour Temperature Plot (°C) for PCCVN Specimens in JP30, Holder 13



JP31, Holder 6, PCCVN Specimens, Center position

Figure 22. Contour Temperature Plot (°C) for PCCVN Specimens in JP31, Holder 6



JP31, Holder 8, PCCVN Specimens, Center position

Figure 23. Contour Temperature Plot (°C) for PCCVN Specimens in JP31, Holder 8

SSJ3 New Designs

The results of the new SSJ3 region designs are described in Table 8. Figure 24 through Figure 25 show the temperature contours for the specimens and thermometry.

Table 8. Design Summary for New SSJ3 Regions

Experiment	Holder (Design Temperature °C)	Design Holder Diameter (mm)	Part	Temperature (°C) Average (Min-Max)
JP30	9 (650°C)	10.88 mm (0.4282")	Housing	75 (74-76)
			Holder	598 (579-620)
			SSJ3 Filler	647 (632-659)
			Spring pin	678 (671-683)
			Thermometry	662 (653-672)
			APFIM Specimen	612 (595-632)
			SSJ3 Specimen	650 (635-664)

Table 8. Design Summary for New SSJ3 Regions

Experiment	Holder (Design Temperature °C)	Design Holder Diameter (mm)	Part	Temperature (°C) Average (Min-Max)
JP31	3 (650°C)	10.69 mm (0.4207")	Housing	70 (69-72)
			Holder	612 (585-641)
			SSJ3 Filler	647 (621-669)
			Spring pin	670 (649-688)
			Thermometry	658 (636-680)
			APFIM Specimen	621 (595-649)
			SSJ3 Specimen	649 (623-673)

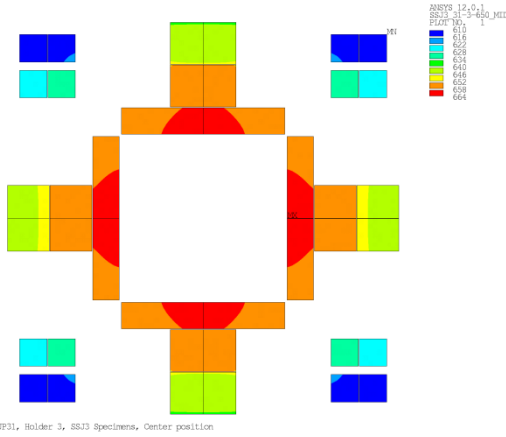


Figure 24. Contour Temperature Plot (°C) for SSJ3 and APFIM Specimens in JP30, Holder 9

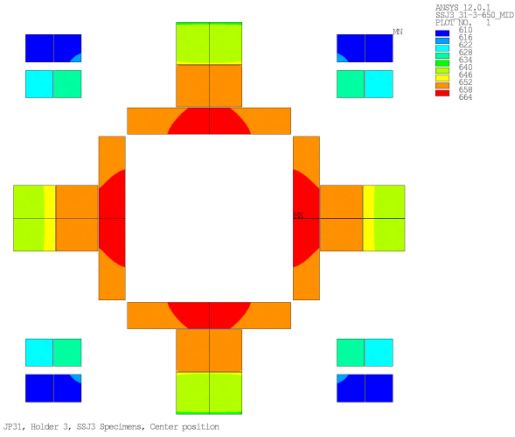


Figure 25. Contour Temperature Plot (°C) for SSJ3 and APFIM Specimens in JP31, Holder 3

SSJ3 Repeat Designs

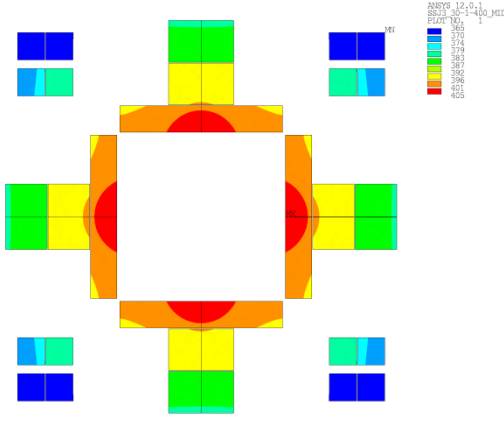
The results of the repeated SSJ3 region designs are described in Table 9. Figure 26 through Figure 33 show the temperature contours for the specimens and thermometry.

Table 9. Design Summary for Repeated SSJ3 Regions

Experiment	Holder (Design Temperature °C)	Design Holder Diameter (mm)	Part	Temperature (°C) Average (Min-Max)
JP30	1 (400°C)	10.67 mm (0.4200")	Housing	65 (65-66)
			Holder	363 (346-380)
			SSJ3 Filler	389 (366-410)
			Spring pin	415 (395-434)
			Thermometry	399 (378-421)
			APFIM Specimen	372 (350-396)
			SSJ3 Specimen	390 (365-413)
JP30	3 (300°C)	11.07 mm (0.4360")	Housing	68 (67-69)
			Holder	238 (232-245)
			SSJ3 Filler	281 (268-291)
			Spring pin	322 (315-329)
			Thermometry	297 (286-312)
			APFIM Specimen	254 (240-272)
			SSJ3 Specimen	283 (266-297)

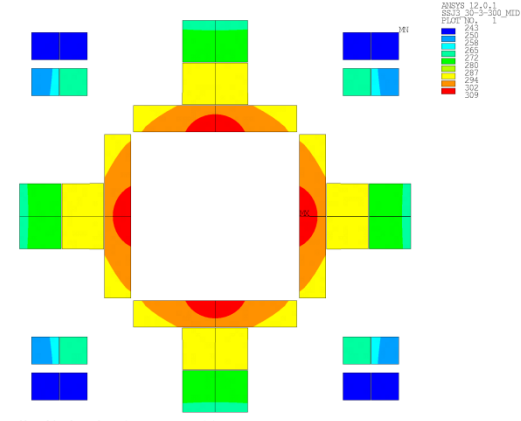
Table 9. Design Summary for Repeated SSJ3 Regions

Experiment	Holder (Design Temperature °C)	Design Holder Diameter (mm)	Part	Temperature (°C) Average (Min-Max)
JP30	7 (400°C)	10.99 mm (0.4328")	Housing	70 (69-71)
			Holder	327 (324-331)
			SSJ3 Filler	376 (366-384)
			Spring pin	424 (422-425)
			Thermometry	396 (389-405)
			APFIM Specimen	345 (333-361)
			SSJ3 Specimen	379 (364-390)
JP31	2 (400°C)	10.70 mm (0.4212")	Housing	65 (65-66)
			Holder	365 (349-381)
			SSJ3 Filler	392 (371-412)
			Spring pin	420 (401-437)
			Thermometry	403 (383-424)
			APFIM Specimen	374 (353-398)
			SSJ3 Specimen	394 (370-416)
JP31	7 (300°C)	11.12 mm (0.4378")	Housing	70 (69-71)
			Holder	232 (228-236)
			SSJ3 Filler	283 (272-291)
			Spring pin	334 (331-336)
			Thermometry	304 (295-316)
			APFIM Specimen	251 (237-268)
			SSJ3 Specimen	286 (270-298)
JP31	10 (300°C)	11.09 mm (0.4368")	Housing	69 (68-70)
			Holder	239 (234-244)
			SSJ3 Filler	285 (273-295)
			Spring pin	332 (326-337)
			Thermometry	304 (294-317)
			APFIM Specimen	256 (242-274)
			SSJ3 Specimen	288 (271-302)
JP31	12 (300°C)	11.02 mm (0.4340")	Housing	67 (66-68)
			Holder	251 (243-259)
			SSJ3 Filler	287 (273-300)
			Spring pin	324 (314-333)
			Thermometry	302 (289-317)
			APFIM Specimen	264 (249-282)
			SSJ3 Specimen	289 (272-305)
JP31	13 (300°C)	10.95 mm (0.4310")	Housing	66 (65-67)
			Holder	261 (250-272)
			SSJ3 Filler	290 (274-305)
			Spring pin	321 (307-333)
			Thermometry	302 (287-320)
			APFIM Specimen	271 (255-291)
			SSJ3 Specimen	292 (273-310)



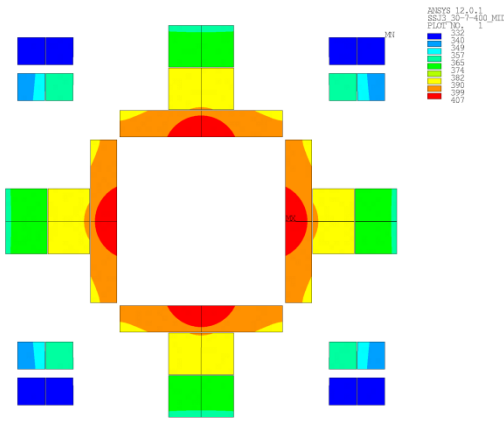
JP30, Holder 1, SSJ3 Specimens, Center position

Figure 26. Contour Temperature Plot (°C) for SSJ3 and APFIM Specimens in JP30, Holder 1



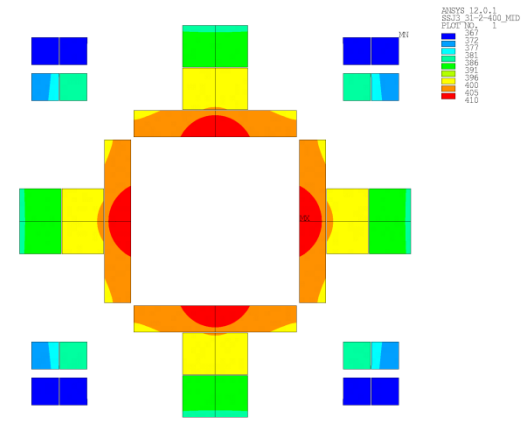
JP30, Holder 3, SSJ3 Specimens, Center position

Figure 27. Contour Temperature Plot (°C) for SSJ3 and APFIM Specimens in JP30, Holder 3



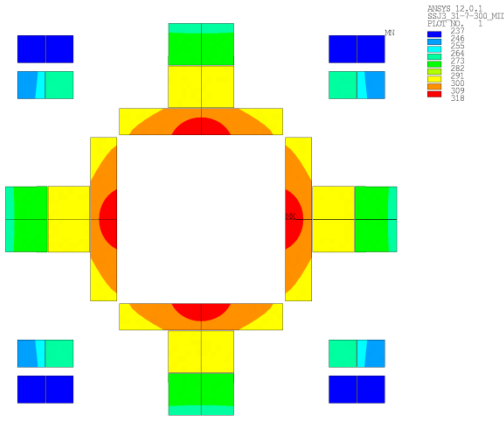
JP30, Holder 7, SSJ3 Specimens, Center position

Figure 28. Contour Temperature Plot (°C) for SSJ3 and APFIM Specimens in JP30, Holder 7



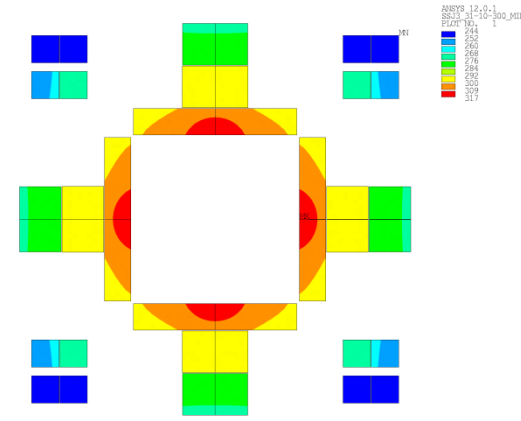
JP31, Holder 2, SSJ3 Specimens, Center position

Figure 29. Contour Temperature Plot (°C) for SSJ3 and APFIM Specimens in JP31, Holder 2



JP31, Holder 7, SSJ3 Specimens, Center position

Figure 30. Contour Temperature Plot (°C) for SSJ3 and APFIM Specimens in JP31, Holder 7



JP31, Holder 10, SSJ3 Specimens, Center position

Figure 31. Contour Temperature Plot (°C) for SSJ3 and APFIM Specimens in JP31, Holder 10

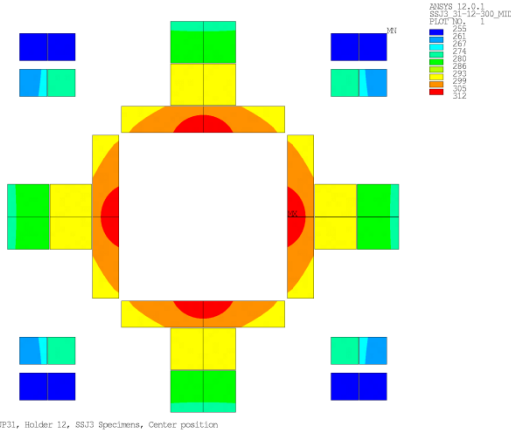


Figure 32. Contour Temperature Plot (°C) for SSJ3 and APFIM Specimens in JP31, Holder 12

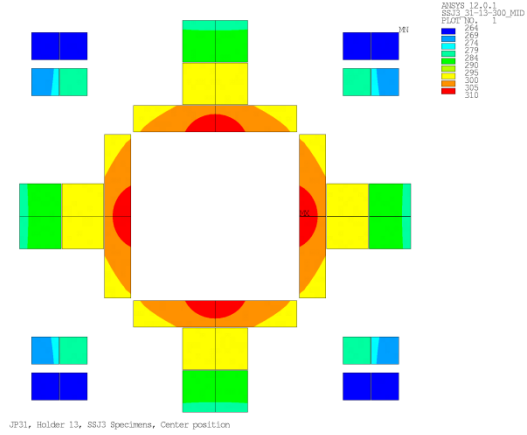


Figure 33. Contour Temperature Plot (°C) for SSJ3 and APFIM Specimens in JP31, Holder 13

TEM New Designs

The results of the new TEM region designs are described in Table 10. Figure 34 shows the temperature contours for the specimens and thermometry.

Table 10. Design Summary for New TEM Regions

Experiment	Holder (Design Temperature °C)	Design Holder Diameter (mm)	Part	Temperature (°C) Average (Min-Max)
JP31	14 (650°C)	10.42 mm (0.4103")	Housing	67 (66-68)
			Holder	628 (602-667)
			Thermometry	671 (656-686)
			TEM Specimen	650 (630-668)

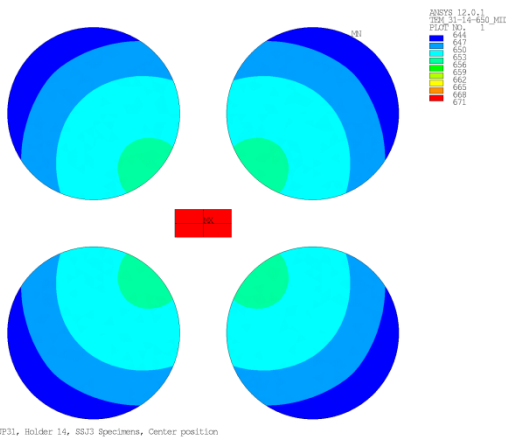


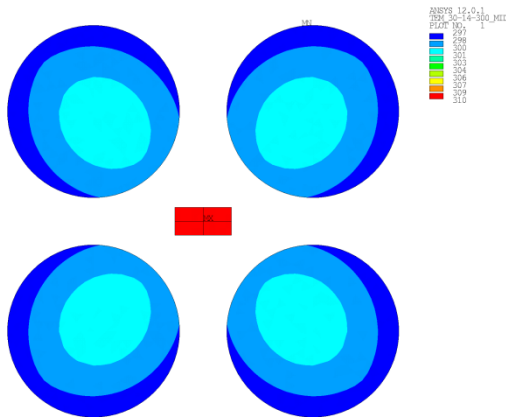
Figure 34. Contour Temperature Plot (°C) for TEM Specimens in JP31, Holder 14

TEM Repeat Designs

The results of the repeated TEM region designs are described in Table 11. Figure 35 through Figure 36 show the temperature contours for the specimens and thermometry.

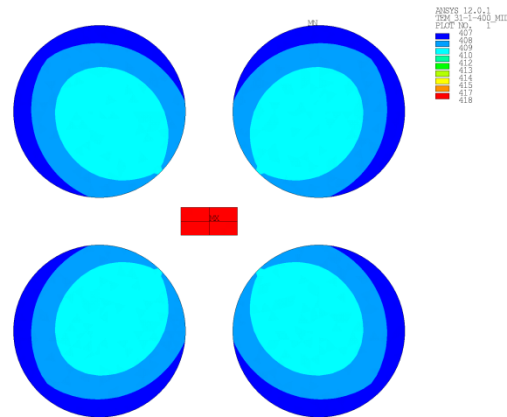
Table 11. Design Summary for Repeated TEM Regions

Experiment	Holder (Design Temperature °C)	Design Holder Diameter (mm)	Part	Temperature (°C) Average (Min-Max)
JP30	14 (300°C)	10.87 mm (0.4280")	Housing	65 (64-65)
			Holder	277 (269-289)
			Thermometry	310 (303-316)
			TEM Specimen	299 (291-306)
JP31	1 (400°C)	10.52 mm (0.4142")	Housing	64 (64-65)
			Holder	390 (379-405)
			Thermometry	418 (408-427)
			TEM Specimen	409 (398-419)



JP30, Holder 14, SS33 Specimens, Center position

Figure 35. Contour Temperature Plot (°C) for TEM Specimens in JP30, Holder 14



JP31, Holder 1, SS33 Specimens, Center position

Figure 36. Contour Temperature Plot (°C) for TEM Specimens in JP31, Holder 1

Summary of Results

Table 12 summarizes the specimen temperatures for each holder in the JP30 and JP31 experiments. Shaded rows indicate new designs. Unshaded rows are re-evaluations of existing designs from the JP28/29 experiments.

Table 12. Design Summary for the JP30 and JP31 Experiments

Capsule	Holder	Design Temperature (°C)	Design Diameter	Specimen Type	Temperature (°C) Avg (Min-Max)
JP30	1	400	10.67 mm (0.4200")	APFIM	372 (350-396)
				SSJ3	390 (365-413)
	2	650	10.82 mm [1-4]* (0.4257") 10.86 mm [5-9]* (0.4274")	DCT	650 (630-666)
	3	300	11.07 mm (0.4360")	APFIM	254 (240-272)
				SSJ3	283 (266-297)
	4	300	11.23 mm (0.4423")	DCT	290 (280-299)
	5	300	11.21 mm (0.4412")	M3PCCVN	267 (235-292)
	6	400	11.19 mm (0.4405")	DCT	385 (378-390)
	7	400	10.99 mm (0.4328")	APFIM	345 (333-361)
				SSJ3	379 (364-390)
	8	400	11.19 mm (0.4405")	DCT	386 (380-390)
	9	650	10.88 mm (0.4282")	SSJ3	650 (635-664)
				APFIM	612 (595-632)
	10	300	11.16 mm (0.4395")	M2PCCVN	300 (267-325)
11	300	11.18 mm (0.4402")	M3PCCVN	270 (239-294)	
12	300	11.12 mm [bottom] (0.4378") 11.17 mm [top] (0.4396")	M3PCCVN	277 (241-305)	
13	300	11.04 mm [bottom] (0.4348") 11.12 mm [top] (0.4378")	M3PCCVN	283 (247-309)	
14	300	10.87 mm (0.4280")	TEM	299 (291-306)	
JP31	1	400	10.52 mm (0.4142")	TEM	409 (398-419)
	2	400	10.70 mm (0.4212")	APFIM	374 (353-398)
				SSJ3	394 (370-416)
	3	650	10.69 mm (0.4207")	APFIM	621 (595-649)
				SSJ3	649 (623-673)
	4	300	11.14 mm (0.4385")	M2PCCVN	299 (268-324)
	5	300	11.23 mm (0.4423")	DCT	290 (279-299)
	6	300	11.20 mm (0.4408")	M3PCCVN	276 (244-301)
	7	300	11.12 mm (0.4378")	APFIM	251 (237-268)
				SSJ3	286 (270-298)
	8	400	11.08 mm (0.4362")	M5PCCVN	391 (359-416)
	9	650	10.96 mm (0.4314")	M5PCCVN	650 (613-676)
	10	300	11.09 mm (0.4368")	APFIM	256 (242-274)
				SSJ3	288 (271-302)
11	300	11.22 mm (0.4416")	DCT	301 (287-312)	
12	300	11.02 mm (0.4340")	APFIM	264 (249-282)	
			SSJ3	289 (272-305)	
13	300	10.95 mm (0.4310")	APFIM	271 (255-291)	
			SSJ3	292 (273-310)	
14	650	10.42 mm (0.4103")	TEM	650 (630-668)	

Conclusions

This calculation establishes design diameters and expected specimen temperatures for the JP30 and JP31 target experiments. The JP30 and JP31 experiments are designed to irradiate F82H specimens of various sizes and types in the flux trap of HFIR at temperatures in the range of 300°C to 650°C. The specimens are typically contained within holders of either DISPAL or a vanadium alloy (V-4Cr4Ti). The primary outer containment is an Al-6061 tube with an outer diameter of 1.27 cm. Helium is used as the fill gas inside the experiment. The specimen temperature is controlled by the size of the gap between the holder and housing. This calculation documents the analyses performed to determine the size of the gas gap for each holder.

References

- [1] J. McDuffee, Thermal Design Analysis for JP30 and JP31, Thermal Hydraulics & Irradiation Engineering Group, Design Analysis and Calculation (DAC), DAC-10-19-JP03, Rev. 1, 2010.
- [2] S. Kim, Design Analysis for JP28/29, Thermal Hydraulics & Irradiation Engineering Group, 2004.
- [3] J. McDuffee, Heat Generation Rates for JP30/31 Materials in the Flux Trap of HFIR, Thermal Hydraulics & Irradiation Engineering Group, Design Analysis and Calculation (DAC), DAC-10-01-JP01, 2010.

8.3 HFIR IRRADIATION EXPERIMENTS – December 31, 2010 - F. W. Wiffen (ORNL)

Summary of Recent, Current and Planned Fusion Materials Program Experiments in the High Flux Isotope Reactor (HFIR)

Experiment Designation	Primary Materials	Specimen Types*	Irradiation Temperature (°C)	Max Exposure (dpa)	Number of Reactor Cycles	Irradiation Period (month/year)
<i>Beryllium reflector (RB) irradiation positions</i>						
RB-15J	F82H	T, F, FT	300, 400	6	10	6/08 – 12/09
<i>Target zone capsules</i>						
JP-25	F82H	T, FT	300, 500	20	10	2/99 - 1/01
JP-26	F82H	T, FT	300,400,500	9	5	12/03-11/04
JP-27	F82H	T, FT	300, 400	21	13	12/03 - 1/08
JP-28	F82H	T, FT	300,400,500	80-?	50	1/05 – 6/13
JP-29	F82H	T, FT	300,400,500	80	50	1/05 - 6/13
JP-30	F82H	T, FT	300,400,650	20	10	6/11 -12/12
JP-31	F82H	T, FT	300,400,650	20	10	6/11 -12/12
<i>Target zone rabbit capsules</i>						
F8A-1	F82H	T, FT	300	50	28	2/09 – 6/13
F8A-2	“	“	“	“	“	“
F8B-1	“	“	“	“	“	“
F8B-2	“	“	“	“	“	“
<i>Target zone rabbit capsules</i>						
JCR-1	SiC/SiC	Bend bars	800	30	15	10/04 – 1/09
JCR-2	“	“	“	“	“	“
JCR-3	“	“	“	“	“	“
JCR-4	“	“	“	“	“	“
JCR-5	“	“	“	>50	>25	10/04 - ??
JCR-6	“	“	“	“	“	“
JCR-7	“	“	“	“	“	“
JCR-8	“	“	“	“	“	“
JCR-9	“	“	500	30	15	10/04 – 1/09
JCR-10	“	“	“	“	“	“
JCR-11	“	“	“	“	“	“
JCR-12	“	“	“	“	“	“

*T = Tensile, F = Fatigue, FT = Fracture Toughness. Most experiments also contain TEM disks, other special purpose specimens, and monitors occupying small spaces.